New developments on the interpretative model of ITER diagnostics using microwaves

P V Tretinnikov

To cite this version:

P V Tretinnikov. New developments on the interpretative model of ITER diagnostics using microwaves. Plasma Physics [physics.plasm-ph]. Université de Lorraine, 2023. English. NNT : 2023LORR0027 . tel-04129152

HAL Id: tel-04129152
https://hal.univ-lorraine.fr/tel-04129152

Submitted on 15 Jun 2023

Thesis

for obtaining the title of
Doctor of the University of Lorraine
in Physics

presented by Pavel TRETINNIKOV

New developments on the interpretative model of ITER diagnostics using microwaves

Public defense on the 13th of April 2023

The jure members:

Prof. Etienne GRAVIER	Jury chairman	Université de Lorraine
Prof. Pascale HENNEQUIN	Referee	LPP Polytechnique
Prof. Elizaveta KAVEEVA	Referee	SPbPU
Prof. Alexey POPOV	Examiner	Ioffe Institute
Dr. Maxime LESUR	Examiner	Université de Lorraine
Dr. Natalia TEPLOVA	Examiner	Ioffe Institute
Prof. Stephane HEURAUX	Supervisor	Université de Lorraine
Prof. Evgeniy GUSAKOV	Co-supervisor	Ioffe Institute

Nancy

2023

Abstract

The turbulence in thermonuclear fusion plasma can lead to increase of the plasma transport coefficient that enhances the particles and energy losses therefore deteriorates the plasma confinement. That is why measurements of the plasma turbulence is important for description of the plasma transport processes. Microwave plasma diagnostics is an efficient kind of the active plasma diagnostics to characterize the turbulence. Their principles are based on the collection of information integrated over the probed plasma volume, and printed on the reflected or scattered waves reaching the detector, for which interpretative models are required to extract the turbulence properties. The radial correlation reflectometry (RCR) and the Doppler reflectometry are widely used technics that provide information on plasma turbulence characteristics. The Collective Thomson Scattering (CTS) is a valuable microwave diagnostic that can give the information about such plasma parameters as the bulk ion temperature, bulk ion composition, the fast particles (alpha particles or ions of a heating beam) velocity distribution. The knowledge of the alpha particle velocity distribution is especially interesting and important to evaluate the ITER performance where the energy amplification of plasma heating power Q is expected to achieve the value about 10. The actual data analysis of the microwave diagnostics, or interpretations of a measured signal is fulfilled assuming a smooth Gaussian probing beam. It was demonstrated that the microwave beams can be significantly distorted due to the edge plasma turbulence, that may lead to misleading interpretations of the diagnostic signal, based on the microwaves, so the diagnostics interpretative models should be analyzed taken into account to the probing beam distortion. The improvement of the microwave diagnostics interpretative models is the main object of the study presented in this thesis. The first PhD task was the description of the edge turbulence influence on an extraordinary polarized (X-mode) probing beam in fusion plasmas. As the extraordinary polarization is planned for the CTS diagnostics on ITER, a first application was devoted to this diagnostic. The existing approach of the microwave beam propagation in the turbulent plasma analytical description for an ordinary polarized (O-mode) beam was adapted for an X-mode beam. The beam distortion and the average broadening of the X-mode beam was investigated numerically for a wide range of the turbulence parameters and probing frequencies, the results are compared to the theory. The second PhD objective was to establish an interpretative analytical model for the CTS experiment with respect to the high edge plasma turbulence. The corresponding improved CTS model was proposed, the importance of taking into account the plasma turbulence in the CTS interpretative model was estimated for a given set of turbulence regimes. The third part of the PhD thesis is devoted to analysis of the edge plasma turbulence influence on the low-threshold parametric decay instability (PDI), which can affect the high power probing or heating microwave beam propagation. The existing theory of the low-threshold PDI describes the parametric decay of a smooth probing beam, it is not applicable for a probing beam significantly disturbed by the plasma turbulence. The numerical investigation of the parametric decay process with respect to the plasma turbulence was another part of the PhD works. The development of the RCR technique data interpretation is the fourth goal in the present thesis. The phase spectrum analysis in the RCR provides the information about the plasma turbulence amplitude, this approach was developed under the Born approximation. The non-linear theory of the RCR gives information about the combination of the plasma turbulence amplitude and the turbulence radial correlation length, the applicability of this method is based on the strong phase modulation due to the plasma turbulence. It was demonstrated that it is possible to combine the two approaches of the RCR data analysis to extract the information about both the turbulence amplitude and radial correlation length.

Key words: microwave beams, plasma turbulence, microwave diagnostics, parametric decay instabilities

Résumé

La turbulence dans le plasma de fusion thermonucléaire peut entraîner une augmentation du coefficient de transport de l'énergie et des particules détériorant ainsi le confinement du plasma. C'est pourquoi les mesures de la turbulence du plasma sont importantes pour la description des processus de transport du plasma. Le diagnostic plasma micro-ondes est un type efficace de diagnostic plasma actif pour caractériser la turbulence. Leurs principes reposent sur la collecte d'informations intégrées dans le volume de plasma sondé, et contenu dans les ondes réfléchies ou diffusées atteignant le détecteur. Pour extraire les propri ´et ´es de turbulence, des modèles interprétatifs sont nécessaires. La réflectométrie de corrélation radiale (RCR) et la réflectométrie Doppler sont des techniques largement utilisées qui fournissent des informations sur les caractéristiques de la turbulence du plasma. La diffusion Thomson collective (CTS) est un diagnostic micro-ondes intéressant qui peut donner des informations sur des paramètres plasma tels que la température des ions en vrac, la composition des ions en vrac, la distribution de vitesse des particules rapides (particules alpha ou ions d'un faisceau chauffant). La connaissance de la distribution de la vitesse des particules alpha est particulièrement recherchée et importante pour évaluer les performances d'ITER où l'amplification énergétique de la puissance de chauffage du plasma Q devrait atteindre la valeur d'environ 10. L'analyse des données réelles des diagnostics micro-ondes, ou les interprétations d'une mesure signal suppose un faisceau de sondage gaussien lisse. Il a été démontré que les faisceaux de micro-ondes peuvent être considérablement déformés en raison de la turbulence du plasma de bord. Ceci peut conduire à des interprétations trompeuses du signal de diagnostic, basées sur les micro-ondes. En conséquence les modèles interprétatifs des diagnostics doivent être analysés en tenant compte de la distorsion du faisceau de sondage. L'amélioration des modèles interprétatifs de diagnostic hyperfréquence est l'objet principal des études présentées dans cette thèse. La première tâche de thèse était la description de l'influence de la turbulence de bord sur un faisceau de sondage polarisé suivant le mode extraordinaire (mode X) dans les plasmas de fusion. Le mode X étant prévue pour le diagnostic CTS sur ITER, une première application a été consacrée à ce diagnostic. L'approche existante de la propagation du faisceau micro-ondes dans la description analytique du plasma turbulent pour un faisceau polarisé ordinaire (mode O) a été adaptée pour un faisceau en mode X. La distorsion du faisceau et l'élargissement moyen du faisceau en mode X ont été étudiés numériquement pour une large gamme de paramètres de la turbulence et de fréquences de sondage, les résultats sont comparés à la théorie de façon satisfaisante. Le deuxième objectif de la thèse était d'établir un modèle analytique interprétatif pour l'expérience CTS en ce qui concerne la turbulence de bord du plasma. Un modèle CTS amélioré a été proposé et l'importance de la prise en compte de la turbulence plasma dans le modèle interprétatif CTS a été estimée pour un ensemble donné de régimes de turbulence. La troisième partie de la thèse est consacrée à l'analyse de l'influence de la turbulence du plasma de bord sur l'instabilité de décroissance paramétrique à bas seuil (PDI), ce qui peut affecter le sondage à haute puissance ou la propagation du faisceau de micro-ondes de chauffage. La théorie existante de la PDI à bas seuil décrit la décroissance paramétrique d'un faisceau sonde lisse, elle n'est pas applicable pour un faisceau sonde fortement perturbé par la turbulence du plasma. L'investigation numérique du processus de décroissance paramétrique par rapport à la turbulence du plasma était une autre partie des travaux de thèse réalisée avec succés. Le développement de l'interprétation des données de la technique RCR est le quatrième objectif de la présente thèse. L'analyse du spectre de phase dans le RCR fournit des informations sur l'amplitude de la turbulence du plasma, cette approche a été développée sous l'approximation de Born. La théorie non linéaire du RCR donne des informations sur la combinaison de l'amplitude de la turbulence du plasma et de la longueur de corrélation radiale de la turbulence, l'applicabilité de cette méthode est basée sur la forte modulation de phase due à la turbulence du plasma. Il a été démontré qu'il est possible de combiner les deux approches de l'analyse des données RCR pour extraire l'information à la fois sur l'amplitude de turbulence et sur la longueur de corrélation radiale.

Mots clés: faisceaux micro-ondes, turbulence plasma, diagnostics micro-ondes, instabilités paramétriques de décroissance

Аннотация

Турбулентность в термоядерной плазме может приводить к увеличению коэффициентов переноса в плазме, это увеличивает потери частиц и энергии, что ухудшает удержание плазмы. Поэтому измерения турбулентности плазмы важны для описания процессов переноса в плазме. Микроволновые диагностики плазмы, как разновидность активных диагностик плазмы, являются эффективным инструментом для получения информации о турбулентности. Их принципы основаны на получении интегральной по зондируемому объему плазмы информации, которая переносится рассеянными или отраженными волнами и регистрируется на детекторе; анализ сигнала на детекторе требует наличия интерпретационной модели для извлечения свойств турбулентности. Радиальная корреляционная рефлектометрия (RCR) и доплеровская рефлектометрия являются широко используемыми методами, позволяющими получить информацию о характеристиках турбулентности плазмы. Коллективное рассеяние Томсона (CTS от англ. Collective Thomson Scattering) является ценной микроволновой диагностикой, которая может дать информацию о таких параметрах плазмы, как объемная температура ионов, объемный ионный состав, распределение по скоростям быстрых частиц (альфа-частиц или ионов греющего пучка). Знание функции распределения альфа-частиц по скоростям особенно интересно и важно для оценки работы ITER, где ожидается, что коэффициент усиления мощности, затраченной на создание и поддержание плазмы, Q достигнет значения около 10. Современный подход к анализу данных микроволновой диагностики или интерпретации измеренных сигналов выполняется в предположении гладкого гауссова зондирующего пучка. Однако было продемонстрировано, что микроволновые пучки могут существенно искажаться из-за пограничной турбулентности плазмы, это может приводить к ошибочной интерпретации диагностических данных, поэтому интерпретационные модели микроволновой диагностики необходимо анализировать с учетом искажения зондирующего пучка. Усовершенствование интерпретационных моделей микроволновых диагностик является основным объектом исследования в данной диссертации. Первой задачей кандидатской работы было описание влияния приграничной турбулентности на зондирующий пучок необыкновенной поляризации (X-мода) в термоядерной плазме, поскольку для диагностики CTS в ITER планируется эта поляризация. Существующий подход к аналитическому описанию распространения микроволнового пучка в турбулентной плазме для пучка обыкновенной поляризации (O-моды) был адаптирован для пучка X-моды. Искажение пучка и среднее уширение пучка необыкновенной поляризации исследованы численно для широкого диапазона параметров турбулентности и частот зондирования, результаты сопоставлены с теорией. Второй задачей кандидатской диссертации было создание интерпретационной аналитической модели для эксперимента CTS с учетом сильной приграничной турбулентности плазмы. Предложена соответствующая усовершенствованная модель CTS, оценена значимость учета турбулентности плазмы в интерпретационной модели для CTS в ряде режимов турбулентности. Третья часть кандидатской диссертации посвящена анализу влияния приграничной турбулентности плазмы на низкопороговую параметрическую распадную неустойчивость (PDI от англ. Parametric Decay Instability), которая может влиять на распространение зондирующего пучка высокой мощности или греющего плазму микроволнового пучка. Существующая теория низкопороговой PDI описывает параметрический распад гладкого микроволнового пучка, она неприменима для пучка, существенно возмущенного плазменной турбулентностью. Численное исследование процесса параметрического распада с учетом турбулентности плазмы является еще одной задачей кандидатской работы. Развитие метода интерпретации данных в диагностике радиальной корреляционной рефлектометрии является четвертой целью настоящей диссертации. Анализ спектра фазы в RCR дает информацию об амплитуде турбулентности плазмы, этот подход был разработан в рамках борновского приближения. Нелинейная теория RCR дает информацию о комбинации амплитуды турбулентности плазмы и ее радиальной корреляционной длины, применимость этого метода основана на сильной фазовой модуляции зондирующей волны, вызванной турбулентностью плазмы. В диссертационной работе продемонстрировано, что возможно комбинировать эти два метода анализа данных в RCR для извлечения информации как об амплитуде турбулентности, так и о ее радиальной корреляционной длине.

Ключевые слова: микроволновые пучки, турбулентность плазмы, микроволновые диагностики, параметрические неустойчивости распада

Résumé étendu en français

La fusion nucléaire

De nos jours, la part dominante des sources d'énergie reste les énergies fossiles : pétrole, charbon et gaz naturel. Ces sources d'énergie sont non seulement limitées pour le siècle actuel, mais aussi une source importante d'émission de dioxyde de carbone. Les émissions de dioxyde de carbone dégradent le climatique en induisant un réchauffement, qui est l'un des problèmes écologiques les plus dangereux de nos jours. Par conséquent, la réduction de l'utilisation des ressources d'énergie fossiles est nécessaire pour la diminution du CO2 dans l'atmospshère mais cela contredit la tendance mondiale à la croissance régulière de la demande d'énergie. Les sources renouvelables ne représentent encore qu'une petite fraction de la quantité totale d'énergie produite. Les centrales éoliennes et solaires ne peuvent pas non plus fournir une quantité stable d'énergie générée. L'énergie nucléaire est réputée très dangereuse, nombre de grands pays ont décidé d'arrêter existantes et d'annuler la construction de futures centrales nucléaires. Pour résoudre la demande énergétique et les problèmes de pollution par le CO2, la fusion thermonucléaire est considérée comme une source d'énergie prometteuse mécanisme de fonctionnement. Il ne produit pas les émissions de dioxyde de carbone et le thermonucléaire source d'énergie - deutérium et tritium (la réaction la plus souvent considérée), est presque illimitée, le deutérium peut être obtenu à partir de l'eau et le tritium peut être produit à partir du lithium dans le réacteur à fusion. Contrairement à l'énergie basée sur la fission nucléaire, elle produit une quantité relativement faible de les déchets radioactifs et il est fondamentalement sûr car seule une petite quantité de combustible présente et brûle dans une chambre de dispositif de fusion en un instant. De plus en principe il n'y a pas de problème d'intermittance de la production d'électricité, typique des sources renouvelables. C'est pourquoi le la fusion nucléaire contrôlée est réputée être une technique prometteuse et la plus favorable pour future source d'énergie. Les recherches sur la fusion nucléaire contrôlée sont au centre de l'actualité société scientifique, le premier réacteur thermonucléaire expérimental international (ITER) a été construit depuis 2010 [3]. Les recherches sur la fusion nucléaire contrôlée sont consacrées à l'investigation du confinement du plasma chaud et de ses régimes de combustion stables. Pour cela des diagnostics sont nécessaires et ici l'étude porte sur ceux utilisant les micro-ondes pour caractériser la turbulence qui influence aussi bien le transport de la chaleur que les diagnostics étudiés dans ce travail.

Turbulence dans les plasmas

Le plasma constitué de particules chargées interagit non seulement avec les champs électromagnétiques, mais génère également ses propres champs électromagnétiques en raison du mouvement local des particules chargées alors que le plasma est neutre à grande échelle (dépassant le rayon d'écrantage électrique dit "de Debye"). Ce comportement complexe du plasma à petite échelle se traduit par une grande variété de modes propres dans le plasma, d'instabilités et à différents régimes de turbulence.

Jusqu'à maintenant, la microturbulence des ondes de dérive est considérée comme la principale source de transport anormale dans un tokamak, ce type de transport entraîne une perte de chaleur beaucoup plus rapide qu'elle ne l'est prédit par l'approche néoclassique - processus de diffusion des particules par rapport à la géométrie toroïdale. Par conséquent, il est important d'étudier les caractéristiques de turbulence du plasma pour dévoiler sa nature, en connexion avec les paramètres du plasma et si possible pour contrôler les échanges d'énergies au sein du plasma. Le transport de chaleur est directement lié au temps de confinement du plasma c'est pourquoi comprendre le régime de turbulence et la possibilité de le contrôler est l'une des principales tâches actuelles de la recherche sur la fusion contrôlée.

Il existe de nombreux diagnostics utilisés pour les mesures de turbulence [17], certains des diagnostics micro-ondes actifs font l'objet de cette étude. De plus, les performances des diagnostics hyperfréquences, qui sont utilisés pour les autres mesures de paramètres plasma tels que la température des ions, la distribution des particules alpha, etc., peuvent être affectées par la turbulence du plasma. Cet effet est également le centre d'intérêt de ce travail.

Diagnostic micro-ondes

Les micro-ondes comme support pour les diagnostics du plasma sont largement utilisées. Il existe deux types de techniques micro-ondes, le premier type est nommé le diagnostic micro-ondes passif. Le général L'idée générale derrière les diagnostics passifs est claire: le plasma, en tant que mélange des charges, ces particules peuvent rayonner, ces émissions dans différentes gammes de fréquences transporte des informations sur les particules chargées et les processus dans lesquels ils sont impliqués. Les diagnostics micro-ondes actifs sont basés sur le plasma sondage par les faisceaux micro-ondes. Il existe de nombreuses techniques micro-ondes actives basées sur la réflexion et diffusion d'un faisceau de sondage, le principe général de ces méthodes est qu'une onde de sondage interagissant avec le plasma provoque une modulation/distorsion de phase ou/et d'amplitude, l'analyse du signal modulé renseigne sur les propriétés du plasma. Les deux types des diagnostics micro-ondes sont largement utilisés dans la recherche sur la fusion, mais les diagnostics passifs sont en dehors des objectifs de cette thèse.

La diffusion Thomson collective (CTS) et la réflectométrie à corrélation radiale (RCR) sont l'objet de cette thèse. Ils sont discutés plus en d´etails dans les sous-sections suivantes.

Réflectométrie

Le diagnostic de réflectométrie est basé sur la réflexion d'une onde de sondage comme un radar, ayant une fréquence f, à partir d'une coupure $x_c(f)$ dans le plasma où l'indice de réfraction s'annule [18]. Le signal enregistré contient les informations sur le plasma dans le volume sondé. Le sondage peut être effectué avec un ensemble de fréquences $\{f_1, f_2, f_3 ...\}$, ce mode opératoire est extrêmement utile pour accéder à des informations sur de nombreuses caractéristiques du plasma. Le signal enregistré transporte les informations sur le plasma dans le volume sondé. Le sondage peut être effectué avec un ensemble de fréquences $f_1, f_2, f_3 ...$, ce qui est extrêmement utile technique qui fournit des informations sur de nombreuses caractéristiques du plasma.

Tout d'abord, il s'agit d'une approche standard pour les mesures de profil de densité de plasma. La méthode d'inversion pour reconstruire la position de la coupure pour chaque fréquence à partir de la variation de phase en fonction de la fréquence est récursive: le profil de densité peut être reconstruit pas à pas [20]. En effet, connaissant le profil de densité jusqu'à la couche de réflexion liée à f, on calcule la phase résultante de ce profil à la fréquence $f + df$. Alors la différence entre cette phase et la phase mesurée pour $f + df$ donne le profil de densité entre les deux couches de réflexion f et $f + df$ et ainsi de suite.

La turbulence du plasma modifie la densité de sorte que la phase d'une onde réfléchie est déformée en raison de la turbulence. La turbulence du plasma est alors caractérisée par son amplitude, sa longueur de corrélation et son temps de corrélation, donc une analyse statistique de la fonction de corrélation des signaux avec des fréquences différentes fournit des informations sur les propriétés de la turbulence.

Réflectométrie de corrélation radiale

La réflectométrie de corrélation radiale est un diagnostic hyperfréquence utilisé pour déterminer les caractéristiques de turbulence. À savoir la longueur de corrélation radiale de la turbulence, son spectre de nombre d'onde et son amplitude [21].

Cette technique fait référence au sondage plasma à plusieurs fréquences (fréquence de balayage ou utilisation de fréquences différentes dans différentes décharges) avec une analyse de corrélation suivante: pour les signaux avec les différentes fréquences et enregistrés à des instants différents. Ce diagnostic possède un large éventail de possibilités pour mesurer les fluctuations de densité plasma [22]. Il est souvent utilisé pour la surveillance des fluctuations dans les flux, en particulier, les études de suppression des transports anormaux dans des régimes de confinement améliorés. Les principaux avantages du RCR sont que ce diagnostic ne se concentre pas uniquement sur les mesures de bord ou de cœur, pratiquement, c'est relativement simple puisqu'il est possible d'avoir un accès unique au plasma. Le fait qu'une onde de sondage diffusant les fluctuations du plasma est dominante au voisinage de la coupure [23] conduit à la localisation des mesures. Il convient de mentionner que, puisque normalement le RCR utilise une incidence d'onde de sondage perpendiculaire, il n'est pas aussi sensible aux effets 2D que la réflectométrie Doppler [24], [25] et la réflectométrie à corrélation poloïdale[26], [27].

Malgré la relative simplicité du RCR mentionné ci-dessus, il faut être prudent avec l'analyse des données. Par exemple, au départ, on a naïvement supposé que la distance entre les positions de coupe à la quelle la corrélation de deux signaux de réflectométrie disparait est la longueur de la corrélation de turbulence, mais cette hypothèse est incorrecte. Cela a été démontré dans des calculs numériques 1D effectués à l'aide de l'approximation de Born [28], interprété par I Hutchinson dans [29], que la longueur de corrélation CCF, à laquelle la fonction de corrélation croisée décroît, peut être significativement plus grande que la longueur de corrélation radiale de la turbulence. Cette dégradation progressive du RCR CCF a été attribuée à la diffusion à petit angle des fluctuations donc à très longue échelle. De plus, les effets non-linéaires peuvent avoir lieu si l'amplitude de la turbulence est suffisamment élevée, selon la théorie développée du RCR non-linéaire en 1D [30] et 2D [31] modèles, lorsque l'amplitude de la turbulence est suffisamment grande, la cohérence du signal décroît sur des échelles inférieures à la longueur de corrélation de la turbulence, typique des expériences RCR dans les grosses machines à fusion. La transition de la réflectométrie de fluctuation du régime de diffusion linéaire au régime de diffusion non linéaire a été décrite dans [30], [31]. Les données de réflectométrie de corrélation dans le régime linéaire sont fortement affectées par la diffusion aux petits angles réduisant la localisation des diagnostics. En régime non linéaire, l'élargissement du spectre du signal réfléchi n'est pas non plus localisé à la coupure et déterminé par la large région de plasma dans laquelle se situe la turbulence. Malgré cela, la décroissance de la cohérence dans la réflectométrie à corrélation radiale dans le régime fortement non linéaire n'est sensible qu'au niveau de turbulence au voisinage de la coupure, d'où la localisation précise. Le rôle d'une mauvaise diffusion localisée aux petits angles dans la décroissance de la cohérence n'y est pas si important.

Diffusion Thomson collective

La diffusion Thomson (incohérente) est un diagnostic couramment utilisé pour les mesures de la température et de la densité des électrons dans un plasma de fusion en le sondant avec un faisceau électromagnétique et en analysant le spectre du rayonnement diffusé reçu [21]. Le diagnostic des ions dans un plasma de fusion est une tâche plus difficile puisque l'interaction des ondes électromagnétiques injectées avec les ions est beaucoup plus faible qu'avec les électrons beaucoup plus légers du fait que le rayonnement dipolaire d'une particule chargée est inversement proportionnel à sa masse, l'interaction directe est donc négligeable. Cependant, dans le plasma de fusion, les ions ont des fluctuations microscopiques collectives, cette dynamique est imprimée dans la distribution des électrons en raison de l'écrantage de Debye. Lorsque les électrons se déplacent, ils provoquent eux aussi des fluctuations microscopiques, mais à des échelles supérieures à la longueur de Debye, ces fluctuations ressemblent à celles un trou d'électrons. Ainsi, à des échelles supérieures à la longueur de Debye, les fluctuations microscopiques collectives des électrons sont essentiellement dues aux ions. Dans les mesures CTS, ces fluctuations collectives de la distribution des électrons interagissent avec un faisceau d'ondes électromagnétique de sondage ainsi, le rayonnement diffusé porte indirectement les informations sur la dynamique des ions.

Le diagnostic CTS permet d'obtenir de nombreuses informations sur les caractéristiques du plasma, à savoir: la température des ions du plasma, la rotation des ions, la concentration des différent ions, la densité des ions et la fonction de distribution de vitesse 1D des particules rapides [34]. La distribution rapide des particules est importante à connaître pour l'étude des particules alpha dans le plasma de fusion [35], [36]; une autre application clé de cette méthode consiste à explorer la dynamique d'un faisceau de particules rapides dans des expériences de chauffage par injection de faisceaux neutres au plasma (NBI), avec ce diagnostic, il est possible de suivre la distribution de la vitesse du faisceau de neutres 1D avec une résolution temporelle [37]-[39].

Propagation de faisceaux micro-ondes dans un plasma turbulent

Les faisceaux électromagnétiques à haute fréquence sont largement utilisé dans la recherche sur la fusion thermonucléaire comme outil de chauffage plasma localisé et commande de courant, par exemple pour chauffage par résonance cyclotron électronique (ECRH) [41] et génération de courant de cyclotron électronique (ECCD) [42]. Un autre domaine d'applications utilisant des faisceaux électromagnétiques quasi-optiques dans la fusion nucléaire est un diagnostic plasma, possédant haute résolution spatiale, comme la diffusion Thomson collective [32] et réflectométrie Doppler [43]. La propagation de faisceaux légèrement divergents est relativement facile à analyser, sa distribution de champ peut être prédite avec précision pour une densité de plasma lisse donnée et les profils de champ magnétique. Néanmoins, il a été démontré que présence de turbulence de bord de plasma est capable de significativement perturber un faisceau injecté depuis l'extérieur [44]-[48].

Les modes de déchirements néoclassiques (NTM) augmentent localement le transport radial qui dégrade les performances du plasma, c'est pourquoi la suppression des NTM est nécessaire pour une opération de réacteur à fusion. Position précise et l'intensité du lecteur de courant influencent l'efficacité de la suppression des NTM [47], [49]-[51]. Le profil de dépôt d'énergie s'élargit, associé à un élargissement du faisceau lancé, peut conduire à réduction de l'efficacité de la stabilisation. En termes de diagnostic plasma micro-ondes l'élargissement du faisceau de sondage se traduit par détérioration de la résolution spatiale et cela peut compliquer l'interprétation des données des diagnostics. La conformation expérimentale du dépôt ECRH élargi a été observée pour le tokamak DIII-D[52]. La puissance des micro-ondes se diffusant sur les blobs et la turbulence de bord a également été examinée expérimentalement sur TORPEX [53, 54] et tokamak TCV [55, 56] respectivement. Pour tenir compte du rôle du turbulence du plasma dans la propagation du faisceau plusieurs méthodes ont été développées. Description statistique de la diffusion des ondes EC, basé sur l'équation de Fokker-Planck, a été dérivé dans [57]. Ce modèle décrit une diffusion de trajectoire de rayon sur les blobs comme un processus multi-diffusion. Cette approche implique une structure spécifique des blobs et permet de obtenir un devis plutôt pertinent pour un faisceau moyen élargissement. Plusieurs codes numériques ont été développés en ce qui concerne l'effet d'un faisceau diffusant la turbulence : WKBeam [58], IPF-FDMC [59], EMIT-3D [60], REFMUL3 [61], COMSOL [62], FWR2D et FWR3D [45]. Propagation d'un faisceau polarisé ordinaire (mode O) dans le plasma turbulent a été analysé analytiquement et numériquement, à l'aide de la suite de codes REFMUL, dans [44]. Il a été démontré que la présence d'une couche de bordure turbulente peut entraîner une distorsion drastique de la forme du faisceau en fonction de l'amplitude de la turbulence. L'approche analytique développée a permis de décrire des géométries moyennes caractéristiques du faisceau dans un plasma turbulent et conduisant à des recommandation pour ITER. Des expériences ECRH ont été faites en particulier dans le cas du contrôle NTM où la largeur du faisceau est crucial pour atteindre l'île magnétique avec dépôt de puissance à la bonne position.

L'élargissement moyen du faisceau de micro-ondes dans un plasma turbulent influence la performances de diagnostic micro-ondes est étudie dans cette thèse et, en particulier, dans le cas de l'onde du mode X utilisé par CTS.

Instabilité de décroissance paramétrique

Les diagnostics micro-ondes sont basés sur une interaction d'onde de sondage avec les particules chargées ou les fluctuations du plasma dans une zone sondée, mais il faut d'abord qu'un faisceau injecté atteigne cette zone d'interaction. Le faisceau micro-onde de sondage peut être déformé par la turbulence du plasma et aussi par l'instabilité de décroissance paramétrique (PDI). Les bases associées à PDI sont passées en revue dans cette section.

Il existe une grande variété de modes plasma électromagnétiques, si les amplitudes des ondes sont suffisamment petites, leur dynamique peut être bien décrite par un système linéaire d'équations de Maxwell. Dans le cas contraire d'une onde de forte amplitude les effets non linéaires se produisent. Le premier effet non linéaire (par la décomposition de l'amplitude des ondes) est l'interaction à trois ondes, conduisant à l'instabilité de décroissance paramétrique [63].

L'excitation de l'instabilité de décroissance paramétrique nécessite non seulement de remplir les conditions de résonance des ondes, mais aussi dépassement du seuil de puissance de décroissance de la pompe. Le seuil est déterminé par le fait que les ondes filles reçoivent l'énergie de la pompe et en même temps perdent également de l'énergie en raison de son flux convectif depuis la zone de résonance ou de sa dissipation. Alors l'excitation d'instabilité effective n'est possible que pour une amplitude d'onde de pompe suffisamment élevée, ce critère de seuil a été analysé par Piliya [64] - [66] et Rosenbluth [67] 50 il y a des ans.

Dans le cas de plasmas inhomogènes à profil non-perturbé monotone, les seuils pour différents scénarios de décroissance de l'onde de pompe paramétrique a été analysé et évalué par différents auteurs il y a plus de trois décennies. Les résultats de ces études, résumées par ex. dans [68], prévoir des seuils de puissance de l'instabilité qui sont beaucoup supérieure à la puissance des gyrotrons modernes en raison de la forte d'énergie de la fille ondes de la zone de couplage, ce qui rend impossible leur amplification significative. Mais les profils de plasma dans un dispositif de fusion ne sont pas toujours monotones, par exemple il peut ne pas être monotone à cause d'un îlot magnétique, donc si une ou les deux ondes filles sont en quelque sorte piégées dans la zone non monotone du plasma et les conditions de désintégration sont remplie là, la perte d'énergie pour ces ondes est considérablement réduite, ce qui réduit considérablement le seuil. Au cours de la dernière décennie, divers scénarios de décroissance paramétrique des micro-ondes ont été analysés. Les résultats de cette analyse, résumés dans [69], prédire le seuil d'instabilité à un niveau inférieur de deux à quatre ordres de grandeur à celui d'un profil de densité monotone.

Objectifs de cette thèse

L'amélioration des modèles interprétatifs de diagnostic hyperfréquence est l'objet principal de cette thèse. L'analyse analytique et numérique d'une distorsion de faisceau hyperfréquence en mode X due à la turbulence du plasma est réalisée dans ce travail pour différents plasmas et scénarios de turbulence. Ce type de polarisation est prévu pour les diagnostics CTS sur ITER. Le modèle analytique de la propagation du faisceau micro-ondes dans le plasma turbulent initialement développé pour un faisceau polarisé ordinaire (mode O) a été adapté pour un faisceau en mode X. La distorsion du faisceau et l'élargissement moyen du faisceau en mode X ont été étudiés numériquement pour une large gamme de paramètres de turbulence et les fréquences de sondage. Les résultats sont comparés à la théorie, des recommandations correspondantes pour les diagnostics ITER CTS sont fournies. Ce travail et les résultats sont décrits dans le deuxième chapitre.

Le troisième chapitre est consacré à la description du modèle analytique interprétatif proposé pour une expérience CTS par rapport à la haute turbulence du plasma de bord. Le modèle CTS amélioré correspondant a été proposé et soutenu par les simulations numériques et évaluations.

Les spectres de rayonnement enregistrés dans le CTS sont évalués avec et sans prise en compte de la en sondant l'effet de distorsion du faisceau, l'importance de la correction du modèle analytique est estimée. L'instabilité de décroissance paramétrique à bas seuil peut affecter un faisceau de micro-ondes de sondage, l'analyse du modèle PDI par rapport à la turbulence du plasma de bord est fourni dans le quatrième chapitre de la présente thèse. La théorie développée du PDI à bas seuil décrit la décroissance paramétrique d'un faisceau de sondage lisse, il n'est pas applicable pour un faisceau de sondage fortement perturbé par la turbulence du plasma. L'étude numérique du processus de décroissance paramétrique par rapport à la turbulence du plasma a été réalisée pour différents régimes de turbulence.

Le cinquième chapitre est consacré au développement de la technique d'analyse RCR. L'analyse du spectre de phase dans le RCR fournit des informations sur l'amplitude de la turbulence du plasma, cette approche a été développée avec l'approximation de Born. La théorie non linéaire du RCR donne des informations sur la combinaison de l'amplitude de la turbulence du plasma et la longueur de corrélation radiale de la turbulence, l'applicabilité de cette méthode est basée sur la forte modulation de phase en raison de la turbulence du plasma. Dans cette thèse, il est démontré qu'il est possible de combiner les deux approches de l'analyse des données RCR pour extraire les informations sur l'amplitude de turbulence et la longueur de corrélation radiale.

Contents

1 Introduction

A brief overview of the problems in the world power engineering together with one of the most promising and reliable technics of the future power engineering - controlled nuclear fusion are described in the first section of the introduction. Microwave plasma diagnostics are part of the main tools in the controlled nuclear fusion researches, the overview of the general microwave plasma diagnostics is given in the second section with the main focus on the radial correlation reflectometry (RCR) and the collective Thomson scattering (CTS). Plasma turbulence and its influence on the microwave diagnostics are discussed in the third part of this chapter. The introduction is concluded with formulation of the goals and the main findings in this PhD work.

1.1 Nuclear fusion

The world's energy consumption steadily grows, the reduction that took place in 2020 due to the COVID-19 pandemic was temporal, the energy demand bounced back to around pre-pandemic levels in 2021 [1]. The dominant part of the energy sources remains to be the fossil ones: oil, coal and natural gas. These energy sources are not only limited for the current century, but also being a significant source of the carbon dioxide emission. Global energy-related CO_2 emissions approached their second-largest annual increase ever in 2021 [2]. The carbon dioxide emissions deteriorate the global warming process, that is one of the most dangerous ecological problem nowadays. Therefore the reduction of using the fossil energy resources is necessary for decrease of the CO_2 emission, but this contradicts the global tendency of the steady growth in the energy demand. The renewable sources are still a small fraction in the total amount of the generated energy, the wind and solar based power plants also can not provide stable amount of the generated power. The nuclear energy is reputed to be highly dangerous, a number of big countries decided to stop existing and to cancel construction of future nuclear power plants.

To solve the energy demand and CO_2 pollution problems the thermonuclear fusion is considered as a promising power generation mechanism. It does not produce the carbon dioxide emissions and the thermonuclear energy source - deuterium and tritium (the most often considered reaction), is almost unlimited, the deuterium can be obtained from water and the tritium can be produced from lithium in the fusion reactor. Unlike the nuclear fission based energy, it produces relatively small amount of the radioactive waste and it is fundamentally safe since only small amount of the fuel presents and burns in a fusion device chamber in a time moment. Moreover in principle there is no the power generation stability problem, that is typical for the renewable sources. That is why the controlled nuclear fusion is reputed to be a promising and the most favorable technics for the future energy source. The controlled nuclear fusion researches are in the focus of the modern scientific society, the first International Thermonuclear Experimental Reactor (ITER) has being constructed since 2010 [3].

The physical mechanism behind the power producing in a future thermonuclear power plant is a fusion of light atomic nucleuses leading to generation of products with high kinetic energies (see figure 1). Nowadays it seems that the reaction between the hydrogen isotopes: deuterium

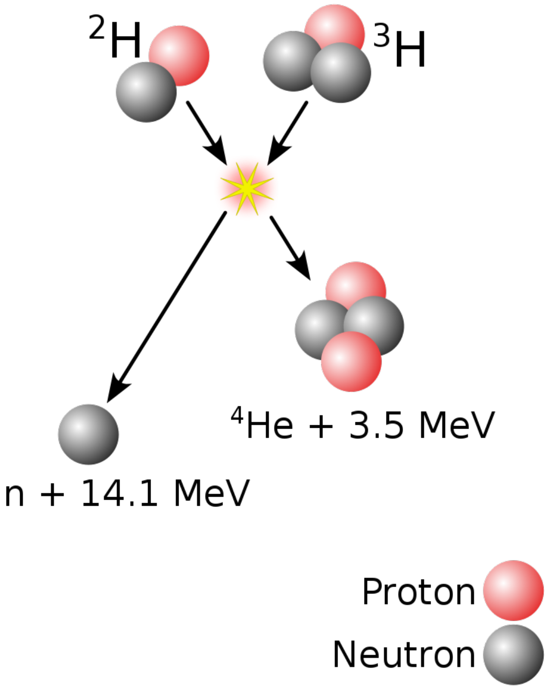

Figure 1: Fusion reaction between deuterium and tritium scheme

and tritium ($D - T$ reaction) is the best candidate because of its relatively large reaction cross-section [4], [5]. The D-T reaction cross-section and its comparison for the other main fusion reactions is demonstrated on the figure 2. Nevertheless even the D-T reaction cross-section is

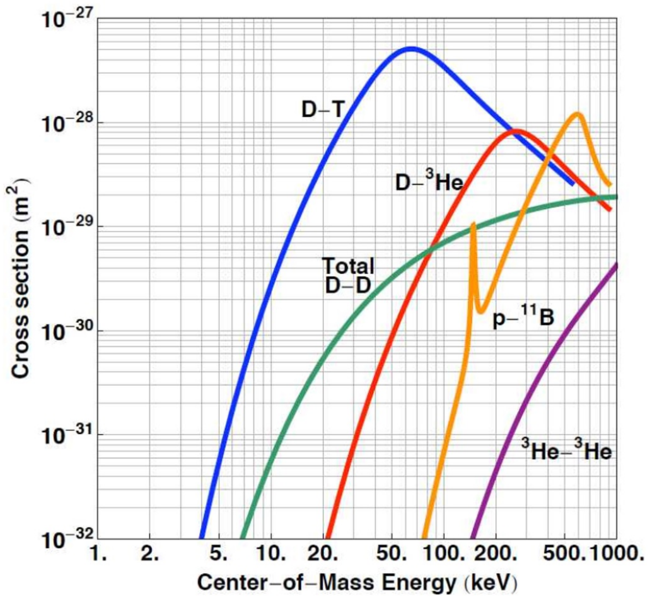

Figure 2: Cross-section versus center-of-mass energy comparison for general fusion reactions

very small due to the fact that the two charged particles has to overcome the Coulomb repulsion barrier by approaching at close enough distance so that the nuclear force became dominant and they can fuse. Therefore the effective fusion energy generation is possible under the certain plasma conditions. First of all the plasma temperature T must be high enough to approach the D-T reaction cross-section maximum (see figure 2), that requires the temperature T of the order of dozen keV, that is of the order of 150 million Kelvin and comparable with the Sun temperature. Also the plasma density must be high enough in order to provide enough number of the fusion reactions so the generated energy, the fusion energy has to overcome the energy losses for heating and maintaining the plasma in order to make the fusion energy profitable.

The requirement describing the plasma thermonuclear burning to be self-sustaining is the Lawson criterion [6]. This criterion, obtained by J D Lawson in 1957, gives the quantitative value for the peak plasma electron density n_e and the global energy confinement time τ_E product that is required for the self-sustaining plasma burning

$$n_e\tau_E > 2 \times 10^{20}\mathrm{m}^{-3} \cdot \mathrm{s} \text{ or } 2 \times 10^{14}\mathrm{cm}^{-3} \cdot \mathrm{s} \tag{1.1.1}$$

The Lawson criterion is a restriction for the two plasma parameters, the extension of the Lawson criterion was derived and accounts for three plasma parameters, it is known as the «triple product»

$$n_e\tau_E T > 3 \times 10^{21}\mathrm{m}^{-3} \cdot \mathrm{s} \cdot \mathrm{keV} \text{ or } 3 \times 10^{15}\mathrm{cm}^{-3} \cdot \mathrm{s} \cdot \mathrm{keV} \tag{1.1.2}$$

this criterion is widely used for the assessment of beneficial fusion energy generation possibility [5].

The implementation of achieving the triple product criterion (1.1.2) is a difficult task for the physicists and engineers. It is clear that the hot plasma ($T \sim 150$ million Kelvin) can not be confined by any material walls. The steady thermonuclear reaction takes place in the stars, the confinement there is provided by the gravity force, of course this plasma confinement mechanism can not be used for the future thermonuclear power plants. One of the possible ways for achieving the triple product criterion is achieving plasma with high density and temperature while having a low energy confinement time. Such an explosive method is called inertial confinement. There are the researches in the inertial confinement, one of the most impressive results in the inertial confinement has been achieved at the end of 2022 in the National Ignition Facility (NIF), it is a laser-based inertial confinement fusion research device, located at Lawrence Livermore National Laboratory in Livermore in the United States. NIF's mission was to achieve fusion ignition with high energy gain, and it achieved the first scientific breakeven controlled fusion experiment on December 5 in 2022, with an energy gain factor of 1.5. But so far (at least before the impressive result on NIF) it seems that the another approach - the magnetic plasma confinement is the most favorable candidate for the future power plants. Plasma as a mixture of the gases - electrons and ions interacts with electromagnetic fields, it can be confined by the magnetic field due to the fact that the charged particles move along a magnetic field line along a spiral trajectory so it seems possible to confine the plasma within closed magnetic surfaces. There were several types of the magnetic confinement schemes, the two main of them are stellarator, proposed by L Spitzer in 1951 [7], and tokamak briefly reviewed in this thesis.

1.2 Tokamak and plasma confinement

As it was stated in the previous section the plasma confinement is possible within a closed magnetic surface, the general scheme for generation the closed magnetic surfaces was a torus-like facility with magnetic coils around the torus, the coils generate the closed magnetic configuration in the torus volume. Since the very beginning of these researches it was evident that the charged particles drift, associated with the magnetic field lines curvature, results in significant particles losses from the plasma volume. To suppress the particles losses a rotational transform (poloidal magnetic field component) has to be introduce to compensate the particle drifts. There were the two main approaches of creating the rotational transform, the first one is by means of extra external magnetic coils and the second approach is generation of the plasma current in the toroidal direction, this current naturally generates the necessary helicoidal magnetic field line. The second scheme is know as the tokamak, it originated from a Russian word «токамак», «ТОроидальная Камера с Магнитными Катушками», that means «toroidal camera with magnetic coils». The tokamak concept was proposed by I Tamm and A Sakharov in 1950, the plasma confinement regime, as a pinch with high toroidal magnetic field, was discovered by Yavlinsky [8] - [11].

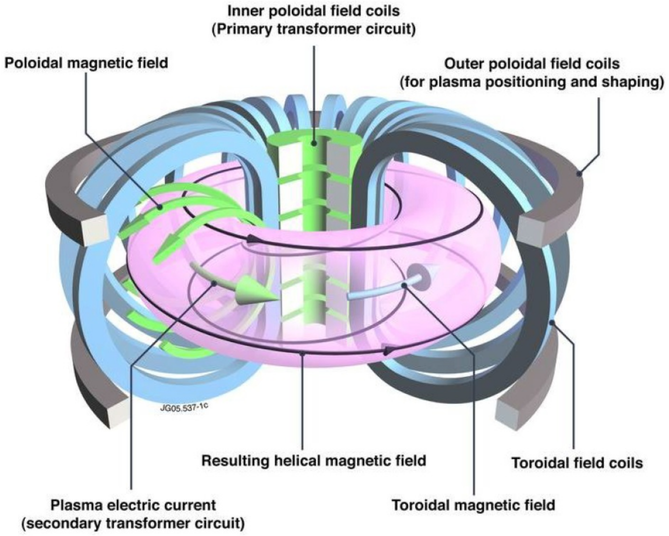

Figure 3: The tokamak principal scheme [12]

A fundamental scheme of a tokamak is shown in the figure 3, it is a doughnut-like facility surrounded by magnetic coils. The primary transformer circuit is situated in the center of toroidal camera, plasma itself forms the secondary winding of the transformer. The system or the surrounding toroidal field coils generates the toroidal magnetic field, the plasma current creates the poloidal magnetic field. The two magnetic field components result in the helical magnetic field configuration that is needed for the plasma confinement, this configuration imposes to the particles that have drifted towards the outside of the ring to go back into the centre, preventing the plasma from escaping.

A charged particle can be confined within a closed magnetic surface, but the confinement is not perfect for the plasma due to the collisions in the plasma. When the charged particles collide they move to a neighbor magnetic surface, if the charged particles appear beyond the last closed magnetic surface (LCS), they are no more confined. Such a mechanism leads to the particles and energy losses from a tokamak.

The collisional mechanism of the energy and particles transport was described by the theory, but it turned out the real losses can be significantly higher, that deteriorates the confinement [13]. The anomalous transport was explained as a consequence of the drift waves in plasma, the instability related to the plasma micro-turbulence, located dominantly at the plasma edge, [14]. That is why study of the plasma turbulence is of prime importance in the nuclear fusion research.

1.3 ITER

There are around 50 operating tokamaks in the world, a number of specific researches have being fulfilled on these facilities. The amount of the fusion energy that a tokamak can produce correlates directly to the number of fusion reactions taking place in its core. It is pretty clear that the larger the vessel, the larger the volume of the plasma, and therefore the greater the potential for fusion energy. According to the ITER design, its plasma volume will be about ten times of the largest fusion machine operating today, the ITER tokamak will be a unique experimental tool, capable of longer fusion plasma burning, producing alpha particles and better confinement. ITER has being built for almost 15 years now, its completion progress is estimated as 77.7% for the time being (on December 2022) [15], the schematic view of this fusion device is depicted on the figure 4.

The ITER machine has been designed specifically to achieve the following goals:

- **Achieving a deuterium-tritium plasma with internal fusion heating being the main source for sustaining the fusion conditions**

  Modern fusion researches are at the threshold of exploring a burning plasma. In a burning plasma, the heat from the fusion reaction is confined within the plasma efficiently enough for the self-heating effect to dominate any other form of heating. As the first such burning plasma device in the world, ITER will offer scientists a unique opportunity to chart new territory in controlled nuclear fusion.

- **Generate 500 MW of fusion power to achieve Q=10**

  The ration of produced fusion power from a total input heating power is the gain factor of plasma heating power Q. In 1997 Joint European Torus (JET tokamak) produced 16 MW of fusion power from a total input heating power of 24 MW so Q=0.67 was achieved. ITER is designed to yield in its plasma a ten-fold return on power Q=10 or 500 MW of fusion power from 50 MW of input heating power. Thought it should be mentioned that ITER will not convert the heating power it produces to electricity.

- **Contribute to the demonstration of the integrated operation of technologies for a fusion power plant**

It will be possible to study plasmas and technologies of heating, diagnostics and plasma control under conditions similar to those expected in a future power plant.

- **Test tritium breeding**

  The world supply of tritium is not enough for the future fusion power plants, the tritium generation in tandem with the fusion energy generation by breeding the tritium in a lithium blanket is a possible solution. Feasibility of the tritium breeding blankets under the conditions close to a future fusion power plant will be demonstrated.

- **Demonstrate the safety characteristics of a fusion device**

  The ITER fusion device became the first in the world to have successfully undergone the rigorous examination of its safety case. One of the primary goals of ITER operation is to demonstrate control of the plasma and fusion reactions with negligible consequences to the environment.

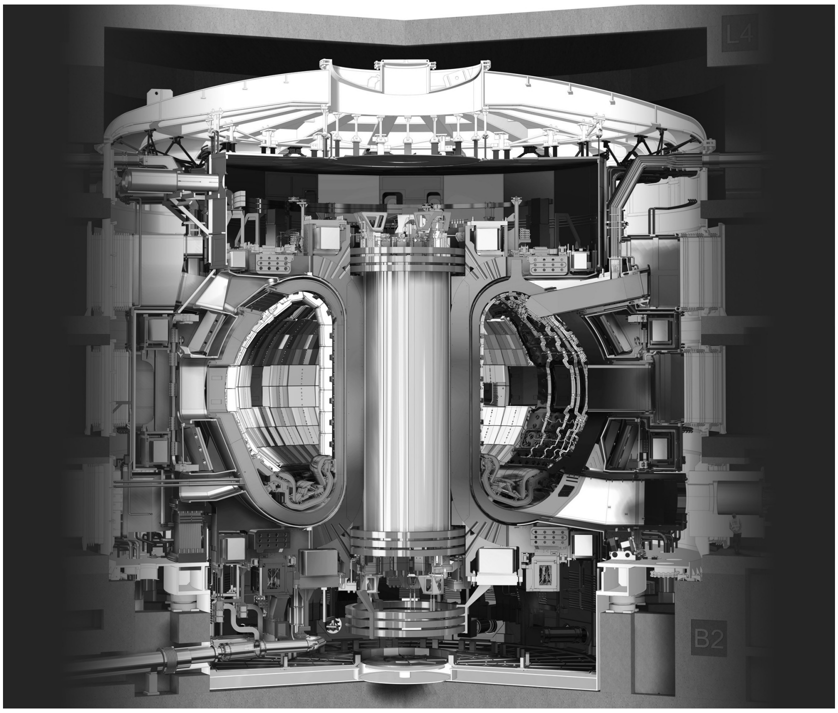

Figure 4: ITER schematic view [15]

The main characteristics that expected to be achieved in ITER are shown in the table 1, more details of the ITER design can be found in [16].

parameter	value	parameter	value
Major radius, m	6.21	Pulse duration, s	~ 500
Minor radius, m	2.0	Average plasma density, m^{-3}	$\sim 10^{20}$
Plasma volume, m^3	837	Heating power, MW	50
Magnetic field, T	5.3	Fusion power, MW	500
Plasma current, MA	15	Energy gain factor Q	$\gtrsim 10$

Table 1: The main ITER characteristics

1.4 Plasma turbulence

Plasma as a mixture of charged particles interacts not only with external electromagnetic fields, but also generates its own electromagnetic fields due to local charged particles movement whereas the plasma is neutral on large scales (exceeding the Debye radius). This complicated plasma behavior on the small scales results in a vast variety of the eigenmodes in plasma, instabilities and turbulence.

Nowadays the drift wave microturbulence is regarded as the main source of the anomalous transport in a tokamak, the anomalous transport results in the heat loss much faster, than it is predicted by neoclassical approach - particles diffusion process with respect to the toroidal geometry. Therefore, it is important to study the plasma turbulence characteristics for understanding its nature, connection with the plasma parameters and eventually for the transport control. The heat transport is directly connected to the plasma confinement time that is why understanding the turbulence regime and possibility to control is one of the major tasks in the controlled fusion research.

There are many diagnostics used for the turbulence measurements [17], some of the active microwave diagnostics are object of this study. Moreover, performance of the microwave diagnostics, that are used for the other plasma parameters measurements such as the ion temperature, alpha particles distribution etc., can be affected by the plasma turbulence. This effect is also in the focus of this work.

1.5 Microwave diagnostics

Microwaves are widely used as a tool for the plasma diagnostics. There are two types of the microwave techniques, the first type is named the passive microwave diagnostics. The general idea behind the passive diagnostics is clear: plasma as a mixture of the charges particles can radiate, that radiation in different frequency ranges carries information on the charged particles and processes they are involved in. The active microwave diagnostics are based on plasma probing by the microwave beams. There are many active microwave techniques based on the reflection and scattering of a probing beam, the general principe in these methods is that a probing wave interacts with plasma that cause a phase or/and amplitude modulation/distortion, analysis of the modulated signal provides information on the plasma properties. The both types of the microwave diagnostics are widely used in the fusion research, but the passive ones are out of the objectives of this thesis.

The collective Thomson scattering (CTS) and radial correlation reflectometry (RCR) are the focus of this thesis. They are discussed in more detail in the following subsections.

1.5.1 Reflectometry

A reflectometry diagnostics is based on the reflection of a probing wave as a radar, having frequency f, from a cut-off $x_c(f)$ in plasma where the refractive index vanishes $N(f) = 0$ [18]. The registered signal carries the information on the plasma within the probed volume, a typical scheme is illustrated on the figure 5.

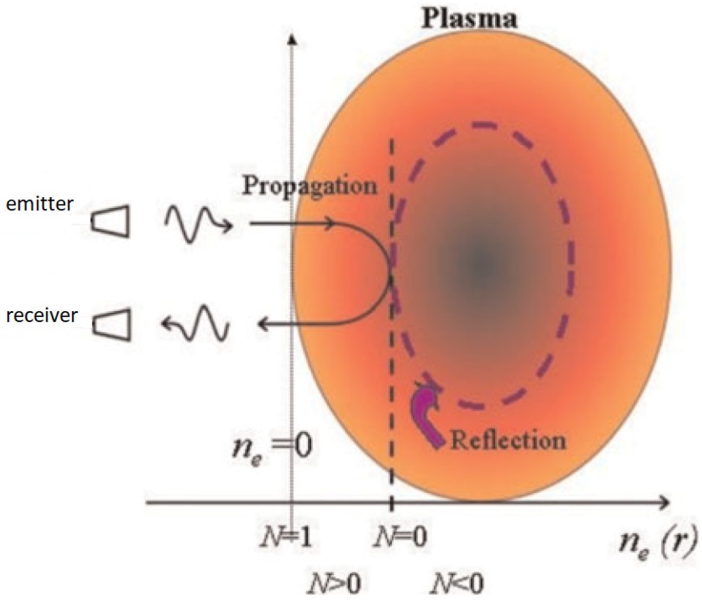

Figure 5: Reflectometry scheme [19]. A probing wave from an emitter propagates in the plasma, possessing a density profile $n_e(\mathbf{r})$, till a cut-off position, that corresponds to the refractive index $N = 0$, turns around and being registered by a receiver

The probing can be performed with a set of the frequencies $f_1, f_2, f_3...$, that is an extremely useful technique that provides information on many plasma characteristics.

First of all this is a standard approach for the plasma density profile measurements. The inversion method to reconstruct the position of the cut-off for each frequency from the time delay of the phase is recursive: the density profile can be reconstructed step by step [20]. Indeed, knowing the density profile up to the reflection layer related to f, the phase resulting from this profile at the frequency $f + df$ is calculated. Then the difference between this phase and the phase measured for $f + df$ gives the density profile between the two layers of reflection f and $f + df$ and so on.

The plasma turbulence modifies the density so the phase of a reflected wave is distorted due to the turbulence. The plasma turbulence is characterized by its amplitude, correlation length and correlation time, therefore a statistical analysis of the correlation function of the signals with different frequencies provides information about the turbulence properties.

1.5.2 Radial correlation reflectometry

The radial correlation reflectometry is a microwave diagnostic that is used for determination of the turbulence characteristics. Namely the turbulence radial correlation length, its wave number spectrum and amplitude [21].

This technique refers to the plasma probing with multiple frequencies $f_1, f_2, f_3...$ (sweeping frequency or using different frequencies in different discharges) with a following correlation analysis for the signals with the different frequencies and registered at different time $A(f_i, t_i)$. The cross-correlation function is defined as

$$CCF\left(\Delta x,\tau\right)=\frac{\left\langle\left(A\left(f_i,t_i\right)-\left\langle A\left(f_i,t_i\right)\right\rangle\right)\left(A^*\left(f_j,t_j\right)-\left\langle A^*\left(f_j,t_j\right)\right\rangle\right)\right\rangle}{\sqrt{\left\langle\left|A\left(f_i,t_i\right)-\left\langle A\left(f_i,t_i\right)\right\rangle\right|^2\right\rangle\left\langle\left|A\left(f_j,t_j\right)-\left\langle A\left(f_j,t_j\right)\right\rangle\right|^2\right\rangle}} \tag{1.5.1}$$

where the difference between the two cut-off positions is $\Delta x = x_c\left(f_i\right) - x_c\left(f_j\right)$, the time delay $\tau = t_i - t_j$ and $\langle ... \rangle$ is the statistical averaging procedure. According to the definition (1.5.1) $CCF\left(0,0\right) = 1$, the reflected signals coherence decays with growing the difference between the probing frequencies, due to the fact that the two signals are related to the random turbulence in the positions separated by Δx and the turbulence possesses its own coherence length.

This diagnostic possesses a wide range of possibilities to measure plasma density fluctuations [22]. It is often used for fluctuations monitoring in discharges, in particular, anomalous transport suppression studies in better confinement regimes. The main advantages of the RCR is that this diagnostic is not focused only on edge or core measurements, technically it is relatively simple since it is possible to have a single-port access to plasma. The fact that a probing wave scattering off the plasma fluctuations is dominant in the cut-off vicinity [23] leads to localization of the measurements. It should be mentioned that since normally the RCR utilizes a perpendicular probing wave incidence, it is not as sensitive to 2D effects as the Doppler reflectometry [24], [25] and the poloidal correlation reflectometry [26], [27].

Despite the relative simplicity of the RCR mentioned above, one has to be careful with the data analysis. For instance initially it was naively assumed that the distance between cut-off positions at which the correlation of two reflectometry signals vanishes is the turbulence correlation length, however this assumption is incorrect. It was demonstrated in 1D numerical computations performed using the Born approximation [28], performed by I Hutchinson in [29], that the CCF correlation length, at witch the cross-correlation function decays, can be significantly bigger than the turbulence radial correlation length. This gradual decay of the RCR CCF was attributed to the small angle scattering off very long scale fluctuations. Besides, the non-linear effects can take place if the turbulence amplitude is high enough, according to the developed theory of the non-linear RCR in 1D [30] and 2D [31] models, when the turbulence amplitude is big enough, the signal coherence decays on the scales smaller that the turbulence correlation length, that is typical for RCR experiments in big fusion machines. The transition of the fluctuation reflectometry from linear to non-linear scattering regime was described in [30], [31]. The correlation reflectometry data in the linear regime are strongly affected by the small angle scattering reducing diagnostics localization. In non-linear regime the reflected signal spectrum broadening is also not localized to the cut-off and determined by the wide region of plasma in which the turbulence is situated. In spite of this, the coherence decay in the radial correlation reflectometry deep in the non-linear regime is only sensitive to the turbulence level in the cut-off vicinity, hence the high localization. The role of poor localized small angle scattering in coherence decay is not so strong there.

1.5.3 Collective Thomson Scattering

The Thomson scattering (incoherent) is a commonly used diagnostics for measurements of the electron temperature and density in a fusion plasma by probing it with an electromagnetic beam and analyzing the spectrum of the received scattered radiation [21]. Diagnosing the ions in a fusion plasma is more challenging task since the interaction of injected electromagnetic waves with the ions is much weaker than with the much lighter electrons due to the fact that the dipole radiation of a charged particle is inversely proportional to its mass, therefor the direct interaction is negligible. However, in fusion plasma the ions have collective microscopic fluctuations, this dynamics is imprinted in the electron distribution due to the Debye shielding. In the CTS measurements these collective fluctuations in the electron distribution interact with a probing electromagnetic beam so the scattered radiation indirectly carries the information about the ion dynamics. The general scheme of registration the scattered radiation in a CTS experiment is illustrated on the figure 6.

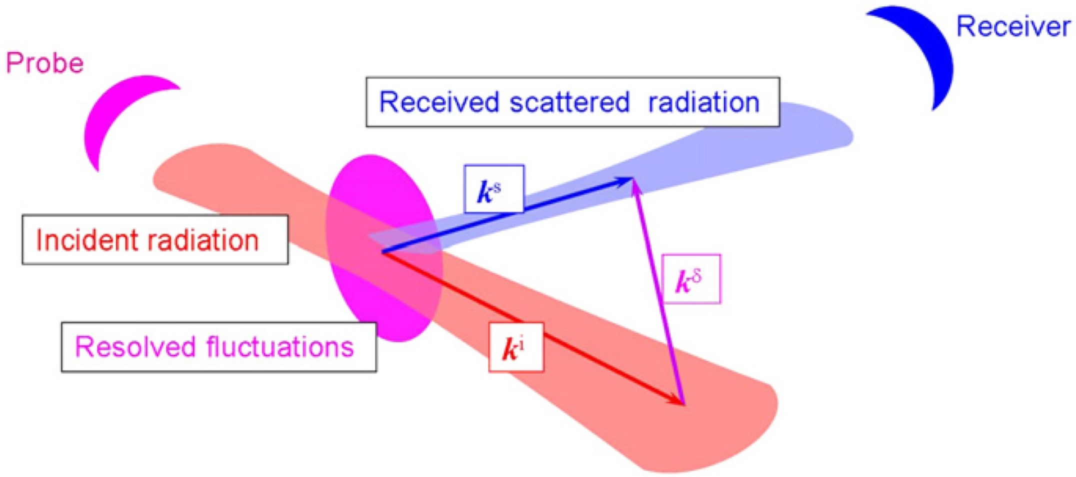

Figure 6: Probing beam scattering in a CTS experiment, the figure is from [32]. A probing beam propagates along the wave vector $\mathbf{k}^i$, the receiver beam position specifies $\mathbf{k}^s$, geometry of the measurements defines the resolved fluctuation wave number $\mathbf{k}^\delta$

The criterion for registration the information about the collective electron dynamics was obtained by Salpeter in 1960 [33]

$$\alpha = \frac{1}{\lambda_D k^\delta} > 1 \tag{1.5.2}$$

where α is called the Salpeter parameter, λ_D is the Debye radius and $\lambda_D k^\delta$ is the resolved fluctuation wave number.

The CTS diagnostics allows to obtain a lot of information about the plasma characteristics, namely: the bulk ion temperature, bulk ion rotation, fuel ion ratio and the fast particles 1D velocity distribution function [34]. The fast particles distribution is important to know for study of the alpha particles in fusion plasma [35], [36]; another key application of this method is exploring a heating particles beam dynamics in a plasma neutral-beam injection (NBI) heating experiments, with this diagnostics it is possible to keep track of the 1D heating beam velocity distribution with high temporal resolution [37]-[39].

The model for the CTS measurements that is planned for ITER [40] is illustrated on the figure 7. A scheme with one probing beam and seven receiver antennas will make it possible to measure the bulk ion and fast particle characteristics on all the magnetic surfaces from the plasma edge up to the core.

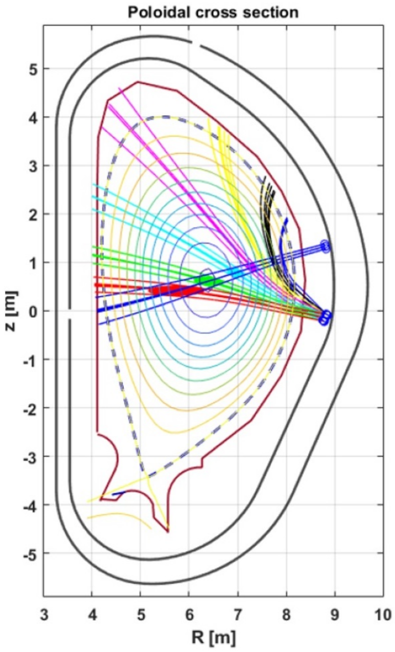

Figure 7: Scheme of the CTS measurements planned for ITER [34]. One probing beam in blue, and the seven receiver antenna beams

1.6 Microwave beam propagation in turbulent plasma

High-frequency electromagnetic beams are widely used in thermonuclear fusion research as a tool for localised plasma heating and current drive, for instance for electron cyclotron resonance heating (ECRH) [41] and electron cyclotron current drive (ECCD) [42]. Another domain of applications using quasi-optical electromagnetic beams in nuclear fusion is plasma diagnostics, possessing high spatial resolution, such as the collective Thomson scattering [32] and Doppler reflectometry [43]. Propagation of slightly divergent beams is relatively easy to analyse, its field distribution can be precisely predicted for given smooth plasma density and magnetic field profiles. Nevertheless, it was demonstrated that presence of plasma edge turbulence is able to significantly disturb a beam launched from outside [44]-[48].

Neoclassical tearing modes (NTMs) increase locally the radial transport that degrades the plasma performance, that is why NTMs suppression is required for a fusion reactor operation. Precise position and intensity of the current drive influence the efficiency of the NTMs suppression [47], [49]-[51]. The energy deposition profile broadening, associated with a launched beam broadening, can lead to the reduction of the stabilization efficiency. In terms of the microwave plasma diagnostics the probing beam broadening results in deterioration of the spatial resolution and it may complicate the diagnostic data interpretation. Experimental conformation of the broadened ECRH deposition was observed for DIII-D tokamak [52]. The microwave power scattering off blobs and the edge turbulence was also experimentally examined on TORPEX [53, 54] and TCV tokamak [55, 56] respectively. To take into account the role of the plasma turbulence in the beam propagation several methods were developed. Statistical description of EC wave scattering, based on the Fokker-Planck equation, was derived in [57]. This model describes a ray trajectory diffusion on blobs as a multi-scattering process. This approach implies specific structure of the blobs and allows to obtain rather a relevant estimate for an average beam broadening. Several numerical codes were developed with respect to the effect of a beam scattering off the turbulence: WKBeam [58], IPF-FDMC [59], EMIT-3D [60], REFMUL3 [61], COMSOL [62], FWR2D and FWR3D [45]. Propagation of an ordinary polarized (O-mode) beam in turbulent plasma was analysed analytically and numerically, using REFMUL code suite, in [44]. It was demonstrated that the presence of a turbulent edge layer can result in a drastic distortion of the beam shape depending on turbulence amplitude. The developed analytical approach allowed to describe averaged geometrical beam characteristics in turbulent plasma. Corresponding recommendation for ITER ECRH experiments were done especially in the case of NTM control where the beam width is crucial to reach the magnetic island with power deposition at the right position.

The average microwave beam broadening in turbulent plasma influence on the microwave diagnostics performance so this effect is studied in this thesis and, in particular, in the case of the X-mode wave used for CTS.

1.7 Parametric decay instability

The microwave diagnostics are based on a probing wave interaction with the charged particles or plasma fluctuations in a probed area, but firstly an injected beam has to reach this interaction area. The probing microwave beam can be distorted by the plasma turbulence and also by the parametric decay instability (PDI). The PDI foundation is reviewed in this section.

There are a vast variety of the electromagnetic plasma modes, if the wave amplitudes are small enough, their dynamics can be described well by a linear system of the Maxwell equations. In the opposite case of a high wave amplitude the non-linear effects take place. The first (by the wave amplitude decomposition) non-linear effect is the three-wave interaction, leading to the parametric decay instability [63].

We consider three waves E_j in an inhomogeneous medium, which are numerated by the index $j \in \{1, 2, 3\}$ and expressed in the standard form

$$E_j = E_{j0} e^{-i\omega_j t + i\int \mathbf{k}_j(\mathbf{x}')\mathbf{dx}'} + c.c. \tag{1.7.1}$$

where E_{j0} is an amplitude, ω_j is a frequency, $\mathbf{k_j}$ is a wave number and *c.c.* stands for the complex conjugated part. The three-wave interaction conditions for these waves read

$$\begin{aligned} \omega_1 &= \omega_2 + \omega_3 \\ \mathbf{k}_1 &= \mathbf{k}_2 \pm \mathbf{k}_3|_{\mathbf{x}_d}, \end{aligned} \tag{1.7.2}$$

$\mathbf{x}_d$ is position (in inhomogeneous medium) where the three-wave interaction takes place, the wave numeration is such that $\omega_1 > \omega_2, \omega_3$. The three waves are in a resonance under the conditions (1.7.2). If we consider the waves as photons or plasmons, an interpretation in terms of the quantum mechanics can be applied to the system (1.7.2), where the first equation represents the energy conservation law, the second one stands for the momentum conservation law.

For an injected microwave, possessing the frequency ω_1 and the wave number $\mathbf{k}_1$, the PDI can occur at the position $\mathbf{x}_d$ if the two modes $(\omega_2, \mathbf{k}_2)$ and $(\omega_3, \mathbf{k}_3)$ exist in the plasma, normally in ECRH and CTS experiments it is the upper hybrid (UH) waves in a fusion device. Under the resonance conditions (1.7.2) the pump wave E_1 energy is transmitted to the so-called daughter waves E_2 and E_3.

Excitation of the parametric decay instability requires not only fulfilling the wave resonance conditions (1.7.2), but also exceeding the power threshold of the pump decay. The threshold is determined by fact that the daughter waves receive the energy from the pump and at the same time also lose the energy due to its convective flow from the resonance area, centered at $\mathbf{x}_d$, or dissipation there. Then the effective instability excitation is possible only for high enough pump wave amplitude, this threshold criterion was analysed by Piliya [64] - [66] and Rosenbluth [67] 50 years ago.

In the case of inhomogeneous plasmas with monotonic background profiles, the thresholds for different scenarios of the parametric pump wave decay was analyzed and evaluated by different authors more than three decades ago. The results of these studies, summarized e.g. in [68], predict power thresholds of the instability which are much higher than the power of modern gyrotrons because of the intensive energy loss of the daughter waves from the decay area, which makes it impossible to amplify them significantly. But the plasma profiles in a fusion device are not always monotonic, for example it can be not monotonic due to a magnetic island, so if one or the both daughter waves are somehow trapped in the plasma non-monotonic area and the decay conditions (1.7.2) are fulfilled there, the energy loss for these waves is significantly suppressed, that drastically reduces the threshold. For the last decade, various microwave decay scenarios have been analyzed. The results of this analysis, summarized in [69], predict the instability threshold at a level that is from two to four orders of magnitude lower than that for a monotonic density profile.

1.8 Scope of this thesis

The improvement of the microwave diagnostics interpretative models is the main focus of this thesis. The analytical and numerical analysis of an X-mode microwave beam distortion due to the plasma turbulence is performed in this work for different plasmas and turbulence scenarios.

This type of the polarization is planned for the CTS diagnostics on ITER. The analytical model for the microwave beam propagation in the turbulent plasma initially developed for an ordinary polarized (O-mode) beam was adapted for an X-mode beam. The beam distortion and the average broadening of the X-mode beam was investigated numerically for a wide range of the turbulence parameters and probing frequencies. The results are compared to the theory, corresponding recommendations for the ITER CTS diagnostics are provided. This work and the results are described in the second chapter.

The third chapter is devoted to the description of the proposed interpretative analytical model for a CTS experiment with respect to the high edge plasma turbulence. The corresponding improved CTS model was proposed and supported by the numerical simulations and evaluations. The registered radiation spectra in the CTS are evaluated with and without taking into account the probing beam distortion effect, the importance of the analytical model correction is estimated.

The low-threshold parametric decay instability can affect a probing microwave beam, the analysis of the PDI model with respect to the edge plasma turbulence is provided in the fourth chapter of the present thesis. The developed theory of the low-threshold PDI describes the parametric decay of a smooth probing beam, it is not applicable for a probing beam significantly disturbed by the plasma turbulence. The numerical investigation of the parametric decay process with respect to the plasma turbulence was performed for different turbulence regimes.

The fifth chapter is devoted to the development of the RCR technique analysis. The phase spectrum analysis in the RCR provides the information about the plasma turbulence amplitude, this approach was developed under the Born approximation. The non-linear theory of the RCR gives information about the combination of the plasma turbulence amplitude and the turbulence radial correlation length, the applicability of this method is based on the strong phase modulation due to the plasma turbulence. In this thesis it is demonstrated that it is possible to combine the two approaches of the RCR data analysis to extract the information about the both the turbulence amplitude and the radial correlation length.

2 X-mode beam propagation in turbulent plasma

In this chapter it is demonstrated that the plasma turbulence at the edge of a fusion machine can lead to significant broadening of the X-mode microwave beam, which impacts the performance of the microwave diagnostics. Based on the similar method developed for the O-mode polarization, the expression for mean microwave power distribution, after the beam passing through the plasma edge turbulence, is obtained, its spatial and probabilistic distributions are analysed. As this polarization is planned for application for the collective Thomson scattering at ITER and used for the electron cyclotron resonance heating (ECRH) at ASDEX Upgrade, the numerical simulations of the beam broadening due to the edge turbulence are performed for the two conditions of plasma parameters, related to the planned CTS experiments at ITER and to the ECRH experiments at ASDEX Upgrade. The ideas to reduce the beam broadening induced by the edge turbulence in the CTS case have been tested and summarized in the discussion part of this chapter.

In this work we apply the developed method, based on the eikonal perturbation analysis, for describing propagation and scattering process of the extraordinary polarized beam in turbulent plasma. In particular the results are discussed in terms of possible problems for the CTS experiments at ITER. Statistical properties of the beam are considered in regimes with strong turbulence, probabilistic distribution function of its intensity is obtained that allows to provide statistical analysis of processes associated with the wave-plasma energy exchange in turbulent plasmas.

This chapter is organized as follows: the theoretical background of an electromagnetic beam propagation in plasma is given in the first section, in the second section we present the analytical approach of the description of the X-mode beam propagating in magnetized turbulent plasma. Numerical analysis, harnessing a full-wave code, and comparison with the theory are illustrated in the third part. The main results are discussed in the last section of this chapter.

2.1 Theoretical background

2.1.1 Wave equation

Before the investigation of the X-mode beam broadening in turbulent plasma, it is necessary to describe and analyse the general equations that characterize the electromagnetic waves in plasma, that is the Maxwell's equations in plasma. The Maxwell's macroscopic equations system in CGS units read:

$$\begin{aligned}
&\nabla \cdot \mathbf{D} = 4\pi\rho \\
&\nabla \cdot \mathbf{H} = 0 \\
&\nabla \times \mathbf{E} = -\frac{1}{c}\frac{\partial}{\partial t}\mathbf{H} \\
&\nabla \times \mathbf{H} = \frac{4\pi}{c}\mathbf{j} + \frac{1}{c}\frac{\partial}{\partial t}\mathbf{D}
\end{aligned} \tag{2.1.1}$$

where c is the light velocity constant, the electric and magnetic fields $\mathbf{E}$ and $\mathbf{H}$ correspondingly, ρ and $\mathbf{j}$ are the external charge density and the current density, they are connected via the charge conservation law

$$\frac{\partial \rho}{\partial t} + \nabla \cdot \mathbf{j} = 0 \tag{2.1.2}$$

$\mathbf{D}$ is the electric induction, the magnetic permeability $\mu \approx 1$ for plasma [63]. The electric induction is connected to the electric field and in the Fourier space it can be written as

$$\mathbf{D} = \hat{\varepsilon}\mathbf{E} \tag{2.1.3}$$

where $\hat{\varepsilon}$ is the permittivity tensor.

To obtain a general description of the electromagnetic wave propagation in plasma we will use a reasonable assumption that the characteristic time of the plasma conditions change is considerably bigger than the wave propagation time signifying that the plasma is stationary on the wave time reference. Damping processes, such as collisional and Landau damping are also neglected. The another assumption that will be used for the wave propagation description is the «cold plasma» approximation, this approximation is based on the assumption that the thermal velocity of the electrons is much less than the phase velocity

$$v_{te}/v_{ph} \ll 1 \tag{2.1.4}$$

where electron thermal velocity $v_{te} = \sqrt{\frac{T_e}{2m_e}}$, m_e is the electron mass and T_e is the electron temperature (in the energetic units), the phase velocity $v_{ph} = \omega/k$, ω is the wave frequency and k is the wave number. For the microwaves in the modern fusion machines with a typical electron temperature T_e of the order of few keV this condition normally holds, unless a plasma resonance takes place where the phase velocity drastically decreases, and thus the cold plasma approximation is failed. Also we will consider the magnetized plasma case, that means plasma in the external magnetic field $\mathbf{B}$, which is much higher than the magnetic field amplitude of the waves in plasma, this model is also typical for the toroidal fusion facilities.

To describe the wave propagation, an electromagnetic wave is considered to be monochromatic, and the plasma medium is assumed to be homogeneous so

$$\mathbf{E}\left(t, \mathbf{r}\right) \propto e^{-i\omega t + i\mathbf{k}\mathbf{r}} \tag{2.1.5}$$

Then the wave equation can be obtain from the system (2.1.1)

$$\left[\delta_{ij}\frac{\partial^2}{\partial x_l^2} - \frac{\partial^2}{\partial x_i \partial x_j} + \frac{\omega^2}{c^2}\varepsilon_{ij}\right] E_j = 0 \tag{2.1.6}$$

the indexes i, j, l denote the direction in Cartesian coordinates $i, j, l = \{x, y, z\}$, the summation for the repetitive indexes is assumed in the equation (2.1.6) and throughout this thesis. The Cartesian coordinates system is chosen as follows: z coordinate is the direction along the external magnetic field $\mathbf{B}$, the parallel wave number notation is $\mathbf{k}_\parallel = \mathbf{e}_z k_z$, and the x coordinate is the direction of the perpendicular wave propagation i.e. along the vector $\mathbf{k}_\perp = \mathbf{e}_x k_x$.

In the «cold plasma» model the permittivity tensor read

$$\hat{\varepsilon} = \begin{pmatrix} \epsilon & ig & 0 \\ -ig & \epsilon & 0 \\ 0 & 0 & \eta \end{pmatrix} \tag{2.1.7}$$

its components have the following form [70]

$$\epsilon = 1 - \tfrac{\omega_{pe}^2}{\omega^2 - \omega_{ce}^2} - \tfrac{\omega_{pi}^2}{\omega^2 - \omega_{ci}^2} \qquad g = \tfrac{\omega_{ce}}{\omega} \tfrac{\omega_{pe}^2}{\omega^2 - \omega_{ce}^2} + \tfrac{\omega_{ci}}{\omega} \tfrac{\omega_{pi}^2}{\omega^2 - \omega_{ci}^2} \qquad \eta = 1 - \tfrac{\omega_{pe}^2}{\omega^2} - \tfrac{\omega_{pi}^2}{\omega^2} \tag{2.1.8}$$

$$\omega_{p\alpha}^2 = \tfrac{4\pi e^2 Z_\alpha^2 n_\alpha}{m_\alpha} \qquad \omega_{c\alpha} = \tfrac{e Z_\alpha B}{m_\alpha c} \tag{2.1.9}$$

where e is the electron charge, the plasma frequency $\omega_{p\alpha}$ and the cyclotron frequency $\omega_{c\alpha}$ for the species α of the particles - electrons and all the ions, m_α, n_α and Z_α are the mass, density and charge number for the particles α.

2.1.2 O-mode and X-mode

Then the full and explicit form of the system (2.1.6)

$$\hat{M} \begin{pmatrix} E_x \\ E_y \\ E_z \end{pmatrix} = \begin{pmatrix} k_z^2 - \tfrac{\omega^2}{c^2}\varepsilon & i\tfrac{\omega^2}{c^2} g & -k_x k_z \\ -i\tfrac{\omega^2}{c^2} g & k^2 - \tfrac{\omega^2}{c^2}\varepsilon & 0 \\ -k_x k_z & 0 & k_x^2 - \tfrac{\omega^2}{c^2}\eta \end{pmatrix} \begin{pmatrix} E_x \\ E_y \\ E_z \end{pmatrix} = 0 \tag{2.1.10}$$

The wave modes that can exist and propagate in the plasma are determined by dispersion relation

$$\det \hat{M} = \left(\frac{\omega^2}{c^2}\varepsilon - k^2\right)\left(\frac{\omega^2}{c^2}\varepsilon k_x^2 + \frac{\omega^2}{c^2}\eta\left(k_z^2 - \frac{\omega^2}{c^2}\varepsilon\right)\right) - \frac{\omega^4}{c^4} g^2 \left(k_x^2 - \frac{\omega^2}{c^2}\eta\right) = 0 \tag{2.1.11}$$

In the case of the perpendicular to the magnetic field $\mathbf{B}$ microwave propagation $k_z = 0$ so $k_x^2 = k^2$, the dispersion relation describes the two modes:

$$k^2 = \frac{\omega^2}{c^2}\eta \tag{2.1.12}$$

$$k^2 = \frac{\omega^2}{c^2}\frac{\varepsilon^2 - g^2}{\varepsilon} \tag{2.1.13}$$

These two independent solutions are called the ordinary (O-mode) (2.1.12) and extraordinary (X-mode) (2.1.13) modes. Both modes are object of the study in this thesis. For the microwaves the following relation

$$\omega \gg \omega_{ci}, \omega_{pi} \tag{2.1.14}$$

normally holds in a tokamak so the ion components in the permittivity tensor are negligible, then the wave numbers have a simplified form

$$k^2 = \frac{\omega^2 - \omega_{pe}^2}{c^2} \tag{2.1.15}$$

$$k^2 = \frac{\left(\omega\left(\omega - \omega_{ce}\right) - \omega_{pe}^2\right)\left(\omega\left(\omega + \omega_{ce}\right) - \omega_{pe}^2\right)}{c^2\left(\omega^2 - \omega_{ce}^2 - \omega_{pe}^2\right)} \tag{2.1.16}$$

The point x_c where the wave numbers (2.1.15), (2.1.16) are equal to zero is called a cut-off position, the reflection of a wave occurs at this point. According to (2.1.15), (2.1.16) it is seen that the O-mode wave has only one cut-off and the X-mode wave number can have two points where it equals to zero. For the O-mode the cut-off position is determined by the expression

$$\omega^2 = \omega_{pe}^2\left(x_c\right) \tag{2.1.17}$$

so x_c depends on the plasma density only, corresponding plasma density value is called the critical density n_c. The cut-off positions determine the accessibility condition for the microwave diagnostics, using certain frequencies and polarizations.

By substituting the wave numbers into the system (2.1.10) we have the expressions for wave polarization in the two modes

$$\underset{\text{O-mod}}{\begin{pmatrix} E_x \\ E_y \\ E_z \end{pmatrix} \propto \begin{pmatrix} 0 \\ 0 \\ 1 \end{pmatrix}} \qquad \underset{\text{X-mode}}{\begin{pmatrix} E_x \\ E_y \\ E_z \end{pmatrix} \propto \begin{pmatrix} i\frac{g}{\varepsilon} \\ 1 \\ 0 \end{pmatrix}} \tag{2.1.18}$$

It is seen that the electric field of the O-mode wave is polarized along the external magnetic field, this field causes the charged particles oscillation along **B** so this oscillatory motion is independent on the magnetic field, that is why the O-mode wave number and polarization are also independent on the external magnetic field.

2.1.3 WKB approximation

A plane wave (2.1.5) is not a solution of the wave equation (2.1.6) in an inhomogeneous medium, nevertheless an approximate solution can be obtained. To describe the approximate solution we will consider a perpendicular to the external magnetic field propagation of a wave (in 1D geometry), the plasma density and the magnetic field are assumed to be inhomogeneous in only one direction x so $\hat{\varepsilon} = \hat{\varepsilon}(x)$. Then the wave equation (2.1.6) can be written in a simplified way

$$\left[\frac{d^2}{dx^2} + k^2\left(x\right)\right] E = 0 \tag{2.1.19}$$

this form of the wave equation is universal for O-mode and X-mode, just for the O-mode $k(x)$ is given by (2.1.12) and for the X-mode by (2.1.13), the electric field E in this form is E_z and either E_x or E_y for O-mode and X-mode respectively. The wave number dependence on the coordinate x is driven by the density and magnetic field dependence according to the wave number definitions (2.1.12), (2.1.13).

The approximate solution of (2.1.19) can be found in the form

$$E = e^{i(\phi_1(x)+\phi_2(x)+\phi_3(x)+\dots)} \tag{2.1.20}$$

where the following relation holds $\phi_{j+1} \ll \phi_j$. By substituting (2.1.20) into (2.1.19) and applying an iterative procedure all the ϕ_j can be defined, normally the first two terms in the ϕ_j series is enough for a physically meaningful wave description. This approach is called the WKB approximation, it is an initialism for Wentzel–Kramers–Brillouin. Then the solution

$$E = E_1 \frac{1}{\sqrt{k(x)}} e^{i\int^x dx' k(x')} + E_2 \frac{1}{\sqrt{k(x)}} e^{-i\int^x dx' k(x')} \tag{2.1.21}$$

describes two waves with amplitudes E_1 and E_2, propagating in opposite directions, the first term in the series $\phi_1(x) = \int^x dx' k(x')$ represents the wave phase in an inhomogeneous medium, the second one $\phi_2(x) = i\frac{1}{2} Ln(k(x))$ describes the wave energy flux conservation. The required condition $\phi_{j+1} \ll \phi_j$ in the iterative procedure results in the following expression

$$\frac{d}{dx} k(x) \ll k^2(x) \tag{2.1.22}$$

that means that the wavelength variation has to be small enough on the scale of the wavelength.

2.2 Analytical description of X-mode beam broadening in turbulent plasma

In this section we consider a microwave X-mode beam 2D propagation in turbulent inhomogeneous magnetised plasma analytically. Plasma edge of a fusion machine can be described in the framework of the Cartesian coordinates. Direction of plasma inhomogeneity is along x axis and coincides with direction of the beam propagation, z axis corresponds to lines of external magnetic field $\mathbf{B}$.

Considering electromagnetic waves possessing the extraordinary polarization and propagating perpendicularly to the external magnetic field in absence of the upper hybrid resonance the wave equation (2.1.6) can be written as

$$\left[\frac{\partial^2}{\partial x^2} + \frac{\partial^2}{\partial y^2} + k^2(x) + \delta k^2(x,y)\right] E_y = 0 \tag{2.2.1}$$

the X-mode wave number k is given by the equation (2.1.16) and the wave number (squared) perturbation is described by the following expression

$$\delta k^2 = -\frac{\omega_{pe}^2}{c^2} \frac{\left(\omega^2 - \omega_{ce}^2\right)\left(\omega^2 - 2\omega_{pe}^2\right) + \omega_{pe}^4}{\left(\omega^2 - \omega_{ce}^2 - \omega_{pe}^2\right)^2} \frac{\delta n}{n} \tag{2.2.2}$$

where ω - probing frequency, n - background plasma density and δn - 2D fluctuation of the density, the equation (2.2.2) is an amendment to (2.1.16), obtained by means of its linearization over the small parameter $\frac{\delta n}{n}$. The equation (2.2.1) can be analysed by means of the geometrical optics approach if the studied area is far the cut-off layer, to this we consider the electric field in the form

$$E_y = \frac{E_{y0}}{2} e^{i\psi(x,y)} e^{-i\omega t} + c.c. \tag{2.2.3}$$

$\psi(x, y)$ is the eikonal, *c.c.* stands for the complex conjugated part. The expression (2.2.3) corresponds to a plane wave locally at a point (x_0, y_0) the eikonal

$$\psi(x_0 + x, y_0 + y) \approx x\frac{\partial \psi}{\partial x}(x_0, y_0) + y\frac{\partial \psi}{\partial y}(x_0, y_0) \tag{2.2.4}$$

The eikonal equation reads as

$$K_x^2 + K_y^2 = k^2\left(x\right) + \delta k^2\left(x, y\right) \tag{2.2.5}$$

where the introduced wave numbers $K_{x_j} = \frac{\partial \psi}{\partial x_j}$, $j = \{1, 2\}$ numerates the two directions x and y. Assuming that the fluctuations level is small $\delta k^2 \ll k^2$ we can use the perturbation method and consider the wave numbers as $K_{x_j} = k_{x_j} + \delta k_{x_j}$, where k_{x_j} is the wave number for plasma without the turbulence, δk_{x_j} is the correction associated with the turbulence. These values are specified as follows

$$k_x^2 + k_y^2 = k^2\left(x\right) \tag{2.2.6}$$

$$\delta k_x + \delta k_y \frac{k_y}{k_x} = \frac{1}{2k_x\left(x\right)} \delta k^2\left(x, y\right) \tag{2.2.7}$$

The ray trajectory $(y = y(x))$ is determined by the unperturbed part

$$\frac{dy}{dx} = \frac{k_y}{k_x} \tag{2.2.8}$$

Taking into account that $k\left(x\right)$ is a function of the radial coordinate only k_y is a constant on the ray trajectory. Then we can write down the eikonal explicitly

$$\psi(x, y; k_y) = \int^x dx' \left[k_x\left(x'\right) + \delta k_x\left(x', y'(x')\right)\right] + yk_y + \int^x dx' \frac{dy'}{dx'} \delta k_y\left(x', y'(x')\right) \tag{2.2.9}$$

using the equations (2.2.6), (2.2.7)

$$\psi(x, y; k_y) = \int^x dx' \sqrt{k^2\left(x'\right) - k_y^2} + yk_y + \frac{1}{2}\int^x dx' \frac{\delta k^2\left(x', y'(x')\right)}{k_x}\left(x'\right) \tag{2.2.10}$$

A probing electromagnetic beam represents a sum of poloidal harmonics numerated by the poloidal wave numbers k_y at the plasma edge. Each harmonic possesses its own amplitude

$$E_{y0}\left(k_y\right) = \int_{-\infty}^{+\infty} dy E_y\left(x = 0, y, t = 0\right) e^{-ik_y y} \tag{2.2.11}$$

(at the plasma edge) and can be described by the presented eikonal approach. Considering an initially Gaussian beam at the plasma edge

$$E_y(x=0,y,t)=Ee^{-\frac{y^2}{\delta^2}}\cos\left(\omega t\right) \tag{2.2.12}$$

the explicit expression for the amplitude

$$E_{y0}\left(k_y\right)=E\sqrt{\pi}\delta e^{-\frac{k_y^2\delta^2}{4}} \tag{2.2.13}$$

Then the electric field distribution for the whole beam

$$E_y\left(x,y,t\right)=\int_{-\infty}^{+\infty}\frac{dk_y}{2\pi}\frac{E_{y0}\left(k_y\right)}{2}\sqrt{\frac{\omega}{ck_x\left(x\right)}}e^{i\psi(x,y;k_y)}e^{-i\omega t}+c.c. \tag{2.2.14}$$

here the coefficient $\sqrt{\frac{\omega}{ck_x(x)}}$ describes the wave energy flux conservation in the geometrical optics approximation. Substituting the eikonal (2.2.10) into (2.2.14) and using the paraxial approximation

$$k_x\approx k\left(x\right)-\frac{k_y^2}{2k\left(x\right)} \tag{2.2.15}$$

we obtain

$$E_y\left(x,y,t\right)=\int_{-\infty}^{+\infty}\frac{dk_y}{2\pi}\frac{E_{y0}\left(k_y\right)}{2}\sqrt{\frac{\omega}{ck\left(x\right)}}e^{ik_yy}e^{i\int_0^x dx'k(x')-i\frac{k_y^2d(x)^2}{2}+i\delta\phi}e^{-i\omega t}+c.c. \tag{2.2.16}$$

where the used notation

$$d(x)^2=\int_0^x dx'\frac{1}{k(x')} \tag{2.2.17}$$

this function is related to the wave diffraction effect, and the random phase

$$\delta\phi=-\int_0^x dx'\kappa(x')\frac{\delta n(x',y'(x,y,x',k_y))}{n(x')} \tag{2.2.18}$$

$$\kappa(x)=\frac{1}{k(x)}\frac{\omega_{pe}^2}{2c^2}\frac{\left(\omega^2-\omega_{ce}^2\right)\left(\omega^2-2\omega_{pe}^2\right)+\omega_{pe}^4}{\left(\omega^2-\omega_{ce}^2-\omega_{pe}^2\right)^2} \tag{2.2.19}$$

This phase perturbation of a partial wave adds up along the wave trajectory according to the geometrical optics

$$y'(x,y,x',k_y)=y-k_yl^2(x',x) \tag{2.2.20}$$

$$l^2(x',x)=\int_{x'}^x ds\frac{1}{k(s)} \tag{2.2.21}$$

In accordance with (2.2.16) the beam passing through turbulent plasma is the more distorted the higher turbulence level. Nevertheless, taking into account random behaviour of the phase perturbation, it is possible to define average and probabilistic characteristics of the beam. To define these characteristics we consider the average intensity of the beam written as follows

$$\left\langle E_y^2\left(x,y\right)\right\rangle = \int_{-\infty}^{+\infty} \frac{dk_{y_1}dk_{y_2}}{\left(2\pi\right)^2}\frac{E_{y0}\left(k_{y_1}\right)}{2}\frac{E_{y0}^*\left(k_{y_2}\right)}{2}\frac{c}{\omega k\left(x\right)}\times$$

$$e^{i\left(k_{y_1}-k_{y_2}\right)y}e^{-\frac{i\left(k_{y_1}^2-k_{y_2}^2\right)d(x)^2}{2}}\left\langle e^{i\left(\delta\phi\left(x,y,k_{y_1}\right)-\delta\phi\left(x,y,k_{y_2}\right)\right)}\right\rangle + c.c. \tag{2.2.22}$$

Supposing the density fluctuations radial correlation length is much smaller than the system size the random phase perturbation $\delta\phi$ is a sum of many independent random values. Thus $\delta\phi$ and $\left(\delta\phi\left(x,y,k_{y_1}\right)-\delta\phi\left(x,y,k_{y_2}\right)\right)$ obey the normal distribution $f_N\left(\delta\phi\right)=\frac{1}{\sqrt{2\pi\left\langle\delta\phi^2\right\rangle}}e^{-\frac{\delta\phi^2}{2\left\langle\delta\phi^2\right\rangle}}$, that results in

$$\left\langle e^{i\delta\phi}\right\rangle = \int_{-\infty}^{+\infty} d\delta\phi e^{i\delta\phi}f_N\left(\delta\phi\right) = e^{-\frac{\left\langle\delta\phi^2\right\rangle}{2}} \tag{2.2.23}$$

so the average intensity of the beam

$$\left\langle E_y^2\left(x,y\right)\right\rangle = \int_{-\infty}^{+\infty} \frac{dk_{y_1}dk_{y_2}}{\left(2\pi\right)^2}\frac{E_{y0}\left(k_{y_1}\right)}{2}\frac{E_{y0}^*\left(k_{y_2}\right)}{2}\frac{c}{\omega k\left(x\right)}\times$$

$$e^{i\left(k_{y_1}-k_{y_2}\right)y}e^{-\frac{i\left(k_{y_1}^2-k_{y_2}^2\right)d(x)^2}{2}}e^{-\frac{\left\langle\left(\delta\phi\left(x,y,k_{y_1}\right)-\delta\phi\left(x,y,k_{y_2}\right)\right)^2\right\rangle}{2}} + c.c. \tag{2.2.24}$$

To evaluate

$$\left\langle\delta\phi\left(x,y,k_{y_i}\right)\delta\phi\left(x,y,k_{y_j}\right)\right\rangle = \int_0^x\int_0^x dx'dx''\kappa(x')\kappa(x'')\times$$

$$\left\langle\frac{\delta n(x',y'(x,y,x',k_{y_i}))}{n(x')}\frac{\delta n(x'',y'(x,y,x'',k_{y_j}))}{n(x'')}\right\rangle \tag{2.2.25}$$

we introduce relative radial coordinates $X=\frac{x'+x''}{2}$, $\Delta=x'-x''$, local relative turbulence amplitude $\frac{\delta\tilde{n}(x)}{n(x)}$ and cross-correlation function $CCF(x,y)$ according to the definition

$$\left\langle\frac{\delta n(x',y'(x,y,x',k_{y_i}))}{n(x')}\frac{\delta n(x'',y'(x,y,x'',k_{y_j}))}{n(x'')}\right\rangle =$$

$$\frac{\delta\tilde{n}^2(X)}{n^2(X)}CCF(\Delta,y'(x,y,X,k_{y_i})-y'(x,y,X,k_{y_j})) \tag{2.2.26}$$

Introducing this definition we supposed that the cross-correlation function is the function of the coordinates difference only and is homogeneous in space. Then

$$\left\langle\delta\phi\left(x,y,k_{y_i}\right)\delta\phi\left(x,y,k_{y_j}\right)\right\rangle = \int_0^x dX\kappa^2(X)\frac{\delta\tilde{n}^2(X)}{n^2(X)}\times$$

$$\int\frac{dq_y}{2\pi}\left|n_{0,q_y}\right|^2 e^{iq_y(y'(x,y,X,k_{y_i})-y'(x,y,X,k_{y_j}))} \tag{2.2.27}$$

where

$$\left|n_{q_x,q_y}\right|^2 = \int dxdyCCF\left(x,y\right)e^{-ixq_x-iyq_y} \tag{2.2.28}$$

is Fourier spectrum of the turbulence. Using the explicit form for $y'(x,y,x',k_y)$, the exponential factor in the equation (2.2.24)

$$\left\langle \left(\delta\phi\left(x,y,k_{y_1}\right)-\delta\phi\left(x,y,k_{y_2}\right)\right)^2\right\rangle = 2\int_0^x dX\kappa^2(X)\frac{\delta\tilde{n}^2(X)}{n^2(X)}\times \int\frac{dq_y}{2\pi}\left|n_{0,q_y}\right|^2\left[1-e^{iq_yl^2(X,x)(k_{y_2}-k_{y_1})}\right] \tag{2.2.29}$$

moreover assuming a symmetric spectrum of the turbulence $\left|n_{0,q_y}\right|^2 = \left|n_{0,-q_y}\right|^2$ we obtain the expression

$$\left\langle \left(\delta\phi\left(x,y,k_{y_1}\right)-\delta\phi\left(x,y,k_{y_2}\right)\right)^2\right\rangle = 2\int_0^x dX\kappa^2(X)\frac{\delta\tilde{n}^2(X)}{n^2(X)}\times \int\frac{dq_y}{2\pi}\left|n_{0,q_y}\right|^2\left[1-\cos\left(q_yl^2\left(X,x\right)\left(k_{y_2}-k_{y_1}\right)\right)\right] \tag{2.2.30}$$

It is seen that in the strong turbulence regime when the following inequality holds

$$\left\langle \delta\phi^2\left(x,y,k_y\right)\right\rangle \gg 1 \tag{2.2.31}$$

only small argument values of the cosine in (2.2.30) contributes to the integral expression (2.2.24), then, keeping the two first terms of the cosine Taylor series expansion in (2.2.30), the averaged difference of the phase perturbations becomes

$$\left\langle \left(\delta\phi\left(x,y,k_{y_1}\right)-\delta\phi\left(x,y,k_{y_2}\right)\right)^2\right\rangle = \int_0^x dX\kappa^2(X)l^4\left(X,x\right)\frac{\delta\tilde{n}^2(X)}{n^2\left(X\right)}\times \int\frac{dq_y}{2\pi}\left|n_{0,q_y}\right|^2q_y^2\left(k_{y_1}-k_{y_2}\right)^2 \tag{2.2.32}$$

Substituting (2.2.32) into (2.2.24) and calculating standard integrals we finally obtain

$$\left\langle E_y^2\left(x,y\right)\right\rangle = \frac{E^2}{2}\frac{\omega}{ck\left(x\right)}\frac{\delta}{\sqrt{2}W\left(x\right)}e^{-\frac{y^2}{W^2(x)}} \tag{2.2.33}$$

with the averaged beam width given by

$$W^2\left(x\right) = \frac{\delta^2}{2}+\frac{2d^4\left(x\right)}{\delta^2}+4\int^x D(x')l^4(x,x')dx' \tag{2.2.34}$$

where

$$D(x) = \frac{1}{2}\kappa^2(X)\frac{\delta\tilde{n}^2(X)}{n^2\left(X\right)}\int\frac{dq_y}{2\pi}\left|n_{0,q_y}\right|^2q_y^2 \tag{2.2.35}$$

The first term in equation (2.2.34) stands for the initial beam width, the second one represents diffraction taking into account refractive index in inhomogeneous medium, the third term describes the effect of beam broadening in the turbulent plasma. To analyse impact of the turbulence on the beam broadening we estimate the third term in (2.2.34)

$$W^2_{Xturb} = 4\int^x D(x')l^4(x,x')dx' \tag{2.2.36}$$

at position beyond the periphery turbulence layer $x \gg x_{turb}$, where x_{turb} is the width of this turbulence layer,

$$W_{Xturb}^2 \approx \frac{1}{2} d^4(x) x_{turb} \int \frac{dq_y}{2\pi} \left| n_{0,q_y} \right|^2 q_y^2 \times \\ \left\langle \frac{\omega_{pe}^4}{c^2} \frac{\left(\left(\omega^2 - \omega_{ce}^2\right) \left(\omega^2 - 2\omega_{pe}^2\right) + \omega_{pe}^4 \right)^2}{\left(\omega^2 \left(\omega^2 - \omega_{ce}^2 - \omega_{pe}^2 \right) + \omega_{pe}^2 \left(\omega_{pe}^2 - \omega^2 \right) \right) \left(\omega^2 - \omega_{ce}^2 - \omega_{pe}^2 \right)^3} \frac{\delta \tilde{n}^2}{n^2} \right\rangle_{x_{turb}} \tag{2.2.37}$$

$\langle ... \rangle_{x_{turb}}$ denotes averaging over the turbulence layer. Comparing the second term in (2.2.34) with (2.2.37) one can see that the turbulence at plasma edge results in an effectively larger diffraction for an averaged beam. Assuming that the cross-correlation function $CCF(\Delta x, \Delta y)$ is monotonous, we can deduce that

$$\int \frac{dq_y}{2\pi} \left| n_{0,q_y} \right|^2 q_y^2 \propto \frac{\lambda_{cx}}{\lambda_{cy}^2} \tag{2.2.38}$$

where λ_{cx} and λ_{cy} are radial and poloidal correlation lengths respectively determined from $CCF(\lambda_{cx}, 0) = CCF(0, \lambda_{cy}) = e^{-1}$. Thus we know how parameters of the turbulence influence the beam broadening

$$W_{Xturb}^2 \propto \delta \tilde{n}_{max}^2 x_{turb} \frac{\lambda_{cx}}{\lambda_{cy}^2} \tag{2.2.39}$$

where $\delta \tilde{n}_{max}$ is the maximum of the turbulence amplitude for the sake of concreteness. Dependence of W_{Xturb}^2 on plasma parameters and probing frequency is more complicated and described by the relative relations of $\omega, \omega_{ce}, \omega_{pe}$ in (2.2.37), also it should be noticed that the W_{Xturb}^2 is independent on the initial beam width. The expression (2.2.37) implies that the edge turbulence contribute to the beam broadening the most. Nevertheless the equation (2.2.34) takes into account even the turbulence in the plasma core. Taking into account that typically the edge turbulence amplitude is much higher than in the plasma core and the correlation length is smaller at the peripheral plasma we can consider the edge turbulence as the main factor of the beam broadening. But one should keep in mind that it is not always the case [71].

The equations (2.2.33) and (2.2.34) specify the spatial distribution of an averaged X-mode beam in turbulent magnetized plasma. To obtain the probabilistic distribution of the intensity, considering the integral over poloidal wave numbers in (2.2.16) as a sum of random values, we assume that the electric field is normally distributed

$$f_E \left[E\left(x,y\right) \right] = \frac{1}{\sqrt{2\pi \left\langle E^2\left(x,y\right) \right\rangle}} e^{-\frac{\left(E(x,y) - \langle E(x,y) \rangle\right)^2}{2\left\langle E(x,y)^2 \right\rangle}} \tag{2.2.40}$$

the dispersion of this distribution is the derived expression (2.2.33). Moreover the average electric field sharply decreases in the strong turbulence regime $\langle \delta\phi^2 \rangle \gg 1$

$$\frac{\langle E(x,y)\rangle}{E(x,y)\Big|_{\delta n=0}} = e^{-\frac{\langle \delta\phi^2\rangle}{2}} \tag{2.2.41}$$

hence $\langle E(x,y)\rangle$ is negligible. The expression (2.2.40) represents parametric distribution of the electric field for each space position (x, y). The distribution function of intensity $f_{E^2}\left[E^2(x,y)\right]$ is defined by equalizing the probabilities

$$dE^2 f_{E^2}\left[E^2(x,y)\right] = dE f_E\left[E(x,y)\right] + dE f_E\left[-E(x,y)\right] \tag{2.2.42}$$

then

$$f_{E^2}\left[E^2(x,y)\right] = \frac{1}{\sqrt{2\pi\left\langle E^2(x,y)\right\rangle}} \frac{1}{\sqrt{E^2(x,y)}} e^{-\frac{E^2(x,y)}{2\langle E(x,y)^2\rangle}} \tag{2.2.43}$$

It should be mentioned that the probability of the relative deviation of intensity from its average value $I = \frac{E(x,y)^2}{\langle E(x,y)^2\rangle}$ is homogeneous in space and independent on plasma and turbulence parameters since the strong turbulence condition holds:

$$f_I[I] = \frac{1}{\sqrt{2\pi I}} e^{-\frac{I}{2}} \tag{2.2.44}$$

The distribution function for a microwave X-mode beam describes probability of the beam energy allocation in plasma volume, that allows to provide statistical analysis of processes associated with the wave-plasma energy exchange in strongly turbulent plasmas. A parametric decay instability is a typical example of such processes, and it is analysed the fourth chapter of this thesis.

The spatial and probabilistic distributions of the beam intensity in the turbulent plasma are described, the average beam broadening due to the plasma turbulence is described in terms of the turbulence and plasma characteristics. Distortion of a probing beam can deteriorate the microwave diagnostics (such as CTS) performance, the detailed analysis is done in the next chapter of this thesis. If the high turbulence regime takes place, it seem possible to mitigate the beam broadening effect by changing the probing frequency. W^2_{Xturb} is a complicated function of the frequencies $\omega, \omega_{ce}, \omega_{pe}$ so it depends on the density and magnetic field profiles, but when all these frequencies are close, W^2_{Xturb} decays with growing the probing wave frequency ω, that can be used to reduce the beam distortion in turbulent plasma.

2.3 Numerical modeling of X-mode beam propagation in turbulent plasma

Numerical simulations of a high-frequency X-mode beam propagation in turbulent plasma provide comparison with the theoretical results established in the previous section. For the both types of the numerical simulations in this section (typical conditions for a CTS experiment on ITER and an ECRH experiment on ASDEX Upgrade) the following applicability criteria of the analytical expressions, derived in the previous section, are fulfilled: the slab model is good for considering a beam propagation through a narrow turbulent layer, especially for reactor-size machines; the geometrical optics approach

$$\frac{d\lambda}{dx} \ll 1 \tag{2.3.1}$$

holds since there is no cut off and resonance for a probing wave under the considered conditions, the turbulence typical scale (correlation length) is bigger than the probing wave length; low turbulence rate $\delta k^2 \ll k^2$ holds almost always for a realistic turbulence amplitude in a fusion machine, other than the case when the turbulence is located in the vicinity of the upper-hybrid (UH) resonance since $\frac{\delta k^2}{k^2} \propto \frac{1}{\omega^2 - \omega_{ce}^2 - \omega_{pe}^2}$. In the simulated plasmas the UH resonance for the probing frequencies does not take place. The main parameter which influence the analytical applicability is the phase variation $< \delta\phi^2 >$. The numerical experiments described further in this section are performed in order to verify over which turbulence parameters domain the obtained analytical expressions are applicable ($< \delta\phi^2 > \gg 1$) in the framework of typical conditions for the CTS and the ECRH experiments, to evaluate the deviation from these expressions, to estimate significance of a beam broadening, caused by the plasma turbulence.

The simulations are performed using the full-wave code IPF-FD3D, this code corresponds to a Maxwell equations solver coupled to a J-solver which provide the linear response of magnetized plasma excited by a propagating wave [72].

2.4 Simulations under the conditions of CTS experiment for ITER

For the first stage of simulations plasma parameters are chosen to be close to the expected ones for the ITER Baseline Scenario. By this choice we aim at modeling relevant conditions for the planned CTS experiments on ITER. Value of magnetic field at the plasma center $B = 5.3$ T, central density $n_{max} = 1.3 \cdot 10^{20}$ m^{-3}. The model profiles are illustrated in figure 8. The probing frequency $f = 64$ GHz. These characteristics being representative of ITER CTS [34], so

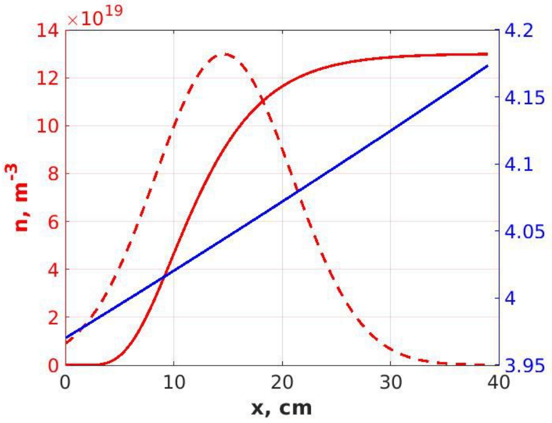

Figure 8: Solid red and blue curves are density and magnetic field profiles respectively, dashed curve is envelope of the turbulence $\sqrt{\langle \delta n^2 (x) \rangle}$ normalized to the maximal value of the background density

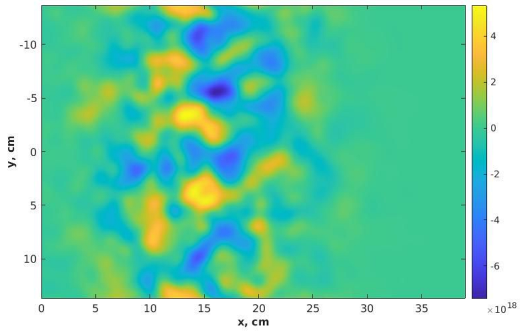

Figure 9: One example of the turbulence map in the computation domain, the turbulence amplitude $\frac{\delta \tilde{n}_{max}}{n_{max}} = 1.7\%$ and the correlation length λ_c=1.6 cm

they are relevant for description of the edge turbulence impact on the probing beam distortion in the CTS experiment at ITER.

In particular the turbulence properties are extrapolated from existing experiments assuming that they are relevant for this work due to the fact the ITER edge turbulence properties are still unknown. This is the reason why the simulations of beam propagation were performed for different values of relative turbulence amplitude defined as $\frac{\delta\tilde{n}_{max}}{n_{max}} = \frac{\sqrt{\langle\delta n^2\rangle_{max}}}{n_{max}}$ and correlation length λ_c which was assumed equal for radial and poloidal directions for simplicity $\lambda_c = \lambda_{cx} = \lambda_{cy}$, but could be performed without this assumption. The used range of the turbulence parameters for these simulations is $\frac{\delta\tilde{n}_{max}}{n_{max}} \in [0.9, 5.0]$ % and $\lambda_c \in [0.8, 6.4]$ cm. The choice of these parameters is aimed at: (I) checking the analytical expression in the wide range of the turbulence parameters, (II) covering the typical range of the turbulence parameters for a fusion machine so far as it is hard to predict what the turbulence properties will be in ITER.

The turbulence was generated on the base of 2D inverse fast Fourier transformation (IFFT2D), $\delta n\left(x,y\right) = \sqrt{\langle\delta n^2\left(x\right)\rangle} IFFT2D\left(S_{2D}\left(q_x,q_y\right)e^{i\xi}\right)$, $S_{2D}\left(q_x,q_y\right)$ is 2D matrix of the turbulence spectrum, ξ is the same size matrix of random phases, $\sqrt{\langle\delta n^2\left(x\right)\rangle}$ is the used turbulence envelope illustrated on figure 8 (normalized to n_{max}), amplitude of the envelope corresponds to the definition of the turbulence amplitude mentioned above. The usual model of symmetric turbulence spectrum was used $S_{2D}\left(q_x,q_y\right) = S_{2D}\left(q_\perp\right)$. The spectrum is constructed taking into account experimental data obtained on ASDEX Upgrade [73]. We applied the turbulence spectrum possessing the same shape (figure 10) but with a shifted knee position $q_\perp\rho_i = 1$, following the standard description of the turbulence k-spectrum [74], ρ_i is the ion Larmor radius, in accordance with higher ion temperatures in ITER plasmas, $T_i \approx 12$ keV. So far as the saturation value q_{sat} (spectrum saturation at low wave numbers, see figure 10) is unspecified in the experimental spectrum measurements, this offers us the possibility to adapt the spectrum through the q_{sat} parameter to access to the wanted correlation length. An example of the turbulence distribution is shown on figure 9 for the following parameters: the turbulence amplitude $\frac{\delta\tilde{n}_{max}}{n_{max}} = 1.7\%$ and the correlation length λ_c=1.6 cm which is symmetric ($\lambda_c = \lambda_{cx} = \lambda_{cy}$) in accordance with the symmetric turbulence spectrum. The cross-correlation function is monotonous in the described turbulence model so the definition of the correlation length is chosen as $CCF\left(0,\lambda_c\right) = CCF\left(\lambda_c,0\right) = e^{-1}$.

The results of numerical calculations of the averaged beam width $W(x)$ (see Eq. (2.2.34)) under the condition of a fixed turbulence correlation length $\lambda_c = 1.6$ cm and different turbulence amplitudes are shown on figure 11. The four simulated cases were done for different conditions in terms of applicability of the analytical description $\langle\delta\phi^2\rangle \gg 1$. For the turbulence level 0.9% the analytical description does not work well, for 1.7% it is at the border of the applicability criteria, for 3.5% and 5.0% the strong turbulence criteria holds well figure 12. One can see that the consistency between the numerical and analytical curves is in a good agreement with the applicability criteria, namely the higher $\langle\delta\phi^2\rangle$ value, the smaller relative discrepancy between the analytical and numerical beam broadening associated with the turbulence. The averaged beam width was analogously compared for different correlation lengths at fixed turbulence level $\frac{\delta\tilde{n}_{max}}{n_{max}} = 3.5\%$ figure 13. Averaging was performed over 400 realizations for each case, which provides confident results with a statistical error bars of 5%.

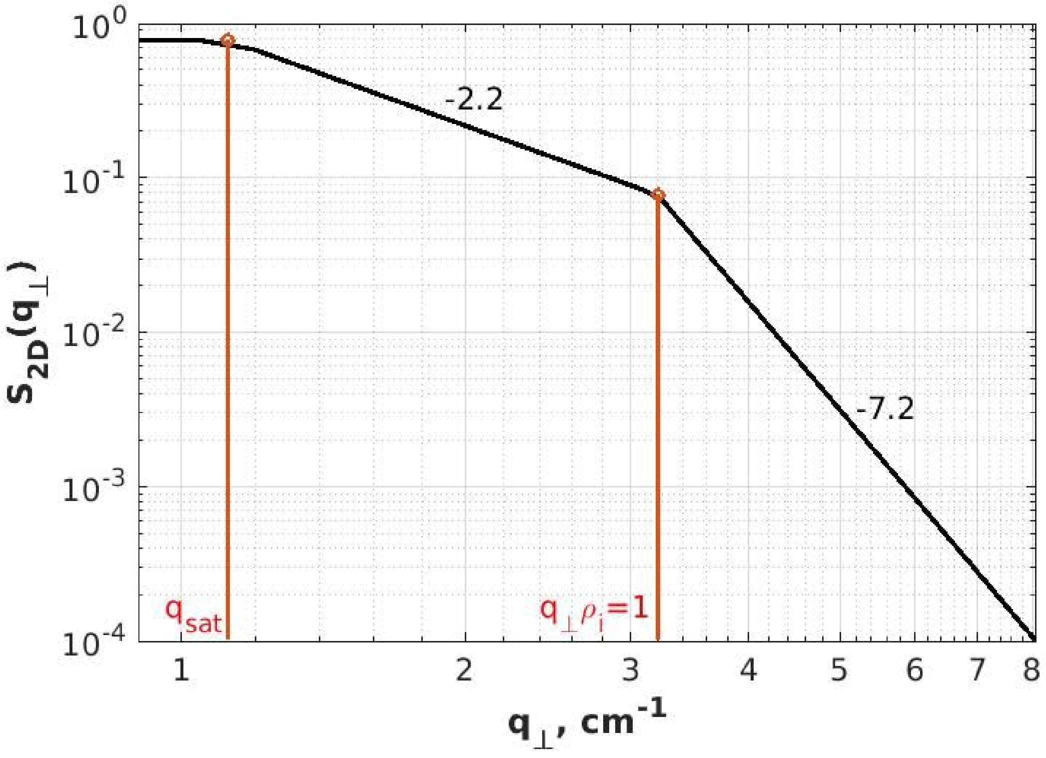

Figure 10: Generic model of generated turbulence wave number spectra

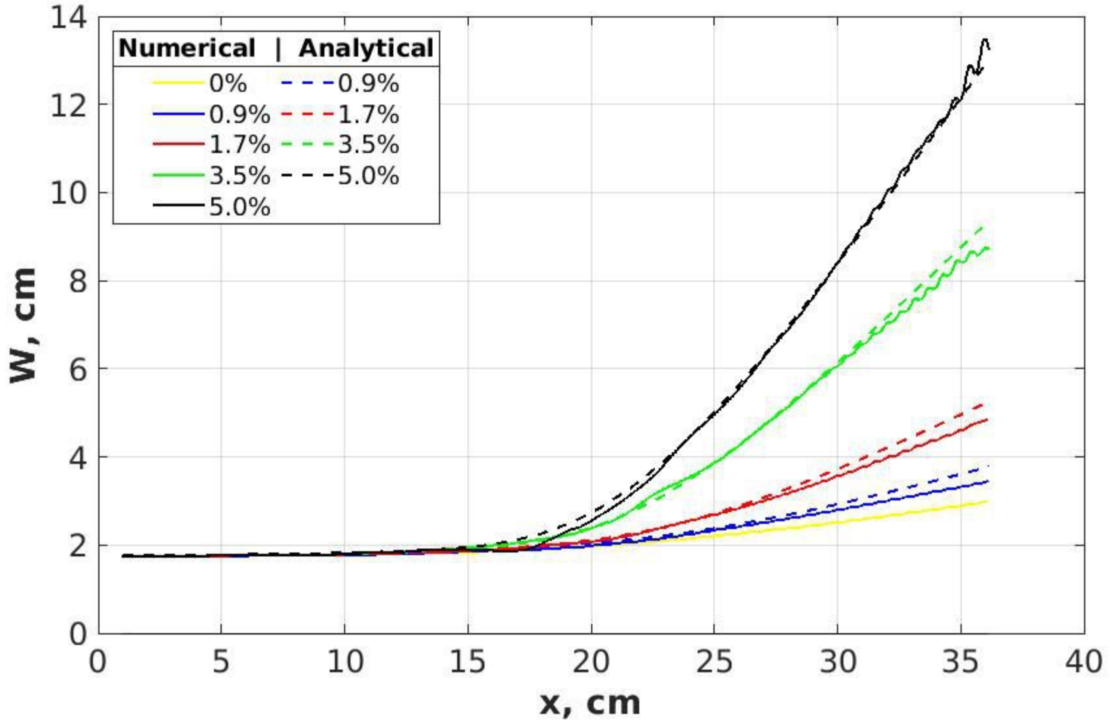

Figure 11: Averaged beam width evolution in turbulent plasma for a fixed turbulence correlation length $\lambda_c = 1.6$ cm and different turbulence normalized amplitudes given in % $\frac{\delta\tilde{n}_{max}}{n_{max}}$

It is seen that presence of the edge turbulence, even possessing a low amplitude, can lead to significant beam spreading and increasing its angular width. In terms of diagnostics that results in a complication of interpretation the microwave diagnostics data and requires the knowledge of the edge turbulence properties. It also deteriorates the spatial resolution of the wave-based

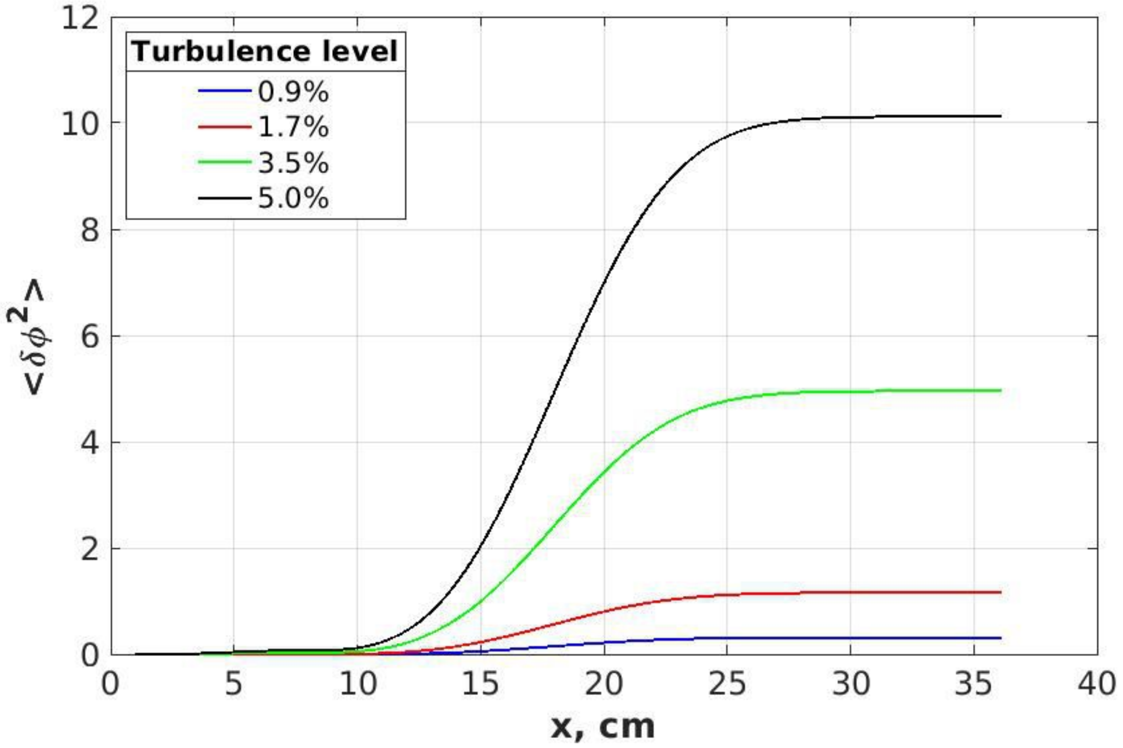

Figure 12: Averaged square of the phase perturbations for different turbulence normalized amplitudes $\frac{\delta \tilde{n}_{max}}{n_{max}}$ measured in percentage

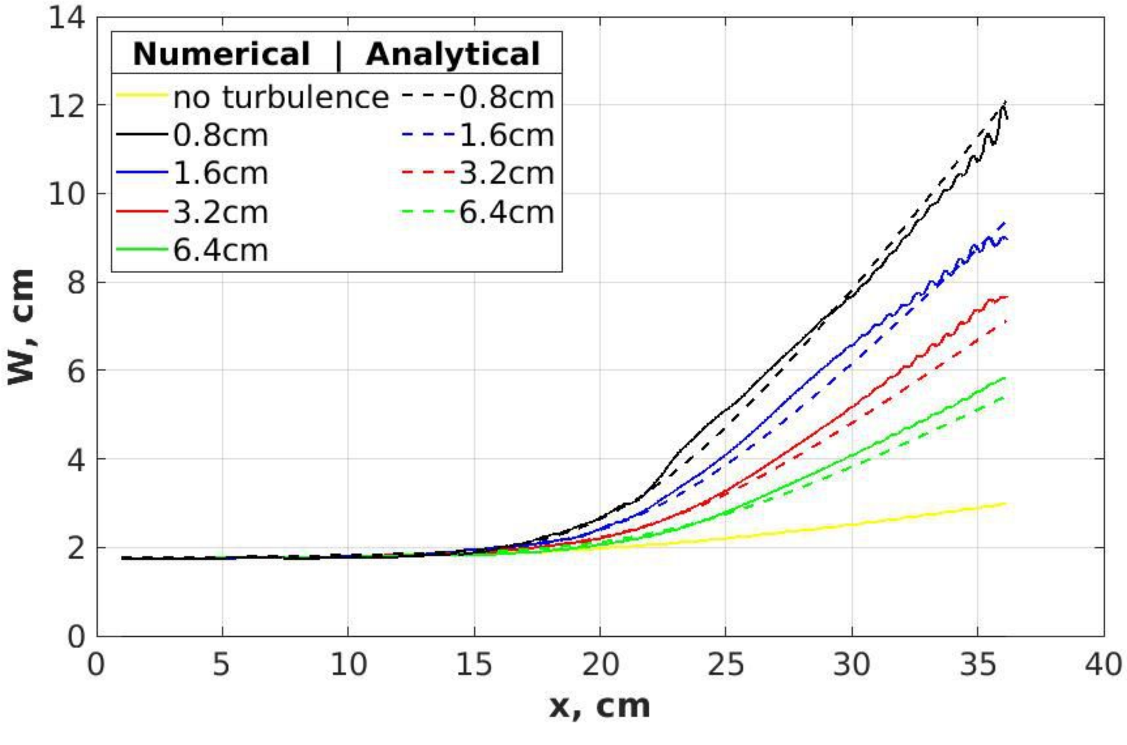

Figure 13: Averaged beam width evolution in turbulent plasma for a fixed turbulence level $\frac{\delta \tilde{n}_{max}}{n_{max}} = 3.5\%$ and different correlation lengths λ_c values which specified for each analytical and numerical curve in cm

diagnostics.

To mitigate these negative effects it is worth considering the use of higher frequencies for the wave-based diagnostics such as CTS for ITER. For instance the evolution of three identical beams with different frequencies in turbulent plasma is presented on figure 14, the turbulence normalized amplitude 5.0%, the correlation length $\lambda_c = 1.6$ cm, the tested frequencies are $F = 64$ GHz, $F = 82$ GHz and $F = 100$ GHz. It is clearly seen that the higher probing frequency the less distortion of a probing beam under the considered conditions of typical parameters for the planned CTS experiment on ITER. The presented numerical results for the chosen three frequencies are aimed only at illustrating the beam broadening sensitivity to the probing frequency under the typical conditions for the planned CTS experiment on ITER. Here we do not propose using some optimal frequency because of the lack of the first-principle predictions about the characteristics of the ITER pedestal and the edge turbulence. This task requires rather precise (not typical) profiles and probably taking into account the real geometry for a concrete experiment.

The significant sensitivity to the frequency can be explained by the expression (2.2.37). To this one can notice that in the case of the probing frequency $F = 100$ GHz the three frequencies $\omega, \omega_{ce}, \omega_{pe}$ are very close in the vicinity of the pedestal figure 15. Assuming that $\frac{\omega^2-\omega_{ce}^2}{\omega^2} \ll 1$ and $\frac{\omega^2-\omega_{pe}^2}{\omega^2} \ll 1$ we can infer that $W_{Xturb}^2 \propto \omega^{-4}$. Of course the assumption does not hold in the whole area of the edge turbulence, nevertheless it gives an estimate for the beam width dependence on the frequencies in the certain frequencies range. The real beam width dependence on the frequency is a complicated function of the cyclotron and plasma frequencies profiles, and can be investigated numerically for the given profiles using the expressions (2.2.34) and (2.2.37). As it was already noted, since the relevant profiles and the turbulence position in the pedestal area are unknown yet, precise investigation is not the object of this study.

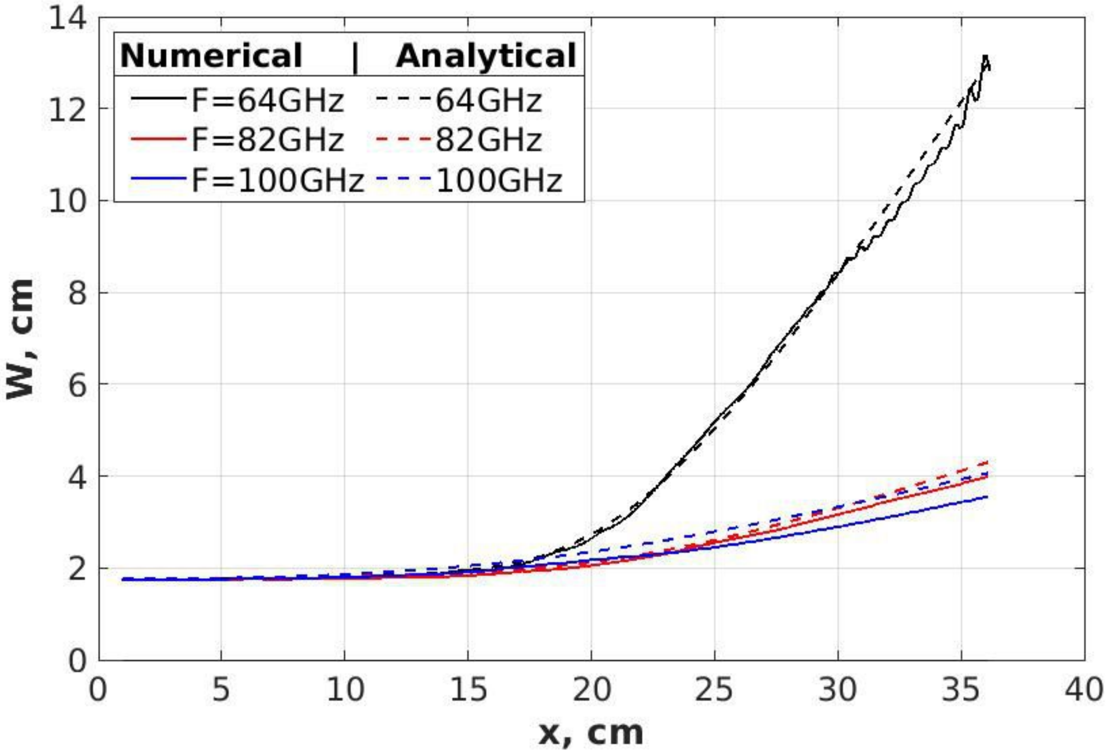

Figure 14: Comparison of the averaged beam width for different frequencies of a probing beam, turbulence rate $\frac{\delta\tilde{n}_{max}}{n_{max}} = 5.0\%$, correlation length $\lambda_c = 1.6$ cm

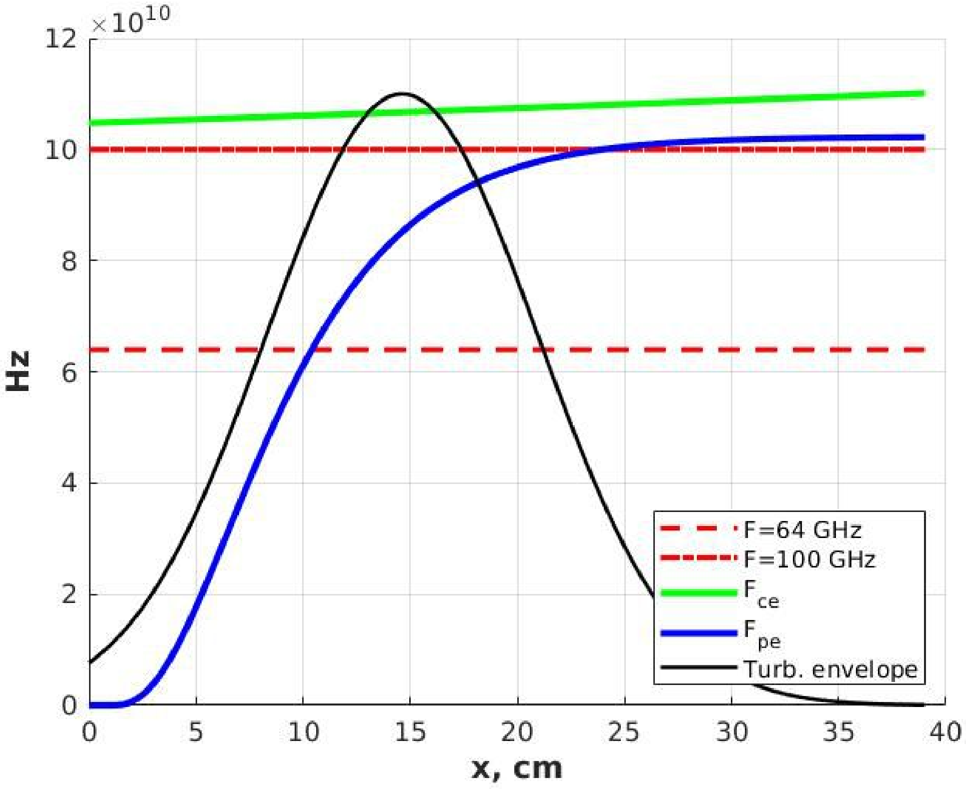

Figure 15: Profiles of the frequencies F_{ce} and F_{pe}, comparison with the probing frequencies F and position of the turbulence envelope (normalized to 1.1×10^{11})

2.5 Simulations under the conditions of ECRH experiment for ASDEX Upgrade

ECRH is a widely used method of plasma heating, normally the heating energy may be deposited at selected location. In the previous studies done [47] a beam ray tracing was used to evaluate the impact of the density fluctuations in particular the enhancement of the power needed to stabilize Neo Classical Tearing modes. In the following works on this subject both polarizations were studied using beam ray tracing and the comparison with a full-wave code was done with O-mode and showed the sensitivity of the beam widening to the turbulence properties [46]. Here to validate the dependencies established in the theoretical part of this paper for X-mode simulations have been performed. These computations were run to investigate the role of the edge turbulence in beam propagation process under conditions of an ECRH experiment. The magnetic field at plasma center $B = 2.5$ T, the maximal value of background density $n_{max} = 0.8 \cdot 10^{20}$ m^{-3}, the probing frequency $F = 140$ GHz provides heating at the second cyclotron harmonic, these characteristics being representative of ASDEX Upgrade. The chosen model profiles are shown on figure 16, an example of the random turbulence distribution is illustrated on figure 17. The correlation length is fixed for these simulation, $\lambda_c = 1.0$ cm. The correlation length and turbulence amplitude values are chosen as typical for the tokamak so far as these parameters vary for different regimes [75] - [77]. Moreover the correlation length depends on the radial position [76, 77], but we used a simplified model with a homogeneous turbulence cross-correlation function for the simulations. The beam width evolution for two

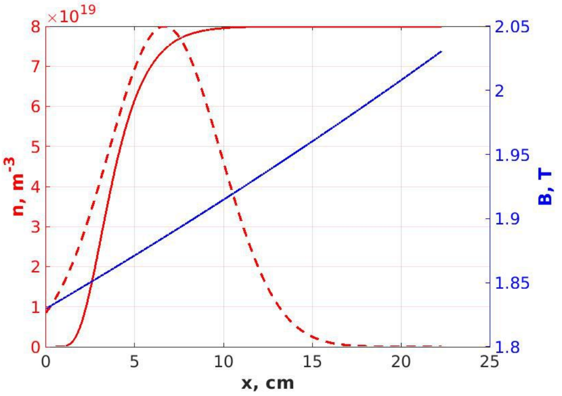

Figure 16: Solid red and blue curves are density and magnetic field profiles respectively, dashed curve is the envelope of the turbulence $\sqrt{\langle \delta n^2(x) \rangle}$ normalized to the maximal value of the background density

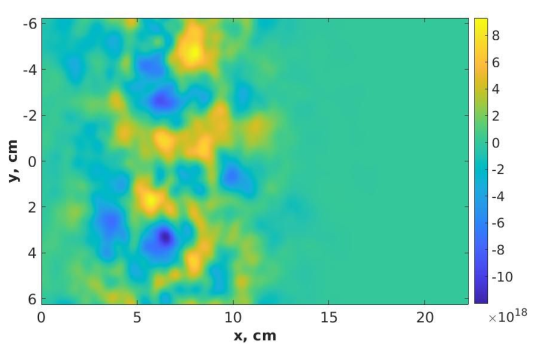

Figure 17: 2D turbulence map for the follow parameters: turbulence level $\frac{\delta \tilde{n}_{max}}{n_{max}} = 5.0\%$, correlation length λ_c=1.0 cm

different turbulence amplitudes: $\frac{\delta \tilde{n}_{max}}{n_{max}} = 5.0\%$ and $\frac{\delta \tilde{n}_{max}}{n_{max}} = 10.0\%$ is obtained numerically and compared with the analytical predictions, see figure 18, the averaging of the numerical distributions is performed over 2600 and 2200 realizations for the two cases respectively. The turbulence level $\frac{\delta \tilde{n}_{max}}{n_{max}} = 5.0\%$ corresponds to the edge of the analytical description applicability, the value $\frac{\delta \tilde{n}_{max}}{n_{max}} = 10.0\%$ is in good agreement with the strong turbulence criteria, checking of the criteria for the two turbulence levels is shown on figure 19.

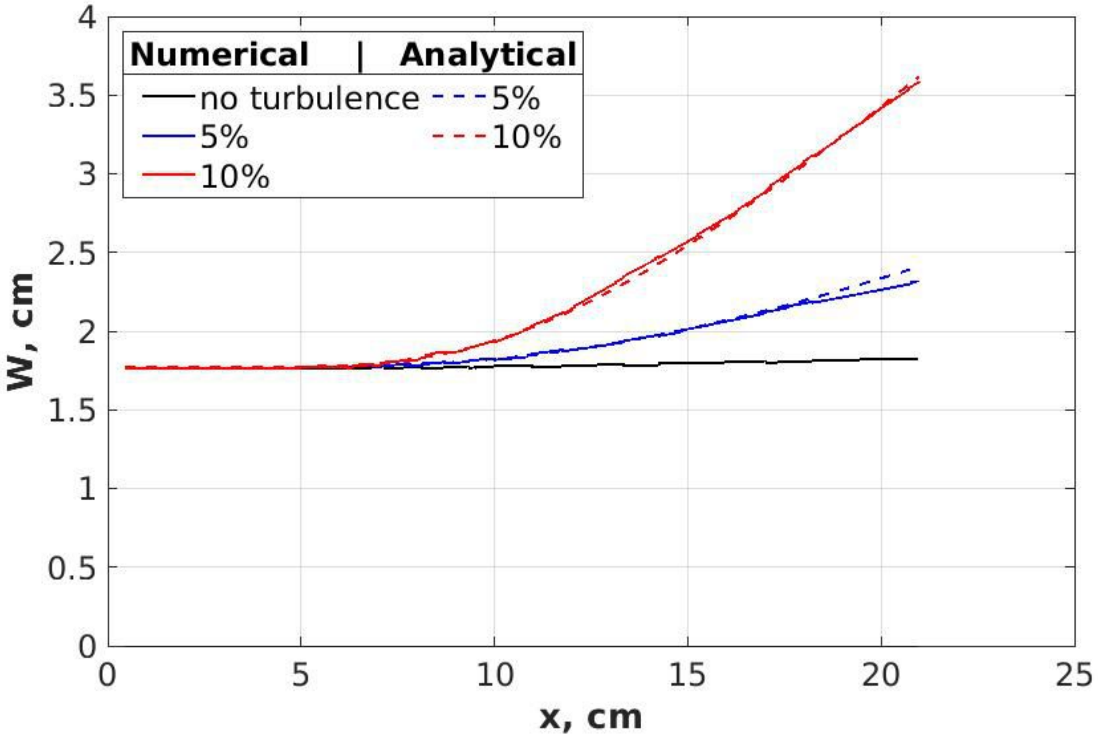

Figure 18: The averaged beam width evolution in turbulent plasma for fixed turbulence correlation length $\lambda_c = 1.0$ cm and different turbulence rates $\frac{\delta \tilde{n}_{max}}{n_{max}}$ which percentage is specified for each analytical and numerical curve

To know the probabilistic properties of the beam energy allocation in strongly turbulent plasma we investigate the intensity distribution at a fixed position. It is convenient to use the intensity normalized to its average value $I = \frac{E(x,y)^2}{\left\langle E(x,y)^2 \right\rangle}$, comparison of the numerical simulations

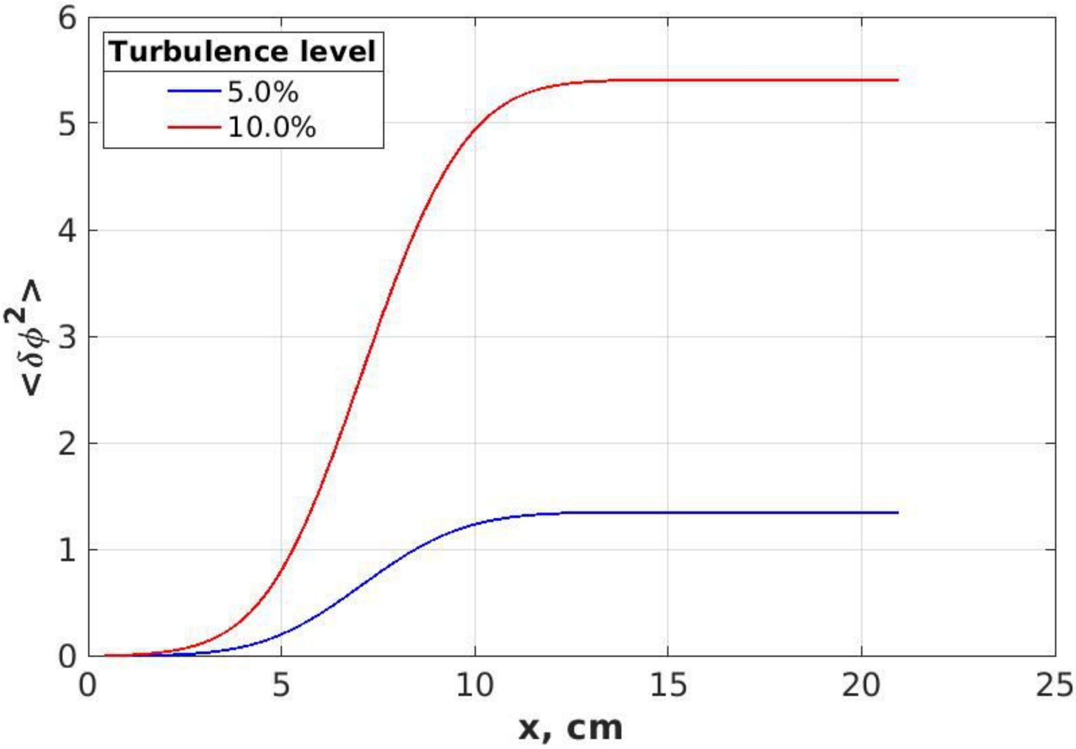

Figure 19: Averaged square of the phase perturbation for the different turbulence normalized amplitudes $\frac{\delta \tilde{n}_{max}}{n_{max}}$ measured in percentage

is provided with the analytical expression (2.2.44). For the turbulence level $\frac{\delta \tilde{n}_{max}}{n_{max}} = 5.0\%$ the relative intensity is shown on figures 20 and 21 for the two spatial points: $(x, y) = (20.5, 0)$ cm and $(x, y) = (20.5, 2.3)$ cm respectively. The radial point $x = 20.5$ cm corresponds to the edge of the calculation domain, the two selected poloidal points correspond to positions of the averaged beam axis and width. Analogous simulations are done for higher turbulence amplitude $\frac{\delta \tilde{n}_{max}}{n_{max}} = 10.0\%$, the intensity distributions are illustrated on figures 22 and 23 for the points: $(x, y) = (20.5, 0)$ cm and $(x, y) = (20.5, 3.6)$ cm, where the poloidal position $y = 3.6$ cm is width of the averaged beam for this turbulence regime.

The averaged spatial distribution of a probing microwave beam in turbulent plasma is examined for different scenarios of the turbulence, it is seen that since the strong turbulence regime holds $\langle \delta\phi^2 \rangle \gg 1$, results of the numerical simulations are in good agreement with the analytical descriptions for the beam width. According to the figures 20-21, the analytical expression for the intensity probabilistic distribution (2.2.44) is able to provide just a relevant estimate of the distribution function profile in the case of the border value of the applicability criterion ($\langle \delta\phi^2 \rangle \sim 1$). In this case the average electric field is not negligible (see (2.2.41)). The discrepancy between the analytical f_{an} and numerical f_{num} distribution profiles $\frac{f_{an} - f_{num}}{f_{an}}$ depends on a position and constitutes up to 50% in the main area of the distribution function, defined as $\int_0^{\xi^*} f_{num}(\xi) d\xi = 0.99$, except for the vicinity of the point $\xi = \frac{E(x,y)^2}{\langle E(x,y)^2 \rangle} = 0$. So far as the simulations number is limited it is impossible to obtain the infinity numerically, which is the analytical prediction. The tail part of the profiles is underestimated in this case. In the case with $\langle \delta\phi^2 \rangle \approx 5.4$, corresponding to the turbulence amplitude 10%, the analytical and numerical profiles are in a relatively good agreement. The discrepancy is more homogeneous

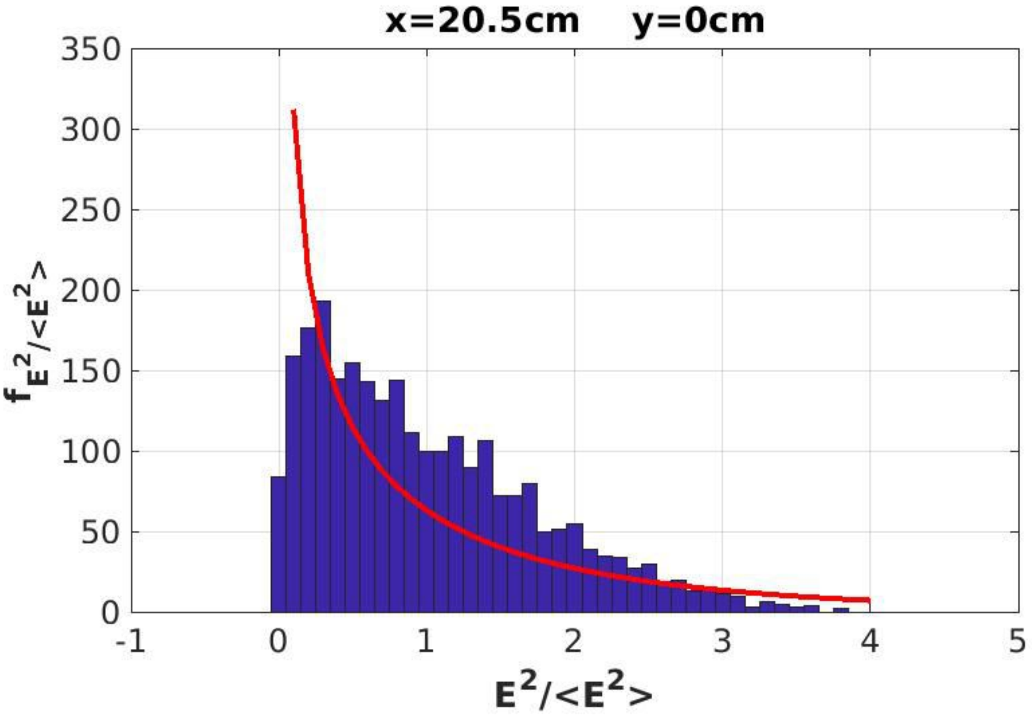

Figure 20: The intensity distributions, blue histogram is the numerical distribution, red curve is the analytical distribution normalized to the number of realizations. Turbulence level $\frac{\delta \tilde{n}_{max}}{n_{max}} = 5.0\%$, radial position $x = 20.5$ cm at the axis of the average beam

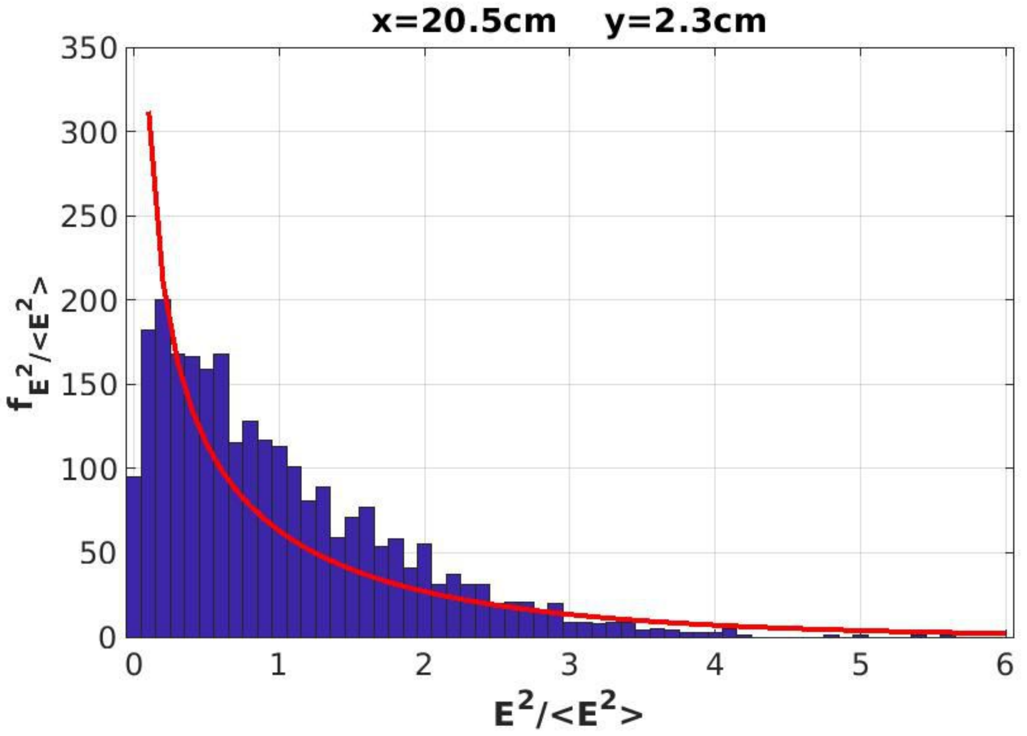

Figure 21: Intensity distributions, blue histogram is the numerical distribution, red curve is the analytical distribution normalized to the number of realizations. The turbulence level $\frac{\delta \tilde{n}_{max}}{n_{max}} = 5.0\%$, radial position $x = 20.5$ cm and poloidal position $y = 2.3$ cm, corresponding to the average beam width

and its average value $\frac{<f_{an} - f_{num}>}{f_{an}} \approx 18\%$ in the main area. It is seen that the tail part of the distribution is approximated much better than in the low turbulence case.

One can see that the theoretical model developed fits much better the numerical results at high turbulence level. However as the turbulence properties at the plasma edge are still

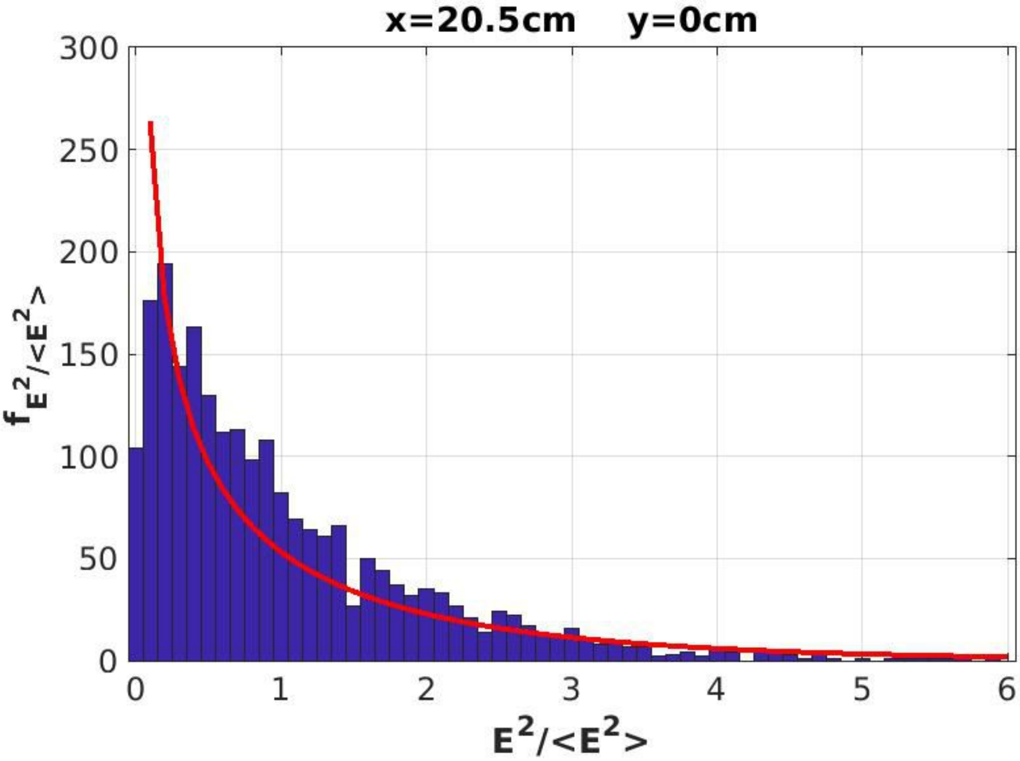

Figure 22: The intensity distributions, blue histogram is the numerical distribution, red curve is the analytical distribution normalized to the number of realizations. Turbulence level $\frac{\delta\tilde{n}_{max}}{n_{max}} = 10.0\%$, radial position $x = 20.5$ cm at the axis of the average beam

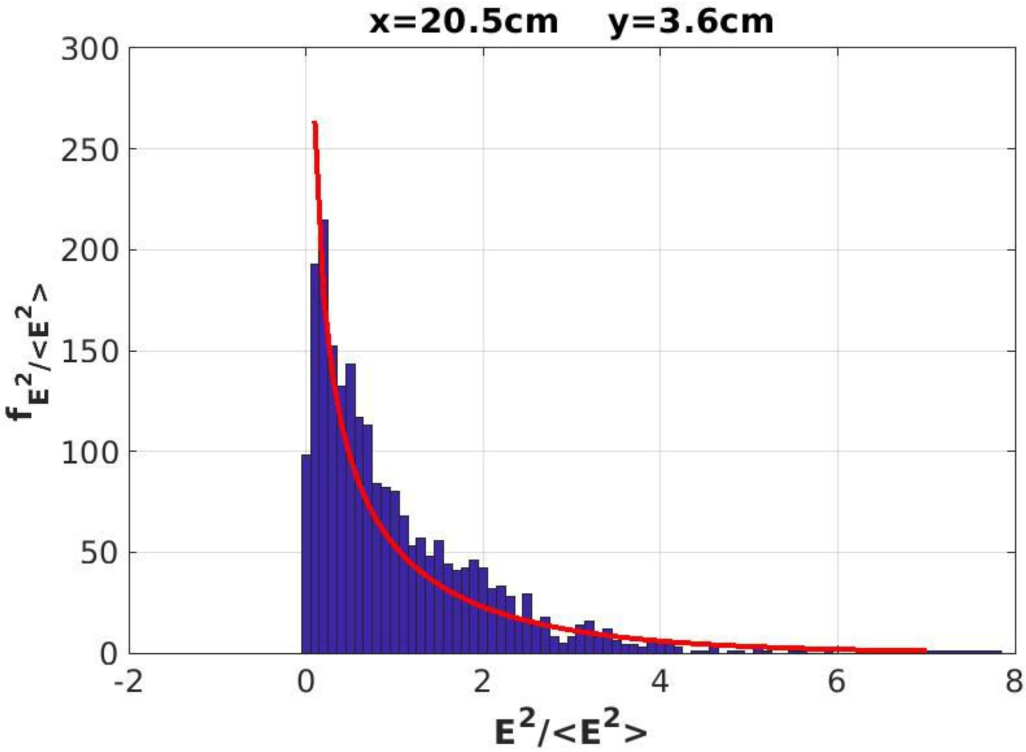

Figure 23: The intensity distributions, blue histogram is the numerical distribution, red curve is the analytical distribution normalized to the number of realizations. The turbulence level $\frac{\delta\tilde{n}_{max}}{n_{max}} = 10.0\%$, radial position $x = 20.5$ cm and poloidal position $y = 3.6$ cm, corresponding to the average beam width

unknown for ITER we can not evaluate the impact the edge turbulence on a microwave beam broadening for this fusion machine, but the tool for its analysis is given and can be used as far as a relevant model for the turbulence description exists.

2.6 Discussion on X-mode propagation in turbulent plasma

The microwave X-mode beam propagation in turbulent magnetized plasma is described analytically and simulated numerically, the spatial and probabilistic distributions of the beam are obtained in regime of strong phase modulation of the beam. The main dependencies are given in the equation (2.2.39), that describes the X-mode beam broadening sensitivity of the edge turbulence properties. The numerical simulations are performed for plasma conditions characteristic for ITER Baseline Scenario and ASDEX Upgrade, representing model conditions of the CTS and ECRH experiments respectively, with different scenarios of the turbulence. It is shown that under conditions of ITER plasma even low-level edge turbulence may cause significant distortions of beam averaged geometrical characteristics namely beam spatial and angular widths. These results are consistent with the simulations and estimates done previously in [48, 57], the expected additional beam broadening, associated with the edge turbulence, is of the order of 100%. This negative effect may be of high importance for the planned CTS diagnostics in ITER. A CTS diagnostics demands high-power probing beam (of the order of 1MW) due to a very low scattering efficiency, that is why decreasing of the registered signal associated with the plasma edge turbulence can be a noticeable problem. Analysis of the signal measured in a CTS experiment taking into account the edge turbulence will be presented in the chapter three of this thesis. It should be mentioned that increasing of a probing frequency for the planned CTS experiments in ITER can drastically reduce the negative effect of the beam spreading. The beam distortions associated with the edge turbulence is significant only for a relatively large turbulence amplitude under the condition of ECRH experiment for ASDEX Upgrade. However to evaluate in an accurate manner the turbulence influence on the ECRH or diagnostics using microwave beams the knowledge of the turbulence properties (correlation lengths, amplitude) is required. If it is possible the probing frequency optimization can improve the spatial resolution of the CTS measurements, taking into account the edge plasma turbulence.

To have predictive tools for the ECRH and CTS experiments some room in the plasma turbulence diagnostics is open to access in real time to the edge turbulence properties. Then it will be possible to introduce the relevant corrections in the NTM control or provided inputs for the CTS interpretative model, integrating the turbulence effects on the measurements as this procedure is described in the next chapter of this thesis.

3 CTS analysis in turbulent plasma

Propagation of an extraordinary polarized microwave beam in turbulent plasma was analysed in the previous chapter analytically and numerically. It was demonstrated that presence of the turbulent edge layer can result in a drastic distortion of a probing beam shape. The higher turbulence amplitude, the more significant the distortion and the higher probing frequency, the less this effect. It is clear that this effect may lead to incorrect interpretation of the CTS registered signal [78], but no publications on the CTS with respect to the edge plasma turbulence are available, an analysis is remained to be done. Results of the classical works devoted to the CTS analysis [81] - [83] can be used for description of the experiments where a significant spatial and angular beam broadening does not take place. The recent works about the planned CTS on ITER [34] rely upon the classical description, mostly on Bindslev's papers, and do not take into account the probing beam distortion due to the edge turbulence. But, as it was demonstrated in the researches [44], [78]-[80] during the last decade, this effect is pretty pronounced even for much higher frequencies than it is planned to use for the CTS on ITER (60 GHz).

The research work described in this chapter is devoted to the analysis of the CTS measurements interpretation with respect to the probing beam distortion due to the edge turbulence. Here we assume that the probing beam distortion is associated with the edge turbulence, implying that the edge zone contributes to a probing beam modification the most. Analytical consideration of the CTS signal in this chapter is based on the method of the probing beam description in turbulent plasma developed and analysed in detail in [44, 78] and presented in the previous chapter of the thesis.

In a CTS experiment there are two microwave beams: a probing and receiving one (in the framework of the reciprocity theorem), and the plasma turbulence can significantly distort them both, this effect can modify registered spectrum in a collective Thomson scattering experiment. The effect of the registered frequency spectrum distortion by the turbulence is evaluated for different turbulence levels for plasma parameters similar to those expected in ITER.

This chapter is organized as follows: in the first section we generalize the model of a probing beam description in turbulent plasma to 3D case in the limit of small toroidal angles, this description and the introduced notations are used in the second part - the explicit derivation of the expression for registered power spectrum in the CTS experiment, numerical estimates of the derived expressions are provided in the third section, the results of the CTS analysis in turbulent plasma are discussed in the last part of this chapter.

3.1 Description of 3D X-mode beam distribution in turbulent plasma

Propagation of a microwave beam in turbulent inhomogeneous plasma in 3D model is analysed first. The 2D analysis was done in [78] and it is described in the previous chapter of this thesis, the generalization of the X-mode beam propagation in turbulent plasma to the 3D geometry is provided in this section. The introduced notations and the 3D description of the beam will be needed for the next step - the scattered radiation analysis.

Here we also introduce the Cartesian coordinates for description of the beam propagation in the slab medium approximation. The slab medium model is normally applicable for description of a microwave beam propagation when the curvature of the density and magnetic field profiles is negligible on the scale of the beam width. The radial coordinate which coincides with plasma inhomogeneity direction is x axis, z axis corresponds to lines of external magnetic field $\mathbf{B}$, y axis represents poloidal coordinate and it is perpendicular to the x and z. The beam propagation is assumed mostly along the radial direction x with a small wave number k_z projection on the magnetic field z determined by the angle ψ. The reason behind taking into account the finite angle ψ (for the emitter or receiver) is that such a geometry of a CTS experiment is used in order to avoid signals from plasma modes propagating perpendicularly to the magnetic field [34]. The discussed model of the beam propagation is illustrated in the figure 24.

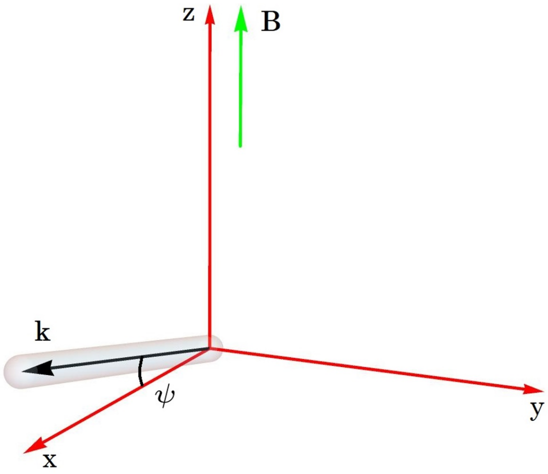

Figure 24: Description of the probing beam at the plasma edge, the beam propagates along the wave vector $\mathbf{k}$, x axis is the direction of the plasma inhomogeneity, z axis coincides with the magnetic field vector $\mathbf{B}$, ψ is the angle between $\mathbf{k}$ and x axis.

The dispersion relation, that describes the X-mode beam propagation with a finite longitudinal wave number k_z reads

$$\det\begin{vmatrix} \frac{\omega^2}{c^2}\varepsilon - k_z^2 & \frac{\omega^2}{c^2}ig & k_\perp k_z \\ -\frac{\omega^2}{c^2}ig & \frac{\omega^2}{c^2}\varepsilon - k_\perp^2 - k_z^2 & 0 \\ k_\perp k_z & 0 & \frac{\omega^2}{c^2}\eta - k_\perp^2 \end{vmatrix} = 0 \tag{3.1.1}$$

where $k_\perp$ is the perpendicular to the magnetic field wave number component, ω - probing frequency and the permittivity tensor components (ε, g, η) in the «cold plasma» model are given by (2.1.8). The perpendicular wave number is the solution of (3.1.1) for a given toroidal mode k_z

$$\begin{aligned} k_\perp^2(x, k_z) = {} & \frac{\omega^2}{c^2}\frac{\varepsilon^2 - g^2 + \varepsilon\eta - (\varepsilon + \eta)\frac{c^2}{\omega^2}k_z^2}{2\varepsilon} \\ & \pm\frac{\omega^2}{c^2}\frac{\sqrt{(\varepsilon^2 - g^2 - \varepsilon\eta)^2 + 2\frac{c^2}{\omega^2}k_z^2\left((\varepsilon+\eta)g^2 - \varepsilon(\varepsilon-\eta)^2\right) + \frac{c^4}{\omega^4}k_z^4(\varepsilon-\eta)^2}}{2\varepsilon} \end{aligned} \tag{3.1.2}$$

Assuming small diffraction for a probing beam launched dominantly in the radial direction $k_x \gg k_y, k_z$ and small enough angle ψ, expression for the radial wave number component can be simplified as

$$k_x \approx k\left(x\right) + \frac{\partial k_\perp}{\partial n}\delta n\left(x,y\right) + \left.\frac{\partial\sqrt{k_\perp^2 - k_y^2}}{\partial k_y^2}\right|_{k_{y,z}=0} k_y^2 + \left.\frac{\partial k_\perp}{\partial k_z^2}\right|_{k_{y,z}=0} k_z^2 \tag{3.1.3}$$

where the second term is the wave number correction associated with the turbulence $\delta n\left(x,y\right)$ which normally have dominantly perpendicular structure and elongated in the toroidal direction, the third and fourth terms describe diffraction of a beam. Also we choose the sign «+» in the expression (3.1.2) for concreteness, that corresponds to the X-mode polarisation which is chosen for the CTS measurements on ITER, then $k^2\left(x\right) = \frac{\omega^2}{c^2}\frac{\varepsilon^2 - g^2}{\varepsilon}$. The density fluctuations are taken into account in (3.1.3) in the framework of the cold plasma dispersion relation under supposition of small wavenumber perturbation (perturbation method). This method was developed in the theory of wave propagation in the turbulent atmosphere and was summarized in [84]. The detailed analysis of the 2D wave propagation on the base of the geometrical optics approach in turbulent plasma is described in the previous chapter of this thesis, here we write down the expression for the electric filed **E** distribution under the considered conditions, including the toroidal direction (3D propagation)

$$\mathbf{E}\left(x,y,z\right) = \mathbf{e}\sqrt{\frac{\omega}{ck\left(x\right)}}\int_{-\infty}^{+\infty}\int_{-\infty}^{+\infty}\frac{dk_y}{2\pi}\frac{dk_z}{2\pi}E_0\left(k_y,k_z\right)\times \\ e^{ik_y y + ik_z z}e^{i\int_0^x dx' k(x') - i\frac{k_y^2 d_y^2(x)}{2} - i\frac{k_z^2 d_z^2(x)}{2} + i\delta\phi} \tag{3.1.4}$$

here the used notations: $d_y^2(x)$ is described by the expression (2.2.17), the random phase $\delta\phi$ and the function $\kappa(x)$ are given by the expressions (2.2.18) and (2.2.19) correspondingly, the phase perturbation of a partial wave $\delta\phi$ is the total perturbation obtained on the wave trajectory, according to the geometrical optics the trajectory $y'(x, y, x', k_y)$ is described by (2.2.20) and (2.2.21), since the ray trajectrory in y and z direction can be considered independently, all the functions that characterize the y trajectory projection have already been derived and discribed in the previous chapter; d_z^2 function describes the beam diffraction in z direction

$$d_z^2(x) = \int_0^x dx' \frac{1}{k(x')}\left(1 - \frac{g^2\left(x'\right)}{\varepsilon\left(x'\right)\left(\varepsilon^2\left(x'\right) - g^2\left(x'\right) - \varepsilon\left(x'\right)\eta\left(x'\right)\right)}\right) \tag{3.1.5}$$

$E_0\left(k_y,k_z\right)$ is the antenna's diagram, **e** is the polarization vector. The four terms in the last exponent in (3.1.4) is the result of integration of k_x (3.1.3) along the radial coordinate. The explicit form of $E_{y0}\left(k_y,k_z\right)$ for a Gaussian diagram

$$E_0\left(k_y,k_z\right) = E_{i0}2\pi\rho^2 e^{-\frac{k_y^2\rho^2}{2}}e^{-\frac{\left(k_z - \frac{\omega}{c}\sin\psi\right)^2\rho^2}{2}} \tag{3.1.6}$$

where $E_{i0} = \left|\mathbf{E}\left(\mathbf{r} = \mathbf{0}\right)\right|$, ρ is the beam width at the waist of a probing beam, the waist is located at $x = 0$.

In accordance with (3.1.4) a beam passing through turbulent plasma is the more perturbed the higher turbulence amplitude. The average beam width can describe this effect quantitatively. In order to define the average beam width in y and z directions we consider the average intensity of the beam

$$\left\langle \left|\mathbf{E}\left(x,y,z\right)\right|^2 \right\rangle = \left|\mathbf{e}\right|^2 \frac{\omega}{ck\left(x\right)} \int_{-\infty}^{+\infty} \int_{-\infty}^{+\infty} \frac{dk_{y_1} dk_{y_2}}{\left(2\pi\right)^2} \frac{dk_{z_1} dk_{z_2}}{\left(2\pi\right)^2} E_0\left(k_{y_1}, k_{z_1}\right) E_0^*\left(k_{y_2}, k_{z_2}\right) \times$$
$$e^{i\left(k_{y_1}-k_{y_2}\right)y} e^{i\left(k_{z_1}-k_{z_2}\right)z} e^{-\frac{i\left(k_{y_1}^2-k_{y_2}^2\right)d_y^2(x)}{2}} e^{-\frac{i\left(k_{z_1}^2-k_{z_2}^2\right)d_z^2(x)}{2}} \left\langle e^{i\left(\delta\phi\left(x,y,k_{y_1}\right)-\delta\phi\left(x,y,k_{y_2}\right)\right)} \right\rangle \tag{3.1.7}$$

If the trajectory $y'(x,y,x',k_y)$ is significantly longer than several correlation lengths, one can consider the normal statistical distribution for $\delta\phi\left(x,y,k_y\right)$ so

$$\left\langle e^{i\left(\delta\phi\left(x,y,k_{y_1}\right)-\delta\phi\left(x,y,k_{y_2}\right)\right)} \right\rangle = e^{-\frac{\left\langle \left(\delta\phi\left(x,y,k_{y_1}\right)-\delta\phi\left(x,y,k_{y_2}\right)\right)^2 \right\rangle}{2}} \tag{3.1.8}$$

The detailed analysis of the phase correlation function $\left\langle \left(\delta\phi\left(x,y,k_{y_1}\right) - \delta\phi\left(x,y,k_{y_2}\right)\right)^2 \right\rangle$ is given in the previous chapter, here we write down the final expression for the average beam 3D distribution

$$\left\langle \left|\mathbf{E}\left(x,y,z\right)\right|^2 \right\rangle = \left|\mathbf{e}\right|^2 E_{io}^2 \frac{\omega}{ck\left(x\right)} \frac{\rho^2}{W_y\left(x\right) W_z\left(x\right)} e^{-\frac{y^2}{W_y^2(x)}} e^{-\frac{\left(z-\frac{\omega}{c}\sin\psi d_z^2(x)\right)^2}{W_z^2(x)}} \tag{3.1.9}$$

the beam width components

$$\begin{aligned} W_y^2\left(x\right) &= \rho^2 + \frac{d_y^4\left(x\right)}{\rho^2} + 4\int^x D(x')l^4(x,x')dx' \\ W_z^2\left(x\right) &= \rho^2 + \frac{d_z^4\left(x\right)}{\rho^2} \end{aligned} \tag{3.1.10}$$

and the introduced function

$$D(x) = \frac{1}{2}\kappa^2(x)\frac{\delta\tilde{n}^2(x)}{n^2\left(x\right)} \int \frac{dq_y}{2\pi} \left|n_{0,q_y}\right|^2 q_y^2 \tag{3.1.11}$$

where the relative turbulence amplitude $\frac{\delta\tilde{n}^2(x)}{n^2(x)}$ and the turbulence spectrum $\left|n_{q_x,q_y}\right|^2$, expressed via its cross-correlation function $CCF\left(\Delta x, \Delta y\right)$ (2.2.28), these two turbulence characteristics are determined by the averaging procedure analogous to (2.2.26). The first term in the expression for W_y^2 (3.1.10) stands for the initial probing beam size squared, the second one represents diffraction, taking into account refractive index in inhomogeneous medium, the third part describes the effect of the beam broadening due to the plasma turbulence. The toroidal broadening W_z^2 is described by the initial beam size and the diffraction only because according to (3.1.7) the poloidal and toroidal beam structures are evaluated independently and the turbulence (since it is elongated in the toroidal direction) does not modify W_z^2. The criterion for the applicability of the averaging method used is the big enough value of the average phase variation squared $< \delta\phi^2 >\gg 1$. The broadening of a microwave beam in turbulent plasma is described by the expressions (3.1.10), this characteristics of the average beam and the notations introduced during this derivation will be used in the following analysis of the average registered power in a CTS experiment.

3.2 CTS signal

Expressions from the previous section describe how the edge plasma turbulence modifies average characteristics of a probing beam in the 3D geometry, now we continue analysis of the beam-turbulence interaction in terms of a CTS experiment. The registered intensity in a time period T in CGS units

$$P = \frac{1}{T} \int_{-T/2}^{T/2} dt \int \mathbf{dS} \frac{c}{4\pi} \left| \mathbf{E}^s \left(t, \mathbf{r}\right) \right|^2 \tag{3.2.1}$$

where $\mathbf{E}^s \left(t, \mathbf{r}\right)$ is the scattered field, its intensity is integrated over the receiver waveguide cross-section $\mathbf{dS}$. Applying the Wiener–Khinchin's theorem one can write the spectral power

$$\frac{dP}{d\omega^s} = \frac{1}{\pi T} \int \mathbf{dS} \frac{c}{4\pi} \left| \mathbf{E}_T^s \left(\omega^s, \mathbf{r}\right) \right|^2 \tag{3.2.2}$$

where

$$\mathbf{E}_T^s \left(\omega^s, \mathbf{r}\right) = \int_{-T/2}^{T/2} dt e^{i\omega^s t} \mathbf{E}^s \left(t, \mathbf{r}\right) \tag{3.2.3}$$

The CTS signal can be described on the base of the reciprocity theorem [85]. A Fourier amplitude of the scattered radiation, possessing the frequency ω^s, is described by the expressions

$$\mathbf{E}^s \left(\omega^s, \mathbf{r}\right) = \mathbf{E}^{out} \left(\mathbf{r}\right) A \left(\omega^s\right) \tag{3.2.4}$$

$$A \left(\omega^s\right) = \frac{1}{4} \int d\mathbf{r} \mathbf{j}^{nl} \left(\omega^s, \mathbf{r}\right) \mathbf{E}^+ \left(\mathbf{r}\right) \tag{3.2.5}$$

$\mathbf{E}^{out}$ is the scattered field normalized to the unit power in the registering apparatus as

$$\frac{c}{4\pi} \int ds \left| \mathbf{E}^{out} \right|^2 = 1 \tag{3.2.6}$$

$\mathbf{E}^+ = \mathbf{e}^+ E^+$ is the receiver antenna radiation normalized to the unit power as well (the index "+" is just a conventional notation from the original work [85], it is not related to the polarization mode in the expression (3.1.2)), this radiation is considered in the medium with inversed sign of the magnetic field, $\mathbf{j}^{nl} \left(\omega^s, \mathbf{r}\right)$ is the Fourier transform of the source nonlinear current. The current $\mathbf{j}^{nl}$ describes bilinear interaction of the probing wave $\mathbf{E}^i = \mathbf{e}^i E^i$, possessing the frequency ω^i, with the plasma fluctuations. The vectors $\mathbf{e}^{i,+}$ stand for the waves polarization.

Then the expression (3.2.2) can be written in the form

$$\frac{dP}{d\omega^s} = \frac{1}{16\pi T} \int \mathbf{dr}_1 \int \mathbf{dr}_2 E^+ (\mathbf{r}_1) E^{+*} (\mathbf{r}_2) \times$$
$$\int_{-T/2}^{T/2} \int_{-T/2}^{T/2} dt_1 dt_2 e^{i\omega^s (t_1 - t_2)} \left(\mathbf{e}^+ \mathbf{j}^{nl} (t_1, \mathbf{r}_1) \right) \left(\mathbf{e}^{+*} \mathbf{j}^{nl*} (t_2, \mathbf{r}_2) \right) \tag{3.2.7}$$

In the framework of the cold fluid model [82] (see the appendix) the source current $\mathbf{j}^{nl}$ reads as

$$\mathbf{e}^+ \mathbf{j}^{nl} (t, \mathbf{r}) = i \frac{e^2}{m_e} \frac{n_e}{\omega^i} \chi_\alpha f^\delta_\alpha (t, \mathbf{r}) e^{-i\omega^i t} E^i (\mathbf{r}) \tag{3.2.8}$$

the expressions for the dimensionless parameters of the plasma fluctuations f^δ and the dimensionless vector χ are

$$f^\delta (t, \mathbf{r}) = \left\{ \frac{n^\delta (t, \mathbf{r})}{n_e}, \frac{B^\delta_j (t, \mathbf{r})}{B_0}, \frac{u^\delta_j (t, \mathbf{r})}{c} \right\} \tag{3.2.9}$$

$$\chi = \Big\{ \left(\mathbf{e}^+ \mathbf{e}_\mu \right) \zeta_\mu, i \frac{\omega_{ce}}{\omega^s} e_{\mu\nu j} \left(\mathbf{e}^+ \mathbf{e}_\mu \right) \zeta_\nu,$$
$$\left(\mathbf{e}^+ \mathbf{e}_\mu \right) \left(\mathbf{e}^i \mathbf{e}_j \right) \frac{c k^i_\mu}{\omega^s} - \left(\mathbf{e}^+ \mathbf{e}^i \right) \frac{c k^i_j}{\omega^s} + \left(\mathbf{e}^+ \mathbf{e}_j \right) \zeta_\mu \frac{c k^i_\mu}{\omega^i} \Big\} \tag{3.2.10}$$

where $\mathbf{k}^i$ is the probing beam ($\mathbf{E}^i$) wave vector in the area of the scattering and

$$\begin{pmatrix} \zeta_x \\ \zeta_y \\ \zeta_z \end{pmatrix} = \begin{pmatrix} \frac{\omega^i}{\omega^{i2} - \omega^2_{ce}} \left(\omega^i \mathbf{e}_x + i\omega_{ce} \mathbf{e}_y \right) \mathbf{e}^i \\ \frac{\omega^i}{\omega^{i2} - \omega^2_{ce}} \left(-i\omega_{ce} \mathbf{e}_x + \omega^i \mathbf{e}_y \right) \mathbf{e}^i \\ \mathbf{e}_z \mathbf{e}^i \end{pmatrix} \tag{3.2.11}$$

Here the vectors $\mathbf{e}_\mu$ with a low index denote unit vectors with $\mu \in \{x, y, z\}$. The two vectors (3.2.9) and (3.2.10) have 7 dimensions, the index j numerates the spatial coordinates $j \in \{x, y, z\}$. It should be noted that the source current $\mathbf{j}^{nl}$ can be written in a number of ways due to linear relations between the fluctuating characteristics. The fields $\mathbf{E}^+$ and $\mathbf{E}^i$ are described with respect to the edge turbulence according to (3.1.4) and (3.1.6) as

$$\mathbf{E}^{i,+} (x, y, z) = \mathbf{e}^{i,+} E^{i,+} 2\pi \rho^{i,+2} \sqrt{\frac{\omega^i}{ck(x)}} e^{i \int^x dx' k(x')} \int_{-\infty}^{+\infty} \int_{-\infty}^{+\infty} \frac{dk_y}{2\pi} \frac{dk_z}{2\pi} \times$$
$$e^{ik_y y + ik_z z} e^{-i \frac{k_y^2 d_y^2 (x)}{2} - i \frac{k_z^2 d_z^2 (x)}{2} + i\delta\phi^{i,+}} e^{-\frac{k_y^2 \rho^{i,+2}}{2}} e^{-\frac{\left(k_z - \frac{\omega^i}{c} \sin \psi^{i,+} \right)^2 \rho^{i,+2}}{2}} \tag{3.2.12}$$

It is worth mentioning that the angle between the probing (or receiving) direction and the magnetic field is $90° - \psi^{i,+}$ so small values of $\psi^{i,+}$ means almost perpendicular propagation. In this expression the reference systems are different and associated with an emitter ($\mathbf{E}^i$) and receiver ($\mathbf{E}^+$) antennas correspondingly, the x and y coordinates stand for the probing and poloidally perpendicular to the probing directions. By writing (3.2.12) we assumed small frequency shift

$$\left|\omega^s - \omega^i\right| \ll \omega^i \tag{3.2.13}$$

so $k(x) = k(x, \omega^i) \approx k(x, \omega^s)$.

Presence of the edge turbulence lead to distortion of the beams $\mathbf{E}^{i,+}$, hence the spectral power becomes a random value as a function of the edge turbulence parameters. Now we consider its average characteristic. Normally, positions of emitter, receiver and domain of the beams cross-section are separated by distances larger than the turbulence correlation length, then the density fluctuations near the receiving and probing antennas and the fluctuations f^δ are mutually independent. To continue the analysis of the power spectrum we introduce the following definition

$$f_\alpha^\delta(\omega, \mathbf{r}) = \int_{-T/2}^{T/2} dt f_\alpha^\delta(t, \mathbf{r})\, e^{i\left(\omega^s - \omega^i\right)t} \tag{3.2.14}$$

here $\omega = \omega^s - \omega^i$, these fluctuating parameters are assumed to be statistically homogeneous in the beams intersection area so $\left\langle f_\alpha^\delta(\omega, \mathbf{r}_1)\, f_\beta^{\delta *}(\omega, \mathbf{r}_2)\right\rangle$ is a function of $(\omega, \mathbf{r}_1 - \mathbf{r}_2)$. Taking into account all the introduced definitions and made assumptions the spectral power can be written in the following way

$$\frac{d\langle P\rangle}{d\omega^s} = \frac{r_e^2 n_e c^4}{16\pi} \frac{\chi_\alpha \chi_\beta^*}{\omega^{i2}} \int \frac{\mathbf{dq}}{(2\pi)^3} S_{\alpha\beta}(\omega, \mathbf{q}) \times$$
$$\int \mathbf{dr}_1 \int \mathbf{dr}_2 \left\langle E^+(\mathbf{r}_1)\, E^{+*}(\mathbf{r}_2)\right\rangle \left\langle E^i(\mathbf{r}_1)\, E^{i*}(\mathbf{r}_2)\right\rangle e^{i\mathbf{q}(\mathbf{r}_1 - \mathbf{r}_2)} \tag{3.2.15}$$

where the classical electron radius is defined by

$$r_e = \frac{e^2}{m_e c^2} \tag{3.2.16}$$

and the fluctuations spectrum $S_{\alpha\beta}(\omega, \mathbf{q})$ is introduced according to the Wiener–Khinchin theorem

$$\int \frac{\mathbf{dq}}{(2\pi)^3} S_{\alpha\beta}(\omega, \mathbf{q})\, e^{i\mathbf{q}(\mathbf{r}_1 - \mathbf{r}_2)} = \frac{n_e}{T} \left\langle f_\alpha^\delta(\omega, \mathbf{r}_1)\, f_\beta^{\delta *}(\omega, \mathbf{r}_2)\right\rangle \tag{3.2.17}$$

To evaluate the double integral over space in (3.2.15) we introduce perpendicular structure of the fields

$$E_\perp^{i,+}(\mathbf{r}) = E^{i,+}(\mathbf{r})\, e^{-i\int^{\mathbf{r}} \mathbf{dr}' \mathbf{k}^{\mathbf{i},+}(\mathbf{r}')} \tag{3.2.18}$$

where $\mathbf{k}^{\mathbf{i},+}$ are the wave vectors of the two beams, the integral is taken along each of the wave vectors $\mathbf{k}^{\mathbf{i},+}$, we will also introduce the residual wave vector

$$\mathbf{\Delta k} = \mathbf{q} + \mathbf{k}^i + \mathbf{k}^+ \tag{3.2.19}$$

then

$$\frac{d\left\langle P\right\rangle}{d\omega^s}=\frac{r_e^2n_ec^4}{16\pi}\frac{\chi_\alpha\chi_\beta^*}{\omega^{i2}}\int\frac{\mathbf{dq}}{\left(2\pi\right)^3}S_{\alpha\beta}\left(\omega,\mathbf{q}\right)\int\mathbf{dr}_1\int\mathbf{dr}_2\left\langle E_\perp^+\left(\mathbf{r}_1\right)E_\perp^{+*}\left(\mathbf{r}_2\right)\right\rangle\times$$
$$\left\langle E_\perp^i\left(\mathbf{r}_1\right)E_\perp^{i*}\left(\mathbf{r}_2\right)\right\rangle e^{i\int^{\mathbf{r}_1}\mathbf{dr}'\boldsymbol{\Delta}\mathbf{k}(\mathbf{r}')-i\int^{\mathbf{r}_2}\mathbf{dr}'\boldsymbol{\Delta}\mathbf{k}(\mathbf{r}')}\tag{3.2.20}$$

The expression

$$\boldsymbol{\Delta}\mathbf{k}\left(\mathbf{r}=\mathbf{0}\right)=\mathbf{0}\tag{3.2.21}$$

determines the main resolved fluctuation wave vector (Bragg's condition), position $\mathbf{r}=\mathbf{0}$ is the point of the beams axes cross-section, that is why as a rule the main contribution to the integral over the fluctuations wave vector $\mathbf{q}$ comes from the vicinity of $\mathbf{q}=-\mathbf{k}^i-\mathbf{k}^+\big|_{\mathbf{r}=\mathbf{0}}$. The wave vectors $\mathbf{k}^i$ and $\mathbf{k}^+$ are set by geometry of an experiment and the refraction. The symbolic expression $\int^{\mathbf{r}_{1,2}}\mathbf{dr}'\boldsymbol{\Delta}\mathbf{k}(\mathbf{r}')$ represents sum of integrals along each of the three wave vectors. To calculate (3.2.20) we introduce local Cartesian coordinates system where x axis corresponds to the local direction of the probing beam propagation perpendicularly to the magnetic field e.i. along $\mathbf{k}_\perp^i$, y axis is perpendicular to x and external magnetic field (z axis). The beam from the receiver (imaginary) crosses the probing one at the angle $\alpha=\angle\left(\mathbf{k}_\perp^i,\mathbf{k}_\perp^+\right)$ in the perpendicular cross-section. The angle α is determined not only by the boundary conditions, but by propagation in plasma as well. The scattering angle in the toroidal direction is $\psi^i+\psi^+$ according to the model. Even though the two beams do not propagate straightforward we assume their rectilinear propagation on the scale of the intersection area, also neglecting their diffraction on this scale. Also we assume that the density profile is a function of x only, this assumption is based on the fact that the probing beam in a CTS experiment is usually launched radially (see figure 7) so that the measurements provide information from different magnetic surfaces. Besides it is assumed that the wave vectors variation on the scale of the beam cross-section is caused dominantly by the variation of the density rather than the magnetic field, that is normally the case when a cut-off or upper-hybrid resonance are outside of the probing volume. Under these assumptions $\mathbf{k}^{i,+}\left(\mathbf{r}\right)=\mathbf{k}^{i,+}\left(x\right)$. The explicit form for the symbolic expression $\int^{\mathbf{r}}\mathbf{dr}'\boldsymbol{\Delta}\mathbf{k}(\mathbf{r}')$ in the discussed geometry

$$\int^{\mathbf{r}}\mathbf{dr}'\boldsymbol{\Delta}\mathbf{k}(\mathbf{r}')=\int^x dx'\left(k(x')+q_x\right)+q_yy+\left(q_z+\frac{\omega^i}{c}\left(\sin\psi^i+\sin\psi^+\right)\right)z$$
$$+\int^{\cos\alpha x+\sin\alpha y}dx'k\left(\sin^2\alpha x-\sin\alpha\cos\alpha y+\cos\alpha x'\right)\tag{3.2.22}$$

and the perpendicular structure of the fields

$$\begin{aligned} E_{\perp}^{i}\left(x,y,z\right) &= E^{i}2\pi\rho^{i2}\sqrt{\frac{\omega^{i}}{ck(x)}}e^{-i\frac{\omega^{i}}{c}\sin\psi^{i}z}\int_{-\infty}^{+\infty}\int_{-\infty}^{+\infty}\frac{dk_y}{2\pi}\frac{dk_z}{2\pi}\times \\ & e^{ik_y y+ik_z z}e^{-i\frac{k_y^2 l_y^{i2}}{2}-i\frac{k_z^2 l_z^{i2}}{2}+i\delta\phi^{i}}e^{-\frac{k_y^2\rho^{i2}}{2}}e^{-\frac{\left(k_z-\frac{\omega^{i}}{c}\sin\psi^{i}\right)^2\rho^{i2}}{2}} \\ E_{\perp}^{+}\left(x,y,z\right) &= E^{+}2\pi\rho^{+2}\sqrt{\frac{\omega^{i}}{ck(x)}}e^{-i\frac{\omega^{i}}{c}\sin\psi^{+}z}\int_{-\infty}^{+\infty}\int_{-\infty}^{+\infty}\frac{dk_y}{2\pi}\frac{dk_z}{2\pi}\times \\ & e^{ik_y(\cos\alpha y-\sin\alpha x)+ik_z z}e^{-i\frac{k_y^2 l_y^{+2}}{2}-i\frac{k_z^2 l_z^{+2}}{2}+i\delta\phi^{+}}e^{-\frac{k_y^2\rho^{+2}}{2}}e^{-\frac{\left(k_z-\frac{\omega^{i}}{c}\sin\psi^{+}\right)^2\rho^{+2}}{2}} \end{aligned} \tag{3.2.23}$$

where $l_{y,z}^{i,+2}$ describe diffractive broadening of the radiations acquired before position of the beams cross-section area, $l_y^{i,+2} = \int_{l^{i,+}}\frac{ds}{k(s)}$ and $l_z^{i,+2} = \int_{l^{i,+}}\frac{ds}{k(s)}\left(1-\frac{g^2(s)}{\varepsilon(s)(\varepsilon^2(s)-g^2(s)-\varepsilon(s)\eta(s))}\right)$, the integration is performed along beams trajectories $l^{i,+}$. It should be noted that, considering the emitter and receiver are in the same poloidal cross-section, the two beams intersection requires fulfilling the equality of the axes toroidal coordinates z so

$$l_z^{i2}\frac{\omega^{i}}{c}\sin\psi^{i} = l_z^{+2}\frac{\omega^{i}}{c}\sin\psi^{+} \tag{3.2.24}$$

The averaging of $\langle E_{\perp}^{i}\left(\mathbf{r}_1\right)E_{\perp}^{i*}\left(\mathbf{r}_2\right)\rangle$ results in

$$\begin{aligned} \left\langle E_{\perp}^{i}\left(\mathbf{r}_1\right)E_{\perp}^{i*}\left(\mathbf{r}_2\right)\right\rangle &= \left|E^{i}\right|^2\frac{\omega^{i}}{ck_0}\frac{\rho^{i2}}{W_y^{i}W_z^{i}}e^{-\frac{l_z^{i4}\frac{\omega^{i2}}{c^2}\sin^2\psi^{i}}{W_z^{i2}}}e^{\frac{-\left(z_1^2+z_2^2\right)+i\left(z_1^2-z_2^2\right)\frac{l_z^{i2}}{\rho^{i2}}}{2W_z^{i2}}}\times \\ & e^{\frac{(z_1+z_2)l_z^{i2}\frac{\omega^{i}}{c}\sin\psi^{i}-i(z_1-z_2)\frac{l_z^{i4}}{\rho^{i2}}\frac{\omega^{i}}{c}\sin\psi^{i}}{W_z^{i2}}}e^{-\frac{(y_1+y_2)^2}{4W_y^{i2}}}e^{-(y_1-y_2)^2\frac{1}{4}\left(\sigma^{i2}-\frac{R^{i2}}{W_y^{i2}}\right)}e^{i\frac{1}{2}(y_1-y_2)(y_1+y_2)\frac{R^{i}}{W_y^{i2}}} \end{aligned} \tag{3.2.25}$$

the used notations in this expression are

$$\sigma^{i,+2} = \frac{1}{\rho^{i,+2}}+4\int_{l^{i,+}}D(x')dx' \tag{3.2.26}$$

$$R^{i,+} = \frac{l_y^{i,+2}}{\rho^{i,+2}}+4\int_{l^{i,+}}D(x')l_y^{i,+2}\left(0,x'\right)dx' \tag{3.2.27}$$

an analogous expression can be written for $\left\langle E_{\perp}^{+}\left(\mathbf{r}_1\right)E_{\perp}^{+*}\left(\mathbf{r}_2\right)\right\rangle$, one just should change the indexes from "i" to "+" and the y coordinate from y to $\cos\alpha y-\sin\alpha x$. The expressions (3.2.26), (3.2.27) are obtained in the framework of the procedure of the average phase variation $\left\langle\left(\delta\phi^{i,+}\left(x_1,y_1,k_{y1}\right)-\delta\phi^{i,+}\left(x_2,y_2,k_{y2}\right)\right)^2\right\rangle$ decomposition, the procedure is described in details in the previous chapter of this thesis. It should be mentioned that the beam widths $W_{y,z}^2$ introduced in (3.1.10) are used in (3.2.25) with the modification $d_{y,z}^2 \mapsto l_{y,z}^{i,+2}$, this substitution accounts for the different beams diffraction up to the scattering area along their paths. The introduced parameter $\sigma^{i,+2}$ has the meaning of the angular beam broadening [44], when the scattering area is deep into plasma beyond the turbulent layer the dimensionless parameter

$R^{i,+}$ has the meaning of the product beam's path with its angular broadening $R^{i,+} \approx l_y^{i,+2} \sigma^{i,+2}$.

Scattering of a probing beam by the edge turbulence may result in significant increase of the two beams overlap domain. If the plasma is inhomogeneous, the Bragg's rule for a fixed fluctuation mode $\mathbf{q}$ (determined in the scattering domain center $\mathbf{\Delta k}\left(\mathbf{r}=\mathbf{0}\right)=0$) is not fulfilled in the whole scattering area. The wider the beams, the less correlated the scattered radiation from different parts of the overlap. To take into account the plasma inhomogeneity on the scale of the beams cross-section we approximate the wave number $k(x)$, assuming a slow spatial variation in the CTS scattering area, by a linear function

$$k(x) = k_0 + \frac{k_0}{L}x \tag{3.2.28}$$

where $\frac{k_0}{L} = \left.\frac{dk}{dx}\right|_{x=0}$, L is a local wave vector gradient. Then the expression (3.2.20) reads as

$$\frac{d\left\langle P\right\rangle}{d\omega^s} = \frac{r_e^2 n_e c^4}{16\pi}\frac{\chi_\alpha \chi_\beta^*}{\omega^{i2}}\int\frac{\mathbf{dq}}{\left(2\pi\right)^3}S_{\alpha\beta}\left(\omega,\mathbf{q}\right)\int\mathbf{dr}_1\int\mathbf{dr}_2\left\langle E_\perp^+\left(\mathbf{r}_1\right)E_\perp^{+*}\left(\mathbf{r}_2\right)\right\rangle\times$$
$$\left\langle E_\perp^i\left(\mathbf{r}_1\right)E_\perp^{i*}\left(\mathbf{r}_2\right)\right\rangle e^{i(k_0(1+\cos\alpha)+q_x)(x_1-x_2)+i(q_y+k_0\sin\alpha)(y_1-y_2)+i\left(q_z+\frac{\omega^i}{c}\left(\sin\psi^i+\sin\psi^+\right)\right)(z_1-z_2)}$$
$$e^{i\frac{k_0}{2L}\left(1+\cos\alpha+\cos\alpha\sin^2\alpha\right)\left(x_1^2-x_2^2\right)-i\frac{k_0}{2L}\sin^2\alpha\cos\alpha\left(y_1^2-y_2^2\right)+i\frac{k_0}{L}\sin^3\alpha(x_1y_1-x_2y_2)} \tag{3.2.29}$$

Summing up description of the scattering model with all the made assumptions the function under the double space integral in (3.2.29) represents an exponential bilinear form that is bulky nevertheless easy to calculate. The linear approximation for the wave vector $k(x)$ implies that the quadratic and the next terms of the decomposition does not play a big role so the estimate of this applicability criterion is

$$L \gg \sqrt{\frac{W^{i,+3}}{\lambda_0}} \tag{3.2.30}$$

where $\lambda_0 = \frac{2\pi}{k_0}$ is a local probing wavelength. Then we write down the result of integration the 6 mixed integrals in (3.2.29)

$$\frac{d\left\langle P\right\rangle}{d\omega^s} = P^i r_e^2 \lambda_0^{i2} n_e \frac{1}{\sqrt{W_z^{i2}+W_z^{+2}}}\frac{1}{4\pi^{3/2}\left|\sin\alpha\right|}G_{\alpha\beta}S_{\alpha\beta}^{eff}\left(\omega,\mathbf{q}^\delta\right) \tag{3.2.31}$$

where the effective turbulence spectrum

$$S_{\alpha\beta}^{eff}\left(\omega,\mathbf{q}^\delta\right) = \int\mathbf{dq}S_{\alpha\beta}\left(\omega,\mathbf{q}^\delta+\mathbf{q}\right)SCF\left(\mathbf{q}\right) \tag{3.2.32}$$

in this expression $SCF\left(\mathbf{q}\right)$ is the spectrum contribution function, the main resolved fluctuation wave number

$$\mathbf{q}^\delta = -\mathbf{e}_x k_0\left(1+\cos\alpha\right) - \mathbf{e}_y k_0\sin\alpha - \mathbf{e}_z\frac{\omega^i}{c}\left(\sin\psi^i+\sin\psi^+\right) \tag{3.2.33}$$

which is determined by the scattering geometry, the $G_{\alpha\beta}$ dimensionless function describes contribution of each type of the fluctuations to the spectral power

$$G_{\alpha\beta} = \chi_\alpha \chi_\beta^* \tag{3.2.34}$$

definition of the spectrum contribution function $SCF\left(\mathbf{q}\right)$ is the main object of this research. This function quantitatively describes contribution of all the fluctuations modes to the registered signal and contains parameters of the edge turbulence

$$SCF\left(\mathbf{q}\right) = \frac{\sqrt{W_z^{i2} + W_z^{+2}}}{\pi^{3/2}\sqrt{\sin^2\alpha\sigma^{i2}\sigma^{+2} + f_1(\frac{k_0}{L})}\sqrt{\frac{W_z^{+2}}{\rho^{i2}} + \frac{W_z^{i2}}{\rho^{+2}} + 2\left(1 + \frac{l_z^{i2}l_z^{+2}}{\rho^{i2}\rho^{+2}}\right)}} \times$$

$$e^{-\frac{W_z^{i2}+W_z^{+2}}{\frac{W_z^{+2}}{\rho^{i2}}+\frac{W_z^{i2}}{\rho^{+2}}+2\left(1+\frac{l_z^{i2}l_z^{+2}}{\rho^{i2}\rho^{+2}}\right)}q_z^2} e^{-L_{xx}q_x^2} e^{-L_{xy}q_xq_y} e^{-L_{yy}q_y^2} \tag{3.2.35}$$

the introduced notations are

$$\begin{aligned}
L_{xx} &= 8\tan^2\left(\frac{\alpha}{2}\right)\frac{\sigma^{i2} + \sigma^{+2}\cos^2\alpha + f_2(\frac{k_0}{L})}{32\sigma^{i2}\sigma^{+2}\sin^4\left(\frac{\alpha}{2}\right) + f_5(\frac{k_0}{L})}\\
L_{xy} &= -8\tan\left(\frac{\alpha}{2}\right)\frac{2\sigma^{+2}\cos\alpha\left(\cos\alpha - 1\right) + f_3(\frac{k_0}{L})}{32\sigma^{i2}\sigma^{+2}\sin^4\left(\frac{\alpha}{2}\right) + f_5(\frac{k_0}{L})}\\
L_{yy} &= \frac{32\sigma^{+2}\sin^4\left(\frac{\alpha}{2}\right) + f_4(\frac{k_0}{L})}{32\sigma^{i2}\sigma^{+2}\sin^4\left(\frac{\alpha}{2}\right) + f_5(\frac{k_0}{L})}
\end{aligned} \tag{3.2.36}$$

where $f_{1-5}\left(\frac{k_0}{L}\right)$ are polynomials of $\frac{k_0}{L}$ and $f_{1-5}\left(0\right) = 0$

$$\begin{aligned}
f_1\left(Q\right) = \quad & Q4\cos^2\left(\frac{\alpha}{2}\right)\left[\left(R^+\sigma^{i2} + R^i\sigma^{+2}\right)\cos\alpha + R^+\sigma^{i2}\sin^2\alpha\right] + Q^2\frac{\cot^2\left(\frac{\alpha}{2}\right)}{8} \times\\
& \Big[-8\left(R^{i2} + R^{+2}\right) + \left(8W_y^{i2} + 7W_y^{+2}\right)\sigma^{i2} + 4\left(W_y^{i2} + 2W_y^{+2}\right)\sigma^{+2}\\
& +4\left(2R^iR^+ + W_y^{+2}\sigma^{i2}\right)\cos\alpha + 4\left(4R^iR^+ + W_y^{i2}\sigma^{+2}\right)\cos 2\alpha\\
& -4\left(2R^iR^+ + W_y^{+2}\sigma^{i2}\right)\cos 3\alpha + W_y^{+2}\sigma^{i2}\cos 4\alpha\Big] - Q^3 8\cos^4\left(\frac{\alpha}{2}\right) \times\\
& \left[\left(R^+W_y^{i2} + R^iW_y^{+2}\right)\cos\alpha + R^iW_y^{+2}\sin^2\alpha\right] + Q^4\frac{1}{4}W_y^{i2}W_y^{+2}\frac{\sin^6\alpha}{\sin^4\left(\frac{\alpha}{2}\right)}\\
f_2\left(Q\right) = \quad & -Q8R^+\sin\alpha\sin 2\alpha + Q^2 8W_y^{+2}\sin^4\alpha\\
f_3\left(Q\right) = \quad & Q\left[2R^i - R^+\left(\cos\alpha + 2\cos 2\alpha - \cos 3\alpha\right)\right] + Q^2 2W_y^{+2}\sin^2\alpha\left(\sin^2\alpha + \cos\alpha\right)\\
f_4\left(Q\right) = \quad & Q4R^+\left(3\cos\alpha - 4\cos 2\alpha + \cos 3\alpha\right)\\
& +Q^2\left[8W_y^{i2} + W_y^{+2}\left(7 + 4\cos\alpha - 4\cos 3\alpha + \cos 4\alpha\right)\right]\\
f_5\left(Q\right) = \quad & Q32\sin^2\left(\frac{\alpha}{2}\right)\left[\left(R^+\sigma^{i2} + R^i\sigma^{+2}\right)\cos\alpha + R^+\sigma^{i2}\sin^2\alpha\right] + Q^2 \times\\
& \Big[-8\left(R^{i2} + R^{+2}\right) + \left(8W_y^{i2} + 7W_y^{+2}\right)\sigma^{i2} + 4\left(W_y^{i2} + 2W_y^{+2}\right)\sigma^{+2}\\
& +4\left(2R^iR^+ + W_y^{+2}\sigma^{i2}\right)\cos\alpha + 4\left(4R^iR^+ + W_y^{i2}\sigma^{+2}\right)\cos 2\alpha\\
& -4\left(2R^iR^+ + W_y^{+2}\sigma^{i2}\right)\cos 3\alpha + W_y^{+2}\sigma^{i2}\cos 4\alpha\Big] - Q^3 16\sin^2\alpha \times\\
& \left[\left(R^+W_y^{i2} + R^iW_y^{+2}\right)\cos\alpha + R^iW_y^{+2}\sin^2\alpha\right] + Q^4 8W_y^{i2}W_y^{+2}\sin^4\alpha
\end{aligned} \tag{3.2.37}$$

If one considers the effect of the angular beam broadening only and ignores the local plasma inhomogeneity in the scattering area, the spectrum contribution function $SCF\left(\mathbf{q}\right)$ is way more compact and its dependence on the poloidal parameters is associated only with the average angular broadening $\sigma^{i,+2}$

$$SCF\left(\mathbf{q}\right) = \frac{\sqrt{W_z^{i2} + W_z^{+2}}}{\pi^{3/2}\sqrt{\sin^2 \alpha \sigma^{i2}\sigma^{+2}}\sqrt{\frac{W_z^{+2}}{\rho^{i2}} + \frac{W_z^{i2}}{\rho^{+2}} + 2\left(1 + \frac{l_z^{i2}l_z^{+2}}{\rho^{i2}\rho^{+2}}\right)}} \times$$
$$e^{-\frac{W_z^{i2}+W_z^{+2}}{\frac{W_z^{+2}}{\rho^{i2}}+\frac{W_z^{i2}}{\rho^{+2}}+2\left(1+\frac{l_z^{i2}l_z^{+2}}{\rho^{i2}\rho^{+2}}\right)}q_z^2} e^{-q_x^2 \frac{\sigma^{i2}+\sigma^{+2}\cos^2\alpha}{\sigma^{i2}\sigma^{+2}\sin^2\alpha}} e^{-2q_xq_y\frac{\cot\alpha}{\sigma^{i2}}} e^{-\frac{q_y^2}{\sigma^{i2}}} \tag{3.2.38}$$

The function $SCF\left(\mathbf{q}\right)$ is normalized as

$$\int \mathbf{dq} SCF\left(\mathbf{q}\right) = 1 \tag{3.2.39}$$

The choice of the CTS geometry (the angles α and $\psi^{i,+}$) determines the main resolved fluctuation wave number $\mathbf{q}^{\delta}$, often this wave vector is considered as the only one which contributes to the scattered radiation. Nevertheless, since a probing beam and receiver radiation pattern possess finite angular beam broadening, it is clear that the Bragg's rule is fulfilled for some range of the fluctuation wave vectors. This angular broadening is usually assumed to be negligible. For instance $S_{\alpha\beta}\left(\omega,\mathbf{q}\right)$ was considered as a slow function in the analogous expression in the work [83] equation (22), then $S_{\alpha\beta}^{eff}\left(\omega,\mathbf{q}^{\delta}\right) \approx S_{\alpha\beta}\left(\omega,\mathbf{q}^{\delta}\right)$. But presence of the edge turbulence can increase the angular broadening significantly. The expression (3.2.31) describes this effect explicitly and quantitatively.

Considering the situation when only one fluctuation mode exists and possesses the wave number $\mathbf{q}^{\delta}$ so $S_{\alpha\beta}\left(\omega,\mathbf{q}\right) \propto \delta\left(\mathbf{q}-\mathbf{q}^{\delta}\right)$. Then we can evaluate the signal damping due to the edge turbulence, to this we compare the scattered power with respect to the edge turbulence and without taking into account the turbulence

$$\frac{d\left\langle P\right\rangle/d\omega^s\big|_{turb\neq0}}{d\left\langle P\right\rangle/d\omega^s\big|_{turb=0}} = \sqrt{\frac{\sin^2\alpha\frac{1}{\rho^{i2}\rho^{+2}} + f_1(\frac{k_0}{L})\big|_{turb=0}}{\sin^2\alpha\sigma^{i2}\sigma^{+2} + f_1(\frac{k_0}{L})\big|_{turb\neq0}}} \tag{3.2.40}$$

This expression describes the decrease of the radiation scattered off the single mode. It is interesting that if we consider the full scattering spectrum with respect to all the modes and the spectrum is almost a constant on the scale of $SCF(\mathbf{q}-\mathbf{q}^{\delta})$ significant variations this mitigation effect for the single mode is compensated by summation over all the others modes. This statement holds for any parameters of the turbulence and the plasma local gradient L.

As it was discussed in the first section, the analytical description of the beam propagation in the turbulent plasma is valid in the strong phase variation regime $\left\langle\delta\phi^2\right\rangle \gg 1$ so this criterion is required for the spectral power (3.2.31). But if the phase variation is zero $\delta\phi^{i,+} = 0$ (absence of the turbulence and the beams are not perturbed),the procedure of the spectral power averaging gives the same expression (3.2.31) where $\delta n = 0$ so it is also applicable for $\left\langle\delta\phi^2\right\rangle = 0$. Of course the expression for the spectral power was already derived and analysed in the previous works (for example [82]), but in this case the equation (3.2.31) describes the dependence on the beam angular and special widths explicitly and with respect to the local plasma gradient.

3.3 Estimate of the turbulence effect on the CTS signal

To estimate how presence of the edge turbulence influence the effective spectrum $S^{eff}_{\alpha\beta}\left(\omega, \mathbf{q}^{\delta}\right)$ we evaluate the derived expression for different turbulence regimes and the scattering geometry.

The used spectrum model is defined by

$$S_{\alpha\beta}\left(\omega, \mathbf{q}\right) = \delta_{\alpha n}\delta_{\beta n}S_{nn}\left(\omega, \mathbf{q}\right) \tag{3.3.1}$$

where the index n in the delta function $\delta_{\alpha n}$ denotes the first component of the vector (3.2.9), thus we consider the scattering off the density fluctuations only, the turbulence spectrum becomes

$$S_{nn}\left(\omega, \mathbf{q}\right) = S_{e}\left(\omega, \mathbf{q}\right) + S_{i}\left(\omega, \mathbf{q}\right) + S_{\alpha}\left(\omega, \mathbf{q}\right) \tag{3.3.2}$$

where $S_{e,i,\alpha}\left(\omega, \mathbf{q}\right)$ are the contribution of the electron, ion and alpha particle components respectively to the scattered radiation. The analytical expressions for the electron spectral density correlation function components $S_{e,i,\alpha}\left(\omega, \mathbf{q}\right)$ depend on the electrons, ions and alpha particles velocity distribution functions. The electron and ion distribution functions are assumed to be Maxwellian, whereas the alpha particles follow the slow-down distribution function [86]. The full explicit expressions for $S_{e,i,\alpha}\left(\omega, \mathbf{q}\right)$ are quite bulky, for their definitions we refer the readers to [87].

All the spectrum evaluations are fulfilled under the parameters and models listed as following: the probing frequency $f^{i} = 60$ GHz, the model density profile and edge turbulence envelope are illustrated on the figure 25, the background density flat-top level is $n_{max} = 1.2 \times 10^{14}$ cm^{-3}. The magnetic field $B\left(x\right) = 5.1 \times \frac{600}{800-x}$ T, where x – radial coordinate is in cm.

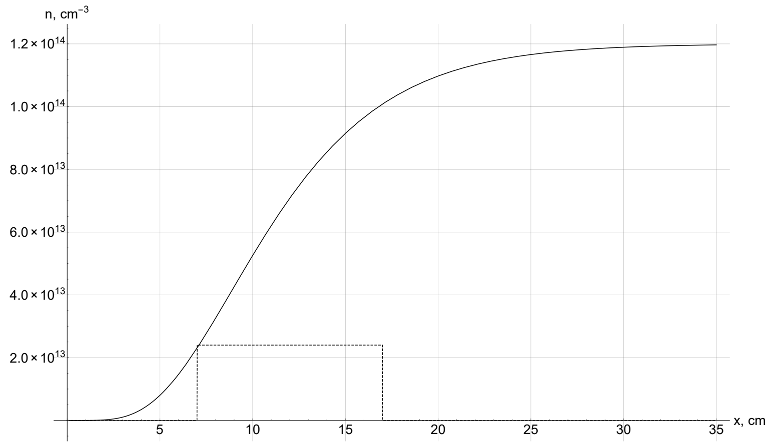

Figure 25: density profile - solid curve and the turbulence envelope for the turbulence amplitude $\frac{\delta n^{rms}(x)}{n_{max}} = 0.2$ - dashed curve

Density of the alpha particles is $n_{\alpha} = 7.5 \times 10^{11}$ cm^{-3}, the electron and ion temperatures are equal $T_e = T_i = 10$ keV. The turbulence cross-correlation function is Gaussian $CCF(x, y) =$

$e^{-\frac{x^2}{l_c^2}-\frac{y^2}{l_c^2}}$ with an isotropic correlation length $l_c = 1$ cm.

The first evaluation of the effective turbulence spectrum is done for the following scattering geometry: $\alpha = 90°$ and $\psi^i = \psi^+ = 15°$ so the probing and receiving angels to the magnetic filed is 75°. According to the introduced notations the probing beam wave vector in the scattering area is $\mathbf{k}^i = \mathbf{e}_x k_0$, the scattered beam wave vector is $\mathbf{k}^s = \mathbf{k}^i + \mathbf{q}^\delta$, then the scattering angle $\theta = \angle(\mathbf{k}^i, \mathbf{k}^s) \approx 106°$, and the angle between the main resolved fluctuations wavenumber $\mathbf{q}^\delta$ and the magnetic field $\beta = \angle\left(\mathbf{q}^\delta, \mathbf{B}\right)$, where $\mathbf{B} = -\mathbf{e}_z B$, $\beta \approx 46°$. The initial beam width $\rho^i = 2$ cm and $\rho^+ = \rho^i$, distance between the emitter and scattering area is 50 cm and the same distance between the receiver and the beams cross-section point. The result of the effective spectrum evaluation $S_{nn}^{eff}\left(\omega, \mathbf{q}^\delta\right)$ for different turbulence amplitudes is depicted on figures 26 and 27 for the cases without and with taking into account the plasma inhomogeneity effect $\frac{k_0}{L} = 0\ \mathrm{cm}^{-2}$ and $\frac{k_0}{L} = 0.04\ \mathrm{cm}^{-2}$ respectively. The turbulence amplitude is defined as $\frac{\delta n_{max}^{rms}}{n_{max}}$. The two plots demonstrate comparison of the fluctuations spectrum $S_{nn}\left(\omega, \mathbf{q}^\delta\right)$ with its effective value $S_{nn}^{eff}\left(\omega, \mathbf{q}^\delta\right)$ for different turbulence amplitudes: 0, 3, 6 and 10 percents.

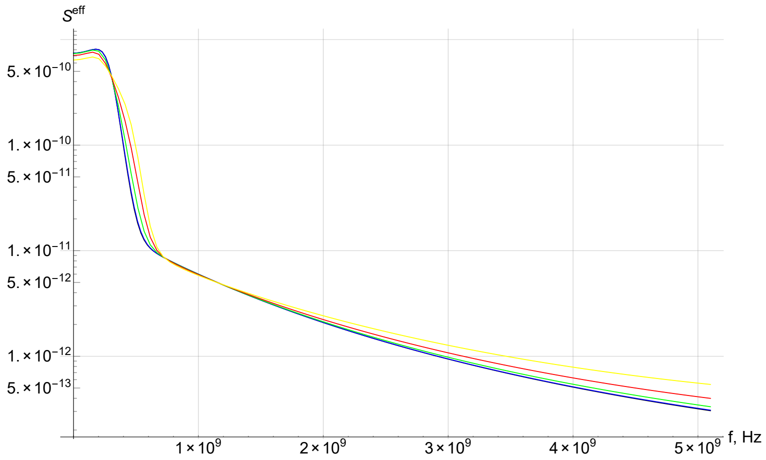

Figure 26: The black curve (almost fully beyond the blue one) is S_{nn}; the blue, green, red and yellow curves stand for S_{nn}^{eff} for different turbulence amplitudes: 0%, 3%, 6% and 10% correspondingly. Without considering the local plasma inhomogeneity $\frac{k_0}{L} = 0\ \mathrm{cm}^{-2}$

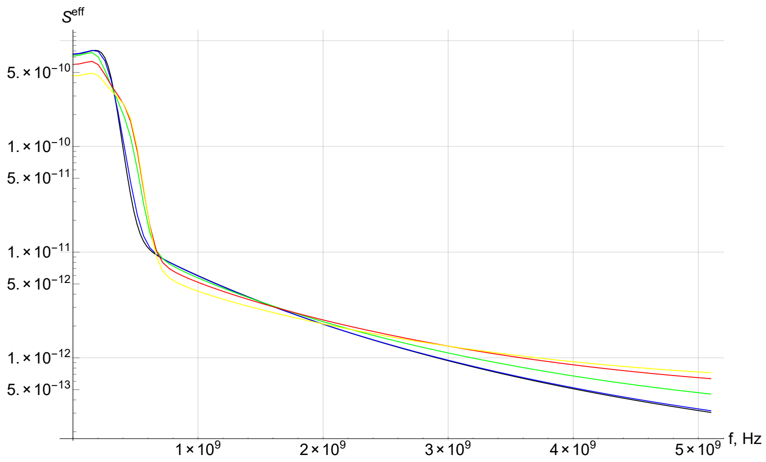

Figure 27: The black curve is S_{nn}; the blue, green, red and yellow curves stand for S_{nn}^{eff} for different turbulence amplitudes: 0%, 3%, 6% and 10% correspondingly. The case with taking into account the local plasma inhomogeneity $\frac{k_0}{L} = 0.04\ \mathrm{cm}^{-2}$

It is seen that when the edge turbulence is absent the effective spectrum $S_{nn}^{eff}\left(\omega, \mathbf{q}^\delta\right)$ almost coincides with the fluctuations spectrum $S_{nn}\left(\omega, \mathbf{q}^{\delta}\right)$, it means that the beam angular broadening, caused only by the natural diffraction, does not play a big role for the registered signal. In the cases with turbulence the effective spectrum distortion effect grows with the turbulence amplitude. Taking into account the plasma inhomogeneity makes this effect only more pronounced. The relatively small impact of the plasma inhomogeneity is due to the small value of $\frac{k_0}{L}$. In the framework of the used plasma model $\frac{k_0}{L} = 0.04$ cm^{-2} entails $L \approx 300$ cm. Even if this plasma is close to be homogeneous, the choice of L is limited with the applicability criterion (3.2.30) (it is a boarder of the applicability for the case with the 10% turbulence rate) so one should understand taking into account the plasma inhomogeneity effect as an estimate in a fairly narrow applicability domain. The both plots (26 and 27) demonstrate that the two spectra S_{nn}^{eff} and S_{nn} shapes are different. In the frequency rage about $0 - 0.3$ GHz the difference is several times, in the frequency domain about $0.3 - 0.6$ GHz it may reach about one order of magnitude for the high turbulence amplitudes. The effective spectrum $S_{nn}^{eff}\left(\omega, \mathbf{q}^{\delta}\right)$ decrease rate is smaller than for $S_{nn}\left(\omega, \mathbf{q}^{\delta}\right)$ in the area of the higher frequencies.

The spectrum contribution function $SCF\left(q_x, q_y, q_z\right)$ (3.2.35) is a normalized exponent of the quadratic form of the three wavenumber components, evaluation of this function provides information on the wavenumber range around $\mathbf{q}^{\delta}$ that contributes to the scattered radiation. For example the combination $\frac{SCF(q_x,0,0)}{SCF(0,0,0)}$ is evaluated for different turbulence amplitudes together with the combination $\frac{SCF(0,0,q_z)}{SCF(0,0,0)}$ (that is independent on the turbulence) on the figure 28 for the plasma conditions and the geometry corresponding to the evaluated spectra on the figure 26. Under these conditions $\frac{SCF(q_x,0,0)}{SCF(0,0,0)} = \frac{SCF(0,q_y,0)}{SCF(0,0,0)}$.

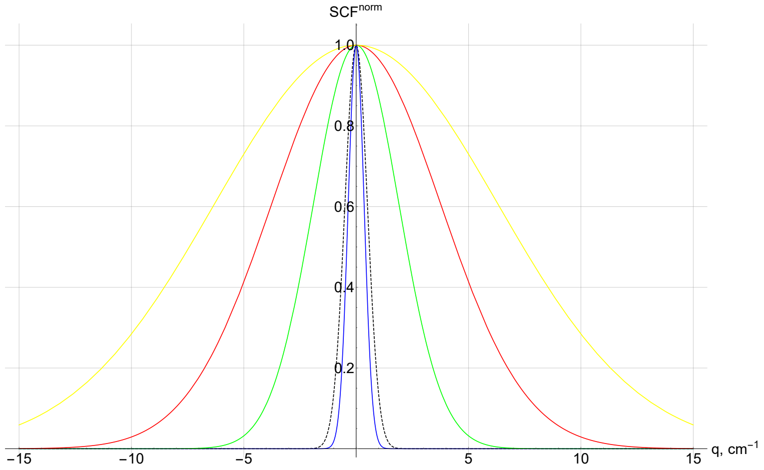

Figure 28: The normalized spectrum contribution function, the dashed curve is $\frac{SCF(0,0,q_z)}{SCF(0,0,0)}$; the solid curves denote $\frac{SCF(q_x,0,0)}{SCF(0,0,0)}$ for the different turbulence amplitudes: the blue, green, red and yellow curves stand for the turbulence amplitudes 0%, 3%, 6% and 10% correspondingly

It is seen that if the turbulence level is high enough, the significant beam angular broadening takes place, that is expressed in the contribution to the scattered radiation from the fluctuations with a wide range of different perpendicular wave numbers comparable with the vacuum probing wavenumber.

The fast particles contribution to the spectrum is significant in the high frequency range ($\gtrsim 0.5$ GHz), whereas the small frequencies carry information about the bulk ions. The spectrum shape is a function of various plasma parameters, if all of them except for the bulk ions temperature are known, the temperature can be defined from fitting a measured spectrum by the analytical expression using the least-squares fitting procedure [88]. Since the spectrum shape is distorted by the edge turbulence, using the spectrum S_{nn} for fitting experimental data instead of the effective spectrum S_{nn}^{eff} leads to an error in the defined ions temperature T_i^{fit}. In order to estimate this error for the different turbulence regimes, the evaluated effective spectra S_{nn}^{eff} are fitted by $S_{nn}\left(T_i^{fit}\right)$ for the conditions corresponding to the spectra S_{nn}^{eff} on the figure 26. The results of the least-squares fitting procedure are demonstrated on the figure 29 (in the linear scale), where the dashed curves are the evaluated spectra S_{nn}^{eff} and the solid curves of the same colors are results of the fitting $S_{nn}\left(T_i\right)$, the relative values are following: $\frac{T_i^{fit}}{T_i} =$ 1.02, 1.09 and 1.22 for the tested turbulence amplitudes 3%, 6% and 10% respectively, T_i is the ions temperature used in the evaluation of the effective spectrum S_{nn}^{eff}. So the relative error in

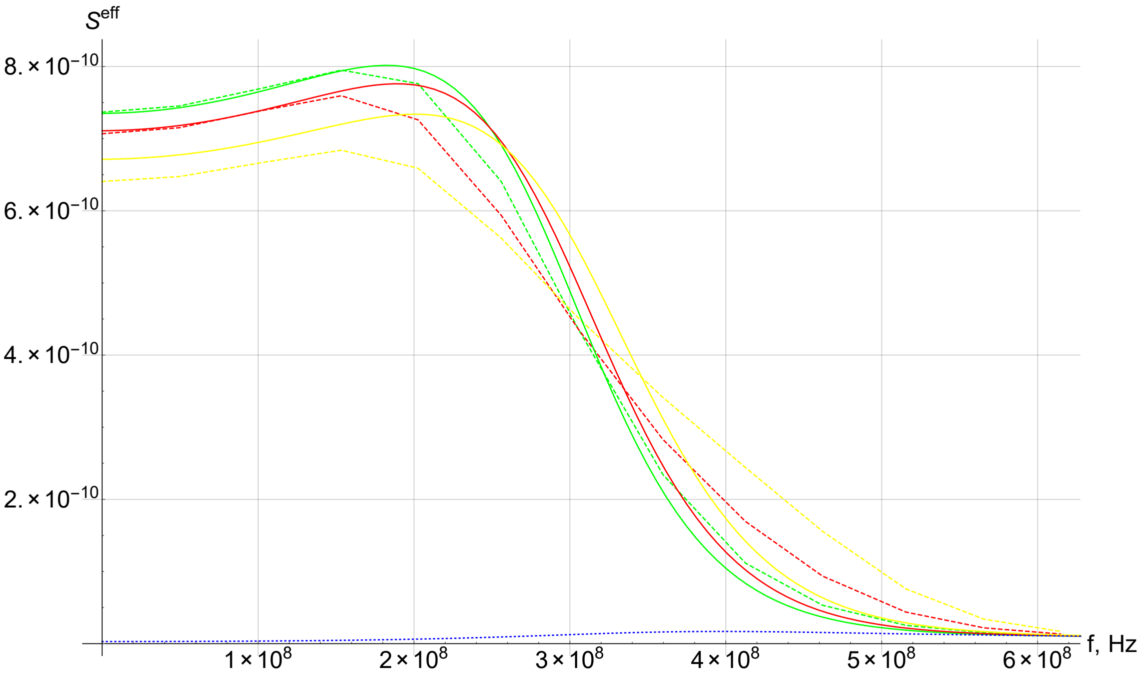

Figure 29: Green, red and yellow dashed curves are S_{nn}^{eff} for the different turbulence amplitudes: 3%, 6% and 10% respectively, the solid curves represent the fitting spectra $S_{nn}\left(T_i^{fit}\right)$ with $\frac{T_i^{fit}}{T_i} = 1.02$, 1.09 and 1.22 correspondingly. The blue dotted curve is S_α

the bulk ions temperature definition can be few percents or even of the order of tens percents for the high turbulence. The blue dotted curve on the figure 29 is S_α - the component of the spectrum which is associated with the fast particles contribution. The behavior of this function specifies the frequency range where the fast particles become the dominant to the scattered radiation. It is seen from the figure 29 that this range starts since about 0.5 GHz.

The next numerical experiment is fulfilled for smaller value of the angels $\psi^i = \psi^+ = 6°$ so the probing and receiving angles to the magnetic field is 84°, it is close to perpendicular probing, $\alpha = 90°$ that leads to the scattering angle $\theta \approx 94°$ and the angle between the main resolved fluctuations wavenumber and the magnetic field $\beta \approx 70°$. The initial beam widths $\rho^+ = \rho^i = 2$ cm are the same. Comparison of the two spectra, under the different turbulence amplitudes 0, 2, 3 and 6 percents, is shown on the figures 30 and 31 for the conditions without and with accounting for the local density gradient $\frac{k_0}{L} = 0\ \mathrm{cm}^{-2}$ and $\frac{k_0}{L} = 0.04\ \mathrm{cm}^{-2}$ respectively.

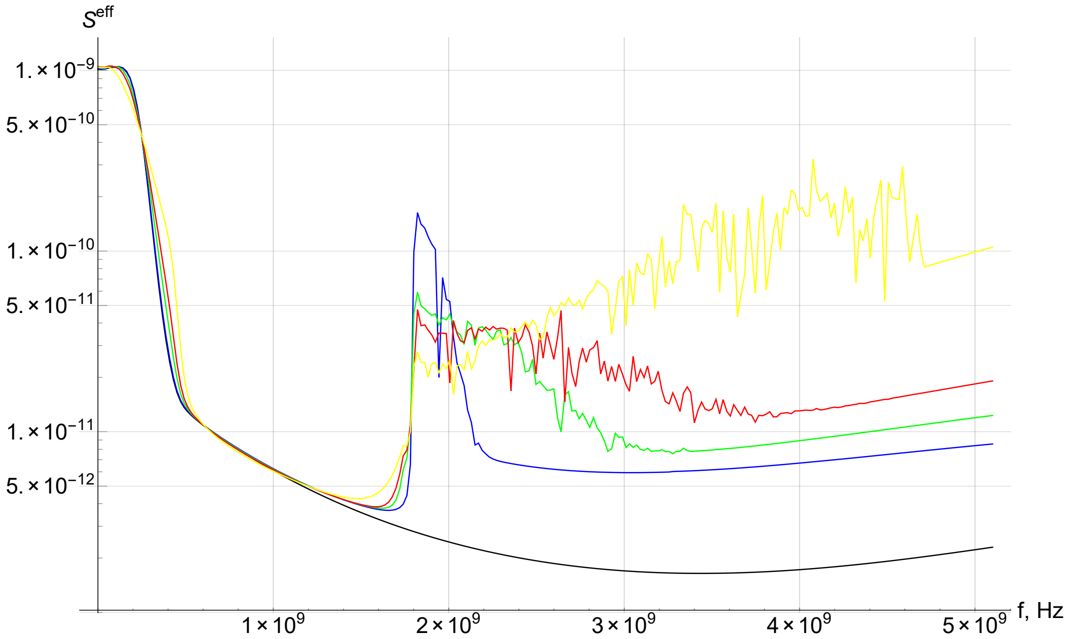

Figure 30: The black curve is S_{nn}; the blue, green, red and yellow curves stand for S_{nn}^{eff} for different turbulence amplitudes: 0%, 2%, 3% and 6% correspondingly. Without considering the local plasma inhomogeneity $\frac{k_0}{L} = 0\ \mathrm{cm}^{-2}$

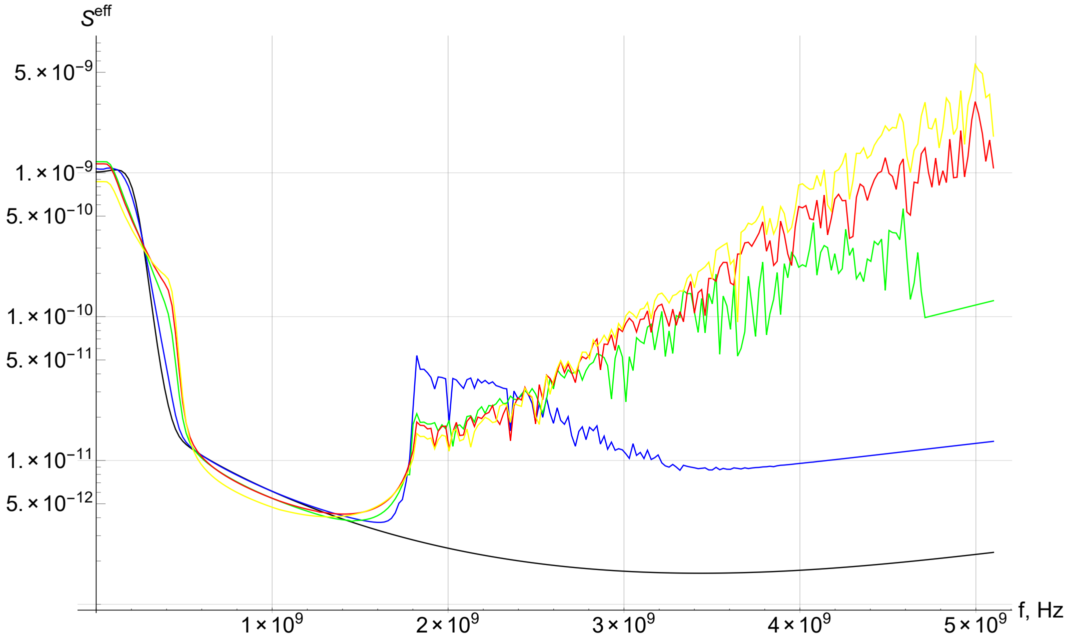

Figure 31: The black curve is S_{nn}; the blue, green, red and yellow curves stand for S_{nn}^{eff} for different turbulence amplitudes: 0%, 2%, 3% and 6% correspondingly. The case with taking into account the local plasma inhomogeneity $\frac{k_0}{L} = 0.04\ \mathrm{cm}^{-2}$

The very significant discrepancy between $S_{nn}^{eff}\left(\omega, \mathbf{q}^{\delta}\right)$ and $S_{nn}\left(\omega, \mathbf{q}^{\delta}\right)$ is associated with the spectrum $S_{nn}\left(\omega, \mathbf{q}^{\delta}\right)$ sensitivity to the very small longitudinal wavenumbers q_z, this effect was noted in [87] and [89]. The spectrum contribution function can be written as

$$SCF\left(\mathbf{q}\right) = SCF_{\perp}\left(q_x, q_y\right) SCF_{\parallel}\left(q_z\right) \tag{3.3.3}$$

with the following normalization $\int dq_x dq_y SCF_{\perp} = \int dq_z SCF_{\parallel} = 1$, the plasma turbulence does not change the longitudinal part $SCF_{\parallel}(q_z)$ so the noticeable discrepancy between the two spectra takes place even in plasma without the turbulence. That is why a finite big enough toroidal angle value is needed to avoid interference in the CTS spectrum from plasma waves propagating perpendicularly to the magnetic field [34]. But there is another parameter that can be used to avoid the interference, according to (3.2.35) $SCF_{\parallel}(q_z)$ depends on the probing beam sizes $\rho^{i,+}$. Increase of the widths $\rho^{i,+}$ leads to reduction of its angular broadening, then the Bragg's selection rule is fulfilled for narrower wave vector $\mathbf{q}_{\parallel}$ range. It should be mentioned that the spectra tail off for the higher frequencies, the demonstrated frequency range is typical for the CTS measurements and allows clearly observe the significant discrepancy around 0.5 GHz.

The significant difference between the spectra S_{nn} and S_{nn}^{eff} in the case without the plasma turbulence is seen on the figures 30, 31 but does not present on the figures 26, 27 because the angle β is closer to 90° for the simulations corresponding to the figures 30, 31. Normally the resonance peak of the spectrum, associated with the lower hybrid resonance (LHR) [87], is observed for the angles $\beta \sim 85 - 95°$, this is correct for the turbulence spectrum S_{nn}. As it was mentioned the effective spectrum S_{nn}^{eff} also depends on the probing and receiving beam widths, the tested values $\rho^i = \rho^+ = 2$ cm were too small for eliminating the effect of the LHR at $\beta \approx 70°$. In order to stress the effect of the LHR influence on the effective spectrum for $\beta \approx 70°$ and the small beam width $\rho^i = \rho^+ = 2$ cm, the function $S_{\parallel}(\delta q_z + q_z) SCF_{\parallel}(q_z)$ where

$$S_{\parallel}(q_z) = \iint dq_x dq_y S_{nn}(q_x, q_y, q_z) SCF_{\perp}(q_x - \delta q_x, q_y - \delta q_y) \tag{3.3.4}$$

is illustrated on the figure 32 for the different frequencies $f = \{1.0, 1.8, 4.0\}$ GHz. The effective turbulence spectrum, with respect to the introduced function (3.3.4), reads

$$S_{nn}^{eff} = \int dq_z S_{\parallel}(\delta q_z + q_z) SCF_{\parallel}(q_z) \tag{3.3.5}$$

It is seen that the exponential decrease of the function $SCF_{\parallel}(q_z)$ is not fast enough to suppress the contribution of the turbulence modes with the small toroidal wave numbers to the effective turbulence spectrum for the frequencies $f = \{1.8, 4.0\}$ GHz, whereas the contribution is negligible for $f = 1.0$ GHz, that corresponds to the spectra on the figures 30, 31. The described effect disappears for the tested angle $\beta \approx 70°$ if the beam widths are not that small, the function $S_{\parallel}(\delta q_z + q_z) SCF_{\parallel}(q_z)$ is evaluated for $\rho^i = \rho^+ = 3$ cm and depicted on the figure 33.

In order to explicitly demonstrate the effect of the interference in the CTS spectrum decrease with growing $\rho^{i,+}$ the effective spectrum $S_{nn}^{eff}\left(\omega, \mathbf{q}^{\delta}\right)$ is evaluated for different values $\rho^+ = \rho^i \in \{2.0, 2.4, 2.8, 3.5, 5.0\}$ cm, see figure 34. The parameters of the simulation: $\psi^i = \psi^+ = 6°$ and the poloidal angle $\alpha = 45°$ so $\theta \approx 133°$ and $\beta \approx 73°$, the plasma is without the turbulence and the local density gradient. It is seen from figure 34 that $S_{nn}^{eff}\left(\omega, \mathbf{q}^{\delta}\right)$ is very sensitive to the initial beam widths. Then the probing beam width is also an instrument to reduce the interference between the elongated in the toroidal direction electron fluctuations.

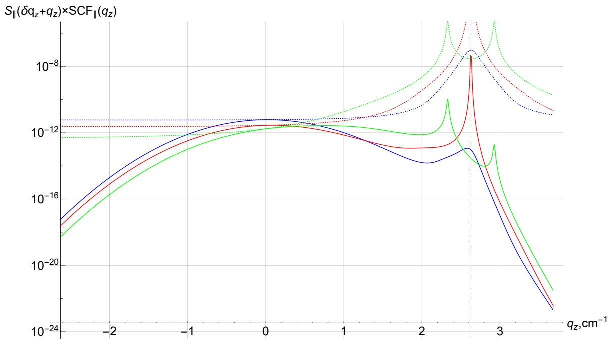

Figure 32: The solid curves are $S_{\|}\left(\delta q_z + q_z\right) SCF_{\|}\left(q_z\right)$ dependence on the toroidal wave number q_z when $\rho^i = \rho^+ = 2$ cm, the dashed curves are $S_{\|}\left(\delta q_z + q_z\right)$, the blue curves stand for $f = 1.0$ GHz, red - $f = 1.8$ GHz and green - $f = 4.0$ GHz; the vertical dashed line specifies -δq_z

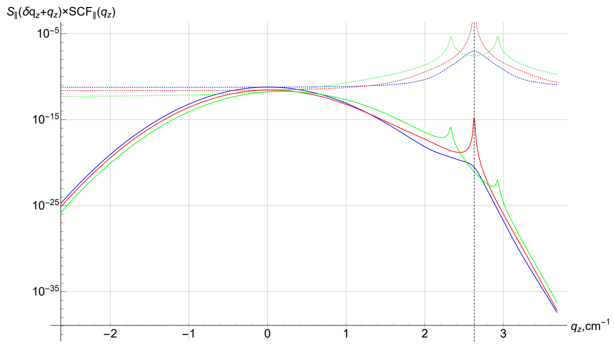

Figure 33: The solid curves are $S_{\|}\left(\delta q_z + q_z\right) SCF_{\|}\left(q_z\right)$ dependence on the toroidal wave number q_z when $\rho^i = \rho^+ = 3$ cm, the dashed curves are $S_{\|}\left(\delta q_z + q_z\right)$, the blue curves stand for $f = 1.0$ GHz, red - $f = 1.8$ GHz and green - $f = 4.0$ GHz; the vertical dashed line specifies -δq_z

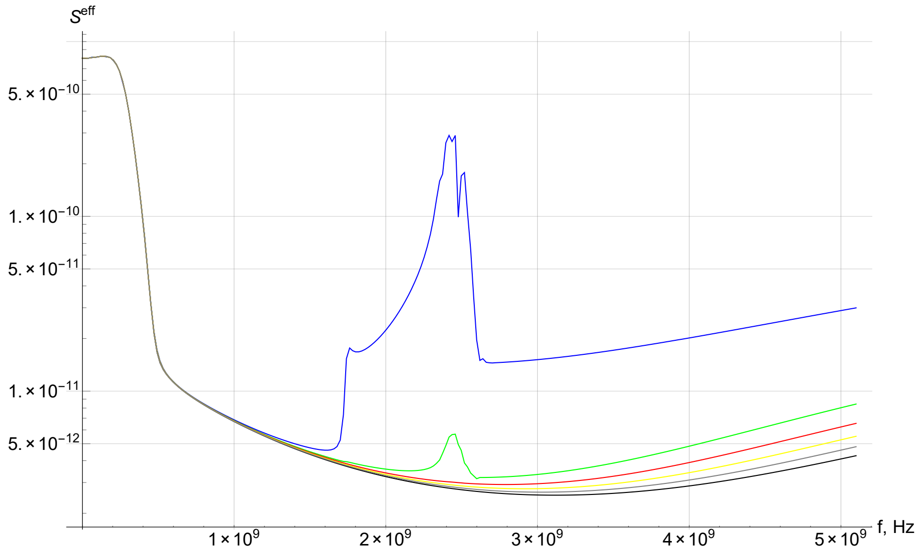

Figure 34: The black curve is S_{nn}; the blue, green, red, yellow and gray curves represent S_{nn}^{eff} for different probing beam sizes $\rho^i = \rho^+$: 2.0cm, 2.4cm, 2.8cm, 3.5cm and 5.0cm correspondingly

3.4 Scattering off a single mode fluctuation

The effective turbulence spectrum $S_{\alpha\beta}^{eff}$ was described analytically and analysed numerically for the standard turbulence spectrum model (3.3.2). The decrease of the main resolved turbulence wave vector $\mathbf{q}^{\delta}$ contribution to the registered spectral power is given by (3.2.40) under the assumption that the wave vector $\mathbf{q}^{\delta}$ is dominant in the turbulence spectrum $S_{\alpha\beta}\left(\omega, \mathbf{q}\right) \propto \delta\left(\mathbf{q} - \mathbf{q}^{\delta}\right)$. Neglecting the local plasma inhomogeneity effect the expression (3.2.40) can be simplified

$$V = \frac{\left\langle P^s \right\rangle \Big|_{turb \neq 0}}{\left\langle P^s \right\rangle \Big|_{turb = 0}} = \frac{1}{\sqrt{\left(1 + 4\rho_p^2 \int_{l_p} dx' D(x')\right)\left(1 + 4\rho^{+2} \int_{l^+} dx' D(x')\right)}} \tag{3.4.1}$$

where V is the introduced power spectrum reduction rate due to the turbulence, which is a relevant parameter to quantify the impact of the edge turbulence on CTS measurements.

3.4.1 Simulation of the scattering off a single mode fluctuation

To estimate the signal reduction rate V for a single turbulence mode $\mathbf{q}^{\delta}$ in a CTS experiment due to the plasma turbulence and to verify the analytical model in this section we demonstrate the results of the CTS 2D full-wave simulation. In order to simplify the scattered radiation interpretation we consider a square 2D box with an emitter on the bottom side and the receiver on the right hand side of the box, the both antennas are directed toward the plasma straightly, see figure 35.

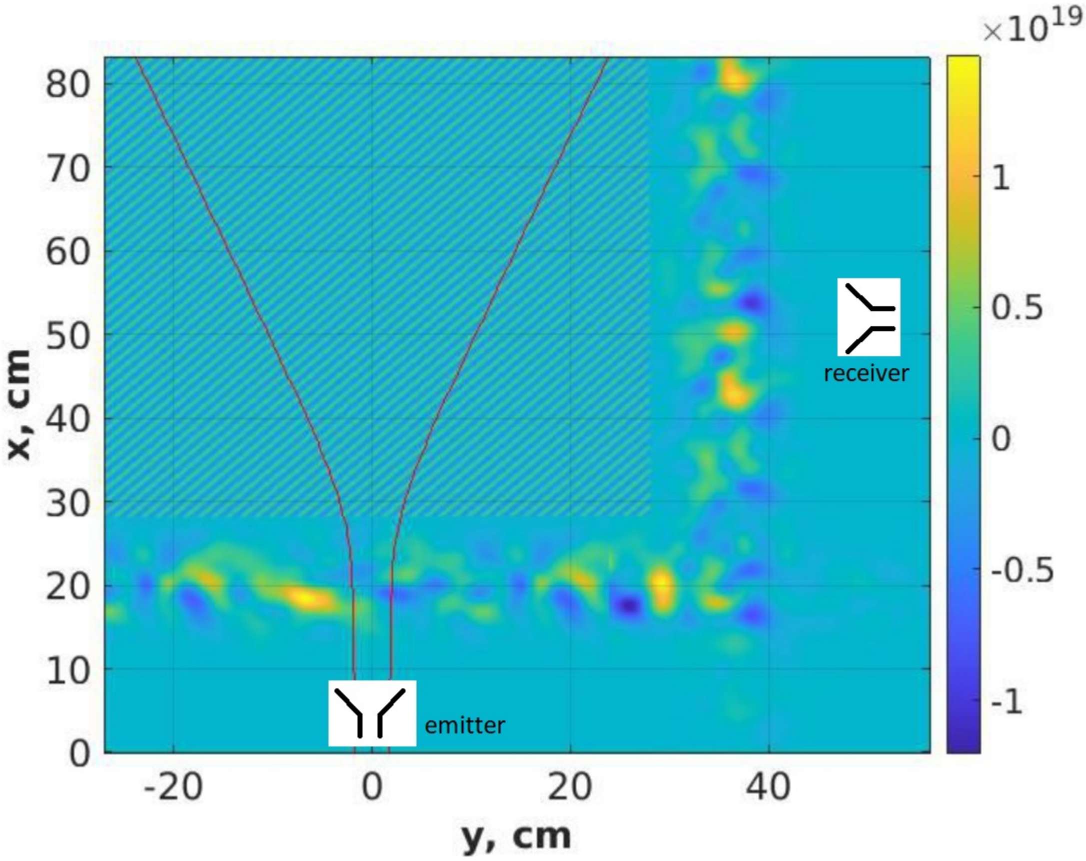

Figure 35: Scheme of the 2D simulation: the 2D domain region with an overlaid turbulence map $\delta n + 100\delta\tilde{n}$. The dark red lines are evolution of the average probing beam width with respect to the plasma turbulence.

Plasma parameters in the simulation are chosen similar for the parameters expected on ITER, the probing frequency $f = 60$ GHz also corresponds to the chosen frequency in the CTS experiment for ITER. Magnetic field $B = 4.25$ T is a constant in the domain of simulation, 1D density profile $n(x)$ and the 1D turbulence envelope $\sqrt{\langle \delta n^2(x) \rangle}$ are shown on the figure 36. The 1D turbulence was generated as

$$\delta n(x) = \sqrt{\langle \delta n^2(x) \rangle} \sqrt{\frac{\Delta q l_c}{\sqrt{\pi}}} \sum_j e^{-\frac{l_c^2 \Delta q^2 j^2}{8}} \cos\left(\Delta q j x + \varphi_j\right) \tag{3.4.2}$$

where φ_j is a random phase, Δq is step of the wave number sampling, $l_c = 1$ cm is the turbulence correlation length. The single mode of the density fluctuations in the core is $\delta\tilde{n}$, which provide the probing radiation scattering at the angle $\alpha = \pi/2$. The relative amplitude of the density fluctuations $\frac{\delta\tilde{n}}{n_{max}} = 0.0003$. The fluctuations $\delta\tilde{n}$ location is depicted by the shaded area on

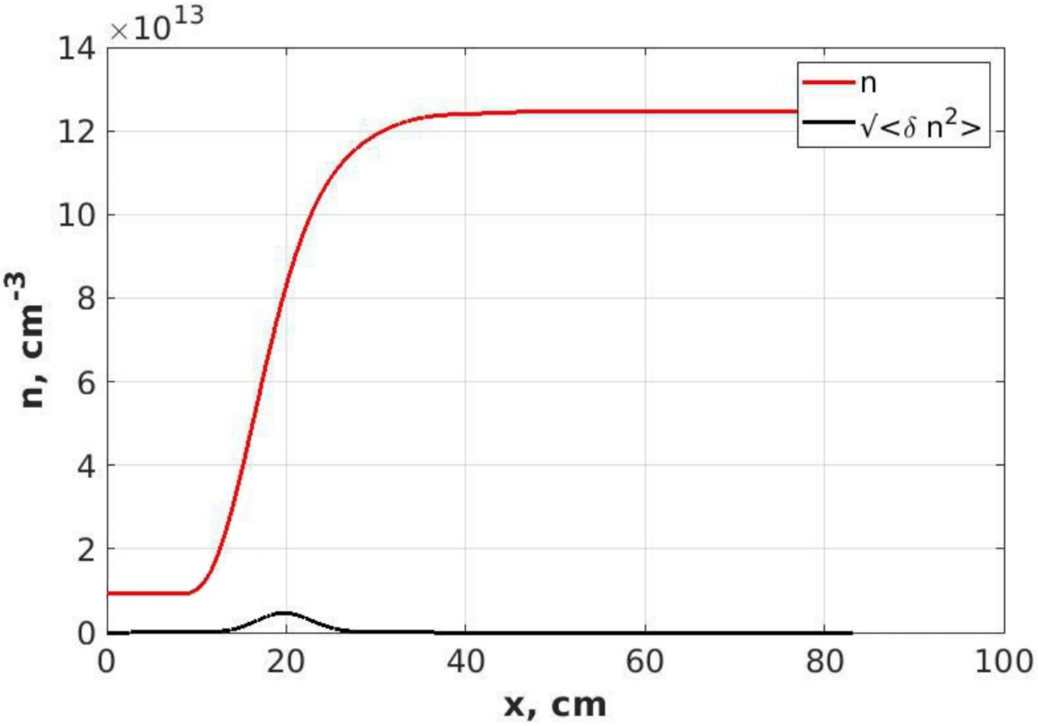

Figure 36: The density $n(x)$ and turbulence envelope $\sqrt{\langle \delta n^2(x) \rangle}$ profiles

the figure 35. The 2D profiles are constructed as 2D mesh $n(x) \times n(y)$, $\delta n(x) \times \delta n(y)$. The simulation scheme is illustrated on the figure 35: the turbulence map $\delta n + 100\delta\tilde{n}$ (the factor 100 is used in order to see the core fluctuations) and evolution of the average probing beam width with respect to the broadening due to the edge turbulence. The receiver antenna position is on the right hand side of the figure 35 at y coordinate $y^r = 45$ cm and x coordinate $x^r = 50$ cm, according to the analytical prediction the registered signal is independent on the receiver radial coordinate. The registered electric field E^{reg} is a product of the scatted field E^s radial distribution with the receiver directivity diagram

$$E^{reg}(x) = E^s(x, y^r) \frac{1}{\sqrt{2\pi}\rho^+} e^{-\frac{(x-x^r)^2}{2\rho^{+2}}} \tag{3.4.3}$$

To estimate the registered power reduction we calculate V (3.4.1) for the specified plasma parameters, that results in $V \approx 0.11$. The numerical evaluation of the spectral power reduction rate

$$V^{num} = \int dx \left\langle E^{reg2}\Big|_{turb\neq0} \right\rangle \Big/ \int dx E^{reg2}\Big|_{turb=0} \tag{3.4.4}$$

gives the value $V^{num} \approx 0.15$ for different radial positions of the receiver x^r as it was expected from the analytical analysis. The signal decrease in the turbulent plasma amounts to about 85%. The analytical prediction for the spectral power reduction (3.4.1), in the case of the scattering off a single fluctuation mode, is in good agreement with the result of the 2D full-wave simulation, the relative discrepancy is $(V^{num} - V)/V^{num} \approx 0.27$. The discrepancy between the analytical and numerical values for the spectral power reduction rate V may be associated with the beams diffraction on the scale of the two beams overlap area, this effect was not accounted for in the analytical model.

3.5 Discussion on CTS

The finite angular broadening of a probing beam can be quite big due to the plasma edge turbulence and it leads to contribution to the scattered signal from various wave numbers in the vicinity of the general one $\mathbf{q}^{\delta}$. This effect was analysed explicitly in this work. The effect results in replacement of the turbulence spectrum $S_{nn}\left(\omega, \mathbf{q}^{\delta}\right)$ with the effective turbulence spectrum $S_{nn}^{eff}\left(\omega, \mathbf{q}^{\delta}\right)$ in the expression for the registered signal. It is demonstrated numerically that the difference between the spectra grows with increasing the edge turbulence level. Various frequency domains demonstrate different relation between $S_{nn}^{eff}\left(\omega, \mathbf{q}^{\delta}\right)$ and $S_{nn}\left(\omega, \mathbf{q}^{\delta}\right)$. The effective spectrum is relatively mitigated for the small frequencies about $0-0.3$ GHz, this frequency range is normally associated with the electrons and bulk ions, whereas contribution of the fast particles is dominant in the tail of the spectrum for the frequencies $\gtrsim 0.5$ GHz. In the domain of higher frequencies $S_{nn}^{eff}\left(\omega, \mathbf{q}^{\delta}\right)$ mostly surpasses $S_{nn}\left(\omega, \mathbf{q}^{\delta}\right)$, the relative increase of effective spectrum is especially pronounced in the range about $0.3-0.6$ GHz.

Since not only the angular but also the spatial beam broadening takes place the effect of the local plasma inhomogeneity can also change the results of the CTS measurements. This contribution is also taken into account in the definition of the effective turbulence spectrum, a criterion of the analytical applicability is provided. Numerical simulations with accounting for the effect of the local inhomogeneity show that this effect slightly increases the difference between $S_{nn}^{eff}\left(\omega, \mathbf{q}^{\delta}\right)$ and $S_{nn}\left(\omega, \mathbf{q}^{\delta}\right)$.

Numerical simulations under quite small toroidal angels $\psi^{i,+} = 6^{\circ}$ demonstrated that there is an enormous contribution to the CTS signal from the electron fluctuations with small $\mathbf{q}_{\|}$ and different from the main resolved according to the Braggs' rule wave number $\delta\mathbf{q}_{\|}$. This result is in agreement with previous works [87], the turbulence spectrum $S_{nn}\left(\omega, \mathbf{q}^{\delta}\right)$ is still affected by the LHR for the almost perpendicular $\mathbf{q}^{\delta}$ to the magnetic field, but the LHR can influence on the effective spectrum $S_{nn}^{eff}\left(\omega, \mathbf{q}^{\delta}\right)$ even for $\beta \approx 70^{\circ}$ if the probing and receiving beam widths are not big enough. It is demonstrated that it is possible to mitigate this effect by the choice of a big enough probing beam width.

Influence of the plasma edge turbulence on the CTS spectrum is described analytically and numerically. An estimate of the possible error in the bulk ions temperature definition is provided, the relative error can be few or even tens percents depending on a turbulence scenario. The detailed analysis of the importance of the registered spectrum correction due to the edge turbulence is yet to be considered, strictly speaking it should be done for determination of all the plasma and the fast particles parameters that are theoretically possible to extract from the CTS measurements.

The developed theoretical model was verified by the 2D full-wave simulation of a probing beam scattering by a single mode fluctuation. The registered spectral power reduction due to the plasma turbulence, corresponding to the V ratio, was evaluated and compared analytically and numerically. It was demonstrated that the relative discrepancy for the scattered power is about 0.27%, the discrepancy may be associated with the beams diffraction on the scale of the two beams overlap area, this effect is not considered in the analytical model.

4 Influence of edge plasma turbulence on the low-threshold parametric decay instability

4.1 State of the art in the low-threshold parametric decay instability and formulation of the problem analysed in this thesis

The electron cyclotron resonance heating (ECRH) is a popular method to produce and heat a fusion relevant plasma in magnetic confinement devices [90], [91]. It is based on the theoretical predictions of localized microwave energy deposition and of suppression of nonlinear phenomena which can accompany the microwave propagation and damping. However, during the last decade various anomalous effects (anomalous microwave scattering producing strong spurious radiation exceeding the electron cyclotron emission (ECE) level by several orders of magnitude [92] - [96] and complicating the performance of the microwave plasma diagnostics [95], ion acceleration in the ECRH experiment when energy exchange between electrons and ions should be very low [97] - [99], significant broadening of the ECRH power deposition profile [100], [101]) were discovered in the ECRH experiments at different toroidal devices. They were interpreted as a consequence of low-power-threshold absolute parametric decay instabilities (PDI) excited in the presence of a non-monotonic (hollow) density profile often encountered in existing fusion devices. The developed theory of the low-threshold PDI not only described the known anomalous effects but also predicted the gyrotron subharmonic emission during the ECRH experiments [102], that was confirmed in the experiment later [94]. The most dangerous scenario discovered in [103] is a PDI leading to excitation of two upper hybrid (UH) daughter waves trapped along the direction of the plasma inhomogeneity and localized on a magnetic surface due to the finite pump width. In the case of inhomogeneous plasmas with monotonic background profiles, thresholds for different scenarios of parametric pump wave decay have been analyzed and evaluated by different authors more than three decades ago. The results of these studies, summarized in [68], predict power thresholds of the instability which are much higher than the power of modern gyrotrons for the fusion-relevant plasma conditions. This is due to the huge energy loss of the daughter waves from the decay layer, which makes it impossible to amplify them significantly and makes one assume that the pump wave is stable at EC heating. Meanwhile, if one or both daughter waves are somehow trapped in the decay region, this suppresses their energy loss and decreases the instability threshold. For a non-monotonic density profile, it becomes possible to localize the daughter wave/waves within the decay layer, thus reducing the instability threshold. In the last decade, various microwave decay scenarios have been analyzed. The results of this analysis, summarized in [69], predict the instability threshold at a level that is two orders of magnitude lower than that for a monotonic density profile and lower than the power of the modern gyrotrons used at tokamaks and stellarators.

The general scenario of the low-threshold PDI, leading to the excitation of a trapped UH wave and a running UH (or X-mode) wave, and its saturation were analyzed analytically in [69], [104], [105] and numerically in [106], [107] for various regimes of the instability assuming smooth Gaussian shape of the pump beam. However the analysis of the microwave beam propagation in turbulent plasma demonstrated that the beam characteristics can be significantly changed in the edge turbulent layer [44] - [46], [78], [108], in particular this effect is analysed for X-mode waves in this thesis. The beam distortions on the average result in angular and spatial beam broadening not affecting the Gaussian beam form, whereas a single random beam distribution may be split into several sub-beams. That leads to the question if the PDI theory, developed for the smooth pumping waves, still describes the instability characteristics well and how significant the difference can be for different scenarios of the edge plasma turbulence.

In the present chapter of the thesis the low-threshold two-UH-plasmon PDI and its saturation are investigated numerically for the pump wave beam distribution altered by the edge plasma turbulence. The key characteristics of the instability are evaluated and statistically analysed. It is shown that the average PDI growth rate is reduced and the excitation threshold is increased, whereas the average instability saturation level and the anomalous energy absorption rate at the pump power substantially exceeding the threshold are almost independent on the plasma edge turbulence.

4.2 Description of the PDI model

First of all analytical description of the PDI process is provided in this section. The analysed instability model is the 2-step parametric decay of the pump under the conditions for which only one UH wave is trapped [69], [105]. This decay, resulting in only one trapped plasmon, corresponds to the experimental conditions of the TEXTOR tokamak ECRH experiment at high and low densities [92],[93]. Normally a low-threshold parametric decay occurs in a small volume within which the decay conditions (conditions of the three-wave interaction resonance) are satisfied. This allows using the Cartesian coordinate system: x axis is a direction of inhomogeneity of the plasma density $n = n(x)$ which is typically associated with the radial coordinate, z axis is a direction of the external magnetic field $\mathbf{B}$ that is assumed to be perpendicular to x, and finally the y coordinate is the axes perpendicular to x and z and associated with the poloidal coordinated of a tokamak (see figure 37). We consider a monochromatic extraordinary

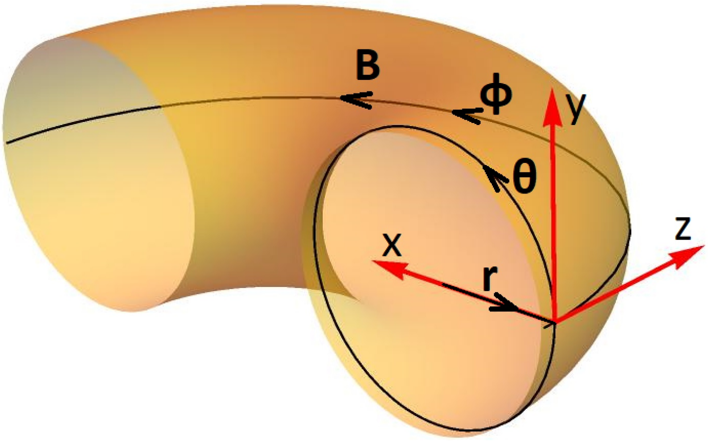

Figure 37: A tokamak (torus) transection, the external magnetic field $\mathbf{B}$ (its dominant toroidal part), the toroidal coordinates (r, θ, Φ) where $\mathbf{r}$ is the radius unit vector, $\boldsymbol{\Theta}$ and $\boldsymbol{\Phi}$ are the poloidal and toroidal unit vectors; the introduced Cartesian coordinates in red (x, y, z)

pumping wave, propagating along the radial coordinate x

$$\mathbf{E}_0 = \mathbf{e}_0 \sqrt{\frac{\omega_0}{ck_0(x)}} \frac{C_0(\mathbf{r})}{2} e^{-i\omega_0 t + i\int^x k_0(x')dx'} + c.c. \tag{4.2.1}$$

where the polarization vector $\mathbf{e}_0 = \frac{\mathbf{e}_y - i\frac{g_0}{\varepsilon_0}\mathbf{e}_x}{\left|\mathbf{e}_y - i\frac{g_0}{\varepsilon_0}\mathbf{e}_x\right|}$, $\mathbf{e}_{x,y}$ are the unit vectors along the corresponding coordinates, $\varepsilon(\omega) = 1 - \frac{\omega_{pe}^2}{\omega^2 - \omega_{ce}^2}$ and $g(\omega) = \frac{\omega_{ce}}{\omega}\frac{\omega_{pe}^2}{\omega^2 - \omega_{ce}^2}$ are components of the «cold» dielectric tensor so $\varepsilon_0 = \varepsilon(\omega_0)$ and $g_0 = g(\omega_0)$ (one should not be confused, ε_0 is not the vacuum electric permittivity constant here), where ω_{ce} and ω_{pe} are the electron-cyclotron and plasma frequencies, ω_0 is the pumping wave frequency; $k_0 = \frac{\omega_0}{c}\sqrt{\frac{\varepsilon_0^2 - g_0^2}{\varepsilon_0}}$ is the X-mode wave number, C_0 is the pump amplitude and c.c. stands for the complex conjugated part.

We consider a two-step decay of the extraordinary pump wave (4.2.1). In the first step, the pump wave experiences a primary decay into a trapped UH wave and a running (non-trapped) UH wave, the UH waves are the plasma modes with a frequency ω close to the upper-hybrid frequency ω_{UH} that is given by the expression

$$\omega_{UH} = \sqrt{\omega_{pe}^2 + \omega_{ce}^2} \tag{4.2.2}$$

and corresponds to the upper hybrid resonance. The waves are called «hybrid» because their characteristics are determined by both the electron plasma frequency and the electron cyclotron frequency. The UH waves are electrostatic waves, they can be described in terms of their scalar potentials, the expressions for the trapped UH wave φ_m and the non-trapped one φ_b are

$$\begin{aligned} \varphi_m &= \frac{C_m(y,z,t)}{2}\psi_m(x)\, e^{-i\omega_m t} + c.c. \\ \varphi_b &= \frac{C_b(\mathbf{r},t)}{2} e^{i(\omega_0 - \omega_m)t + i\int^x q_x^-(x', \omega_0 - \omega_m)dx'} + c.c. \end{aligned} \tag{4.2.3}$$

$C_{m,b}$ are amplitudes of the two waves, frequency of the trapped wave is ω_m, $q_x^{\pm}(x,\omega)$ are two roots of the UH waves dispersion equation in warm plasma

$$D_{UH}(q_x, \omega; x) = \frac{3}{2}\frac{\omega_{pe}^2}{\omega^2 - \omega_{ce}^2}\frac{v_{te}^2}{4\omega_{ce}^2 - \omega^2} q_x^4 + \varepsilon q_x^2 + \frac{\omega^2}{c^2} g^2 + \eta q_z^2 = 0 \tag{4.2.4}$$

describing the slow and fast modes with $q_y = 0$. In the equation (4.2.4) $v_{te} = \sqrt{\frac{2T_e}{m_e}}$ is the electron thermal velocity, the electron temperature T_e and mass m_e, $\eta = 1 - \frac{\omega_{pe}^2}{\omega^2}$, $q_{x,z}$ are the wave number components, the first term in (4.2.4) is the thermal amendment to the cold plasma model, that is needed to describe the vicinity of the UH resonance, this dispersion relation with the thermal amendment can be found in [70]. Since one wave is trapped the Bohr–Sommerfeld quantization condition (quantization of the phase volume in the phase space) must be fulfilled

$$\int_{x_l}^{x_r} dx' \left(q_x^+(x', \omega_m) - q_x^-(x', \omega_m)\right) = 2\pi\left(m + \frac{1}{2}\right) \tag{4.2.5}$$

$x_{l,r}$ are the two turning points $q_x^-(x_{l,r},\omega_m) = q_x^+(x_{l,r},\omega_m)$, $\psi_m(x)$ is the corresponding eigenfunction for the mode number m and represented by means of the WKB approximation as follows

$$\psi_m(x) = L_m^+(x)^{-1/2} e^{i\int_{x_l}^{x} dx' q_x^+(x',\omega_m) - i\frac{\pi}{4}} + L_m^-(x)^{-1/2} e^{-i\int_{x_l}^{x} dx' q_x^-(x',\omega_m) + i\frac{\pi}{4}} \tag{4.2.6}$$

where

$$L_m^\pm = \left|D_{qm}^\pm\right| \int_{x_l}^{x_r} dx' \left(\left|D_{qm}^+\right|^{-1} + \left|D_{qm}^-\right|^{-1} \right) \tag{4.2.7}$$

and $D_{qm}^\pm = \frac{\partial D_{UH}}{\partial q}\Big|_{q^\pm(x,\omega_m)}$ [105]. The primary decay takes place nearby the point where the decay resonance conditions for the wave numbers and frequencies are fulfilled that is to say for the momentum and energy in the quantum interpretation

$$\begin{aligned} \omega_m &= \omega_0 - (\omega_0 - \omega_m) \\ q_x^-(\omega_m) &= k_0 + q_x^-(\omega_0 - \omega_m)\Big|_{x_d} \end{aligned} \tag{4.2.8}$$

where x_d is the decay point coordinate. A principal scheme of the pump wave parametric decay into a trapped UH wave and a running UH wave is illustrated on the figure 38, the low-threshold PDI occurs in an inhomogeneous plasma, when the resonance conditions (4.2.8) for the wave numbers and frequencies are fulfilled. It should be mentioned that, as it is seen in the figure 38, in the general scenario the wave number resonance condition can be fulfilled in two radial points if the green curve in the figure 38 crosses $q_x^\pm(\omega_m)$ and two points.

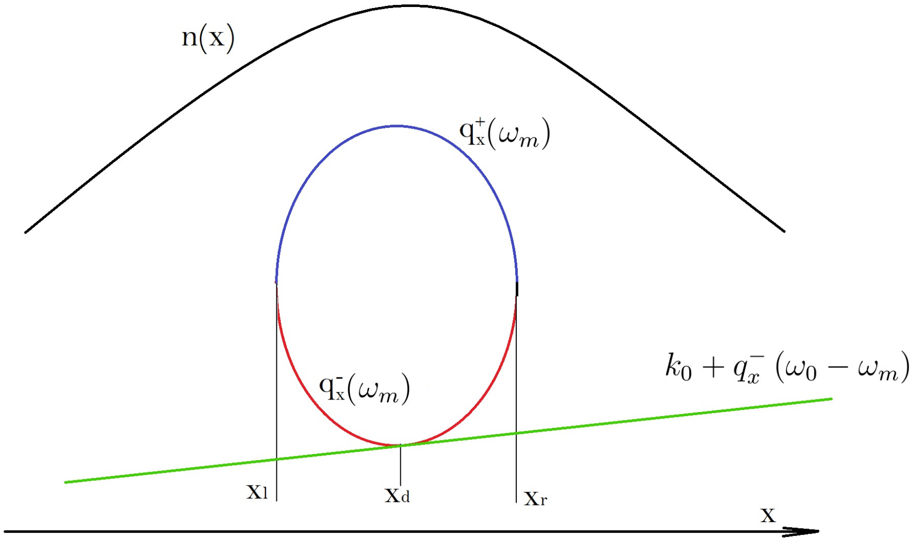

Figure 38: Illustration of the wave number profiles in the considered scenario of the pumping wave decay into a trapped and running UH waves with one point of the parametric decay at x_d. The two wave number branches $q_x^\pm(\omega_m)$ correspond to the trapped UH wave with the turning points at $x_{l,r}$, the green curve is a sum of the wave numbers $k_0 + q_x^-(\omega_0 - \omega_m)$ of the pump and the running UH wave.

The trapped UH wave, when its amplitude $C_m(y,z,t)$ during the primary instability becomes large enough to overcome the secondary instability threshold, decays into a trapped UH wave

φ_n and a running ion Bernstein (IB) wave

$$\begin{aligned}\varphi_n &= \frac{C_n\left(y,z,t\right)}{2}\psi_n\left(x\right)e^{-i\omega_n t}+c.c.\\ \varphi_I &= \frac{C_I\left(x,t\right)}{\sqrt{\left|\partial D_{IB}/\partial q_{Ix}\right|}}e^{-i\omega_I t+i\int^x dx' q_{Ix}(x')}+c.c.\end{aligned} \tag{4.2.9}$$

where C_n - the amplitude of the secondary trapped UH mode n, ψ_n is the corresponding eigenfunction defined by the equation (4.2.6), C_I is the IB wave amplitude, $\omega_I = \omega_m - \omega_n$, q_{Ix} is the wave number of the IB wave, which requires a kinetic plasma description, it is a solution of the local dispersion equation

$$D_{IB} = \mathbf{q}^2 + \chi_e + \chi_i = 0 \tag{4.2.10}$$

where χ_e and χ_i are the electron and ion plasma susceptibilities, their explicit forms for the hot plasma description [70] are following

$$\chi_\alpha = \frac{2\omega_{p\alpha}^2}{v_{t\alpha}^2}\left(1+\frac{\omega}{\left|q_\|\right|v_{t\alpha}}\sum_{p=-\infty}^{+\infty}Z\left(\frac{\omega-p\omega_{c\alpha}}{\left|q_\|\right|v_{t\alpha}}\right)e^{-\frac{q_\perp^2 v_{t\alpha}^2}{2\omega_{c\alpha}}}I_p\left(\frac{q_\perp^2 v_{t\alpha}^2}{2\omega_{c\alpha}}\right)\right) \tag{4.2.11}$$

where $\alpha = e, i$, $v_{t\alpha}$ is the thermal velocity of the electrons and ions correspondingly, I_p is the modified Bessel function of the first kind, Z is the plasma dispersion function

$$Z\left(\lambda\right) = i\sqrt{\pi}e^{-\lambda^2}\left(1+\frac{2}{\sqrt{\pi}}\int_0^{i\lambda}dt e^{t^2}\right) \tag{4.2.12}$$

The secondary decay occurs in the vicinity of the point x_s where the decay conditions are satisfied

$$\begin{aligned}&\omega_n = \omega_m - \omega_I\\ &q_x^-\left(\omega_n\right) = q_{Ix} - q_x^-\left(\omega_m\right)\Big|_{x_s}\end{aligned} \tag{4.2.13}$$

In this case of a two-step cascade decay of the pump wave (4.2.1), its depletion is negligible [69]. This allows omitting the equation describing the pump wave and considering its amplitude to be constant along the direction of its propagation - x coordinate. Then the set of the equations describing the two-step cascade decay reads

$$\begin{aligned}\int\frac{\mathbf{dq}dr'}{(2\pi)^3}D_{UH}\left(\mathbf{q},\omega_m,\frac{\mathbf{r}+\mathbf{r}'}{2}\right)e^{i\mathbf{q}(\mathbf{r}\text{-}\mathbf{r}')}\varphi_m\left(\mathbf{r}'\right) &= -\frac{\chi_{nl}^a}{B_0}\frac{\partial}{\partial x}\left(\left(\mathbf{E}_0\mathbf{e}_x\right)\frac{\partial\varphi_b}{\partial x}\right)\\ &\quad -\frac{\chi_{nl}^b c}{2\left|\omega_{ce}\right|B_0}\frac{\partial^2}{\partial x^2}\left(\frac{\partial\varphi_I}{\partial x}\frac{\partial\varphi_n^*}{\partial x}\right)\\ \int\frac{\mathbf{dq}dr'}{(2\pi)^3}D_{UH}\left(\mathbf{q},\omega_0-\omega_m,\frac{\mathbf{r}+\mathbf{r}'}{2}\right)e^{i\mathbf{q}(\mathbf{r}\text{-}\mathbf{r}')}\varphi_b\left(\mathbf{r}'\right) &= -\frac{\chi_{nl}^a}{B_0}\frac{\partial}{\partial x}\left(\left(\mathbf{E}_0^*\mathbf{e}_x\right)\frac{\partial\varphi_m}{\partial x}\right)\\ \int\frac{\mathbf{dq}dr'}{(2\pi)^3}D_{UH}\left(\mathbf{q},\omega_n,\frac{\mathbf{r}+\mathbf{r}'}{2}\right)e^{i\mathbf{q}(\mathbf{r}\text{-}\mathbf{r}')}\varphi_n\left(\mathbf{r}'\right) &= -\frac{\chi_{nl}^b c}{2\left|\omega_{ce}\right|B_0}\frac{\partial^2}{\partial x^2}\left(\frac{\partial\varphi_I}{\partial x}\frac{\partial\varphi_m^*}{\partial x}\right)\\ \int\frac{\mathbf{dq}dr'}{(2\pi)^3}D_{IB}\left(\mathbf{q},\omega_I,\frac{\mathbf{r}+\mathbf{r}'}{2}\right)e^{i\mathbf{q}(\mathbf{r}\text{-}\mathbf{r}')}\varphi_I\left(\mathbf{r}'\right) &= -\frac{\chi_{nl}^b c}{2\left|\omega_{ce}\right|B_0}\frac{\partial^2}{\partial x^2}\left(\frac{\partial\varphi_n}{\partial x}\frac{\partial\varphi_m}{\partial x}\right)\end{aligned} \tag{4.2.14}$$

where the coefficient

$$\chi^a_{nl} = \frac{\omega_{pe}^2\omega_m\left(\omega_0-\omega_m\right)\omega_{ce}^2}{\left(\omega_0^2-\omega_{ce}^2\right)\left(\omega_m^2-\omega_{ce}^2\right)\left(\left(\omega_0-\omega_m\right)^2-\omega_{ce}^2\right)}\frac{k_0 c}{\omega_0}\left(7+3\frac{g_0}{\varepsilon_0}\frac{\omega_0}{|\omega_{ce}|}-4\frac{\omega_{ce}^2}{\omega_0^2}\right) \tag{4.2.15}$$

describes the coupling efficiency of an extraordinary wave with two electrostatic waves, and the coefficient

$$\chi^b_{nl} = \frac{\omega_{pe}^2\omega_m\omega_n\omega_{ce}^2}{\left(\omega_m^2-\omega_{ce}^2\right)\left(\omega_n^2-\omega_{ce}^2\right)\left(\omega_I^2-\omega_{ce}^2\right)} \tag{4.2.16}$$

describes the coupling efficiency of the three electrostatic waves in the secondary decay [69]. The system (4.2.14) can be reduced to a system of two non-linear equations, the running wave amplitudes φ_b and φ_I can be expressed in terms of the trapped waves φ_n, φ_m and the pump E_0 amplitudes explicitly. To demonstrate this we solve the last equation in (4.2.14) in the WKB approach, the IB wave amplitude C_I obeys the following ODE

$$i\frac{\partial D_{IB}}{\partial q_{Ix}}\frac{e^{i\int^x dx' q_{Ix}(x')}}{\sqrt{|\partial D_{IB}/\partial q_{Ix}|}}\frac{dC_I}{dx} = -\chi^b_{nl}\frac{c}{2B_0}C_nC_m\frac{d^2}{dx^2}\left(\frac{d\psi_n}{dx}\frac{d\psi_m}{dx}\right) \tag{4.2.17}$$

Integrating this equation with the appropriate boundary condition $C_I\big|_{x\to-\infty}\to 0$ we arrive at

$$\begin{aligned}\varphi_I\left(\mathbf{r}\right) = i\chi^b_{nl}\frac{c}{2B_0}\frac{1}{\partial D_{IB}/\partial q_{Ix}}\Big|_{x_d} C_n\left(y,z,t\right)C_m\left(y,z,t\right)\times\\ \int_{-\infty}^{x} dx' e^{i\int_{x'}^{x} dx'' q_{Ix}(x'')}\frac{d^2}{dx^2}\left(\frac{d\psi_n}{dx}\frac{d\psi_m}{dx}\right)+c.c.\end{aligned} \tag{4.2.18}$$

We assume here that the secondary instability growth rate is much smaller than the IB wave frequency and moreover, much smaller than the ion cyclotron frequency. This assumption, which is valid for parameters of the present day tokamak experiments, allows correct consideration of both the instability saturation phase and the stage of its exponential growth. The IB wave amplitude (4.2.18) depends on the coordinates y, z and time t parametrically through the dependence of the UH m and n modes amplitudes on them. Thus the IB wave can be excluded from the whole system describing the two-step decay cascade, an analogous procedure can be applied for the non-trapped UH wave described by the potential φ_b. Then substituting the IB wave and the non-trapped UH wave potentials into the equations describing the primary and the secondary trapped UH waves, assuming small pumping wave depletion, results in the set of the non-linear equations

$$\begin{aligned}&\frac{\partial}{\partial t}a_m - i\Lambda_{my}\frac{\partial^2}{\partial y^2}a_m - i\Lambda_{mz}\frac{\partial^2}{\partial z^2}a_m = \gamma_p A\left(y,z\right)a_m - \gamma_s\left|a_n\right|^2 a_m\\ &\frac{\partial}{\partial t}a_n + i\Lambda_{ny}\frac{\partial^2}{\partial y^2}a_n + i\Lambda_{nz}\frac{\partial^2}{\partial z^2}a_n = \gamma_s\left|a_m\right|^2 a_n\end{aligned} \tag{4.2.19}$$

where the normalized amplitudes of the first trapped UH wave (m) and the secondary one (n)

$a_{n,m} = C_{n,m}\sqrt{\frac{\omega \partial D_{UH}/\partial \omega \rho_z^2}{16\pi}}\Big|_{\omega=\omega_{n,m}}$, the amplitudes are normalized so that $|a_{n,m}|^2$ being multiplied by $\frac{T_e}{\pi \rho_z^2}$ gives the 2D energy density of the trapped plasmons, the energy of the plasmons $\epsilon_m = \frac{T_e}{\pi\rho_z^2}\iint dydz\,|a_m|^2$; the values $\Lambda_{my,mz} = \frac{\partial^2 D_{UH}}{2\partial q_{y,z}^2}\Big|_{\omega_m, q_{y,z}=0}$ have the meaning of the diffraction coefficients for the UH waves, the function $A\left(y,z\right)$ describes the spatial distribution of the pump beam intensity, which is calculated accounting for the edge plasma turbulence, the coefficient $\gamma_p \propto P_0/\rho_y\rho_z$ describes the nonlinear coupling between the waves participating in the primary decay, $\gamma_s \propto 1/\rho_z^2$ is the coefficient describing the interaction between the primary trapped UH wave, the secondary one and the IB wave, which is calculated with the due account of the thermal effects [109]. The explicit description for these coefficients and the derivation of the expressions (4.2.19) itself is quite long, now we are focused on the analysis of the system (4.2.19), for the details we refer the readers to [69], [105]. Dependence of these coefficients on the pump power and the beam radius is analyzed in [110]. The system (4.2.19) describes the UH waves evolution averaged within the trapping volume so the diffraction of the pump beam is neglected in this volume.

Normally the analytical and numerical investigation of the PDI processes are fulfilled in the model with a non-perturbed Gaussian pump beam distribution, i.e. the square of the pump wave amplitude modulus, being represented as follows

$$A^G\left(y,z\right) = e^{-\frac{y^2}{\rho_y^2}-\frac{z^2}{\rho_z^2}} \tag{4.2.20}$$

where the poloidal and toroidal beam widths $\rho_{y,z}$, and typically $\rho_y = \rho_z$. This standard pump beam shape will be used in the following analysis of (4.2.19). First of all the system (4.2.19) describes the exponential growth of the primary UH wave (the growth rate of the instability) and its saturation. The nonlinear term in the right-hand side of the first equation in (4.2.19) is negligible at the instability excitation stage. The solution of the corresponding linear equation is represented in terms of superposition of its 2D eigenfunctions, possessing its own growth rate. For the fundamental mode, characterised by the maximal growth rate Γ, well above the threshold we get the instability growth rate (see [104],[105])

$$\Gamma = Re\left(\gamma_p\right) - \cos\left(\frac{\arg\left(\gamma_p\right)}{2} - \frac{\pi}{4}\right)\sqrt{|\gamma_p|}\left(\sqrt{\frac{\Lambda_{my}}{\rho_y^2}} + \sqrt{\frac{\Lambda_{mz}}{\rho_z^2}}\right) \tag{4.2.21}$$

which is decreasing with widening of the pump beam in y and z directions. By putting $\Gamma = 0$ and recalling $\gamma_p \propto P_0/\rho_y\rho_z$ we can use the expression (4.2.21) also to estimate the instability excitation power threshold corresponding to $P_0^{th} \propto \rho_y\rho_z\left(\sqrt{\frac{\Lambda_{my}}{\rho_y^2}} + \sqrt{\frac{\Lambda_{mz}}{\rho_z^2}}\right)^2$.

The second expression in the system (4.2.19) provides an estimate of the primary UH wave saturation amplitude. The saturation is determined by the balance between the secondary plasmon excitation source and its diffractive loss from the spot of the pump beam. Thus the estimate of the saturation amplitude provides the following expression:

$$\left|a_m^{sat}\right|^2 \approx \max\left\{\frac{\Lambda_{ny}}{\rho_y^2}, \frac{\Lambda_{nz}}{\rho_z^2}\right\}\frac{1}{\gamma_s} \tag{4.2.22}$$

normally $\Lambda_{nz} \gg \Lambda_{ny}$ so $|a_m^{sat}|^2 \propto 1$. The saturation of the secondary trapped UH wave is defined by the energy loss of the primary one

$$\left|a_n^{sat}\right|^2 \approx \frac{\gamma_p}{\gamma_s} \propto \frac{\rho_z}{\rho_y} \tag{4.2.23}$$

The pump beam loses some part of its initial power ΔP_0 due to the energy transfer to the daughter waves, this power does not serve to the purposes of the ECRH at the prescribed localization, thus the anomalous power absorption rate $\frac{\Delta P_0}{P_0}$ is an important characteristics. In the considered model the anomalous power absorption rate is given by the expression

$$\frac{\Delta P_0}{P_0} \approx \frac{2\omega_0}{\omega_m} \frac{T_e}{P_0} \gamma_p \frac{\rho_y}{\rho_z} \left|a_m^{sat}\right|^2 \propto 1/\rho_z^2 \tag{4.2.24}$$

see [111]. The system (4.2.19) is universal to describe the decay of an X-mode wave as well as an O-mode wave for the considered mechanism of the two-step cascade of the parametric decay. So the expression (4.2.24), derived in [111] for the O-mode pump, is applicable for the X-mode. The expression (4.2.24) provides an analytical value of the absorbed power ΔP_0, the numerical evaluation of this characteristic can be defined as the total energy increase of the primary and secondary trapped UH waves per a time unit

$$\Delta P_0 = \frac{d}{dt} \left(\epsilon_m + \epsilon_n\right) \tag{4.2.25}$$

All the described characteristics of the PDI process are possible to analyse analytically in the case of the Gaussian non-perturbed pumping beam profile. If the probing beam intensity distribution A is a random function, corresponding to a random turbulence realization, numerical analysis of the system (4.2.19) is required to evaluate the PDI characteristics. The numerical solution of (4.2.19) in various turbulence regimes is analysed in the next section.

4.3 Pump beam distribution in turbulent plasma

4.3.1 Analytical description

The edge plasma turbulence can significantly distort an extraordinary pump microwave beam [78]. If the turbulence amplitude is high enough, the radiation pattern can be split into several sub-beams whereas the average distribution of the electromagnetic field has the Gaussian shape. The parametric decay process will be analysed numerically with respect to the pump beam distortion due to the plasma turbulence, the PDI characteristics will be averaged and compared to results of the simulations with the averaged (broadened by the turbulence) smooth pump beams. In this section we describe the pump beam 3D model in turbulent plasma, using the main results of the average beam 3D structure analysis from the previous chapter.

The turbulence structure is strongly elongated along the magnetic field direction normally so the electron density turbulence δn is considered as a function of the radial and poloidal coordinates, in our geometry model $\delta n = \delta n\left(x, y\right)$. We consider an X-mode pumping microwave beam propagating in such turbulent plasma along the direction of the plasma inhomogeneity x. The wave structure at the plasma edge

$$E\left(x=0,y,z\right)=E_0 e^{-\frac{y^2}{2\rho_0^2}-\frac{z^2}{2\rho_0^2}} \tag{4.3.1}$$

ρ_0 is the initial beam width and E_0 is the beam amplitude at the plasma edge, it is connected to the pump power P_0, defined as

$$E_0=\sqrt{\frac{8\pi}{c}\frac{P_0}{\pi\rho_0^2}} \tag{4.3.2}$$

Since the turbulence is independent on z coordinate the beam width broadening in this direction is determined only by the diffraction. The analysis of the average field intensity in the 3D geometry was described in the previous chapter, for the considered pump beam E_0 it results in the following expression for the average radiation intensity

$$\left\langle\left|\mathbf{E}\left(x,y,z\right)\right|^2\right\rangle=E_0^2\frac{\omega_0}{ck_0\left(x\right)}\frac{\rho_0^2}{\rho_y\left(x\right)\rho_z\left(x\right)}e^{-\frac{y^2}{\rho_y^2(x)}}e^{-\frac{z^2}{\rho_z^2(x)}} \tag{4.3.3}$$

the poloidal $\rho_y\left(x\right)$ and toroidal $\rho_z\left(x\right)$ beam widths components are described by the equations in the system (3.1.10). It is worth mentioning that the average poloidal beam width ρ_y is determined by the beam diffraction and the plasma turbulence, whereas the toroidal beam width in the area where the PDI takes place ρ_z is associated with the diffraction only. The criterion for the applicability of this analysis is a big enough value of the average phase variation associated with the turbulence fulfilling the condition $\langle\delta\phi^2\rangle\gg 1$.

4.3.2 Numerical modelling

A probing microwave beam poloidal distribution in turbulent plasma is simulated in this section. The 2D beam propagation is considered in the slab model, the x axis is the direction of the density $n\left(x\right)$ and magnetic field $B\left(x\right)$ inhomogeneity, the y axis represents poloidal direction, propagation in the toroidal direction z is not simulated since the turbulence is normally elongated in this direction and does not perturb ρ_z. The beam propagates along the direction of the inhomogeneity x, the probing frequency is $f=82.4$ GHz, the initial beam width $\rho_0=1.0$ cm. The size of the numerical cells is $\lambda_0/24$ in the x and y directions with λ_0 being the vacuum wave number for the probing frequency, the choice of the spatial numerical step being much smaller than λ_0 allows to simulate the beam propagation accurately. The 2D simulation domain is 1000×1000 cells, the time step is $\Delta t=1/48f$, the full time of each simulation is $20000\Delta t$ which is enough for the probing beam pass through the simulation domain. The simulation is performed for the plasma conditions similar to the ECRH experiment at TCV, which will be used to study the impact of the turbulence on the PDI characteristics. The density and magnetic field profiles measured in the shot 41384_1_1 were used, figures 39 and 40 respectively, where $x=0$ represent the vicinity of the last closed surface, the measured profiles were extrapolated to the region $x<0$. The frozen turbulence, that is adequate for the high-frequency pump, was generated as a sum of harmonics of the Gaussian spectrum with random phases

$\phi_{k,l}$, this is a standard approach often used for modeling the turbulence, that allows to control the turbulence parameters easily

$$\delta n\left(x,y\right) = \delta n^{rms}\left(x\right)\left(\frac{1}{2}\sum_{k,l}\exp\left[-\frac{1}{4}\left(q_k^2+q_l^2\right)l_c^2\right]\right)^{-1/2} \times \\ \sum_{k,l}\exp\left[-\frac{1}{8}\left(q_k^2+q_l^2\right)l_c^2\right]\cos\left[q_k x + q_l y + \phi_{k,l}\right] \qquad (4.3.4)$$

$q_{k,l}$ are the discrete wavenumbers, $\delta n^{rms}\left(x\right)$ is the root mean square value of the turbulence, $l_c = 0.5$ cm is the used correlation length, which is commonly observed [112]. The turbulence amplitude Q is defined as $Q = \frac{\delta n^{rms}(0)}{n(0)}$. The shape of $\delta n^{rms}\left(x\right)$ is illustrated on the figure 39 (the dashed curve) for the turbulence amplitude $Q = 0.2$. The simulations of the beam propagation in the turbulent plasma are performed by using the full-wave code IPF-FD3D.

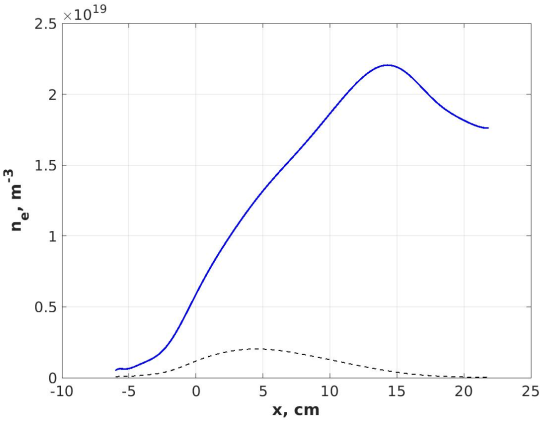

Figure 39: The profiles of the density $n\left(x\right)$ and the turbulence root mean square value $\delta n^{rms}\left(x\right)$ for the case of the amplitude $Q = 0.2$, the solid and dashed curves respectively

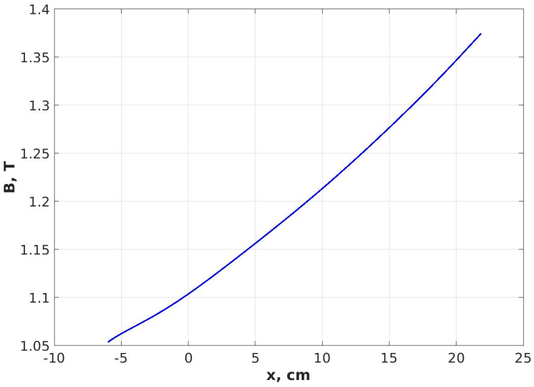

Figure 40: The magnetic field profile used in the simulation

The simulations were performed in the three turbulence regimes for the different turbulence amplitudes $Q = \{0.1, 0.2, 0.4\}$ and in the case without the turbulence $Q = 0$. The poloidal distribution of the pump beam intensity is evaluated around the position $x = 20$ cm, where the PDI takes place. The examples of the normalized distributions are illustrated on the figures 41 - 43 for the different turbulence amplitudes. It is seen that the injected beam can be significantly distorted by the edge turbulence, the relatively weak turbulence $(Q = 0.1)$ perturbs the microwave beam, whereas the beam can be split into several smaller ones in the case of the high turbulence amplitude $(Q = 0.4)$.

The profiles of the normalized intensity averaged over 400 realizations are illustrated on the figure 44. The average numerically evaluated profiles are compared with the analytical prediction (4.3.3) given by the dashed curves. For the relatively small turbulence amplitudes $Q = \{0.1, 0.2\}$ the pump phase modulation is not big enough $\langle\delta\phi^2\rangle \approx \{0.3, 1.4\}$ to guarantee the applicability of the analytical averaging procedures. This explains a non-perfect fit of a numerical computation averaging result by the analytical expression (4.3.3) for the pump beam seen in figure 44. The agreement is better in the case of the higher turbulence amplitude $Q = 0.4$ when

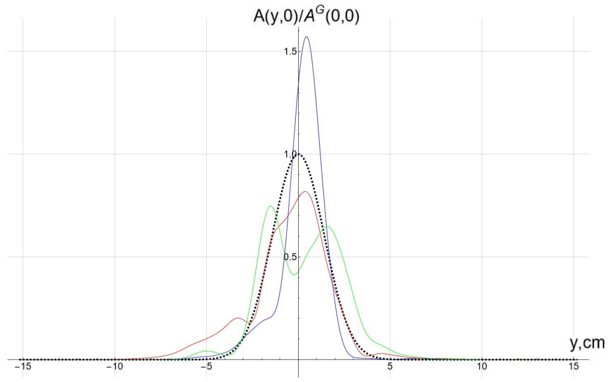

Figure 41: The normalized random poloidal profiles of the pump beam - the solid curves, the turbulence amplitude $Q = 0.1$; the dashed curve is the poloidal distribution in the case without the turbulence

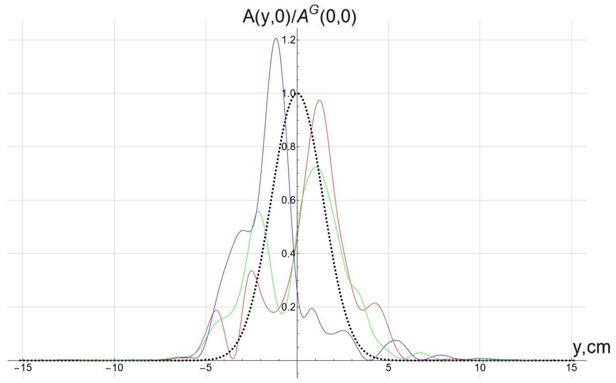

Figure 42: The normalized random poloidal profiles of the pump beam - the solid curves, the turbulence amplitude $Q = 0.2$; the dashed curve is the poloidal distribution in the case without the turbulence

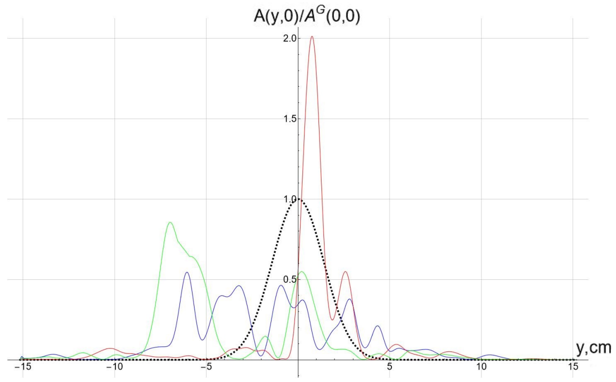

Figure 43: The normalized random poloidal profiles of the pump beam - the solid curves, the turbulence amplitude $Q = 0.4$; the dashed curve is the poloidal distribution in the case without the turbulence

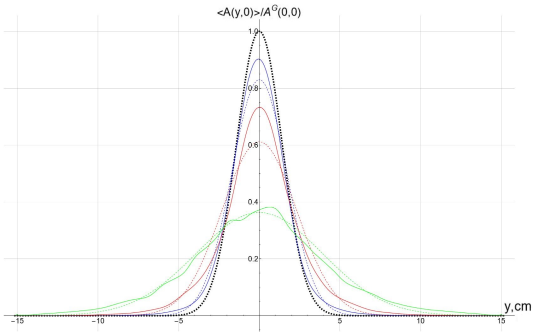

Figure 44: The solid curves are the average over 400 realizations poloidal profiles of the intensity, the blue, red and green colors correspond to the turbulence amplitudes $Q = \{0.1, 0.2, 0.4\}$ respectively, the dashed curves of the same colors are the analytical prediction of the nonlinear theory; the black dashed curve is the poloidal distribution in the case without the turbulence

$\langle \delta\phi^2 \rangle \approx 5.6$. The numerically evaluated average poloidal beam widths $\rho_y \approx \{2.0, 2.4, 3.3, 5.5\}$ cm for the four considered turbulence regimes $Q = \{0, 0.1, 0.2, 0.4\}$ respectively.

The scheme of simulation of the pump beam propagation in turbulent plasma is illustrated on the figure 45, the beam width evolution is compared for the two simulated cases: plasma without the turbulence and the turbulent plasma with $Q = 0.4$.

As it was mentioned the toroidal distribution of the beam intensity $A\left(0, z\right)$ is not perturbed by the turbulence, its shape is Gaussian, the poloidal distribution $A\left(y, 0\right)$ was evaluated from the numerical modelling in the three turbulence scenarios $Q = \{0.1, 0.2, 0.4\}$, their combination describes the 2D spatial distribution of the pump beam (at a fixed radial point x where the PDI is localized). The 2D distribution is used in the system (4.2.19) for the evaluation of the PDI characteristics, the results are compared with the PDI characteristics in the case of the non-perturbed beam $A\left(y, z\right) = A^G\left(y, z\right)$.

4.4 The PDI numerical analysis

The parametric decay of a Gaussian beam is described analytically in the first section of this chapter, its characteristics can be expressed in terms of the beam width and power. The

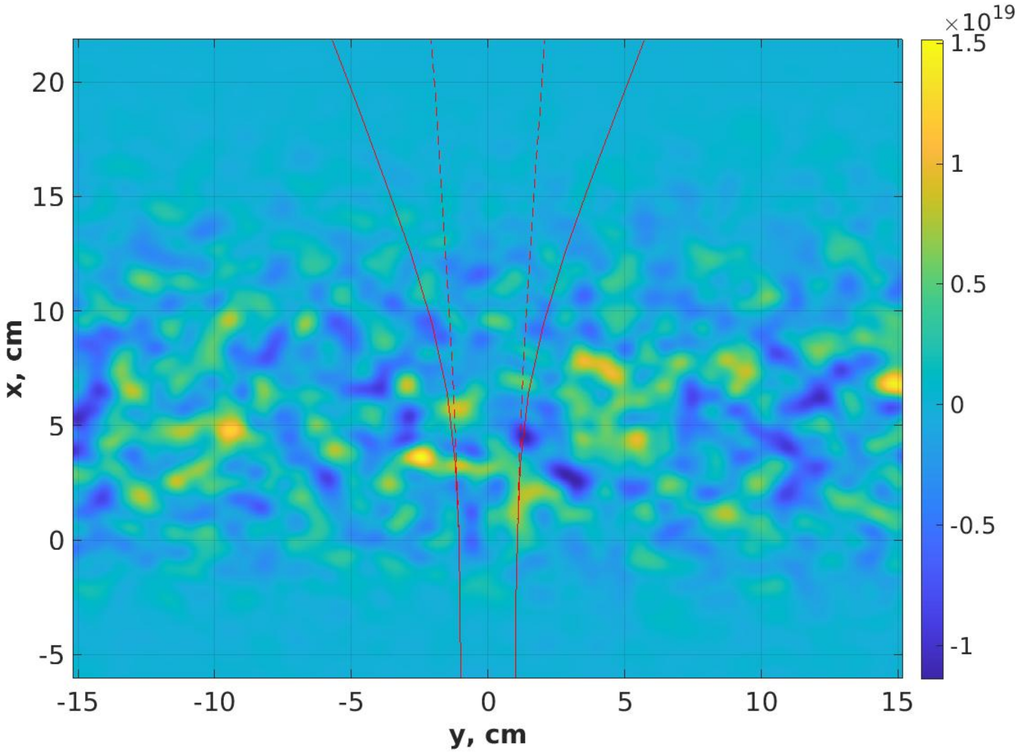

Figure 45: Scheme of the pump beam propagation in turbulent plasma, the dashed curve is the beam width $\rho_y(x)$ position for the simulation without the plasma turbulence, the solid curve is the average pump beam width for the simulations with the turbulence amplitude $Q = 0.4$; the color map represents a random turbulence realization.

obtained results could be applied both to the case of unperturbed pump beam and to the case of the averaged beam (4.3.3). The PDI process in turbulent plasma, when the heating radiation poloidal distribution is a random function, can be analysed numerically. The numerical solution of the system (4.2.19) in the different turbulence scenarios for the various turbulence amplitudes Q, described in the previous section, is analyzed in this section. The PDI characteristics averaged over a large set of independent turbulence realizations, having the same correlation lengths, spectrum and amplitude, are evaluated and compared against the results of the modeling without the turbulence.

The system (4.2.19) is solved with the coefficients typical for the ECRH experiments at TCV and with the initial condition of the thermal noise level amplitudes $a_{n,m} = 1$, the electron temperature $T_e = 2$ keV, the pump beam power $P_0 = 600$ kW and the width of the non-perturbed Gaussian beam $\rho = \rho_{y,z} = 2$ cm (the initial pump beam width is $\rho_0 = 1$ cm at the waist position, corresponding to the bottom on the figure 45, but an unperturbed beam is widened due to the diffraction). The periodic boundary conditions were used, however the effect of the trapped UH waves multiple transitions through the parametric decay area, which is possible to model with these conditions, was not considered.

4.4.1 Growth rate and saturation

The growth rate of the instability is described by the stage of the exponential growth of the primary trapped UH wave amplitude. The wave energy averaged within the pumping beam area

$$\epsilon_m^{av} = \frac{T_e}{\pi \rho_z^2} \iint dydz \left|a_m\right|^2 A\left(y, z\right) \tag{4.4.1}$$

is convenient for the analysis of the growth rate and the saturation amplitude, the full energy ϵ_m grows with time without the saturation, this is demonstrated later in the text. The statistically average function $\text{Ln}\frac{\epsilon_m^{av}(t)}{\epsilon_m^{av}(0)}$ is depicted on the figure (46) for the four turbulence amplitudes $Q = \{0, 0.1, 0.2, 0.4\}$. The numerically evaluated energy evolution in the instability excitation

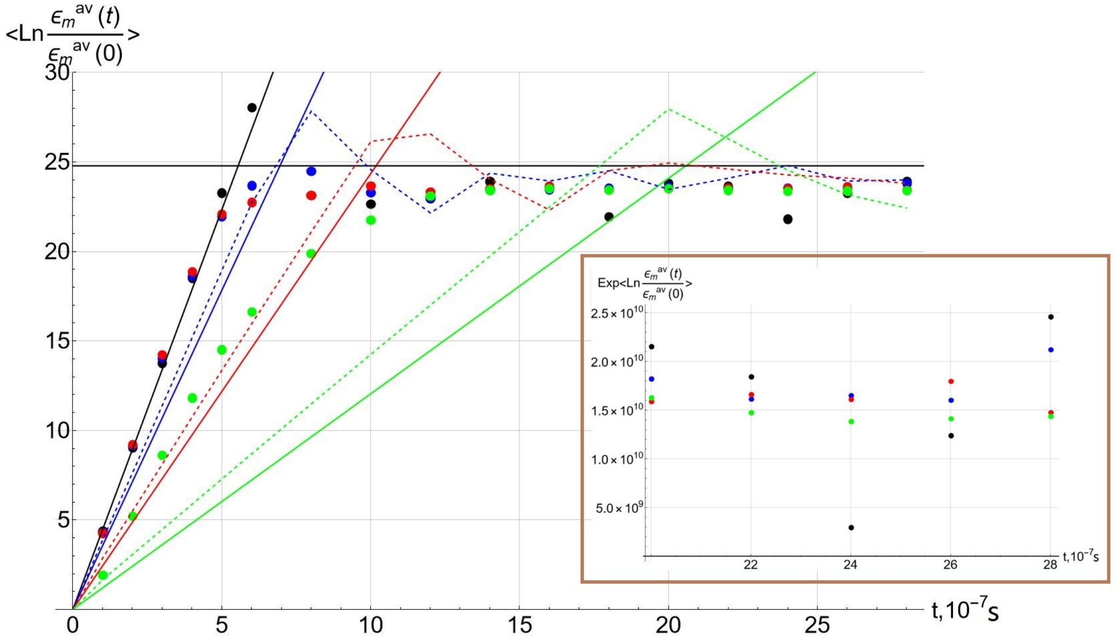

Figure 46: The primary trapped UH wave energy evolution $\left\langle \text{Ln}\frac{\epsilon_m^{av}(t)}{\epsilon_m^{av}(0)} \right\rangle$, the black, blue, red and green dotted curves, provided by the numerical solution of (4.2.19), represent the case without the turbulence and the simulations with $Q = \{0.1, 0.2, 0.4\}$ respectively, the solid lines of the same colors provide the $2\Gamma t$ value, with the growth rate Γ evaluated using (4.2.21) for the different averaged beam widths, corresponding to the turbulence amplitudes Q, the dashed curves are provided by the numerical solutions of (4.2.19) for the unperturbed Gaussian pump with the corresponding (the same color) average beam widths ρ_y, the horizontal line is the estimate of the saturation level for the non-perturbed pump beam; the saturation stage is depicted in the framed graphic in the linear scale

stage is compared with the analytical prediction (4.2.21) for $2\Gamma t$, where the growth rate Γ is evaluated for the different average pump beam widths ρ_y, corresponding to the different turbulence regimes. The qualitative concordance between the theory prediction (4.2.21) and the numerical results for the averaged Gaussian pump beams is acceptable. The simulations demonstrate that the relatively small turbulence amplitudes $Q = \{0.1, 0.2\}$ almost do not change the average growth rate. The higher level of the turbulence $Q = 0.4$ reduces the average growth rate, but the analytical prediction for the averaged beam overestimates by a factor of 2 the effect of the growth rate decrease (see figure 46). A possible explanation for this is provided by the dependence of the growth rate not on the beam power or width, but on the pump electric field amplitude, which can be large in the disturbed beam. The saturation level of the primary plasmon energy located within the pump beam is fluctuating, however remaining almost the same for all the turbulence regimes. This result corresponds to the expression (4.2.22) since usually $\Lambda_{nz} \gg \Lambda_{ny}$ so that the saturation level is determined by the pump beam distribution along the magnetic field, not affected by the turbulence, and independent on the poloidal beam structure.

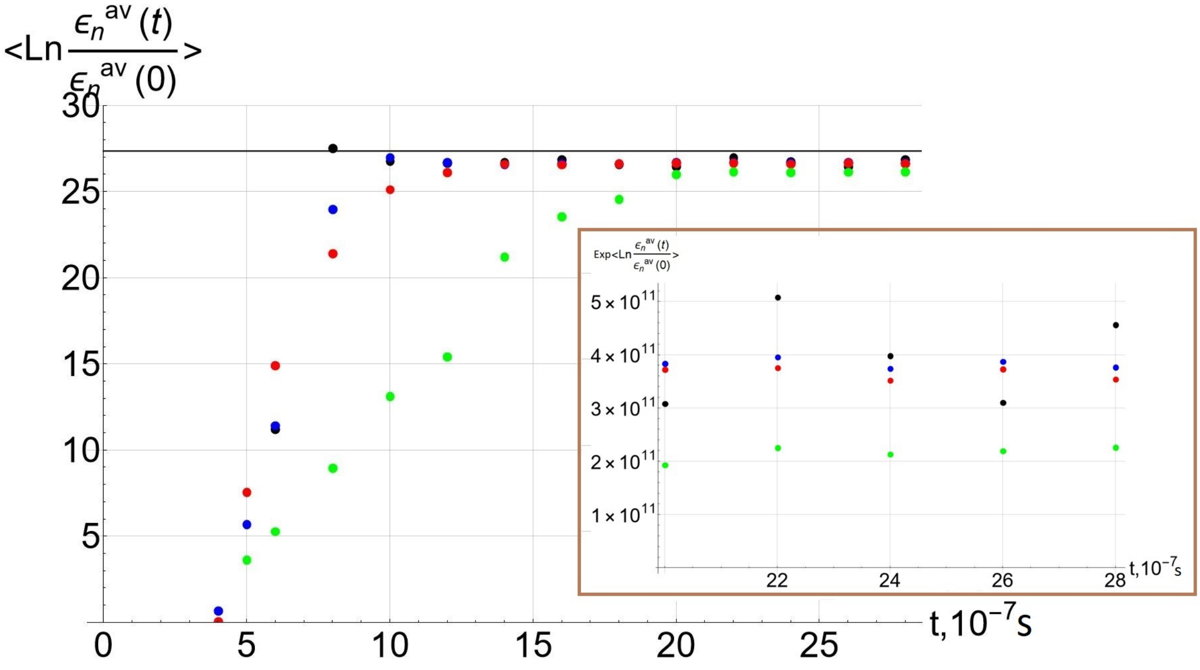

Figure 47: The secondary trapped UH wave energy evolution $\left\langle \mathrm{Ln}\frac{\epsilon_n^{av}(t)}{\epsilon_n^{av}(0)} \right\rangle$, the black, blue, red and green dotted curves represent the case without the turbulence and the simulations with $Q = \{0.1, 0.2, 0.4\}$ respectively, the horizontal line is the estimate of the saturation level for the non-perturbed beam; the saturation stage is depicted on the framed plot in the linear scale

The energy evolution of the secondary trapped plasmon is illustrated on the figure 47. It is seen that the energy saturation level decreases with increasing the turbulence amplitude. This tendency can be explained if one considers the PDI process driven by the averaged pump beam. Namely, according to the analytical estimate (4.2.23) $|a_n^{sat}|^2 \propto \rho_z/\rho_y$, the average poloidal beam width ρ_y is increasing due to the edge turbulence. The analytical estimates of the energy saturation level slightly overestimate the saturation values of $\epsilon_{m,n}^{av}$.

4.4.2 Anomalous absorbtion

The total energy of the primary and secondary trapped UH waves $\epsilon_m + \epsilon_n$ increase per second determines the amount of the anomalously absorbed pumping power according to the expression (4.2.25). The total energy evolution was evaluated and averaged in the saturation stage of the instability for the different turbulence regimes $Q = \{0, 0.1, 0.2, 0.4\}$, the results are depicted on the figure 48. As it is seen, the total energy can be approximated well by a linear function, the least mean squares fitting is illustrated on the figure 48. The linear approximation is used for evaluating the energy anomalous absorbtion rate $\frac{\Delta P_0}{P_0} \approx \{4.8, 4.3, 4.5, 4.3\} \times 10^{-4}$ for the different turbulence amplitudes correspondingly. It is seen that presence of the turbulence results in only a small (of about 10%) mitigation of the anomalously absorbed power. This result agrees with the analytical prediction (4.2.24) which provides the dependency $\Delta P_0 \propto 1/\rho_z^2$

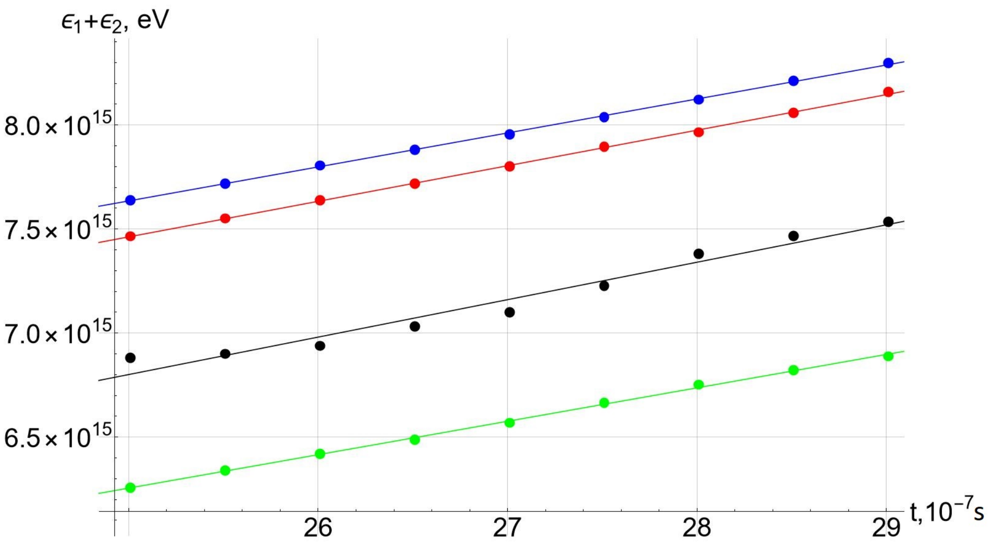

Figure 48: The total energy of the first and second trapped UH waves $\langle\epsilon_m+\epsilon_n\rangle$, the black, blue, red and green dotted curves represent the case without the turbulence and the simulations with $Q=\{0.1,0.2,0.4\}$ respectively; the solid lines of the same colors are the least mean squares fitting of the energy

(assuming that normally $\Lambda_z \gg \Lambda_y$) so the anomalously absorbed power is not related to the poloidal pump beam width ρ_y, that is why one could expect the independence of ΔP_0 on the turbulence level. The energy $\langle\epsilon_m+\epsilon_n\rangle$ evolution curve for the case with the unperturbed plasma density is located between the curves corresponding to the high and low turbulence regimes (see figure 48), this effect is due to the energy transition to the saturation process, which is oscillatory, and it has not got an analytical description yet.

4.4.3 Power threshold

The turbulence reduces the pump beam amplitude on average (figure 44), that leads to the increase of the instability threshold P_0^{th}. First of all it worth considering the threshold in the unperturbed beam case. According to the definition done in the first section the power threshold is determined from the relation $\Gamma=0$ (see (4.2.21)), in the framework of the simulation model that results in $P_0^{th}\approx 47.1$ kW. The solution of the linearized first equation in the system (4.2.19) is illustrated on the figure 49 for the case without the plasma turbulence $Q=0$. The solutions are obtained for the different power values P_0 in the range from $0.9P_0^{th}$ to $2.0P_0^{th}$. It is seen that the excitation does not occur when the pump power is lower than the threshold $P_0=0.9P_0^{th}$, if the power exceeds the threshold value, the energy evolution corresponds to the analytical prediction for its growth rate $Ln\left(|a_m(t)|^2/|a_m(0)|^2\right)=2\Gamma\left(P_0\right)t$. The evolution of the average local energy density $|a_m(t)|^2$ is depicted on the figures 50-52 for the simulations with the turbulence amplitudes $Q=\{0.1,0.2,0.4\}$ respectively. One can see that presence of the low-level turbulence $Q=\{0.1,0.2\}$ only slightly decreases the local energy density growth rate when the pump power is well above the threshold. The reliable exponential growth is observed on the figures 50 and 51 even for the simulations with $P_0=1.2P_0^{th}$. The excitation threshold is noticeably higher in the simulation with the high turbulence amplitude $Q=0.4$. The clearly exponential growth of the energy density starts since the power amplitude $P_0=1.6P_0^{th}$. The estimate of the average power threshold is illustrated on the figure 53, the estimated values are

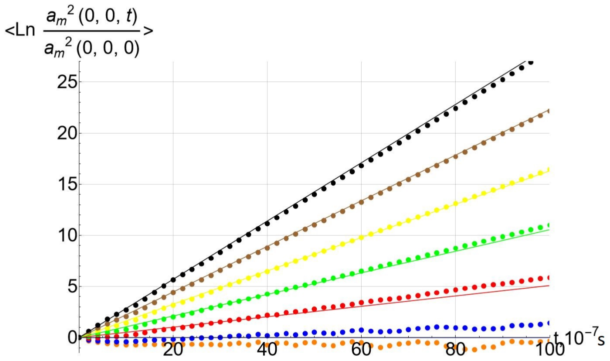

Figure 49: Evolution of $Ln\left(|a_m(t)|^2\,/\,|a_m(0)|^2\right)$ evaluated in the point $(y=0, z=0)$ the case without the turbulence, the dotted orange, blue, red, green, yellow, brown and black curves are the numerical solutions for the power amplitudes $P_0 = 0.9, 1.0, 1.2, 1.4, 1.6, 1.8, 2.0\ P_0^{th}$ respectively, the solid lines are $2\Gamma t$ with the growth rate Γ evaluated for the corresponding power P_0

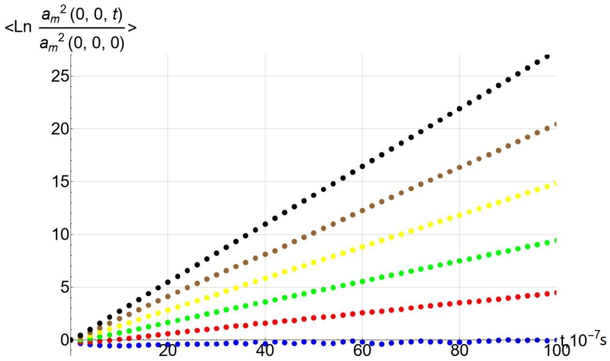

Figure 50: Evolution of $Ln\left(|a_m(t)|^2\,/\,|a_m(0)|^2\right)$ evaluated in the point $(y=0, z=0)$ for the turbulence amplitude $Q = 0.1$, the dotted blue, red, green, yellow, brown and black curves are the numerical solutions for the power amplitudes $P_0 = 1.0, 1.2, 1.4, 1.6, 1.8, 2.0\ P_0^{th}$ respectively

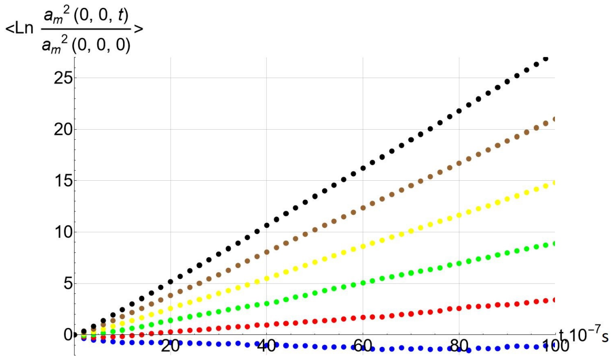

Figure 51: Evolution of $Ln\left(|a_m(t)|^2\,/\,|a_m(0)|^2\right)$ evaluated in the point $(y=0, z=0)$ for the turbulence amplitude $Q = 0.2$, the dotted blue, red, green, yellow, brown and black curves are the numerical solutions for the power amplitudes $P_0 = 1.0, 1.2, 1.4, 1.6, 1.8, 2.0\ P_0^{th}$ respectively

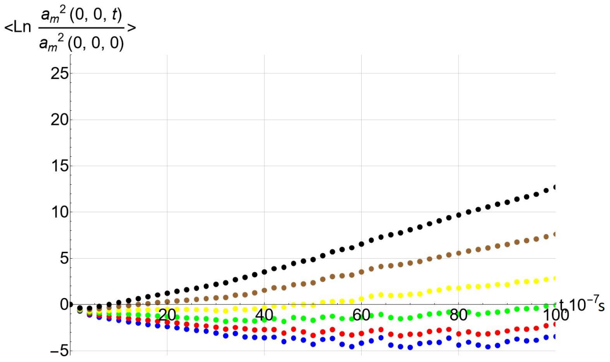

Figure 52: Evolution of $Ln\left(|a_m(t)|^2\,/\,|a_m(0)|^2\right)$ evaluated in the point $(y=0, z=0)$ for the turbulence amplitude $Q = 0.4$, the dotted blue, red, green, yellow, brown and black curves are the numerical solutions for the power amplitudes $P_0 = 1.0, 1.2, 1.4, 1.6, 1.8, 2.0\ P_0^{th}$ respectively

determined as the power for which the clear exponential growth is seen (the figures 50 - 52), whereas the error bar is provided by the range between the determined power threshold and the lower value of the power tested on the figures 50 - 52. The averaged power thresholds are compared to the threshold values for the Gaussian beams with the poloidal beam widths ρ_y corresponding to the averaged beam widths for the examined turbulence scenarios. The amplitudes of the evaluated power thresholds were defined in the same way as for the unperturbed Gaussian beam on the figure 49. It is seen from the figure 53 that if one considers the PDI process driven by a pump disturbed in a strongly turbulent plasma as a parametric decay of the averaged pump beam, the evaluated power threshold can be overestimated for about 20-30%.

4.5 Discussion on PDI in turbulent plasma

The parametric decay instability in the turbulent plasma was simulated and analysed in this work under the plasma conditions close to the experimental ones on TCV tokamak. The tested turbulence regimes can be considered as the low turbulence $Q = 0.1$, $(\langle \delta\phi^2 \rangle \ll 1)$ the high turbulence $Q = 0.4$ $(\langle \delta\phi^2 \rangle \gg 1)$ and the intermediate turbulence $(\langle \delta\phi^2 \rangle \approx 1)$ scenarios. The investigated characteristics of the PDI process are the instability growth rate, its saturation

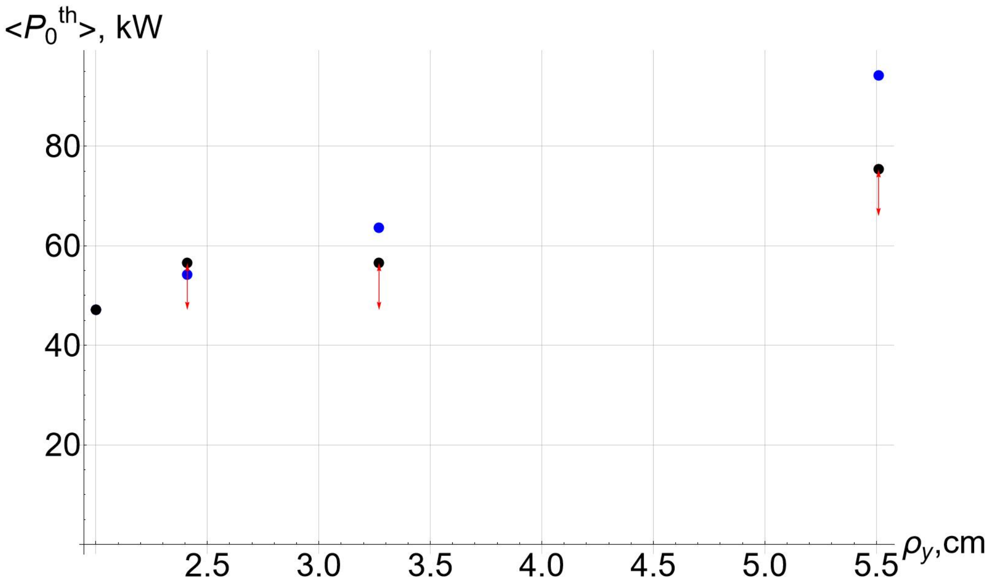

Figure 53: The average power threshold in the turbulent plasma is given by the black dots, the different ρ_y correspond to the different average beam widths in the considered turbulence regimes, the red arrows represent the error range of the threshold definition; the blue dots are the power threshold values for the Gaussian beams with the corresponding poloidal beam width determined by the turbulent broadening.

level, the excitation threshold and the anomalous energy absorbtion rate. The simulations demonstrated that the instability growth rate in the small and intermediate turbulence regimes remains almost the same whereas the high turbulence slightly reduces the growth rate. The saturation level of the UH wave energy is independent on the turbulence amplitude for the primary trapped UH wave and decreased for the secondary trapped plasmon with growing the turbulence amplitude Q. The both tendencies are in agreement with the analytical predictions for the PDI considered in the field of the average pump beam. The average power threshold of the decay instability is just a little bit increased in the small and intermediate turbulence regimes whereas the threshold increase is about 50% for the high turbulence scenario. One of the most important in practice characteristics - the anomalous absorbtion rate is only slightly modified by the plasma turbulence. Its reduction constitutes only about 10% of the unperturbed value, and this mitigation remains the same for all the tested turbulence regimes.

In general presence of the plasma turbulence, well above the threshold, do not modify the PDI characteristics drastically. The physical picture of a PDI process in the turbulent plasma is the nonlinear interaction of the waves (4.2.19), when the pump beam shape is slightly disturbed or even split into several sub-beams with their local peaks smaller or higher than the unperturbed beam amplitude and the different local sub-beam width. There is no analytical model that can describe the PDI characteristics in such a disturbed beam, one of the possible ways to predict the PDI characteristics in the case of the pump modulated by the edge plasma turbulence is to consider the parametric decay in the field of the average pump beam, however keeping in mind that the numerical study has demonstrated that this approach overestimates the turbulence influence on the PDI threshold and growth rate.

5 Radial correlation reflectometry analysis in high-turbulence plasma scenario

The radial correlation reflectometry (RCR) is a widely used technique proposed to diagnose the plasma turbulence in magnetic fusion machines. It was believed that probing plasma with multiple frequencies can be used to determine the turbulence radial correlation length locally simply from the difference in the cut-off positions where the correlation of the signals disappears. However, it turned out that this naive approach is not always correct, leading both to the correlation length overestimation in the linear scattering regime [29], [113] and to its underestimation in the non-linear regime typical for large devices, as it was demonstrated in the non-linear theory of the RCR in 1D [30] and 2D [31] models and confirmed by the numerical analysis in the 1D case [114]. According to the developed models in the case of strong turbulence the signal spatial correlation length depends on both the turbulence radial correlation length and its amplitude and thus seems to be not helpful for determination of any of them.

Another method of the reflectometry signal analysis was developed for extracting information on the turbulence spectrum and its amplitude [115]. This approach is based on the relation between the radial wave-number spectrum of the density fluctuations and the phase fluctuation wave-number spectrum of a reflectometer signal via a transfer function established under the Born approximation [116]. Assuming that the main contribution comes mainly from the vicinity of the cut-off layer, the Parceval's theorem is used to recover the density fluctuation level, and thus the density fluctuation profile. It was demonstrated that it is not possible to reconstruct the wave number spectrum when the Born approximation is not fulfilled, however, it was noticed that the turbulence amplitude still can be determined from the Parceval's theorem [117]. This effect was observed in 1D RCR simulations when the turbulence amplitude was big enough to break the Born approximation, but still small to consider the RCR to be deep in the non-linear regime [117]. Validity of the developed approach in the non-linear regime is tested in this work.

Hypothetically the two methods can be combined for obtaining the information on both the turbulence amplitude and its radial correlation length under the conditions when the non-linear regime of the RCR takes place. Nevertheless this idea has not been used in practice yet. The research work, described in this chapter of the thesis, is devoted to the demonstration and verification of the possibility to use the two methods of the RCR signal interpretation simultaneously, and to evaluation of the applicability domain for the two techniques. On the base of numerical simulations of a RCR experiment it is shown that this approach allows us to resolve the turbulence amplitude and the turbulence radial correlation length.

5.1 Theoretical background for the CCF analysis in non-linear regime

We assume the slab geometry which is normally good enough for characterizing microwave beam propagation in big machines. The Cartesian coordinates are chosen as follows: x is the direction of plasma inhomogeneity, a probing ordinary mode polarization beam is launched along this axis, z axis represents to the external magnetic field direction, y axis is perpendicular to x and z and normally treated as the poloidal coordinate. The wave equation for the O-mode in this model reads as

$$\left[\frac{\partial^2}{\partial x^2}+\frac{\omega^2}{c^2}\left(1-\frac{\omega_{pe}^2\left(x\right)}{\omega^2}-\frac{\delta n\left(x\right)}{n_c}\right)\right]E=0 \tag{5.1.1}$$

where E is the O-mode electric field amplitude (**E** is directed along z for the O-mode polarization) the electron plasma frequency ω_{pe} is given by (2.1.9), the background density $n(x)$, the critical density

$$n_c=\frac{\omega^2 m_e}{4\pi e^2} \tag{5.1.2}$$

corresponds to a given probing frequency ω, e and m_e are the electron charge and mass, the critical density determines a cut-off position x_c according to the equality $\omega_{pe}\left(x_c\right)=\omega$, δn is the density turbulence. The O-mode wave number k is given by the expression

$$k^2\left(x,\omega\right)=\frac{\omega^2-\omega_{pe}^2\left(x\right)}{c^2} \tag{5.1.3}$$

The radial correlation reflectometry is based on the plasma probing with a set of the probing frequencies, the fundamental scheme is illustrated in the figure 54. One of the limitations in the RCR interpretative model is a single cut-off position x_c for a probing frequency ω. The plasma turbulence modifies the density profile so the exact cut-off position $\tilde{x}_c$ is slightly different from x_c which is defined neglecting the turbulence. Definition for $\tilde{x}_c$, considering a locally linear density profile, can be written as

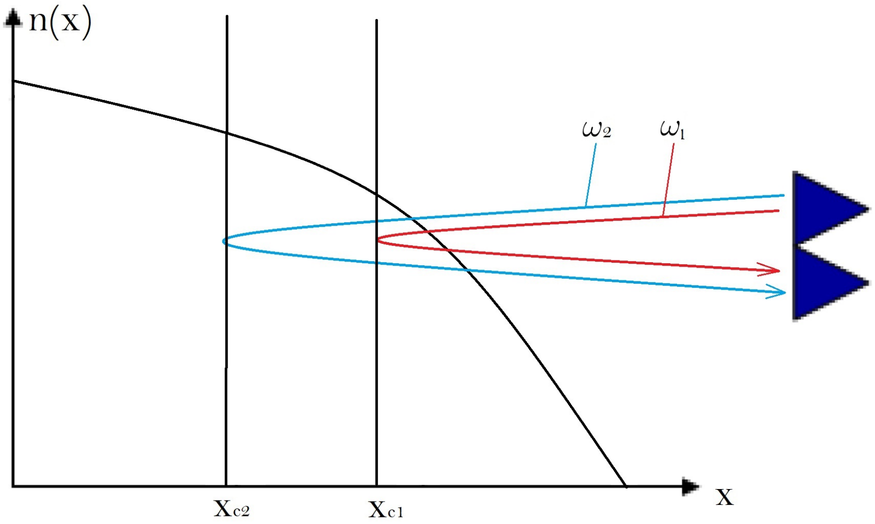

Figure 54: Radial correlation reflectometry scheme, plasma probing with two frequencies ω_1 and ω_2 that have the cut-offs at x_{c1} and x_{c2}

$$1-\frac{\tilde{x}}{x_c}-\frac{\delta n\left(\tilde{x}\right)}{n_c}=0 \tag{5.1.4}$$

so the criterion of a single cut-off position $|\tilde{x}-x_c|\ll l_{cx}$ with respect to (5.1.4) reads as

$$\frac{|\delta n|}{n_c}\ll\frac{l_{cx}}{x_c} \tag{5.1.5}$$

Also the frozen turbulence model is used, we assume that the turbulence characteristic time of change is much higher than the time of the probing wave flight, that is normally the case.

We consider here the monostatic reflectometry experiment. The reflected electric field at the receiver E_r in the WKB approach reads as

$$E_r\left(\omega_j\right) = E_i e^{i\varphi_r(\omega_j)} \tag{5.1.6}$$

where E_i is the probing wave electric field amplitude and $\varphi_r = \varphi_0 + \delta\varphi$ is the reflected field phase which consists of the phase associated with the wave propagation in the background plasma φ_0 and the phase perturbation due to the plasma turbulence $\delta\varphi$. In the WKB approach the phase variation can be written as

$$\delta\varphi\left(\omega\right) \approx -\frac{\omega^2}{c^2}\int_0^{x_c}\frac{dx'}{k\left(x',\omega\right)}\frac{\delta n\left(x'\right)}{n_c} \tag{5.1.7}$$

where δn is the plasma density fluctuation the radial coordinate $x = 0$ corresponds to emitter and receiver position. In this analysis we follow the approach of the analytical description developed in [30]. The cross-correlation function (CCF) of the signal, corresponding to two probing frequencies ω_i and ω_j so the two cut-off positions x_{ci} and x_{cj}, is given by the following expression

$$CCF\left(x_{ci}-x_{cj}\right) = \frac{\left\langle\left(E_r\left(\omega_i\right)-\left\langle E_r\left(\omega_i\right)\right\rangle\right)\left(E_r^*\left(\omega_j\right)-\left\langle E_r^*\left(\omega_j\right)\right\rangle\right)\right\rangle}{\sqrt{\left\langle\left|\left(E_r\left(\omega_i\right)-\left\langle E_r\left(\omega_i\right)\right\rangle\right)\right|^2\right\rangle\left\langle\left|\left(E_r\left(\omega_j\right)-\left\langle E_r\left(\omega_j\right)\right\rangle\right)\right|^2\right\rangle}} \tag{5.1.8}$$

It should be mentioned that the analysis of the signal cross-correlation function in the non-linear regime is considered here in the 1D reflectometry model (the 1D wave equation is considered (5.1.1)). According to [31], when the emitter and receiver are located close enough, the 2D CCF analytical analysis results in the same expressions as in the 1D model, this analytical result is also checked numerically in this work.

Supposing the density fluctuations radial correlation length l_{cx}, to be much smaller than the system size $l_{cx} \ll x_c$ and taking into account that in this case the random phase perturbation $\delta\varphi$ is a sum of many independent random values, we conclude that its evolution should be a normal random process. Then the average scattered electric field can be evaluated as

$$\left\langle E_r\left(\omega_i\right)\right\rangle = E_i e^{i\varphi_0(\omega_i)} e^{-\frac{\left\langle\delta\varphi^2(\omega_i)\right\rangle}{2}} \tag{5.1.9}$$

and the scattered radiation correlation function $\left\langle E_r\left(\omega_i\right)E_r^*\left(\omega_j\right)\right\rangle$, that is needed for the CCF (5.1.8) description,

$$\left\langle E_r\left(\omega_i\right)E_r^*\left(\omega_j\right)\right\rangle = E_i^2 e^{i(\varphi_0(\omega_i)-\varphi_0(\omega_j))} e^{-\frac{\left\langle\delta\varphi^2(\omega_i)\right\rangle}{2}-\frac{\left\langle\delta\varphi^2\left(\omega_j\right)\right\rangle}{2}+\left\langle\delta\varphi(\omega_i)\delta\varphi(\omega_j)\right\rangle} \tag{5.1.10}$$

The averaging procedure of the scattered field $\left\langle E_r\left(\omega_i\right)\right\rangle$ and correlation function $\left\langle E_r\left(\omega_i\right)E_r^*\left(\omega_j\right)\right\rangle$ is the same as it was used for description of an X-mode beam propagation in turbulent plasma (2.2.24), presence of a cut-off does not put limitation on this approach. In the strong phase modulation regime

$$\left\langle \delta\varphi^2\left(\omega_i\right)\right\rangle \gg 1 \tag{5.1.11}$$

the coherent part of the scattered field is suppressed $\langle E_r\rangle \ll E_i$ so the cross-correlation function can be written in the simplified form

$$CCF\left(x_{ci}-x_{cj}\right)=e^{i\left(\varphi_0\left(\omega_i\right)-\varphi_0\left(\omega_j\right)\right)}e^{-\frac{\left\langle \delta\varphi^2\left(\omega_i\right)\right\rangle}{2}-\frac{\left\langle \delta\varphi^2\left(\omega_j\right)\right\rangle}{2}+\left\langle \delta\varphi\left(\omega_i\right)\delta\varphi\left(\omega_j\right)\right\rangle} \tag{5.1.12}$$

Coherence of the phase variation describes the cross-correlation function (5.1.12), it can be written as

$$\begin{aligned}\left\langle \delta\varphi\left(\omega_i\right)\delta\varphi\left(\omega_j\right)\right\rangle = \frac{\omega_i^2\omega_j^2}{c^4}\int_0^{x_{ci}}\int_0^{x_{cj}}\frac{dx'}{k\left(x',\omega_i\right)}\frac{dx''}{k\left(x'',\omega_j\right)} \times \\ \frac{\delta\tilde{n}^2\left(\left(x'+x''\right)/2\right)}{n_{ci}n_{cj}}CCF_{\delta n}\left(x'-x''\right)\end{aligned} \tag{5.1.13}$$

where the turbulence amplitude $\delta\tilde{n}$ and the turbulence cross-correlation function $CCF_{\delta n}$ are defined according to the averaging procedure

$$\left\langle \delta n\left(x'\right)\delta n\left(x''\right)\right\rangle = \delta\tilde{n}\left(\left(x'+x''\right)/2\right)CCF_{\delta n}\left(x'-x''\right) \tag{5.1.14}$$

To evaluate (5.1.13) we will consider a linear density profile $n\left(x\right)=n_{ci}\frac{x}{x_{ci}}$ and homogeneous turbulence amplitude $\delta\tilde{n}$, also we will express the turbulence cross-correlation function $CCF_{\delta n}$ via its turbulence spectrum $\tilde{n}_{q_x}^2$ as

$$CCF_{\delta n}\left(x\right)=\int\frac{dq_x}{2\pi}\tilde{n}_{q_x}^2e^{iq_xx} \tag{5.1.15}$$

then the following expression can be obtained

$$\begin{aligned}\left\langle \delta\varphi\left(\omega_i\right)\delta\varphi\left(\omega_j\right)\right\rangle = 4\frac{\omega_i\omega_j}{c^2}\frac{\delta\tilde{n}^2}{n_{ci}n_{cj}}\sqrt{x_{ci}x_{cj}}\int\frac{dq_x}{2\pi}\frac{\tilde{n}_{q_x}^2}{\left|q_x\right|}e^{iq_x\left(x_{ci}-x_{cj}\right)} \times \\ \int_0^{\sqrt{\left|q_x\right|x_{ci}}}ds'e^{-is'^2}\int_0^{\sqrt{\left|q_x\right|x_{cj}}}ds''e^{is''^2}\end{aligned} \tag{5.1.16}$$

In the case of the Gaussian turbulence spectrum given by the expression

$$\tilde{n}_{q_x}^2=\sqrt{\pi}l_{cx}e^{-\frac{l_{cx}^2q_x^2}{4}} \tag{5.1.17}$$

the averaged phase variation squared $\left\langle \delta\varphi^2\left(\omega_i\right)\right\rangle$ is given by the following expression

$$\left\langle \delta\varphi^2\left(\omega_i\right)\right\rangle \approx \sqrt{\pi}\frac{\omega_i^2}{c^2}\frac{\delta\tilde{n}^2}{n_{ci}^2}x_{ci}l_{cx}\left(Ln\left(\frac{x_{ci}}{l_{cx}}\right)-\gamma_E\right) \tag{5.1.18}$$

where $\gamma_E \approx 0.577$ is the Euler constant. In the case of an arbitrary turbulence spectrum, the average phase variation squared can be estimated with the logarithmic accuracy as

$$\left\langle \delta\varphi^2\left(\omega_i\right)\right\rangle \sim \frac{\omega_i^2}{c^2}\frac{\delta\tilde{n}^2}{n_{ci}^2}x_{ci}l_{cx}Ln\left(\frac{x_{ci}}{l_{cx}}\right) \tag{5.1.19}$$

where the turbulence radial correlation length is determined as $l_{cx} = \frac{1}{\sqrt{\pi}}\int dxCCF_{\delta n}\left(x\right)$.

According to (5.1.9) at high density perturbations level an extinction of the probing line in the reflected wave spectrum takes place and the CCF is not vanishing only in the region, where

$$\frac{\left\langle \delta\varphi^2\left(\omega_i\right)\right\rangle}{2} + \frac{\left\langle \delta\varphi^2\left(\omega_j\right)\right\rangle}{2} - \left\langle \delta\varphi\left(\omega_i\right)\delta\varphi\left(\omega_j\right)\right\rangle \leqslant 1 \tag{5.1.20}$$

If the condition (5.1.11) holds, the inequality (5.1.20) can be only fulfilled for $\left|x_{ci} - x_{cj}\right| \ll l_{cx}$. In this parameter region we obtain the left hand side of (5.1.20) in the form of a Taylor series by decomposition of $e^{iq_x\left(x_{ci}-x_{cj}\right)}$ up to quadratic terms (first non-vanishing contribution, assuming a symmetric turbulence spectrum $\tilde{n}_{q_x}^2 = \tilde{n}_{-q_x}^2$) in (5.1.16), then the following expression is obtained

$$-\frac{\left\langle \delta\varphi^2\left(\omega_i\right)\right\rangle}{2} - \frac{\left\langle \delta\varphi^2\left(\omega_j\right)\right\rangle}{2} + \left\langle \delta\varphi\left(\omega_i\right)\delta\varphi\left(\omega_j\right)\right\rangle = -\frac{\left(x_{ci} - x_{cj}\right)^2}{l_{ceff}^2} \tag{5.1.21}$$

where l_{ceff} is the effective correlation length of the signal, it is given by the following expression

$$l_{ceff} = \left(\frac{\omega_i^2 x_{ci}}{4c^2}\frac{\delta\tilde{n}^2}{n_{ci}^2}\int dq_x\left|q_x\right|\tilde{n}_{q_x}^2\right)^{-1/2} \tag{5.1.22}$$

in the case of the Gaussian turbulence spectrum (5.1.17) the effective correlation length has the following form

$$l_{ceff} = \pi^{-1/4}\frac{c}{\omega_i}\frac{n_{ci}}{\delta\tilde{n}}\sqrt{\frac{l_{cx}}{x_{ci}}} \tag{5.1.23}$$

According to the accurate 2D analysis of the radial correlation reflectometry in the non-linear regime [31], when an emitter and receiver are placed close enough to each other, the signal cross-correlation function is described by the same expression

$$CCF\left(x_{ci} - x_{cj}\right) = e^{i\left(\varphi_0\left(\omega_i\right) - \varphi_0\left(\omega_j\right)\right)}e^{-\frac{\left(x_{ci}-x_{cj}\right)^2}{l_{ceff}^2}} \tag{5.1.24}$$

as in the 1D description demonstrated here, with the 1D normalized turbulence spectrum $\tilde{n}_{q_x}^2 = \int\frac{dq_y}{2\pi}\tilde{n}_{q_x,q_y}^2$, where $\tilde{n}_{q_x,q_y}$ is the 2D spectrum.

It is seen that the CCF measurement in the non-linear regime of the radial correlation reflectometry provides information on the combinations of the turbulence amplitude $\delta\tilde{n}$ and its radial correlation length l_{cx}, if the turbulence amplitude is known, the radial correlation length can be obtained.

5.2 Phase spectrum analysis

The phase variation spectrum in a RCR experiment can provide information about the turbulence amplitude due to connection between the phase variation spectrum and the turbulence spectrum. This method developed under the Born approximation was described in detail in [117]. It was demonstrated that even when the Born approximation is not fulfilled and the turbulence spectrum can not be reconstructed, the turbulence amplitude still can be determined. This effect was observed in 1D RCR simulations when the turbulence amplitude was big enough to break the Born approximation, but still small to consider the RCR to be deep in the non-linear regime [117]. We will consider the radial correlation reflectometry scheme with an O-mode probing wave in the 1D geometry. Also a linear density profile will be assumed in this model $n(x) = n_c \frac{x}{x_c}$. In the WKB approach the phase variation associated with the plasma density turbulence $\delta n(x)$ is given by the expression (5.1.7), the turbulence will be expressed via its Fourier transform

$$\delta n(x) = \int \frac{dq_x}{2\pi} n_{q_x} e^{iq_x x} \tag{5.2.1}$$

one should not confuse the turbulence Fourier transform n_{q_x} with the turbulence wave number spectrum $\tilde{n}_{q_x}$, introduced in (5.1.15) and defined without taking into account the turbulence amplitude. After substituting (5.2.1) into (5.1.7) the phase variation has the following form

$$\delta\varphi(x_c) = -\int \frac{dq_x}{2\pi} \left[\sqrt{\pi}\frac{\omega}{c} \frac{x_c^{1/2}}{|q_x|^{1/2}} \frac{\delta n_{q_x}}{n_c} e^{-i\frac{\pi}{4}\mathrm{sign}(q_x)} \mathrm{erf}\left(\sqrt{iq_x x_c}\right) \right] e^{iq_x x_c} \tag{5.2.2}$$

where the error function $\mathrm{erf}(x) = \frac{2}{\sqrt{\pi}} \int_0^x ds e^{-s^2}$. For the turbulence modes with $q_x > \frac{1}{x_c}$ the function $\mathrm{erf}\left(\sqrt{iq_x x_c}\right)$ is almost a constant and equals 1. We will assume that the dominant contribution to the phase variation comes from the turbulence modes with $q_x > \frac{1}{x_c}$, a characteristic turbulence wave number can be estimated as $q_x^* \sim \frac{1}{l_{cx}}$ so the following criterion is assumed

$$x_c \gg l_{cx} \tag{5.2.3}$$

Under this condition we can neglect the error function in (5.2.2) so this equation becomes a natural definition for the phase perturbation Fourier transform $\delta\varphi_{q_x}$. Then the relation between the turbulence spectrum and the phase perturbation spectrum by modulus squared is following

$$\left\langle |\delta\varphi_{q_x}|^2 \right\rangle = \pi \frac{\omega_i^2}{c^2} \frac{x_{ci}}{n_{ci}^2} \frac{1}{|q_x|} \left\langle |n_{q_x}|^2 \right\rangle \tag{5.2.4}$$

where $\langle ... \rangle$ is the statistical averaging procedure. This relation between the turbulence and phase perturbations spectra was obtained under the Born approximation for the first time in [116] and analyzed in [117]. According to (5.2.4) measurements of the phase perturbation wave number spectrum provides information on the turbulence spectrum and the turbulence amplitude.

In a RCR experiment plasma is probed with multiple frequencies (or the frequency sweeping is used) [117], then we have a set of N_ω cut-off positions from its minimal to maximal value

$\{x_{c_{min}} : x_{c_{max}}\}$, corresponding to the probing frequencies rage $\{\omega_{min} : \omega_{max}\}$. A set of N frequency sweep samples is needed for the following statistical analysis procedure. The phase perturbation can be evaluated for each cut-off position x_{ci} as

$$\delta\varphi\left(x_{ci}\right) = \varphi\left(x_{ci}\right) - \left\langle \varphi\left(x_{ci}\right)\right\rangle_N \tag{5.2.5}$$

where $\varphi\left(x_{ci}\right)$ is the total phase of a reflected wave with the frequency ω_i, $\left\langle \varphi\left(x_{cj}\right)\right\rangle_N$ is the statistically average phase due to the wave propagation to the cut-off position and back, assuming uncorrelated samples and steady state plasma conditions during the measurement of the N samples.

The two assumptions for the acquisition time are implied in the described procedure of the reflected wave phase analysis. The assumption of independent samples implies that the correlation time of the density fluctuations must be smaller than the time between two consecutive sweeps. For micro-turbulence measurements, this condition is satisfied for a repetition rate lower than 100 kHz because the correlation of the micro-turbulence is typically of 10 μs in tokamak plasmas. The second assumption of stationary plasma means that the averaged plasma parameters, especially the density profile, should stay constant during the acquisition time of the N sweeps. Due to this condition the MHD activity can locally perturb the results and must be taken into account for their interpretation.

The phase perturbation wave number spectrum is given by the discrete Fourier transform

$$\delta\varphi_{q_x} = \tilde{F}\left[\delta\varphi\left(x_c\right)\right] \tag{5.2.6}$$

But, as normally the sampling is made with a regular frequency step the cut-off positions are irregularly spaced. The use of the Fourier transform needs a constant radial step, this point is essential. So the phase $\delta\varphi\left(x_c\right)$ re-sampling on a regular mesh has to be performed.

The phase spectrum wave number resolution is determined by the cut-off positions sampling as

$$q_{x_{min}} = \frac{2\pi}{R} \tag{5.2.7}$$

where the probed radial window $R = x_{c_{max}} - x_{c_{min}}$, the maximal resolved wave number is given by

$$q_{x_{max}} = \frac{2\pi}{\Delta x_c} \tag{5.2.8}$$

where $\Delta x_c = \frac{x_{c_{max}} - x_{c_{min}}}{N_\omega}$ is the cut-off position step after the cut-offs re-sampling. Assuming a monotonous plasma density profile the maximal wave number probed in the radial window R is $k\left(x_{c_{min}}, \omega_{max}\right)$ (5.1.3) so according to the Bragg's rule the maximal resolved wave number of the phase perturbations spectrum in the selected window R is limited by

$$q_{x_{cut}} = 2k\left(x_{c_{min}}, \omega_{max}\right) \tag{5.2.9}$$

In the strong phase modulation regime the small-angle scattering provides significant contribution to the phase spectrum, but the highest resolved wave number is still determined by the Bragg's backscattering rule as well as in the weak turbulence regime, described in the framework of the Born approximation. From the Bragg's relation the q_x spectrum component of the density fluctuations located between $\{x_{c_{min}} : x_{c_{max}}\}$ and having a wave number larger than $q_{x_{cut}}$ can not be probed within the frequency range $\{\omega_{min} : \omega_{max}\}$. But the phase fluctuation components with $q_x > q_{x_{cut}}$ are necessarily induced by the density fluctuations located before $x_{c_{min}}$ in the plasma so the local spectra must be truncated at $q_{x_{cut}}$.

Finally the average over N sweep samples turbulence spectrum $\left\langle |n_{q_x}|^2 \right\rangle_N$ can be obtained from (5.2.4) and according to the Parseval's theorem

$$\sum_{i=1}^{N_\omega} \left\langle |\delta n\left(x_{c_i}\right)|^2 \right\rangle_N = \frac{1}{N_\omega} \sum_{i=1}^{N_\omega} \left\langle |n_{q_{xi}}|^2 \right\rangle_N \tag{5.2.10}$$

the RMS (over N sweep samples) turbulence amplitude, spatially averaged within the probed radial window R, can be evaluated

$$\left\langle \delta n^{rms} \right\rangle_R = \frac{1}{N_\omega} \sqrt{\sum_{q_x = q_{x_{min}}}^{q_{x_{cut}}} \left\langle |n_{q_x}|^2 \right\rangle_N} \tag{5.2.11}$$

Basically the Fourier analysis of the phase perturbation can be done within different radial windows $R_{ij} = x_{ci} - x_{cj}$ so the whole radial profile of the turbulence amplitude can be obtained. But the minimal resolved wave number q_{min} is increased in this approach (5.2.7) so the impact of the small-angle scattering, that is crucial in the non-linear reflectometry regime, is described worse. Also it should be mentioned that the turbulence amplitude is described in the 1D model in this approach, so far there is no a 2D theory for the phase perturbation analysis. To evaluate the 2D effects the numerical simulations are performed in the next section.

5.3 Numerical simulation of the RCR

The two techniques of the radial correlation reflectometry signal analysis were described in the previous sections. The phase perturbation spectrum analysis is not applicable for the wave number spectrum definition when the Born approximation is not fulfilled, however, the turbulence amplitude still can be determined from the Parceval's theorem. This effect was observed in 1D RCR simulations when the turbulence amplitude was big enough to break the Born approximation, but still small to consider the RCR to be deep in the non-linear regime [117]. The possibility of the turbulence amplitude definition in the strongly non-linear regime of the RCR is tested numerically in this section by means of the 2D RCR simulations. If this approach is correct far beyond the Born approximation, the phase perturbations spectrum provides information about the plasma turbulence amplitude in the non-linear regime of the radial correlation reflectometry. Then, assuming that the turbulence amplitude is known, the signal cross-correlation function describes the radial correlation length of the turbulence. In order to verify possibility of extraction the information about the both turbulence amplitude and its radial correlation length in a RCR experiment simultaneously by means of the two described methods the numerical simulations of the RCR experiment were fulfilled.

The simulations were performed in the 2D geometry by the full-wave code IPF-FD3D. A linear density profile (in the slab 2D model) was used in the simulations with plasma parameters similar to those encountered in experiments

$$n(x) = n_0 \frac{x}{L} \tag{5.3.1}$$

with $L = 16.2$ cm and the density amplitude at $x = L$ $n_0 = 1 \times 10^{14}\text{cm}^{-3}$. The probing frequency range $f \in \{50 : 80\}$ GHz with the frequency step $\Delta f = 100$ MHz. This frequency range corresponds to a set of the cut-off positions from $x_{c_{min}} = 4.9$ cm to $x_{c_{max}} = 12.4$ cm. The probing beam width is $\rho = 2$ cm in all the simulations except for one case, when the 2D geometry influence on the RCR simulation results is investigated, in this case the probing beam width $\rho = 5$ cm was also used.

The homogeneous turbulence was used in the simulations, its RMS amplitude relative level is defined as

$$A = \frac{\delta n^{rms}}{n\left(x_{c_{max}}\right)} \tag{5.3.2}$$

The Gaussian turbulence spectrum is used in most of the simulations in the regimes with different symmetric correlation lengths $l_c = 1$ cm and $l_c = 3$ cm. The choice of the Gaussian spectrum allows to control the turbulence parameters clearly, that is helpful for comparison of the numerical results with the analytics. The Gaussian turbulence spectrum (5.1.17) in the 2D model specifies the turbulence cross-correlation function

$$CCF_{\delta n}\left(x, y\right) = e^{-\frac{x^2+y^2}{l_c^2}} \tag{5.3.3}$$

A simulation with a realistic turbulence spectrum, based on the experimental measurements, was also performed. The turbulence radial correlation length l_c (the correlation length is also considered to be symmetric in the 2D space) in the realistic case is defined as

$$l_c = \frac{1}{\sqrt{\pi}} \int dx CCF_{\delta n}\left(x, 0\right) \tag{5.3.4}$$

where the turbulence cross-correlation functions $CCF_{\delta n}$ is defined by the averaging procedure (5.1.14). The simulations are performed for different turbulence amplitudes and different turbulence spectra, the results of the cross-correlation function and the phase spectrum analysis are averaged over 1000 random turbulence realizations.

In order to make the comparison between the analytics and results of the numerical modeling easier to interpret, the cross-correlation function (5.1.24) can be reduced to the following expression

$$CCF\left(x_{ci} - x_{cj}\right) = e^{-\frac{\left(x_{ci}-x_{cj}\right)^2}{l_{ceff}^2}} \tag{5.3.5}$$

The unperturbed phase $\varphi_0\left(\omega\right)$, associated with the wave propagation in plasma, can be defined according to the phase averaging procedure (5.2.5) and excluded from the registered signal. Thus, the simulated cross-correlation function can be fitted by a Gaussian function to determine the effective correlation length l_{ceff}, hence, assuming that the turbulence amplitude is known, the radial correlation length l_c of the turbulence. The reference point for building the cross-correlation function is $x_{c_{max}}$ so CCF is a function of $CCF\left(x_{c_{max}} - x\right)$ in all the figures presented further in this work.

5.3.1 RCR simulation with Gaussian turbulence spectrum, $l_c = 1$ cm

The first set of the radial correlation reflectometry 2D simulations is performed in the regime with the Gaussian turbulence spectrum with the correlation length $l_c = 1$ cm for different turbulence amplitudes from $A = 1.3\%$ to $A = 12.6\%$. The results of the signal cross-correlation function CCF numerical evaluation and its comparison to the predictions of the analytical model are demonstrated in the figure 55. By fitting the numerical CCF with a Gaussian function, the effective correlation length l_{ceff} is determined, its dependence on the average phase variation squared (5.1.18) is illustrated in the figure 56. Assuming that the turbulence amplitude is known, the radial correlation length l_c can be found from (5.1.23), the radial correlation length obtained numerically is depicted in the figure 57 for the simulated scenarios of the turbulence. It should be noted that the agreement between the analytical l_{ceff} and numerically evaluated effective correlation lengths is relatively good (see figure 56), whereas the discrepancy for the radial correlation length l_c much more pronounced 57. This is due to the fact that $l_c \propto l_{ceff}^2$ (5.1.23).

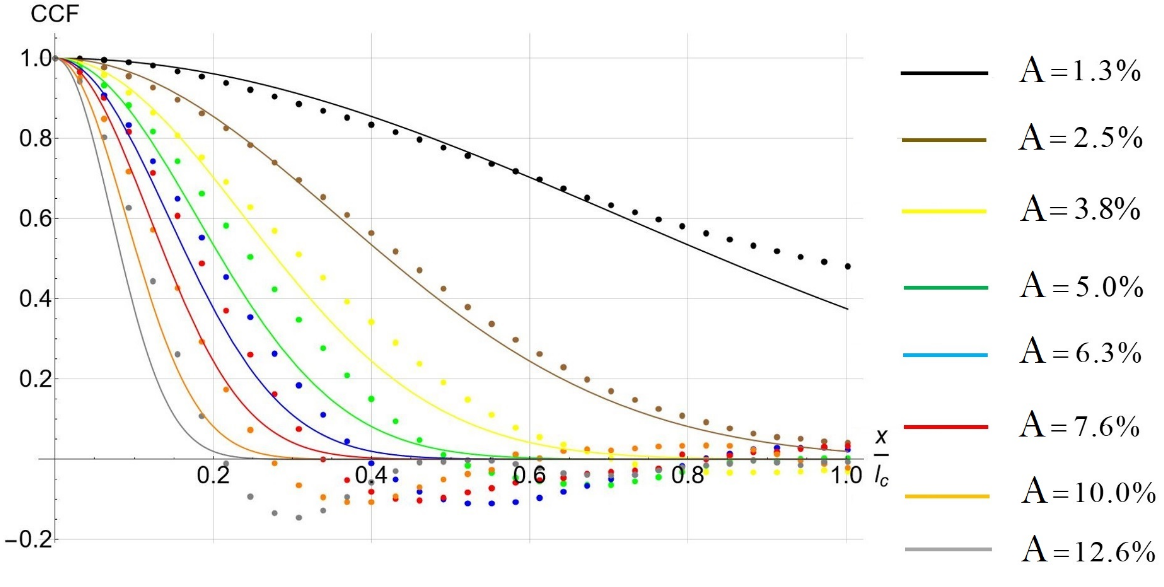

Figure 55: CCF for the different turbulence amplitudes A, the analytical cross-correlation function is represented by the solid curves, the dotted curves stand for the numerical results. The turbulence spectrum is Gaussian with $l_c = l$ cm, the probing beam width $\rho = 2$ cm.

There are two applicability criteria of the non-linear radial correlation reflectometry theory, that describes the signal cross-correlation function. The first criterion is the strong modulation

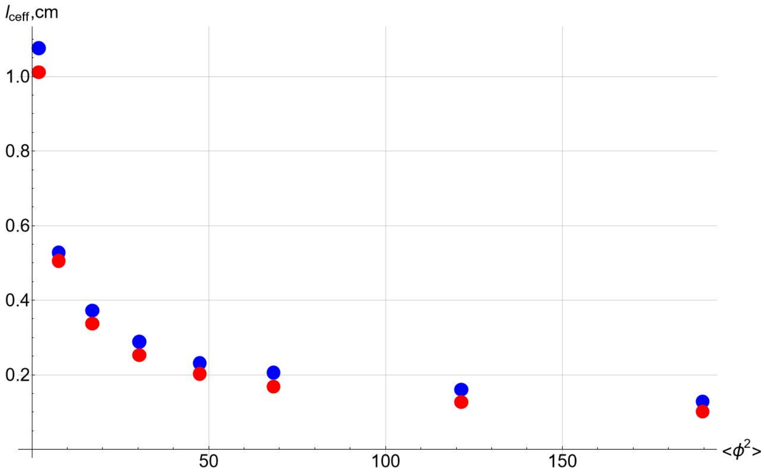

Figure 56: The signal correlation length l_{ceff} versus the average phase variation squared, the different points correspond to the different turbulence amplitudes, the turbulence amplitudes set is shown in the figure 55. The blue points represent the numerically evaluated l_{ceff}, the red ones are the analytical values. The turbulence spectrum is Gaussian with $l_c = l$ cm, the probing beam width $\rho = 2$ cm.

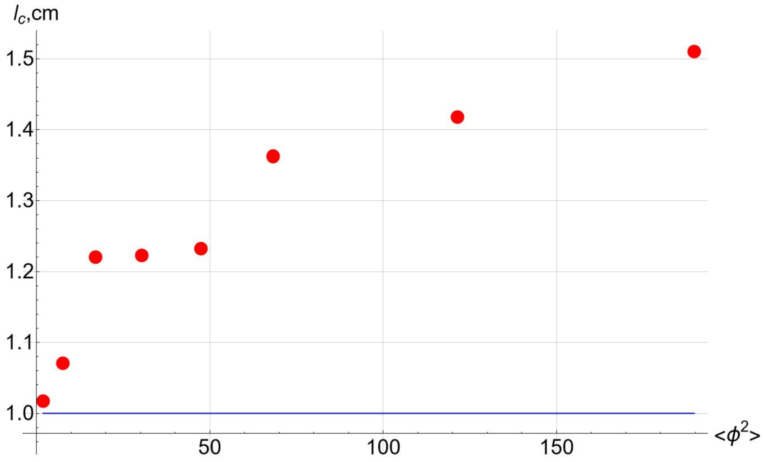

Figure 57: The turbulence radial correlation length l_c evaluated numerically versus the average phase variation squared, corresponding to the different turbulence amplitudes, the turbulence amplitudes set is shown in the figure 55. The solid line is the analytical value of the turbulence correlation length l_c in the tested turbulence regime. The turbulence spectrum is Gaussian with $l_c = l$ cm, the probing beam width $\rho = 2$ cm.

of the phase perturbations (5.1.11), that means that the turbulence amplitude A is assumed to be high enough. The second criterion is related to the RCR model with a single cut-off (5.1.5), that limits the maximal turbulence amplitude. The first point on the figure 56 demonstrates that the average phase variation is about 1 for the turbulence amplitude $A = 1.3\%$, this is the boarder of the applicability for the criterion (5.1.11). All the other points, corresponding to higher turbulence amplitude values, satisfy the strong phase modulation regime. It is also clearly seen from the figure 56 that in the strong phase modulation regime the following relation holds $l_{ceff} \ll l_c$, that was used in the CCF analytical description. In the framework of the simulation model of the radial correlation reflectometry $\frac{l_c}{x_{cmax}} \approx 0.08$, then the boarder of the applicability criterion for a single cut-off existence (5.1.5) is the turbulence amplitude value about $A = 8\%$. Thus, the simulated turbulence amplitude set that roughly satisfies the both criteria is following

$$A \in \{2.5, 3.8, 5.0, 6.3\}\% \tag{5.3.6}$$

This amplitude range corresponds to the points since the second to fifth on the figures 56, 57. The relative error of the radial correlation length l_c obtained in the turbulence amplitude range (5.3.6) is within 23%. The upper limit of the turbulence amplitude for the theory applicability explains the discrepancy increase clearly seen since the 6th point in the figure 57.

The next set of the numerical simulations was performed for the same Gaussian turbulence spectrum with $l_c = 1$ cm and the same range of the tested turbulence amplitudes as it is specified in the figure 55, but with a wider probing beam width $\rho = 5$ cm. Increase of the probing beam makes the radial correlation reflectometry experiment closer to the 1D model. As it was stated in the CCF analytical description section the 1D and 2D models of the RCR in the non-linear regime result in the same expression for the cross-correlation function. Nevertheless the 1D non-linear RCR theory was tested by the 1D numerical simulations in [114], the comparison between the 2D RCR numerical simulations and the non-linear theory is performed first in this work. Moreover the phase perturbations spectrum analytical analysis is considered in the framework of the 1D geometry, importance of the 2D effects for this analysis should be evaluated.

The results of the signal cross-correlation function CCF numerical evaluation in the simulations set with the different turbulence regimes (the turbulence amplitude range from $A = 1.3\%$ to $A = 12.6\%$) are demonstrated in the figure 58. The effective correlation length l_{ceff}, evaluated from fitting the simulated cross-correlation function is depicted in the figure 59. Finally the turbulence radial correlation length l_c, determined from the evaluated effective correlation length l_{ceff}, is shown in the figure 60. The applicability conditions in the simulations with a wider probing beam width remain the same as in the first set of the simulations with $\rho = 2$ cm so the analytical analysis is applicable for the same range of the tested turbulence amplitudes (5.3.6). Comparing the results of the simulations with the different probing beam width $\rho = 2$

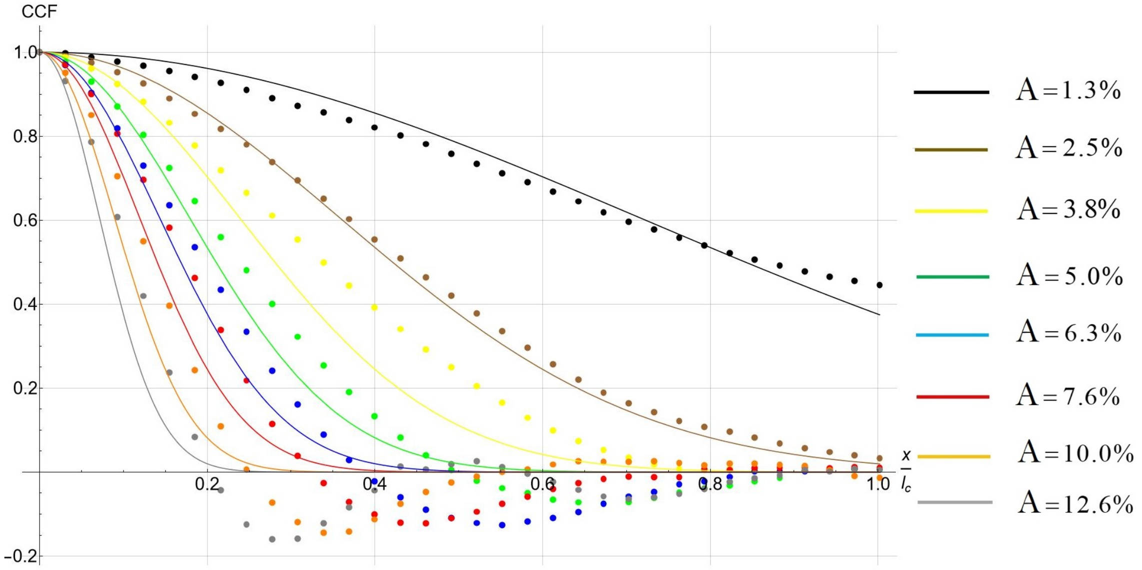

Figure 58: CCF for the different turbulence amplitudes A, the analytical cross-correlation function is represented by the solid curves, the dotted curves demonstrate the numerical results. The turbulence spectrum is Gaussian with $l_c = l$ cm, the probing beam width $\rho = 5$ cm.

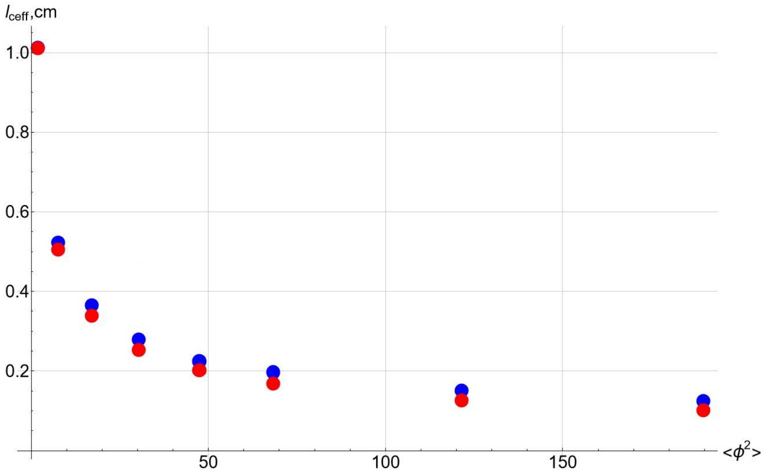

Figure 59: The effective correlation length l_{ceff} versus the average phase variation squared, the different points correspond to the different tested turbulence amplitudes, the corresponding turbulence amplitudes set is shown in the figure 58. The blue points represent the numerically evaluated l_{ceff}, the red ones are the analytical values. The turbulence spectrum is Gaussian with $l_c = l$ cm, the probing beam width $\rho = 5$ cm.

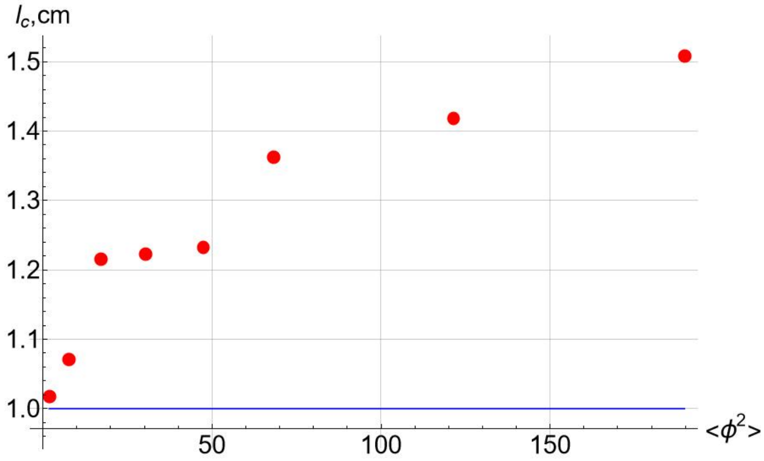

Figure 60: The turbulence radial correlation length l_c as a function of the average phase variation squared, corresponding to the different turbulence amplitudes, the corresponding turbulence amplitudes set is shown in the figure 58. The solid line is the tested value of the turbulence radial correlation length l_c. The turbulence spectrum is Gaussian with $l_c = l$ cm, the probing beam width $\rho = 5$ cm.

cm and $\rho = 5$ cm one can see that the signal cross-correlation function CCF, demonstrated in the figures 55 and 58, is almost the same in the two numerical experiments. Hence there is almost no difference in the the evaluated radial correlation length l_c depicted in the figure 57 and 60. The 2D theory of the radial correlation reflectometry in the non-linear regime has been verified using the simulations.

5.3.2 RCR simulation with Gaussian turbulence spectrum, $l_c = 3$ cm

The next set of the radial correlation reflectometry numerical simulations is performed in the regime with the Gaussian turbulence spectrum with higher radial correlation length $l_c = 3$ cm. The increase in the turbulence radial correlation length allows to extend the turbulence amplitude range where the non-linear RCR theory is applicable (5.1.5) The CCF for the different turbulence amplitudes is illustrated in the figure 61. The effective correlation length l_{ceff} and the radial correlation length of the turbulence l_c, obtained from the evaluated value

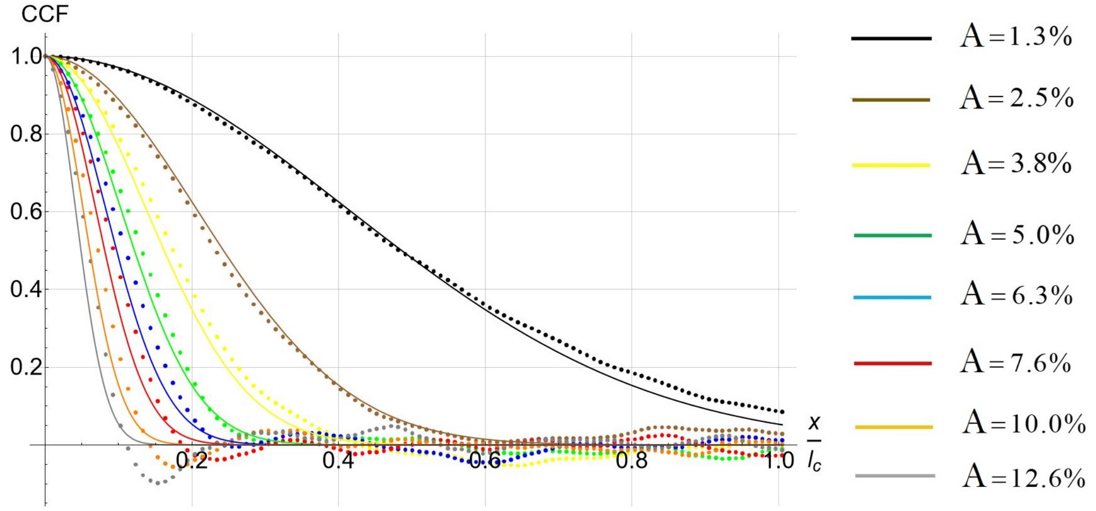

Figure 61: CCF for the different turbulence amplitudes A, the analytical cross-correlation function is represented by the solid curves, the dotted curves stand for the numerical results. The turbulence spectrum is Gaussian with $l_c = 3$ cm, the probing beam width $\rho = 2$ cm.

l_{ceff}, are demonstrated in the figures 62 and 63 respectively. According to the simulated RCR

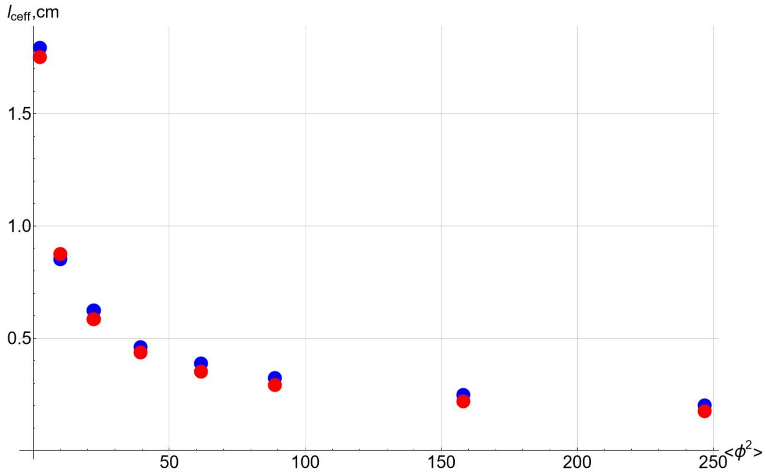

Figure 62: The signal correlation length l_{ceff} versus the average phase variation squared, the different points correspond to the different turbulence amplitudes. The blue points represent the results of the CCF fitting by the exponential function l_{ceff}, the red ones are the analytical values. The turbulence spectrum is Gaussian with $l_c = 3$ cm, the probing beam width $\rho = 2$ cm.

model $\frac{l_c}{x_{cmax}} \approx 0.24$, then the turbulence amplitude limit, restricting the non-linear RCR theory applicability (5.1.5), is about $A \approx 24\%$. Also it should be noted that even for the first point on the figure 62, corresponding to the turbulence amplitude $A = 1.3\%$ and the average phase modulation squared $\langle \delta\varphi^2 \rangle \approx 2.5$, the signal correlation length l_{ceff} is about two times smaller than the turbulence correlation length l_c, signifying that the RCR is almost in the non-linear regime (though the formal criterion is $\langle \delta\varphi^2 \rangle \gg 1$). Thus all the simulated regimes with the different turbulence amplitudes can be described in the framework of the non-linear theory of the radial correlation reflectometry. The maximal relative error in the definition of the radial

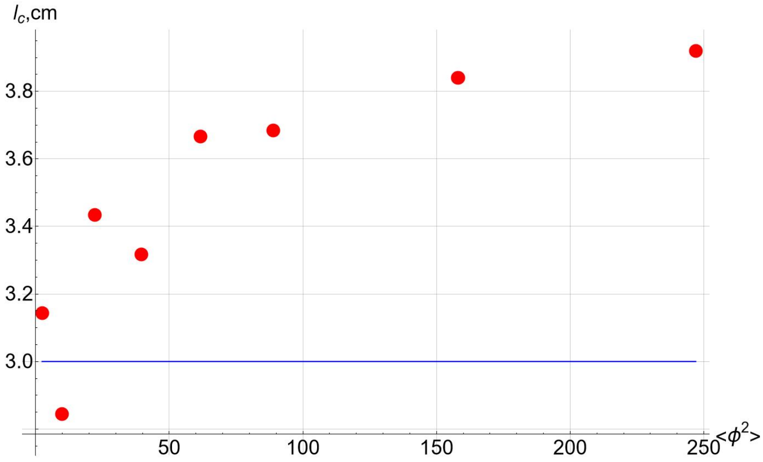

Figure 63: The turbulence radial correlation length l_c evaluated numerically versus the average phase variation squared, corresponding to the different turbulence amplitudes. The solid line is the simulated value of the turbulence correlation length l_c. The turbulence spectrum is Gaussian with $l_c = 3$ cm, the probing beam width $\rho = 2$ cm.

correlation length reaches about 30%.

5.3.3 RCR simulation with experimental turbulence spectrum

The analogous simulations of the RCR described above were performed in the same model, but with a turbulence spectrum, adapted from the experimental measurements at ASDEX Upgrade [73]. The spectrum $n_{q_\perp}$ is illustrated in the logarithmic scale in the figure 64, the spectrum is cut at $n_{q_{\perp 0}} = \frac{2\pi}{2a}$, where a represents the minor radius, ρ_i on the figure 64 is the ion Larmor radius, for the ITER parameters $a = 200$ cm, and $\rho_i \approx 0.3$ cm. The radial correlation length of the turbulence l_c, corresponding to the realistic turbulence spectrum and given by the definition (5.3.4), constitutes about 0.75 cm.

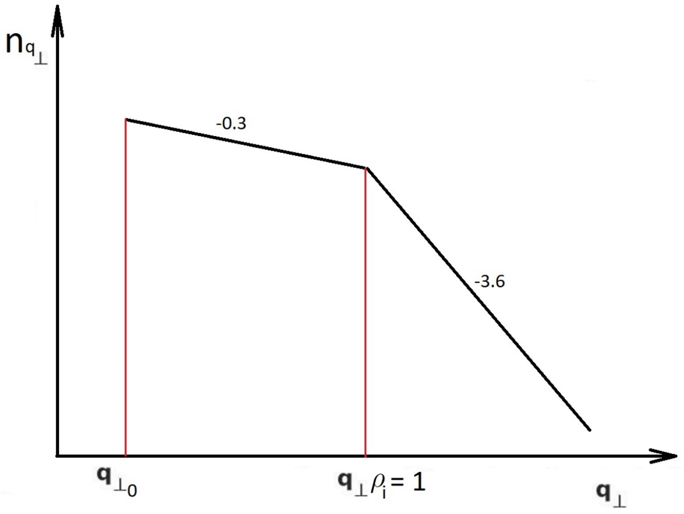

Figure 64: The turbulence spectrum adapted from the experimental measurements at ASDEX Upgrade. The model spectrum is in logarithmic scale, the spectrum is cut at $q_{\perp 0}$.

The cross-correlation function CCF evaluated for the turbulence regime with the experimental spectrum $n_{q_\perp}$ is demonstrated in the figure 65 for the different turbulence amplitudes A. The effective correlation length l_{ceff}, defined from fitting the simulated CCF, is depicted

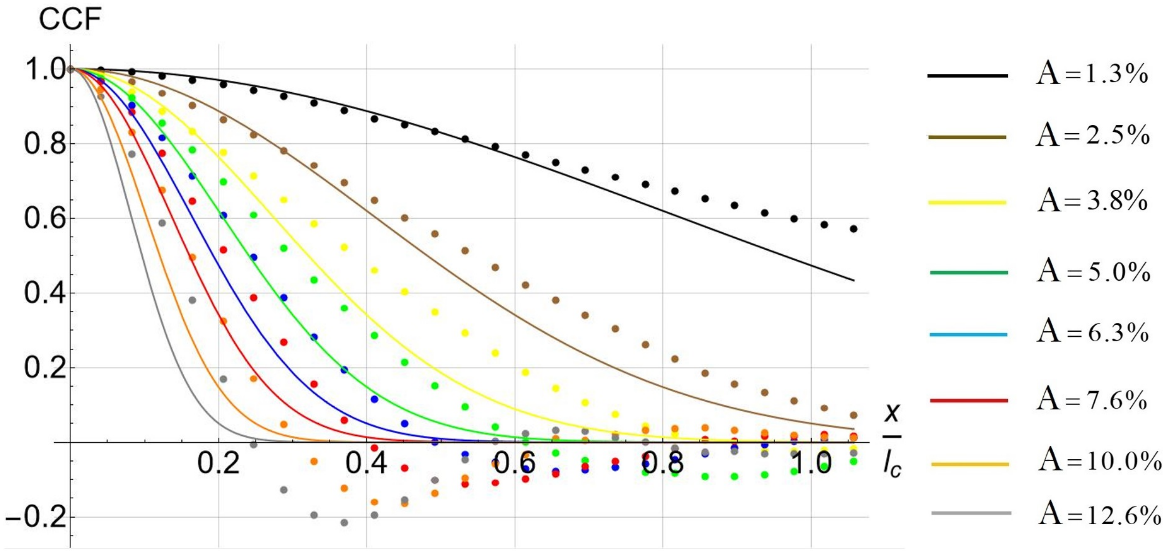

Figure 65: CCF for the different turbulence amplitudes A, the analytical cross-correlation function is represented by the solid curves, the dotted curves stand for the numerical results. The turbulence spectrum is adapted from the experimental measurements at ASDEX Upgrade, the probing beam width $\rho = 2$ cm.

in the figure 66. To obtain the turbulence radial correlation length l_c from l_{ceff} the relation (5.1.23) is used, thought it was derived for the Gaussian turbulence spectrum. The effective correlation length l_{ceff} in the case of an arbitrary turbulence spectrum is given by the expression (5.1.22), but to obtain the turbulence radial correlation length l_c the normalized turbulence spectrum $\tilde{n}^2_{q_x}$ has to be described with a single parameter l_c. Since the turbulence spectrum in the considered model is described with two factors, which describe the wave number spectrum behavior before the knee position $q_\perp \rho_i = 1$ and after it (factors -0.3 and -3.6 in the figure 64), and it also depends on the the ion temperature and the tokamak size a, characterising of the spectrum with a single parameter l_c is not possible. So the approximation base on the Gaussian

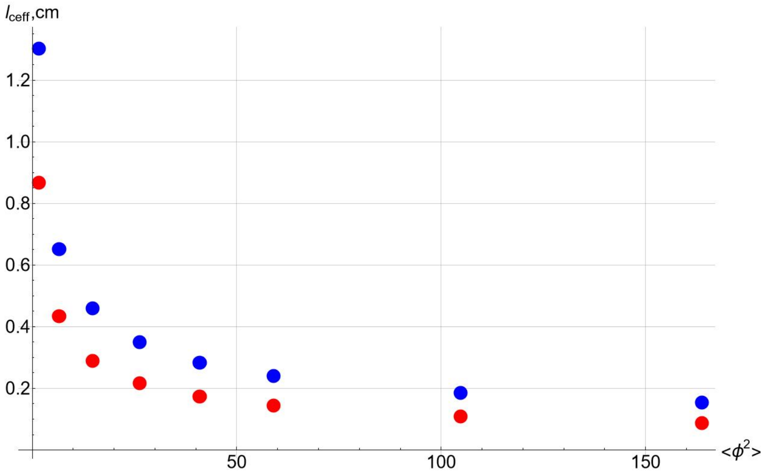

Figure 66: The signal correlation length l_{ceff} versus the average phase variation squared, the different points correspond to the different turbulence amplitudes, the turbulence amplitudes set is shown in the figure 65. The blue points represent the numerically evaluated l_{ceff}, the red ones are the analytical values. The turbulence spectrum is adapted from the experimental measurements at ASDEX Upgrade, $l_c \approx 0.75$ cm, the probing beam width $\rho = 2$ cm.

turbulence spectrum (5.1.23) is used for evaluation the turbulence radial correlation length l_c, the results of its evaluation are demonstrated in the figure 67. The significant discrepancy between the tested turbulence radial correlation length l_c and the numerically evaluated values is seen, the relative error ranges from about 24% at the low turbulence amplitude value up to about 73% for the highest tested turbulence level. The pronounce discrepancy is also observed for l_{ceff} in the figure 66, the numerically evaluated values for l_{ceff} are also significantly bigger than the theory predicts (5.1.22), that means that the variance is not related to the Gaussian spectrum interpretative model used for l_c definition.

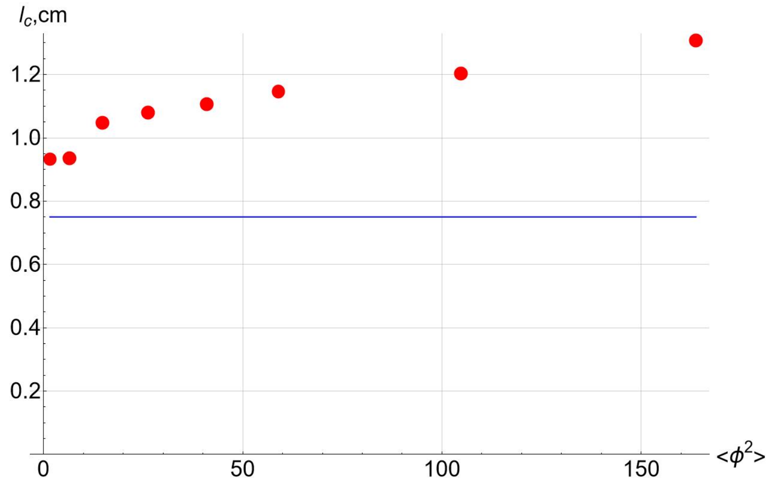

Figure 67: The turbulence radial correlation length l_c evaluated numerically versus the average phase variation squared, corresponding to the different turbulence amplitudes, the turbulence amplitudes set is shown in the figure 65. The solid line is the analytical value of the turbulence radial correlation length $l_c \approx 0.75$, evaluated according to (5.3.4) in the tested regime of the turbulence based on the experimental measurements. The probing beam width $\rho = 2$ cm.

According to the applicability criteria of the RCR non-linear theory ((5.1.11) and (5.1.5)), the first tested turbulence amplitude $A = 1.3\%$ corresponds to $\langle \delta\varphi^2 \rangle \approx 1.6$ so the reflectometry is not deep in the non-linear regime, the criterion (5.1.5) also sets the upper limit for the turbulence amplitude. For $l_c \approx 0.75$ cm, the turbulence amplitude is restricted by the value $A \approx 0.6\%$ (this is the boarder of the applicability criterion (5.1.5), the tractable in terms of the theory turbulence amplitudes should be much smaller), that explains the growing variance between the simulated turbulence radial correlation length l_c and the evaluated values starting since the fifth point in the figure 67. Nevertheless, even for the smaller amplitudes A the relative error for l_c is within 43%, it should be mentioned that the WKB approach, used for the CCF analysis, also works well only for the turbulence components with long wavelength. This fact is consistent with the results of the CCF simulations in the tested turbulence regimes. Namely the consistency (in terms of the relative match between the theory and simulations) is the best for the simulations with the Gaussian turbulence spectrum possessing $l_c = 3$ cm and it is the worst for the simulations with the realistic turbulence spectrum with $l_c = 0.75$ cm.

5.3.4 Turbulence level evaluation

The turbulence amplitude can be defined from phase spectrum analysis according to the equation (5.2.11). We used the homogeneous turbulence distribution in the described radial correlation reflectometry simulations, then the average within the radial window $R = x_{c_{max}} -$

$x_{c_{min}}$ RMS turbulence amplitude should coincide with the tested values δn^{rms}. The tested analytical values of the turbulence amplitude, denoted as δn^{an}, are compared to the numerically evaluated values δn^{num} in the figure 68. It is seen that the phase spectrum analysis provides the information about the turbulence amplitude with maximal relative error about 30% in all the simulated turbulence regimes with different spectra and the turbulence amplitudes. The most significant discrepancy between δn^{num} and δn^{an} is observed in the regime with the high turbulence correlation length $l_c = 3$ cm. The possible reason of the pronounced variance is a relatively high (comparing to the other tested turbulence spectra) contribution of the turbulence modes with small wave numbers q_x to the phase variation (5.2.2). In the analytical description the error function assumed to be approximately equal to 1 in (5.2.2), but when the turbulence wave number spectrum is narrow enough, that is typical for high l_c, this assumption is no longer correct. Also it should be noted that the turbulence amplitude obtained from the phase spectrum analysis is almost the same in the two simulations with the Gaussian turbulence spectrum $l_c = 1$ cm and different probing beam width $\rho = 2$ cm and $\rho = 5$ cm. This signifies that the 2D effects does not play a big role in the phase analysis technique so the 1D description is correct for the phase spectrum analysis.

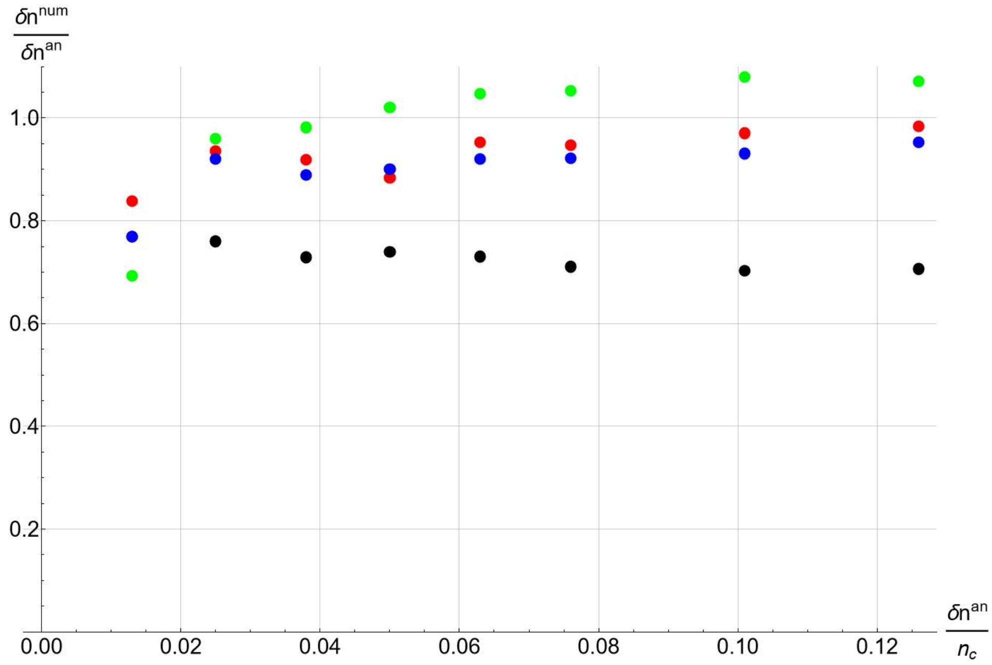

Figure 68: The relation between the turbulence amplitudes evaluated from the phase perturbations spectrum analysis δn^{num} and the simulated amplitudes δn^{an} versus the relative tested turbulence amplitudes $A = \frac{\delta n^{an}}{n_c}$. The blue and red colors represent the results for the simulations with the Gaussian turbulence spectrum with $l_c = 1$ cm for $\rho = 2$ cm and $\rho = 5$ cm respectively, the black color stands for the simulation with the Gaussian spectrum with $l_c = 3$ cm, and the green color correspond to the simulations set with the experimental-like turbulence spectrum.

5.4 Discussion on the radial correlation reflectometry simulations

The phase perturbations spectrum analysis can provide information about the turbulence amplitudes, the analytical description of this technique was developed under the Born approximation in [115] - [117]. In this work it is demonstrated that this method can be generalized far beyond the Born approximation criterion in the range of higher turbulence amplitudes.

Then we have a technique of the turbulence amplitude measurements in a RCR experiment for regimes with high turbulence amplitudes. This technique can be combined with the non-linear theory of the RCR which describes the signal cross-correlation function in the non-linear regime (5.1.11) and provides information about combination of the turbulence amplitude and its radial correlation length. The possibility of combining the two data analysis methods was verified by means of the 2D full-wave numerical simulation in this work. It is demonstrated that the turbulence amplitude and the turbulence radial correlation length can be measured simultaneously in the high-turbulence plasma scenario in a RCR experiment.

The numerical simulations demonstrated that the turbulence amplitude can be determined from the phase perturbations spectrum analysis with the relative error from few percents up to 30% depending on the turbulence spectrum regime, see figure 68. The effective correlation length l_{ceff} can be evaluated from fitting the cross-correlation function, then the radial correlation length of the turbulence l_c can be defined according to the analytical relation (5.1.23). The simulations showed that the l_c is normally overestimated for all the tested turbulence regimes and the best agreement between the non-linear RCR theory and the results of the modeling is observed for the simulations with high radial correlation length $l_c = 3$ cm. But even in this turbulence regime l_c can be overestimated by about $20 - 30\%$. In the simulated turbulence regimes with the relatively low turbulence radial correlation lengths $l_c \approx 0.75$ cm (which can be considered as realistic) the error in definition of l_c is significantly bigger (see figure 67). This is associated with the applicability limits of the non-linear RCR theory, mostly due to the single cut-off condition that can strongly restrict the applicable for analytical treatment turbulence amplitudes when the radial correlation length is small enough (5.1.5). In order to improve the interpretative model of the CCF analysis in RCR experiments a correcting procedure should be performed. Namely, the radial correlation length l_c, evaluated according to the described procedure of the CCF analysis, should be multiplied by a correcting factor. Assuming that the turbulence amplitude is known from the phase spectrum analysis, the correcting factor can be obtained from interpolation of the results of the simulations, performed for the realistic turbulence spectrum and demonstrated in the figure 67.

The both techniques of RCR data analysis were previously tested by 1D numerical modeling, the 2D simulations for testing and verifying the two techniques were performed in the present work first. It is demonstrated that the 2D geometrical effects do not play an important role for the data analysis, this fact was predicted by the 2D analytical analysis of the cross-correlation function in the non-linear regime, but it was not clear for the phase perturbation spectrum analysis.

6 Conclusions

The plasma turbulence plays a major role in the transport mechanisms, that the reasons why it is necessary to characterize the turbulence. It was known that the turbulence distorts and broadens on average a probing microwave beam, that influences on the physical parameters measured by means of the microwave diagnostics. The aim of this PhD work is to build improved interpretative models of the microwave diagnostics, takin into account the turbulence or other physical mechanisms able to influence the diagnostics measurements and the role of the turbulence on these physical mechanisms. During the improvements of the interpretative models it was clear that the turbulence characteristics are required to described the turbulence effects that is the reason why we propose a method to extend the extraction of the turbulence properties in the non-linear regime of the wave - density fluctuation interaction.

The microwave plasma diagnostics is a highly valuable instrument for characterizing the plasma parameters, properties of the plasma turbulence and distributions of the fast particles. Development of the interpretative models of the microwave diagnostics was the main object of study in this PhD thesis. The collective Thomson scattering and the radial correlation reflectometry were in the focus of the study, in particular the improved interpretative models are proposed for using in ITER. Many of the numerical simulations in this PhD work, performed for evaluating and verifying the results of the developed interpretative models, were performed for the plasma conditions similar to the parameters expected in ITER.

As it was discovered earlier the plasma turbulence can significantly distort a probing microwave beam, then the corresponding corrections in the interpretative models should be done. The microwave beam distortion in turbulent plasma was analysed analytically for an O-mode beam [44], an X-mode beam propagation in turbulent plasma was previously investigated numerically [45]. First of all the analytical treatment of the X-mode beam propagation in turbulence plasma was performed in the similar analytical approach used in [44]. The average beam width was expressed in terms the plasma parameters and the turbulence characteristics. Moreover the analytical expression for the probabilistic distribution function of the probing beam intensity in strongly turbulent plasma was proposed. This distribution function can be used for statistical analysis of the processes associated with a microwave beam energy exchange with plasma, such as the plasma heating or the parametric decay instability. The obtained analytical expressions were evaluated numerically and compared to the results of the full-wave 2D simulations, corresponding recommendation for the CTS experiments in ITER was done, namely the increase of the probing frequency can mitigate the effect of the probing beam broadening the in the turbulent plasma.

The collective Thomson scattering technique was analysed analytically with respect to the plasma turbulence. The turbulence was assumed to be located dominantly at the plasma edge, that is typical for tokamaks. Since a probing microwave beam possesses a finite angular wave number spectrum, the Bragg's scattering condition is fulfilled for a finite range of the wave numbers of the probing beam. Normally this effect is negligible and the main central wave number of the probing beam describes characteristics of the scattered radiation and the registered signal spectrum. But in the presence of the plasma turbulence the probing beam can be significantly broaden spatially and angularly, then the contribution from the different wave numbers to the scatted radiation can be significant. This effect was analysed explicitly in this work. Since not only the angular but also the spatial beam broadening takes place, the effect of the local plasma inhomogeneity can also change the results of the CTS measurements. This effect was also taken into account in the registered signal frequency spectrum. The effect of the probing beam distortion due to the edge plasma turbulence results in replacement of the fluctuation wave number spectrum $S_{nn}\left(\omega, \mathbf{q}\right)$ with the effective fluctuation spectrum $S_{nn}^{eff}\left(\omega, \mathbf{q}\right)$ in the expression for the registered signal. The effective fluctuation spectrum was described analytically as a function of the edge plasma turbulence characteristics, it was evaluated numerically and compared to the fluctuation spectrum for various turbulence regimes. It is demonstrated numerically that the difference between the spectra grows with increasing of the edge turbulence level. Various frequency domains demonstrate different relation between $S_{nn}^{eff}\left(\omega, \mathbf{q}\right)$ and $S_{nn}\left(\omega, \mathbf{q}\right)$. It should be noted that the various frequencies in the registered frequency spectrum describe the various characteristics such as the ion temperature at the frequencies bellow ~ 0.5 GHz and the fast particles distribution function at the higher frequencies. Influence of the plasma edge turbulence on the CTS spectrum is described analytically and numerically. An estimate of the possible error in the bulk ions temperature definition is provided, the relative error can be few or even tens percents depending on a turbulence scenario. The detailed analysis of the importance of the registered spectrum correction due to the edge turbulence is yet to be considered, strictly speaking it should be done for determination of all the plasma and the fast particles parameters that are theoretically possible to extract from the CTS measurements. Besides, sensitivity of the CTS spectra on the probing beam width was analysed. It is demonstrated that it is possible to mitigate the interference between the fluctuation modes, propagating perpendicularly to the magnetic field, in the registered spectrum by choosing a big enough probing beam width. This can be helpful to perform an almost perpendicular probing to the external magnetic field. The developed theoretical model was also verified by the 2D full-wave simulation of a probing beam scattering by a single mode of the fluctuations.

As the CTS uses a high power microwave beam, the probing can suffer of the low-threshold parametric decay instability. This instability deteriorates the high-power microwave diagnostics performance thought it is a more typical effect for the electron cyclotron plasma heating experiments. The analysis of the edge plasma turbulence influence on the low-threshold parametric decay instability was also performed in this PhD work. The existing theory of the low-threshold PDI describes the parametric decay of a smooth probing beam, it is not applicable for a probing beam significantly disturbed by the plasma turbulence. The numerical investigation of the parametric decay process with respect to the plasma turbulence was fulfilled. The parametric decay instability in the turbulent plasma was simulated and analysed in this work under the plasma conditions close to the experimental ones at TCV tokamak. The simulations were performed in the three different turbulence regimes, the tested regimes can be considered as the low turbulence amplitude, corresponding to small average phase variation of the pump beam squared $\langle \delta\varphi^2 \rangle \ll 1$, the high turbulence amplitude when $\langle \delta\varphi^2 \rangle \gg 1$ and the intermediate turbulence level $\langle \delta\phi^2 \rangle \approx 1$. The investigated characteristics of the PDI process are the instability growth rate, its saturation level, the excitation threshold and the anomalous energy absorbtion rate. The simulations demonstrated that the instability growth rate in the small and intermediate turbulence regimes remains almost the same whereas the high turbulence slightly reduces the growth rate. The saturation level of the UH wave energy is almost independent on the turbulence amplitude for the primary trapped UH wave and it decreases for the secondary trapped UH wave with growing the turbulence amplitude in the tested two-step PDI model. The both tendencies are in agreement with the analytical predictions if the PDI is considered in the field of the average pump beam. The average power threshold of the decay instability is just a little bit increased in the small and intermediate turbulence regimes whereas the threshold increase is about 50% for the high turbulence scenario. One of the most important in practice characteristics - the anomalous absorbtion rate is only slighted modified by the plasma turbulence. Its reduction constitutes only about 10% of the unperturbed value, and this mitigation remains the same for all the tested turbulence regimes. In general the presence of the plasma turbulence, well above the threshold, do not modify the PDI characteristics drastically. The physical picture of a PDI process in the turbulent plasma is the nonlinear interaction of the waves, when the pump beam shape is slightly disturbed or even split into several sub-beams with their local peaks smaller or higher than the unperturbed beam amplitude and the different local sub-beam width. There is no analytical model that can describe the PDI characteristics in such a disturbed beam, one of the possible ways to predict the PDI characteristics in the case of the pump modulated by the edge plasma turbulence is to consider the parametric decay in the field of the average pump beam, however keeping in mind that the numerical study has demonstrated that this approach overestimates the turbulence influence on the PDI threshold and growth rate.

The development of the RCR diagnostics data interpretation approach was the last task solved in this PhD thesis. The phase perturbations spectrum analysis in the RCR can provide the information about the plasma turbulence amplitude. This approach was developed under the Born approximation, in this PhD thesis it was tested and verified in deeply non-linear regime of the RCR. The non-linear theory of the RCR gives information about the combination of the turbulence parameters: the turbulence amplitude and the turbulence radial correlation length, the applicability of this method is based on the strong phase modulation due to the plasma turbulence. In this work it is demonstrated that it is possible to combine the two approaches of the RCR data analysis to extract the information about both the turbulence amplitude and its radial correlation length. The first step for integration of the two data analysis approaches was the demonstration that the phase spectrum analysis method can be generalized beyond the Born approximation criterion in the range of higher turbulence amplitudes. Then this technique can be combined with the non-linear theory or the RCR which describes the cross-correlation function CCF of the signal in the non-linear regime and provides information about the turbulence amplitude and the radial correlation length. The possibility of combining the two data analysis methods was verified by means of the 2D full-wave numerical simulation in this work. It is demonstrated that the turbulence amplitude and the turbulence radial correlation length can be measured simultaneously in the high-turbulence plasma scenario in a RCR experiment. In order to improve the interpretative model of the cross-correlation function analysis in the RCR experiments a correcting procedure is proposed.

7 Outlook

The further improvement and analysis of the microwave diagnostics interpretative models described in this thesis (the collective Thomson scattering and the radial correlation reflectometry) can be performed in future works. Also the passive diagnostics, based on the plasma microwave radiation measurements, can be analysed with respect to the plasma density turbulence in the similar way how it was done for CTS in the present PhD work. More simulations of the radial correlation reflectometry can be performed for the plasma parameters typical for different fusion machines. Then the correction procedure for the radial correlation length definition can be improved and used with better precision for the RCR measurements at different tokamaks.

The radial correlation reflectometry and the collective Thomson scattering were analysed and numerically simulated for the plasma parameters typical for ITER. But the simulations were performed in the different turbulence regimes, since there is no information about predictions for the turbulence in ITER. When the understanding of the possible turbulence scenarios in ITER appears, the RCR simulations with the actual turbulence spectra and its spatial distribution will allow to describe the interpretative model better with more accurate procedure of correcting the measured parameters of the turbulence. Also the effect of the plasma turbulence on the measured spectra in a CTS experiment will be possible to evaluate more accurately for ITER.

The radial correlation reflectometry and the collective Thomson scattering diagnostics can also be integrated. The proper interpretation of the bulk ions temperature and the fast particles distribution function requires the information about the edge plasma turbulence characteristics: the turbulence amplitude and the turbulence wave number spectrum (that can be connected to the turbulence correlation length for a given spectrum model). These characteristics can be measured by the RCR diagnostics locally and in a real-time regime.

The proposed method of the generalized data analysis for the RCR measurements should be verified in an experiment. Description of such an experiment is also an object of the future research.

8 Acknowledgements

This thesis embraces the results of my three years work, but it would not be possible without the assistance of a great number of people. I would like to thank all of them.

First of all I would like to express my gratitude to my research supervisors Professor Stephane Heuraux and Professor Evgeniy Gusakov. The quality of my planning and performing of a research work has significantly increased after these years due to their very useful advices and constructive critiques.

Professor Heuraux spent for me numerous hours with discussion of the physical mechanisms and effects behind the microwave diagnostics and peculiarities of the numerical simulations. I am very grateful for his willingness to help and patience during these discussions. Since France is a foreign country for me, Professor Heuraux helped me very much with the bureaucracy part and all the difficulties I encountered there.

I really grateful to Professor Gusakov for his guidance during this PhD work. Many times when I felt like my research work is stuck, after a discussion with Professor Gusakov the way how to proceed the work was clear, it always inspired me. This was possible because of his profound knowledge and neat methodologies of a scientific research that I am looking up to.

I would like to thank Oleg Krutkin who helped me a lot by teaching me how to work with the numerical full-wave code that I used for the simulations. Also I am grateful to Natalia Teplova and Oleg Krutkin for their advices about the peculiarities of living in France.

Also I would like express my gratitude to Georgiy Zadvitskiy and Dr Carsten Lechte for their assistance with use of the full-wave numerical code.

I would like to thank Dr Alexey Popov, who was my supervisor for my master's thesis, for his assistance and very useful discussions during this PhD work.

Also I would like to thank the French Embassy in Moscow for awarding me with Vernadsky scholarship which was an important source of funding that allowed to perform my joint PhD project.

9 References

[1] bp "Statistical Review of World Energy" 2022, www.bp.com

[2] IEA "Global Energy Review" 2021, www.iea.org/reports/global-energy-review-2021

[3] "summary of the ITER final design report", printed by the IAEA in Vienna 2001, www.iaea.org/publications/6442/summary-of-the-iter-final-design-report

[4] M Kikuchi, K Lackner and M Q Tran "Fusion Physics" 2012 International Atomic Energy Agency, www.iaea.org/books

[5] J Wesson, D J Campbell "Tokamaks" 2004 the 3rd edition, Clarendon Press, Oxford, England

[6] J D Lawson 1957 *Proc. Phys. Soc.* **B** 70 6

[7] L Spitzer Jr, "A Proposed Stellarator", PM-S-l, USAEC NYO-993, 1951

[8] I E Tamm «Theory of the magnetic thermonuclear reactor, part 1» 1959 *Plasma Physics and the Problem of Controlled Thermonuclear Reactions* (transl), New York Pergamon, pp 3–19

[9] A D Sakharov «Theory of the magnetic thermonuclear reactor, part 2» 1959 *Plasma Physics and the Problem of Controlled Thermonuclear Reactions* (transl), New York Pergamon, pp 20–30

[10] I E Tamm «Theory of the magnetic thermonuclear reactor, part 1» 1959 *Plasma Physics and the Problem of Controlled Thermonuclear Reactions* (transl), New York Pergamon, pp 31–41

[11] V P Smirnov 2010 *Nucl. Fusion* **50** 014003

[12] S Li, H Jiang, Z Ren, C Xu S Li et al "Optimal Tracking for a Divergent-Type Parabolic PDE System in Current Profile Control" 2014 *Abstract and Applied Analysis*

[13] A J Wootton, B A Carreras, H Matsumoto et al "Fluctuations and anomalous transport in tokamaks" 1990 *Physics of Fluids B: Plasma Physics* **2** 2879

[14] P H Diamond et al "Zonal flows in plasma — a review" 2005 *Plasma Phys. Control. Fusion* **47** R35

[15] www.iter.org

[16] R Aymar, P Barabaschi and Y Shimomura "The ITER design" 2002 *Plasma Phys. Control. Fusion* **44** 519

[17] G D Conway "Turbulence measurements in fusion plasmas" 2008 *Plasma Phys. Control. Fusion* **50** 124026

[18] R Cano and A Cavallo 1980 *Proceedings of the 5th International Conference on Infrared and Millimeter Waves*

[19] J C Giacalone, R Sabot, F Clairet, C Bottereau and D Molina “Measurement of the density of magnetized fusion plasma using microwave reflectometry” 2009 *International Journal of Microwave and Wireless Technologies* **1(6)** 505-509

[20] H Bottolier-Curtet, G Ichtchenko “Microwave reflectometry with the extraordinary mode on tokamaks: Determination of the electron density profile of Petula-B” 1987 *Rev. Sci. Instrum.* **58** 539–546

[21] I Hutchinson “Principles of Plasma Diagnostics” second edition 2002 Cambridge University Press

[22] E Mazzucato and R Nazikian “Radial scale length of turbulent fluctuations in the main core of TFTR plasmas” 1993 *Phys. Rev. Lett.* **71** 1840

[23] B B Afeyant, A E Cbout and B I Cohent “The scattering phase shift due to Bragg resonance in one-dimensionalfluctuation reflectometry” 1995 *Plasma Phys. Control. Pusion* **37** 315-327

[24] E Z Gusakov and A Yu Surkov “Spatial and wave number resolution of Doppler reflectometry” 2004 *Plasma Phys. Control. Fusion* **46** 1143

[25] E Z Gusakov, A V Surkov and A Yu Popov “Multiple scattering effect in Doppler reflectometry” 2005 *Plasma Phys. Control. Fusion* **47** 959

[26] A Yu Popov, E Z Gusakov “Spatial Resolution of Poloidal Correlation Reflectometry” 2005 *32nd EPS Conference on Plasma Phys.* Vol. **29C** P-1.088

[27] E Z Gusakov and A Yu Popov “Measurements localization in poloidal correlation reflectometry” 2006 *Nucl. Fusion* **46** 829–835

[28] X L Zou, L Laurent and J M Rax “Scattering of an electromagnetic wave in a plasma close to a cut-off layer. Application to fluctuation measurements” 1991 *Plasma Phys. Control. Fusion* **33** 903 - 918

[29] I H Hutchinson “One-dimensional full-wave analysis of reflectometry sensitivity and correlations” 1992 *Plasma Phys. Control. Fusion* **34** 1225

[30] E Z Gusakov and A Yu Popov “Non-linear theory of fluctuation reflectometry” 2002 *Plasma Phys. Control. Fusion* **44** 2327-2337

[31] E Z Gusakov and A Yu Popov “Two-dimensional non-linear theory of radial correlation reflectometry” 2004 *Plasma Phys. Control. Fusion* **46** 1393-1408

[32] S B Korsholm, H Bindslev, V Furtula, F Leipold, F Meo, P K Michelsen, D Moseev, S K Nielsen, M Salewski, M Stejner 2010 *Nuclear Instruments and Methods in Physics Research* **A 623** 677–680

[33] E E Salpeter “Electron Density Fluctuations in a Plasma” 1960 *Phys. Rev.* **120** 1528

[34] S B Korsholm, B Gonçalves, H E Gutierrez, E Henriques, V Infante, T Jensen, M Jessen, E B Klinkby, A W Larsen, F Leipold, A Lopes, R Luis, V Naulin, S K Nielsen, E Nonbø, J

Rasmussen, M Salewski, M Stejner, A Taormina, A Vale, C Vidal, L Sanchez, R M Ballester and V Udintsev "Design and development of the ITER CTS diagnostic" 2019 *EPJ Web of Conferences* **203** 03002

[35] J Egedal, H Bindslev, R V Budny and P Woskov "Impact of beam ions on α-particle measurements by collective Thomson scattering in ITER" 2005 *Nucl. Fusion* **45** 191–200

[36] U Tartari, S Nowak, and G Ramponi "Perspectives of millimeter-wave collective Thomson scattering of confined alphas in ignited plasmas" 1996 *Review of Scientific Instruments* **67** 3847

[37] J Rasmussen, S K Nielsen, M Stejner, J Galdon-Quiroga, M Garcia-Munoz, B Geiger, A S Jacobsen1, F Jaulmes, S B Korsholm, N Lazanyi, F Leipold, F Ryter, M Salewski, M Schubert, J Stober, D Wagner, the ASDEX Upgrade Team and the EUROFusion MST1 Team "Collective Thomson scattering measurements of fast-ion transport due to sawtooth crashes in ASDEX Upgrade" 2016 *Nucl. Fusion* **56** 112014 9pp

[38] J Rasmussen, S K Nielsen, M Stejner, M Salewski, A S Jacobsen, S B Korsholm, F Leipold, F Meo, P K Michelsen, D Moseev, M Schubert, J Stober, G Tardini, D Wagner and the ASDEX Upgrade Team "Improved Collective Thomson Scattering measurements of fast ions at ASDEX Upgrade" arXiv:1310.2406v1 [physics.plasm-ph]

[39] M Salewski, S K Nielsen, H Bindslev, V Furtula, N N Gorelenkov, S B Korsholm, F Leipold, F Meo, P K Michelsen, D Moseev and M Stejner "On velocity space interrogation regions of fast-ion collective Thomson scattering at ITER" 2011 *Nucl. Fusion* **51** 083014

[40] S B Korsholm, F Leipold, B Goncalves et al "High power microwave diagnostic for the fusion energy experiment ITER" 2016 *41st International Conference on Infrared, Millimeter and Terahertz waves*,

[41] F Leuterer et al, 2003 *Nucl. Fusion* **43** 1329-1342

[42] H Zohm et al, 1999 *Nucl. Fusion* **39(5)** 577-580

[43] M Hirsch, E Holzhauer, J Baldzuhn, B Kurzan and B Scott, 2001 *Plasma Phys. Control. Fusion* **43** 1641-1660

[44] E V Sysoeva, F da Silva, E Z Gusakov, S Heuraux and A.Yu. Popov, 2015 *Nucl. Fusion* **55(3)** 033016

[45] N Bertelli , G J Kramer and E J Valeo, 2019 *Plasma Phys. Control. Fusion* **61** 105018

[46] A Snicker et al, 2018 *Plasma Phys. Control. Fusion* **60** 014020

[47] E Poli et al, 2015 *Nucl. Fusion* **55** 013023

[48] A Snicker et al, 2018 *Nucl. Fusion* **58** 016002

[49] R J La Haye, 2006 *Phys. Plasmas*, **13** 055501

[50] O Sauter et al., 2010 *Plasma Phys. Control. Fusion* **52** 025002

[51] N Bertelli et al., 2011 *Nucl. Fusion* **51** 103007

[52] M W Brookman, 2017 *EPJ Web of Conferences* **147** 03001

[53] O Chellaï et al., 2018 *Phys. Rev. Lett.* **120** 105001

[54] I Furno et al., 2015 *J. Plasma Phys.* **81** 345810301

[55] O Chellaï et al., 2017 *EPJ Web of Conferences* **157** 03008

[56] O Chellaï et al., 2019 *Plasma Phys. Control. Fusion* **61** 014001

[57] C Tsironis et al., 2009 *Phys. Plasmas*, **16** 112510

[58] H Weber et al., 2015 *EPJ Web of Conferences* **87** 01002

[59] A Köhn et al., 2008 *Plasma Phys. Control. Fusion* **50** 085018

[60] T R N Williams et al., 2014 *Plasma Phys. Control. Fusion* **56** 075010

[61] J M Santos, E Ricardo, F J da Silva, T Ribeiro, S Heuraux, A Silva "A 3D CAD model input pipeline for REFMUL3 full-wave FDTD 3D simulator" 2021 *Journal of Instrumentation* **16 (11)** C11013

[62] COMSOL Multiphysics Reference Manual, 2019 doc.comsol.com/5.5/doc/com.comsol.help.comsol/COMSOL_ReferenceManual.pdf

[63] V L Ginzburg "The propagation of electromagnetic waves in plasmas" 1964 Oxford Pergamon

[64] A D Piliya, *Proceedings of the 10th Conference on Phenomena in Ionized Gases*, Oxford, 1971, edited by Franklin R. N. (Donald Parsons & Co., Ltd., Oxford) 1971, p 320.

[65] A D Piliya "Threshold of decay instabilities in an inhomogeneous plasma" 1973 *JETP Letters* **17** 374-376

[66] A D Piliya "Nonstationary theory of decay instability in a weakly inhomogeneous plasma" 1973 *JETP* **64** 1237-1244

[67] M N Rosenbluth "Parametric Instabilities in Inhomogeneous Media" 1972 *Phys. Rev. Lett.* **29** 565

[68] B I Cohen, R H Cohen, W M Nevins, T D Rognlien "Theory of free-electron-laser heating and current drive in magnetized plasmas" 1991 *Rev. Mod. Phys.* **63** p. 949

[69] E Z Gusakov, A Yu Popov "Low-power-threshold parametric decay instabilities of powerful microwave beams in toroidal fusion devices" 2020 *Phys. Usp.* **63** 365

[70] A I Akhiezer, I A Akhiezer, R V Polovin, A G Sitenko, K N Stepanov "Plasma electrodynamics" 1974

[71] O Chellaï S Alberti, I Furno, T Goodman, O Maj, G Merlo, E Poli, P Ricci, F Riva, H Weber and the TCV Team "Millimeter-wave beam scattering and induced broadening by plasma turbulence in the TCV tokamak" 2021 *Nucl. Fusion* **61** 066011

[72] C Lechte et al, 2017 *Plasma Phys. Control. Fusion* **59** 075006

[73] T Happel, T Görler, P Hennequin, C Lechte, M Bernert, G D Conway, S J Freethy, C Honoré, J R Pinzón, U Stroth and The ASDEX Upgrade Team "Comparison of detailed experimental wavenumber spectra with gyrokinetic simulation aided by two-dimensional full-wave simulations" 2017 *Plasma Phys. Control. Fusion* **59** 054009

[74] P Hennequin, R Sabot, C Honoré, et al, 2004 *Plasma Phys. Control. Fusion* **46** B121

[75] A Medvedeva, 2017 "Experimental study of turbulence at the plasma edge of ASDEX Upgrade tokamak with an ultra-fast swept reflectometry" PhD theris TUM

[76] J Schirmer et al, 2007 *Plasma Phys. Control. Fusion* **49** 1019

[77] D Prisiazhniuk et al, 2018 *Plasma Phys. Control. Fusion* **60** 079602

[78] P Tretinnikov, E Gusakov and S Heuraux 2021 *Plasma Phys. and Control. Fusion* **63** 085003

[79] N Bertelli , G J Kramer and E J Valeo 2019 *Plasma Phys. and Control. Fusion* **61** 105018

[80] A Snicker et al 2018 *Plasma Phys. Control. Fusion* **60** 014020

[81] H Bindslev 1991 *Plasma Phys. Control. Fusion* **33** 1775

[82] H Bindslev 1993 *Plasma Phys. Control. Fusion* **35** 1615-1640

[83] R E Slusher and C M Surko 1980 *Phys. Fluids* **23** 472

[84] S M Rytov, Yu A Kravtsov, V I Tatarskii "Principles of Statistical Radiophysics" Vol. 3 (Berlin: Springer-Verlag, 1989)

[85] A D Piliya and A Yu Popov, 2002 *Plasma Phys. Control. Fusion* **44** 467–474

[86] J D Gaffey 1976 *Plasma Phys.* **16** 149

[87] L Vahala et al 1986 *Nucl. Fusion* **26** 51

[88] S K Nielsen et al 2008 *Phys. Review E* **77** 016407

[89] J Rasmussen et al 2019 *Nucl. Fusion* **59** 096051

[90] B I Cohen, R H Cohen, W M Nevins, T D Rognlien 1991 *Rev. Mod. Phys.* **63** 949

[91] D Strauss, G Aiello, R Bertizzolo, A Bruschi, N Casal, R Chavan, D Farina, L Figini et al "Nearing final design of the ITER EC H&CD Upper Launcher" 2019 *Fusion Engineering and Design* **146** 23-26

[92] E Westerhof, S K Nielsen, J W Oosterbeek, M Salewski, M R De Baar, W A Bongers, A Bürger, B A Hennen, S B Korsholm, F Leipold, D Moseev, M Stejner, D J Thoen and the TEXTOR Team 2009 *Phys. Rev. Lett.* **103**, 125001

[93] S K Nielsen, M Salewski, E Westerhof, W Bongers, S B Korsholm, F Leipold, J W Oosterbeek, D Moseev, M Stejner and the TEXTOR Team 2013 *Plasma Phys. and Control. Fusion* **55**, 115003

[94] S K Hansen, S K Nielsen, J Stober, J Rasmussen, M Stejner, M Hoelzl, T Jensen and the ASDEX Upgrade team 2020 *Nucl. Fusion* **60** 106008

[95] S K Hansen, A S Jacobsen, M Willensdorfer, S K Nielsen, J Stober, K Höfler, M Maraschek, R Fischer, M Dunne, the EURO fusion MST team and the ASDEX Upgrade team, 2021 *Plasma Phys. Control. Fusion* **63** 095002

[96] A Tancetti, S K Nielsen, J Rasmussen, E Z Gusakov, A Yu Popov, D Moseev, T Stange, M G Senstius, C Killer, M Vecsei, T Jensen, M Zanini, I Abramovic, M Stejner, G Anda, D Dunai, S Zoletnik, H Laqua 2022 *Nucl. Fusion* **62** 074003

[97] S Coda and for the TCV Team 2015 *Nucl. Fusion* **55** 104004

[98] B Zurro, A Baciero, V Tribaldos, M Liniers, A Cappa, A Lopez-Fraguas, D Jimenez-Rey, J M Fontdecaba and O Nekhaieva 2013 *Nucl. Fusion* **53** 083017

[99] M Martínez, B Zurro, A Baciero, D Jimenez-Rey and V Tribaldos 2018 *Plasma Phys. Controlled Fusion* **60** 025024

[100] Yu N Dnestrovskij, A V Danilov, A Yu Dnestrovskij, S E Lysenko, A V Melnikov, A R Nemets, M R Nurgaliev, G F Subbotin, N A Solovev, D Yu Sychugov and S V Cherkasov 2021 *Plasma Phys. Control. Fusion* **63** 055012

[101] A I Meshcheryakov, I Yu Vafin and I A Grishina 2020 *Plasma Phys. Rep.* **46** 1144

[102] E Z Gusakov, A Yu Popov and P V Tretinnikov 2019 *Nucl. Fusion* **59** 106040

[103] A Yu Popov, E Z Gusakov 2015 *Plasma Phys. Control. Fusion* **57** 025022

[104] A Yu Popov, E Z Gusakov 2016 *Europhys. Lett.* **116** 45002

[105] E Z Gusakov, A Yu Popov, A N Saveliev 2018 *Physics of Plasmas* **25** 062106

[106] M G Senstius, S K Nielsen and R G L Vann 2021 *Plasma Phys. Control. Fusion* **63** 065018

[107] M G Senstius, E Z Gusakov, A Yu Popov, S K Nielsen 2022 *Plasma Phys. Control. Fusion* **64** 115001

[108] M W Brookman, M E Austin, C C Petty, R J La Haye, K Barada, T L Rhodes, Z Yan, A Kohn, M B Thomas, J Leddy, and R G L Vann 2021 *Phys. Plasmas* **28** 042507

[109] E Z Gusakov and A Yu Popov and P V Tretinnikov 2019 *Plasma Phys. Control. Fusion* **61** 085008

[110] E Z Gusakov and A Yu Popov 2022 *Plasma Physics Reports* **48** 327–336

[111] E Z Gusakov and A Yu Popov 2021 *Plasma Phys. Control. Fusion* **63** 015016

[112] J Ruiz Ruiz et al "Interpreting radial correlation Doppler reflectometry using gyrokinetic simulations" 2022 *Plasma Phys. Control. Fusion* **64** 055019

[113] E Z Gusakov and B O Yakovlev 2002 *Plasma Phys. Control. Fusion* **44** 2525

[114] G Leclert, S Heuraux, E Z Gusakov, A Yu Popov, I Boucher and L Vermare "Full-wave test of the radial correlation reflectometry analytical theory in linear and nonlinear regimes" 2006 *Plasma Phys. Cont. Fusion* **48** 1389-1400

[115] S Heuraux et al 2003 *Rev. Sci. Instrum.* **74** 1501

[116] C Fanack et al 1996 *Plasma Phys. Cont. Fusion* **38** 1915

[117] L Vermare, S Heuraux, F Clairet, G Leclert and F da Silva "Density fluctuation measurements using X-mode fast sweep reflectometry on Tore Supra" 2006 *Nucl. Fusion* **46** S743–S759

A Appendix

Derivation of the source current in the framework of the cold fluid model is described in this appendix section.

The expression for the bilinear current (multiplied by $\mathbf{e}^{+}$) in general terms reads as

$$\mathbf{e}^{+}\mathbf{j}^{nl} = \mathbf{e}^{+}e\left[n_e\mathbf{u}^{nl} + n^{\delta}\mathbf{u}^{i} + n^{i}\mathbf{u}^{\delta}\right] \tag{A1}$$

where $\mathbf{u}^{i}$ and n^{i} are linear perturbations of the electron velocity and density caused by a probing wave $\mathbf{E}^{i}$, $\mathbf{u}^{\delta}$ and n^{δ} are analogous linear perturbations associated with the fluctuations, $\mathbf{u}^{nl}$ is a quadratic perturbation - product of the probing wave interaction with the fluctuations. Linearization of the motion equations set and the charge balance equation (in the Fourier transformed form) gives

$$\mathbf{u}^{i} = \mathbf{e}_{\mu}\frac{ie}{m_e\omega^{i}}\zeta_{\mu}E^{i} \tag{A2}$$

$$n^{i} = \frac{n_e}{\omega^{i}}k^{i}_{\mu}u^{i}_{\mu} \tag{A3}$$

Keeping all the quadratic terms in the motion equations set we have

$$u^{nl}_{\mu} = \frac{ie}{cm_e\omega^{s}}e_{\mu jk}\left[u^{i}_{j}B^{\delta}_{k} + u^{\delta}_{j}\frac{c}{\omega^{i}}e_{knm}k^{i}_{n}\left(\mathbf{e}_m\mathbf{e}^{i}\right)E^{i}\right] \tag{A4}$$

here e_{ijk} is the Levi-Civita symbol. Finally, making use of the equality $e_{ijk}e_{i\alpha\beta} = \delta_{j\alpha}\delta_{k\beta} - \delta_{j\beta}\delta_{k\alpha}$ and performing the inverse Fourier transform, we end up with

$$\mathbf{e}^{+}\mathbf{j}^{nl}\left(t,\mathbf{r}\right) = i\frac{e^{2}}{m_e}\frac{n_e}{\omega^{i}}\chi_{\alpha}f^{\delta}_{\alpha}\left(t,\mathbf{r}\right)e^{-i\omega^{i}t}E^{i}\left(\mathbf{r}\right) \tag{A5}$$

This expression can be used for any probing wave polarization $\mathbf{e}^{i}$, also one should keep in mind that the source current $\mathbf{j}^{nl}$ can be expressed in various ways due to the linear relations between the fluctuating characteristics, the expression in the presented form is convenient for analysing the scattering process for a certain dominant type of the fluctuations.